

https://dspace.org/

Petrogenesis and mode of emplacement of the Doros Gabbroic Complex, Namibia

Owen-Smith, Trishya M.

2014-07-01
http://hdl.handle.net10539/14842

Downloaded from a DSpace repository. https://dspace.org/

PETROGENESIS AND MODE OF EMPLACEMENT OF THE DOROS GABBROIC COMPLEX, NAMIBIA

Trishya M. Owen-Smith

A thesis submitted to the Faculty of Science, University of the Witwatersrand, Johannesburg, in fulfilment of the requirements for the degree of

Doctor of Philosophy

Supervised by Profs. L. D. Ashwal (Wits), T. H. Torsvik (Oslo) & C. Harris (UCT)

Johannesburg, January 2014

The financial assistance of the National Research Foundation (NRF) towards this research is hereby acknowledged. Opinions expressed and conclusions arrived at are those of the author and are not necessarily to be attributed to the NRF.



Declaration

I, Trishya Owen-Smith, declare that this thesis is my own unaided work. It is being submitted for the degree of Doctor of Philosophy at the University of the Witwatersrand, Johannesburg. It has not been submitted before for any degree or examination at any other university.



(Signature of candidate)

Date: ___31/01/14_____ Place: _____Johannesburg_____

Abstract

The ~132 Ma Paraná-Etendeka Large Igneous Province consists of an extensive succession of bimodal flood volcanic rocks and intrusions across Brazil, Paraguay, Uruguay, Argentina, Namibia and southern Angola. This magmatism has been attributed to the impact of the Tristan mantle plume and the associated opening of the South Atlantic Ocean, during the Early Cretaceous breakup of West Gondwana. In southern Africa, this is preserved as the Etendeka flood volcanic succession and dyke suites, and the Damaraland Intrusive Suite, a series of subvolcanic intrusions that occur in a north-east-trending band within the Neoproterozoic Damara Orogenic Belt.

The Doros Gabbroic Complex is a relatively small (~3.5 km x 7.5 km) layered mafic intrusion that forms part of the Damaraland Suite in north-western Namibia. It is hosted by deformed Damaran metaturbidites, Damaran granitoids and Karoo-age metasedimentary strata in the Southern Kaoko Zone of the Damara Belt. The intrusion is a shallow lopolith, with an estimated thickness of at least 500 m, which consists of a sequence of roughly-concordant, sill-like gabbro layers, dipping in towards the centre, cross-cut by dolerite and bostonite dykes. It is undeformed and unmetamorphosed.

The fundamental mineralogy is essentially the same throughout the main body of the intrusion (plagioclase + calcic clinopyroxene + oxy-exsolved Fe-Ti oxides ± olivine). However, variations in the modal proportions of these minerals, and in the mineral and rock textures and compositions, define a series of layers. The stratigraphy broadly comprises: 1) a fine-grained gabbroic sill with chilled margin, present mostly as subcrop; 2) a sequence of massive, olivine-cumulate melagabbros (the Lower Zone), with a basal chilled margin, that form the outer ring of the complex; 3) a massive, plagioclase-cumulate olivine gabbro (the Intermediate Zone), comprising the inner ring of the complex; and 4) a sequence of variable, strongly foliated, plagioclase-, olivine- or magnetite-cumulate gabbros (the Upper Foliated Series), in the core of the complex. A syenitic (bostonite) phase occurs as cross-cutting dykes or enclaves within the gabbros.

In this thesis, I present a detailed petrographic study, an extensive set of whole-rock and mineral major and trace element analyses, whole-rock Sr-, Nd- and Pb-isotopic analyses, melt inclusion analyses and aeromagnetic data for the Doros intrusion. Interpretation of these data, combined with major element and trace element modelling, shows that the stratigraphic order of appearance of cumulus minerals and overall trends in rock compositions in the Doros intrusion are consistent with the fractional crystallisation of olivine, clinopyroxene, plagioclase, magnetite, K-feldspar and apatite, accompanied by variable degrees of accumulation, from a basaltic parental magma. From this combined evidence, I have put forward a compelling argument in favour of an origin for the Doros Complex by multiple, closely-spaced influxes of crystal-bearing magmas (magma mushes). This evidence includes intrusive layer relations, textural evidence for primocrysts, disequilibrium features, and stratigraphic reversals in mineral and whole-rock chemistry and magnetic properties. At least seven distinct major injections of magma have been identified in the stratigraphy, as well as several smaller pulses. Based on this interpretation, a comprehensive emplacement history for the Doros intrusion has been compiled. These

findings represent a departure from the traditional model for the formation of such intrusions by the post-emplacement differentiation of a single batch of crystal-free melt, and have fundamental implications for our understanding of layered mafic intrusions in general, which I elaborate on.

The Doros suite shows depleted ε_{Nd} of +3.67 to +6.46, moderate initial $^{87}Sr/^{86}Sr$ = 0.703970 - 0.709525, $^{206}Pb/^{204}Pb$ = 18.17 - 18.47, $^{207}Pb/^{204}Pb$ = 15.55 - 15.59 and $^{208}Pb/^{204}Pb$ = 37.93 - 38.42, at 132 Ma. The clustering of isotopic data and trends in incompatible trace element ratios indicate that all the magmas in the complex were derived from the same mantle source. I demonstrate, with the assistance of quantitative isotopic modelling, that this source comprised a dominant depleted MORB-like mantle component (60 - 80%), with a significant Tristan plume-derived, asthenospheric component (20 - 40%) and a minor contribution likely from recycled oceanic crust (< 5%). I further demonstrate that chilled margin to the complex is the only rock type that shows significant evidence of crustal contamination, due to local assimilation of the Damaran host rock on emplacement.

In addition, this research shows that the Doros suite has strong geochemical affinities with the Tafelkop group "ferropicrite" lavas of the Etendeka Province. Common features include their near-Bulk Silicate Earth initial Sr ratios, low positive ε_{Nd}, trends in ^{207}Pb-space and relatively low heavy rare earth element concentrations. Furthermore, trace element modelling of the Doros cumulates from their whole-rock chemistry suggests primary liquid compositions remarkably similar to the Tafelkop magma type. This provides crucial evidence in support of Doros as the eruptive site for the Tafelkop lavas, and thereby links the Doros magmatism to the earliest eruptive phase in the Paraná-Etendeka event. The distinctive chemistry of this magma group is attributed to the early, relatively deep, decompression melting of pyroxenitic material in the heterogeneous Tristan plume starting head, corresponding with the initial impact of the plume on the base of the lithosphere.

Acknowledgements

This research would not have been possible without the financial assistance of the National Research Foundation and the Mellon Foundation Postgraduate Mentoring Programme. I am also deeply indebted to Dr R. McG. Miller, whose experience and guidance in the field were invaluable to the project. Dr G. Schneider and the staff of the Geological Survey of Namibia are further acknowledged for the facilitation of access to the field area and the provision of geophysical data at no cost. Dr J. K. Keiding played a pivotal role in the analysis of melt inclusions in the Doros rocks. Dr R. Trumbull and Prof. J. Marsh provided cartographic material and advice. I would particularly like to thank my primary advisor, Prof. L. D. Ashwal, for his tireless supervision and mentorship. Lastly, a note of appreciation must go to the many individuals who provided support, guidance and assistance at all stages and with all aspects of the project.

Contents

Declaration ii
Abstract iii
Acknowledgements v
List of Figures ix
List of Tables xvii
Chapter 1: Introduction 1
1.1 Geological setting 1
1.2 Previous research 6
1.3 Aims and objectives of the project 16
Chapter 2: Analytical Methods 17
2.1 Major and trace element analyses 17
2.2 Radiogenic isotope analyses 18
2.3 Electron microprobe mineral analyses 19
2.4 Melt inclusion analyses 19
Chapter 3: Mapping and Field Relations 20
3.1 Introduction 20
3.2 Mapping 20
3.3 Stratigraphy and field relations 22
3.4 Comparison with the literature 35
3.5 Comparison with other layered mafic intrusions 36
3.6 Summary of findings 37
Chapter 4: Petrography and Mineral Chemistry 38
4.1 Introduction 38
4.2 Petrography 38
4.3 Rock classification 52
4.4 Layering and mineral stratigraphy 53
4.5 Hydrothermal alteration and oxidation 61
4.6 Comparison with other layered mafic intrusions 62
4.7 Summary of findings 63
Chapter 5: Whole-rock Chemical Compositions 64
5.1 Introduction 64
5.2 Whole-rock major element compositions 64
5.3 Rare earth element abundances 68
5.4 Multiple trace element variations 70
5.5 Hydrothermal alteration 74
5.6 Fractional crystallisation and evolution of the Doros magma(s) 76

5.7 Summary of findings 83
Chapter 6: Radiogenic Isotope Compositions 84
6.1 Introduction 84
6.2 Sr- and Nd-isotopic compositions 84
6.3 Pb-isotopic compositions 87
6.4 Doros dolerite and bostonite dykes 90
6.5 Summary of findings 90
Chapter 7: Melt Inclusion Mineralogy and Chemistry 92
7.1 Introduction 92
7.2 Melt inclusions 92
7.3 Petrographic characteristics of the Doros inclusion suite 93
7.4 Melt inclusion chemistry 94
7.5 Origin of Doros melt inclusions: Identification of magmas and their relation to the host rocks 99
7.6 Summary of findings 106
Chapter 8: Geophysical Analysis 107
8.1 Introduction and geological model 107
8.2 Previous geophysical research of this nature 107
8.3 Objectives of the geophysical study 108
8.4 Details of the aeromagnetic survey and data processing 109
8.5 Data images 109
8.6 Physical properties 115
8.7 Image analysis 117
8.8 Forward modelling 118
8.9 Implications of the study 125
8.10 Summary of findings 127
Chapter 9: Emplacement Dynamics and Evolution of the Suite 128
9.1 Introduction 128
9.2 Mode of emplacement 128
9.3 Conditions of emplacement 129
9.4 Origin of the Doros layering: Multiple mingling magma mushes 131
9.5 Petrogenesis of each rock type 144
9.6 Chronology of emplacement 146
9.7 Implications for Doros and other layered mafic intrusions 150
9.8 Summary of findings 151
Chapter 10: Nature of the Doros Mantle Source 152
10.1 Introduction 152
10.2 Are all the Doros units derived from a common source? 152
10.3 Nature of the Doros mantle source 155

10.4 Doros in the context of the Damaraland Intrusive Suite 161
10.5 Doros in the context of the Etendeka LIP, with particular reference to the Tafelkop group 163
10.6 A petrogenetic model for Doros-Tafelkop magmatism 167
10.7 Summary of findings 168
Chapter 11: Conclusions 169
11.1 Introduction 169
11.2 Geology and geometry of the Doros intrusion 169
11.3 Emplacement dynamics and the magmatic mush column hypothesis 170
11.4 Nature of the Doros source and implications for the LIP 171
References 173
Appendix A: Mapping 190
Appendix B: Petrography 195
Appendix C: Whole-rock chemistry 197
Appendix D: Mineral chemistry 206
Appendix E: Modelling 225
Appendix F: Melt inclusions 231
Appendix G: Geophysical data 241

List of Figures

Figure 1.1: Simplified map showing the current outcrop of the Paraná volcanic succession in South America and the Etendeka volcanic succession in Africa. 2

Figure 1.2: Distribution of the early Cretaceous Damaraland Intrusive Suite. 3

Figure 1.3: Reconstructed palaeopositions of South America, Africa and the Tristan Plume at 130 Ma 4

Figure 1.4: Geological map of the Doros Complex from Hodgson & Botha (1974). 5

Figure 1.5: Simplified map showing the present-day outcrop of the Tafelkop lavas in relation to the Doros intrusion. 8

Figure 3.1: Georeferenced satellite image of the Doros intrusion showing observation and sampling sites from this study. 20

Figure 3.2: Simplified geological map of the Doros Intrusion, depicting the main lithological units identified in this study. 21

Figure 3.3: Inferred schematic cross-section from north-west to south-east through the widest part of the Doros intrusion. 22

Figure 3.4: Generalised schematic stratigraphic section through the Doros Complex showing the main lithological units described in the text. 23

Figure 3.5: a) Remnants of Karoo sedimentary strata on the northern flank of the complex. b) Sharp contact between Karoo sandstone and chilled vesicular basal gabbro. c) Brecciation and calcite infill in the contact zone. d) Fragments of Damaran metasedimentary wall-rock entrained in the chilled gabbroic sill.. 24

Figure 3.6: a) Basal olivine melagabbro with feldpsathic schlieren. b) Close-up of feldspathic schlieren within coarse-grained BOM 25

Figure 3.7: a) Intermingling of magmas in the basal olivine melagabbro-massive olivine gabbro transition zone. b) Rounded xenoliths of olivine-rich material enclosed in massive olivine gabbro near the MOG lower contact in the tail of the complex 25

Figure 3.8: a) Linear sub-parallel concentrations of plagioclase in intrusive olivine melagabbro. b) Aligned elongate massive olivine gabbro xenoliths within intrusive olivine melagabbro in the contact zone. c) Large partially-digested raft of gabbro pegmatite within IOM. d) Fingered extension of IOM in massive olivine gabbro in the contact zone 27

Figure 3.9: a) Typical massive olivine gabbro boulder piles in the inner ring of the complex. b) MOG xenolith in foliated olivine gabbro in the contact zone. c) Small-scale interlayering of massive and foliated olivine gabbros in the contact zone. 28

Figure 3.10: Inferred approximate locations of the foliated gabbro units in the core of the ‘head’ of the complex. 29

Figure 3.11: a) Foliated olivine gabbro demonstrating the disappearance of the magmatic foliation where the rock becomes coarser grained. b) Foliated magnetite gabbro containing large coin-shaped haematised magnetite 30

Figure 3.12: a) Foliated leucogabbro showing a poikilitic texture of aligned platy plagioclase and interstitial clinopyroxene and magnetite. b) Plagioclase vein intruding coarse-grained foliated olivine gabbro. c) Interlayering of foliated gabbro and foliated leucogabbro. d) Plagioclase vein displacing the adjacent foliation in the direction of movement. 31

Figure 3.13: a) Clinopyroxene cumulate with minor interstitial plagioclase and magnetite. b) Magnetite cumulate. c) Olivine cumulate viewed perpendicular to the plane of foliation. 32

Figure 3.14: a) Pegmatitic lens within coarse-grained gabbro. b) Dyke-like body of gabbro pegmatite..... 32

Figure 3.15: Bostonitic enclave showing a typical pyroxene-rich pegmatite margin and a feldspathic centre..... 33

Figure 3.16: a) Close-up section of a bostonitic dyke. b) Bostonite dyke intruding massive olivine gabbro. c) Dolerite dyke intruding MOG. 34

Figure 3.17: a) Brecciated fragments of basaltic material within a red siliceous matrix derived from local Karoo sandstone. b) Contact between the breccia pipe and coarse-grained olivine gabbro. 35

Figure 4.1: Compositions, from mineral spot analyses, of selected a) feldspars, b) pyroxenes, c) olivines and d) Fe-Ti oxides in the Doros rocks. 40

Figure 4.2: a) Cross-polarised light (XPL) photomicrograph showing the sharp contact between glassy chilled gabbro at the margin of the gabbroic sill and siliceous Damaran metasediments. b) Back-scattered electron (BSE) image of calcic diffusion haloes surrounding relict olivine phenocrysts. c) Photomicrograph of skeletal magnetite in the chilled gabbroic sill..... 42

Figure 4.3: a) Photomicrograph of haematised subhedral olivine with interstitial plagioclase in basal olivine melagabbro. b) BSE image of interstitial ilmenite with remnant magnetite sectors..... 43

Figure 4.4: Typical intrusive olivine melagabbro, showing the variation in size of the cumulus olivine grains.. 44

Figure 4.5: Boundary between a finer-grained, more olivine-rich xenolith and coarser-grained olivine gabbro host. 44

Figure 4.6: a) Typical massive olivine gabbro. b) Ti-rich zoned clinopyroxene in MOG xenolith. c) BSE image of both trellis-type and composite-type oxy-exsolution. 45

Figure 4.7: Aligned plagioclase laths and elongate altered olivine hosted in large clinopyroxene oikocrysts in foliated olivine gabbro..... 46

Figure 4.8: Photomicrograph of typical foliated gabbro..... 46

Figure 4.9: Rounded cumulus Fe-Ti oxides in foliated magnetite gabbro, a) surrounded by haematised fractures, and b) showing trellis-type oxy-exsolution textures of variable coarseness. c) Zoned plagioclase with a K-feldspar-filled interstice. d) FMG from the base of the unit containing aligned plagioclase laths with subhedral clinopyroxene and Fe-Ti oxides..... 47

Figure 4.10: Photomicrograph showing typical foliated magnetite olivine gabbro. 48

Figure 4.11: Whole thin section view of a typical foliated leucogabbro. 48

Figure 4.12: Pyroxene-rich gabbro TOD77 showing haematised euhedral clinopyroxene with interstitial altered plagioclase. 49

Figure 4.13: a) Weakly foliated olivine-rich gabbro showing prismatic cumulus olivine grains. b) Haematised olivine grain with elliptical plagioclase inclusion. 50

Figure 4.14: a) The central pegmatitic zone of a bostonite dyke. b) BSE image of zoned euhedral clinopyroxene. c) Symplectitic radial clinopyroxene lamellae (with secondary magnetite) in feldspar. d) Exsolved Fe-Ti oxides showing preferential alteration of the host phase, in the bostonite marginal zone.. 51

Figure 4.15: Typical porphyritic dolerite showing olivine phenocrysts and plagioclase-clinopyroxene aggregates in a fine-grained plagioclase-rich matrix. 52

Figure 4.16: a) Modal plagioclase, olivine and clinopyroxene abundances for all Doros samples in this study. b) Normative mineral abundances for Doros materials. c) Oxygen norm for the end members total feldspar (FSP), clinopyroxene (AUG) and olivine (OLHY). 53

Figure 4.17: Trends in mineralogy and representative mineral chemistry (olivine forsterite content, plagioclase anorthite content, pyroxene Mg # and ulvöspinel mole fraction in titanomagnetite) through the stratigraphic succession. 54

Figure 4.18: Reconstructed stratigraphic profiles through the Doros intrusion showing changes in mineral abundances with relative height. a) Olivine; b) clinopyroxene; c) plagioclase and d) magnetite and ilmenite 55

Figure 4.19: Changes in mineral chemistry with reconstructed stratigraphic height. a) Spot analyses of anorthite content of zoned cumulus and intercumulus plagioclase grains. b) Magnesium number of single olivine grains, relative to whole-rock Mg #. c) Mg # of clinopyroxenes relative to the whole-rock. d) Mole fraction of ulvöspinel in host titanomagnetites of the Fe-Ti oxide phase 56

Figure 4.20: Variations in Fe contents of cumulus and intercumulus plagioclase with stratigraphic height. 57

Figure 4.21: Ni contents against magnesium number in olivine in the olivine-bearing units of the Doros intrusion. 57

Figure 4.22: Variations in Cr contents of clinopyroxene with stratigraphic height in the Doros intrusion 58

Figure 4.23: TiO_2, FeO, Al_2O_3, Cr_2O_3, V_2O_3 and NiO contents of spot analyses of the titanomagnetite host phase of Fe-Ti oxide grains in the Doros intrusion 59

Figure 4.24: Concentrations of MgO vs. MnO in ilmenite lamellae of Fe-Ti oxides in the Doros intrusion. 60

Figure 4.25: Equilibrium temperatures and oxygen fugacities calculated from co-existing magnetite-ilmenite pairs. 61

Figure 5.1: Classification of all Doros samples using the total alkalis versus silica diagram for plutonic rocks . 64

Figure 5.2: CIPW normative diopside, olivine, hypersthene, nepheline and quartz in the Doros rocks. 65

Figure 5.3: Whole-rock SiO_2 vs. a) MgO and b) total Fe as FeO, for the complete Doros suite. 66

Figure 5.4: Whole-rock MgO against a) Al_2O_3, b) CaO, c) TiO_2, d) total FeO, e) Na_2O and f) K_2O, for the complete Doros suite. 67

Figure 5.5: Reconstructed stratigraphic profiles through the main body of the Doros intrusion showing changes in major element contents. a) MgO, b) total FeO, c) Na_2O and d) magnesium number. 68

Figure 5.6: Rare earth element abundances for the Doros intrusive suite. a) Basal olivine gabbro, intrusive olivine gabbro, gabbro pegmatite, chilled gabbroic sill and chill margin samples. b) Massive olivine gabbro, bostonite and pyroxene cumulate enclave. c) Foliated gabbro and foliated olivine gabbro, foliated magnetite and foliated magnetite olivine gabbro, and foliated leucogabbro 69

Figure 5.7: Normative anorthite abundances against the magnitude of the europium anomaly. 70

Figure 5.8: Primordial mantle-normalised multi-element diagram for a) the Upper Foliated Series, massive olivine gabbro, pyroxene cumulate enclave and bostonite dykes, and b) the Lower Zone units, chill margin and sill, gabbro pegmatite and olivine-rich xenoliths of the Doros suite. 71

Figure 5.9: Whole-rock trace element compositions for the complete Doros suite plotted against MgO content. a) Sr, b) Ni, c) Cr, d) V, e) Zr, and f) Y 73

Figure 5.10: Reconstructed stratigraphic profiles through the main body of the Doros intrusion showing changes in selected incompatible trace element concentrations. 74

Figure 5.11: a) Cu and b) Li concentrations for the Doros suite, shown against MgO 75

Figure 5.12: Total volatile content (LOI + SO_3 + H_2O) plotted against the Chemical Index of Alteration (CAI) for the Doros suite. 76

Figure 5.13: Modified version of the Fo-Di-An ternary system using oxygen norms. 77

Figure 5.14: Selected major and trace elements against MgO showing the Doros samples alongside the trends identified by Marsh *et al*. (2001) and Marsh & Duncan (2008). 78

Figure 5.15: Calculated trace element compositions of the original liquids of each of the major units in the Doros intrusion, in comparison to the complete Doros cumulate suite and bostonites. 80

Figure 5.16: Results of MELTS major element modelling shown with the complete Doros suite 82

Figure 6.1: Initial Sr- and Nd-isotopic compositions for the Doros intrusive suite, relative to approximate compositions of the mantle reservoirs. 84

Figure 6.2: Initial Sr ratios against Li concentrations for the Doros units analysed in this study 86

Figure 6.3: Initial Sr- and Nd-isotopic compositions of the Doros intrusive suite, compared with representative fields for the Tafelkop lavas, other Paraná-Etendeka mafic magma groups and modern-day Tristan group lavas. 87

Figure 6.4: Measured Pb-isotopic compositions of the Doros gabbroic suite in relation to the approximate compositions of the mantle end member components. 88

Figure 6.5: Measured Pb-isotopic compositions of the Doros and Tafelkop suites with the Pb evolution curves. 89

Figure 6.6: Initial (132 Ma) Pb-isotopic compositions of the Doros intrusive suite, in comparison with the main Etendeka mafic magma groups and Tristan group lavas 90

Figure 7.1: Photomicrographs (a) and backscattered electron (BSE) images (b-f) of unhomogenised olivine-hosted melt inclusions in the Doros melagabbros. 94

Figure 7.2: Total alkalis versus silica for olivine-hosted melt inclusions analysed in each of three samples, TOD70 (IOM), DO-09-2 (BOM) and DO-09-9 (not *in situ*, but inferred to be BOM), compared with the Doros whole-rock suite. 95

Figure 7.3: a) MgO and b) total FeO against SiO_2 for the Doros olivine-hosted melt inclusions, in relation to the whole-rock suite. 96

Figure 7.4: Major element compositions against MgO for the Doros olivine-hosted melt inclusions, in relation to the whole-rock suite. 97

Figure 7.5: a) Rare earth element and b) mantle-normalised trace element abundances for olivine-hosted melt inclusions in intrusive olivine melagabbro sample TOD70, in relation to the Doros whole-rock suite . 98

Figure 7.6: Incompatible trace element bivariate plots for the Doros melt inclusions (sample TOD70), shown with the whole-rock suite. 99

Figure 7.7: Major element trends in the Doros melt inclusion suite, suggesting mixing between an Mg-rich component A and Mg-poor component B 102

Figure 7.8: CaO/Al_2O_3 versus Mg # for the Doros melt inclusions, compared to the whole-rock suite. 103

Figure 7.9: Th/Yb and Nb/Yb for melt inclusions (sample TOD70) alongside the Doros whole-rock suite, Damaran country rock and representative mantle and crustal components. 104

Figure 7.10: Rare earth element ratios for the Doros melt inclusions (sample TOD70), in comparison to the whole-rock suite, typical MORB and OIB, and modern-day Tristan plume basalts. 105

Figure 8.1: Gridded total magnetic intensity data (in nT) for the study area 110

Figure 8.2: Map of reduced-to-pole magnetic anomaly data for the Doros gabbroic intrusion and surrounding Damaran granitoid plutons and schists, overlain with the mapped surface geology from this study and satellite imagery 111

Figure 8.3: First vertical derivative of the pole-reduced aeromagnetic data over the Doros intrusion (in nT/m), overlain with the mapped surface geology 112

Figure 8.4: Second vertical derivative of the pole-reduced aeromagnetic data (nT/m^2) over the Doros intrusion and surrounding regions. 113

Figure 8.5: Analytical signal of the RTP data (unitless) over the Doros intrusion, with the mapped surface geology. 114

Figure 8.6: RTP magnetic data upward continued at an elevation of 2 000 m, overlain with the mapped surface geology. 115

Figure 8.7: Two models for a section of profile L150 through the tail of the Doros Complex. a) Model 15 considers only a simple, shallow, inwardly-dipping body of Doros gabbro (BOM). b) Model 13 considers the same Doros body, with the addition of a mafic sill to the east that is not exposed on surface. 121

Figure 8.8: Three models for the center section of profile MP1 through the head of the Doros Complex. a) Model 34 considers a layered Doros body (only those units mapped on surface) with a constant dip (approximately as measured). b) Model 25 considers a layered Doros body with a variable dip that flattens out at depth. c) Model 30 considers the effect of an additional gabbro layer not exposed on surface that may represent an ultramafic zone, as well as a northward-dipping granite pluton 123

Figure 8.9: Modelled gravity response for a section of profile MP1, considering two different configurations for the Doros granitoid pluton 125

Figure 8.10: A revised schematic cross-section (roughly 1:1) through the widest part of the Doros intrusion (close to profile MP1), incorporating the findings of the aeromagnetic survey 126

Figure 8.11: Map of the Doros intrusion showing the extents inferred from geophysics (not surface exposures) of the BOM outer contact, the chilled gabbroic sill, the magnetite-bearing gabbros, dolerite dykes outside the complex and the granite plutons. 127

Figure 9.1: Compositions of quartz latite clasts in the Doros breccia pipe relative to the main silicic magma types of the Etendeka succession. a) Cu against TiO_2. b) The canonical variables from the discriminant function analysis of Milner & Duncan (1987). 131

Figure 9.2: Plagioclase schlieren in a boulder of basal olivine melagabbro. 135

Figure 9.3: Modal layering with a gradational upward decrease in olivine content in a boulder in the core of the head of the complex. 137

Figure 9.4: Fine-grained, red, chilled material marginal to a pyroxene-rich coarse-grained gabbro, mingling with leucocratic gabbro in the core of the head of the complex. 138

Figure 9.5: An intruding coarse-grained gabbro layer showing accumulations of cumulus clinopyroxene crystals against the basal contact with homogeneous massive olivine gabbro. 139

Figure 9.6: Whole-rock Al_2O_3 vs. MgO compositions for the Doros suite showing the major trends in fractionation in stratigraphic order. 140

Figure 9.7: REE abundances for the major units of the Doros intrusion. 141

Figure 9.8: Magnetic stratigraphy of the Doros intrusion inferred from the quantitative modelling of aeromagnetic data in Chapter 8. 142

Figure 9.9: Schematic stratigraphic column for the Doros intrusion indicating the levels of intrusion inferred for each magma influx 143

Figure 9.10: A schematic representation of the proposed emplacement model for the Doros Intrusion. 148

Figure 10.1: Initial $^{206}Pb/^{204}Pb$ against elemental Pb concentrations for the Doros units, compared with the Horingbaai dolerite dyke suite, fields for the other Etendeka mafic magma types, Mid-Atlantic Ridge basalts, and Tristan group lavas..... 153

Figure 10.2: Simple fractionation model in terms of the REE indicating that a liquid of bostinitic composition may plausibly be derived by 86% fractional crystallisation (specifically 41% plagioclase, 32% clinopyroxene, 11% olivine and 11% magnetite) from a Doros gabbro (in this case the chilled gabbroic sill) 154

Figure 10.3: Rare earth element concentrations for the major units of the Doros suite, in relation to fields for the Tafelkop, Khumib and Horingbaai magma groups of the Etendeka, as well as modern-day Tristan group lavas. 155

Figure 10.4: Initial a) Sr- and b) Nd-isotopic compositions against initial ^{206}Pb for the Doros suite, Etendeka mafic magma groups and southern Mid-Atlantic Ridge basalts. 156

Figure 10.5: Initial Sr versus 1/Sr for the Doros suite, Etendeka mafic magma groups, Tristan group lavas and southern Mid-Atlantic Ridge basalts, as well as global subducting sediment (GLOSS) and Damaran metasedimentary rocks. 157

Figure 10.6: Modelled Sr-Nd mixing curves between plume-free southern Mid-Atlantic Ridge (MAR) basalt, representing a depleted mantle component, and average Tristan basalt, representing a plume component, with an additional enriched a) crustal component, represented by average Damaran metasediments, or b) mantle component, represented by global subducting sediment (GLOSS) 158

Figure 10.7: Th/Yb vs. Nb/Yb for the Doros suite, in relation to Tristan group compositions, the Etendeka mafic magma groups and average Damara metasediments. 160

Figure 10.8: Th/Ta against Th/Tb for the Doros suite, compared with compositions for modern-day Tristan lavas and the mafic magma groups of the Paraná-Etendeka Province.. 161

Figure 10.9: Initial Sr- and Nd-isotopic compositions for the Doros intrusion in relation to the Damaraland Suite, specifically the Okenyenya, Messum, Erongo, Etaneno, Kalkfeld, Brandberg, Paresis, Ondurakorume, Okorusu and Osongombo Complexes. 162

Figure 10.10: Zr/Yb versus Nb/Yb for the Doros suite, Tristan group lavas, Etendeka mafic magma groups and the field of mafic rock types in the Damaraland intrusive suite 163

Figure 10.11: REE and Y compositions of calculated original liquids for the Doros mushes with the field of Tafelkop group lavas from the Etendeka succession. 165

Figure 10.12: The possible original extent of the Tafelkop basalts. 165

Figure 10.13: Schematic illustration of the petrogenetic model envisaged for the Doros-Tafelkop magmatism. 168

Figure A.1: Geological map of the Doros Intrusion showing the major lithological units and selected minor units and dykes defined in this study. 193

List of Tables

Table 2.1: Detection limits (wt. % oxide) and RMS deviations for major element analyses by XRF 17

Table 2.2: Within-run REE analyses (ppm) of BHVO-2 compared to published reference values 18

Table 3.1: Comparison of lithological classification systems for the Doros Complex 36

Table 4.1: Approximate visually-estimated modal abundances for each of the Doros lithological components . 39

Table 4.2: Microprobe analyses (unnormalised) and CIPW normative abundances of glass in the Doros chill margin 41

Table 7.1: Approximate compositions (in wt. %) of melt inclusion mixing components, based on either MgO or SiO_2 contents 101

Table 8.1: Averages of measured magnetic susceptibilities (*k*) of selected rock types 116

Table 9.1: Results of olivine-clinopyroxene geothermobarometry for the Doros gabbros 130

Table 10.1: Modelled mantle source compositions of the Etendeka mafic magma types from Ewart *et al*. (2004a) 164

Table A.1: Locations of all sampled material (waypoints correspond to map in Figure A.1) 191

Table B.1: Details of sample material available for petrographic analysis 196

Table C.1: Whole-rock major (wt. %) and trace element (ppm) compositions of the Doros suite 198

Table C.2: Additional whole-rock major and trace element analyses from this study 202

Table C.3: CIPW normative mineral abundances for all analyses 203

Table C.4: Whole-rock Sr-, Nd- and Pb-isotopic analyses for the Doros suite and an associated dolerite dyke 205

Table D.1: Microprobe analyses of olivines in rocks of the Doros suite 207

Table D.2: Microprobe analyses of feldspars in rocks of the Doros suite 209

Table D.3: Microprobe analyses of pyroxenes in rocks of the Doros suite 214

Table D.4: Microprobe analyses of Fe-Ti oxides in rocks of the Doros suite 220

Table D.5: Microprobe analyses of amphiboles in the Doros bostonite 223

Table D.6: Equilibrium conditions determined from co-existing Fe-Ti oxides using the program ILMAT. 224

Table E.1: Results of MELTS fractional crystallisation modelling (pressure at 1 kbar; fO_2 at QFM) 226

Table E.2: Modelled liquid REE compositions for selected Doros samples, calculated from whole-rock chemistry 227

Table E.3: Partition coefficients for REE in plagioclase used in modelling of the Doros liquid, calculated from the An# 228

Table E.4: Partition coefficients for REE in olivine used in modelling of the Doros liquid, calculated from the melt MgO content 229

Table E.5: Parameters for end members used in isotopic mixing modelling of the Doros source 230

Table E.6: Partition coefficients for gabbroic sill TOD58 used in the modelling of bostonitic daughter compositions 230

Table F.1: Major element compositions (wt. %) of daughter phases and glass in unhomogenised olivine-hosted melt inclusions 232

Table F.2: Uncorrected major element compositions (wt. %) of homogenised melt inclusions 235

Table F.3: Major element compositions (wt. %) of homogenised melt inclusions 238

Table F.4: Trace element compositions (ppm) of homogenised melt inclusions determined by ion probe 240

Table G.1: Measured magnetic susceptibilities (*k*) for selected samples 242

Table G.2: Typical densities for the Doros intrusion and host rocks 243

Chapter 1: Introduction

This thesis is a petrographic, geochemical and geophysical investigation into the petrogenesis of the Doros Complex, a shallow-level layered mafic intrusion within the early Cretaceous Paraná-Etendeka Large Igneous Province in Namibia. Such intrusive cumulate bodies have long been prized for the link they provide between magmatic events deep in the mantle and the volcanic end-products erupted on surface, and specifically for the record they preserve of the spectrum of melting and differentiation processes that occur in this interval, that would otherwise be inaccessible to us. The Doros Complex is particularly valuable because of the contribution it can make to two main avenues of controversial current research. Firstly, it provides unique insight into the workings of a Large Igneous Province (LIP), in this case the Paraná-Etendeka system, specifically with regard to the nature and source of the primary magmas, the mechanisms of magma ascent and the role of mantle plumes. Secondly, it contributes to our understanding of the magma dynamics and crystallisation history of layered mafic intrusions, particularly pertaining to the nature of the input material, the style of emplacement, the conditions and processes of differentiation, the formation of layering and the connection between magma chambers and the greater magmatic system. These contributions are valued, not only for the insight they provide into major tectonomagmatic events in Earth's history, but also for the implications this has for mineralisation processes and the formation of economic ore bodies.

1.1 Geological setting

1.1.1 The Paraná-Etendeka Large Igneous Province

The ~132 Ma Paraná-Etendeka Large Igneous Province (Fig. 1.1) consists of an extensive succession of bimodal flood volcanic rocks and intrusions across Brazil, Paraguay, Uruguay and Argentina (Paraná), and Namibia and southern Angola (Etendeka; Miller, 2008c). This ranks as one of the largest LIPs known, with a preserved surface area of approximately 1.5 x 10^6 km^2 and an original magma volume estimated at more than 2.3 x 10^6 km^3 (Courtillot & Renne, 2003). The majority of volcanism occurred within a period of 1 m. y. (Renne *et al*., 1992).

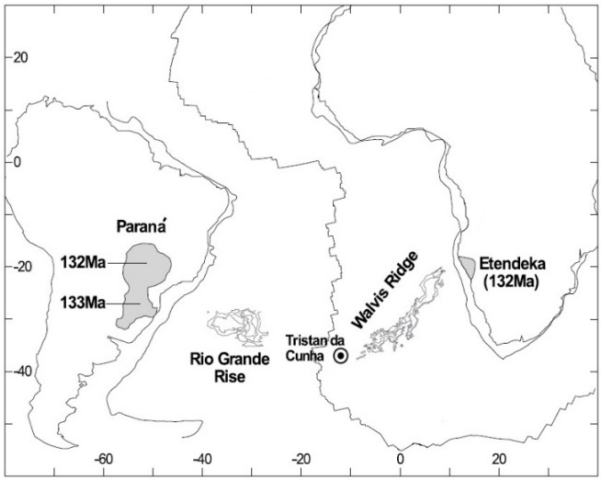


Figure 1.1: Simplified map showing the current outcrop of the Paraná volcanic succession in South America and the Etendeka volcanic succession in Africa (after Ernesto *et al*., 2002). Together these form the Paraná-Etendeka Large Igneous Province. Also shown is the present-day position of the Tristan mantle plume, under Tristan da Cunha Island, as well as the Walvis Ridge and Rio Grande Rise, remnants of offshore plume volcanism.

The African component of the LIP (Fig. 1.1) is relatively minor in volume, but much better exposed than its South American counterpart (Marsh *et al*., 2001). In Namibia, this is preserved as the Etendeka volcanic succession and dyke suites and the Damaraland Intrusive Suite.

The approximately 1 km-thick Etendeka volcanic sequence comprises tholeiitic basalts, basaltic andesites, latites and quartz latites (Miller, 2008c). Within the mafic and siliceous suites, distinct magma types may be recognised by their geochemical compositions and regional distribution (Miller, 2008c). Several of these have been chemically correlated with equivalent magma types in the Paraná (Peate *et al*., 1992; Milner *et al*., 1992, 1995; Ewart *et al*., 1998a; Marsh *et al*., 2001). Previous dating of the Etendeka volcanic rocks by $^{40}Ar/^{39}Ar$ and $^{87}Rb/^{86}$ Sr isochron methods has yielded ages between 132 and 127 Ma, the majority clustering around 132 Ma (Milner *et al*., 1995; Renne *et al*., 1996; Kirstein *et al*., 2001).

The Damaraland Intrusive Suite consists of more than 20 ring complexes, stocks, plugs and diatremes, occurring in a NE-trending band across Namibia, predominantly within the Neoproterozoic Damara Orogenic Belt (Fig. 1.2; Miller, 2008b). The intrusions exhibit a wide range of rock types, but can generally be classified as those consisting mainly of gabbro, alkali granite, syenite and foyaite, carbonatite, or most commonly, combinations of these (Miller, 2008b). There is substantial evidence relating intrusive activity in the Damaraland Complexes to the Etendeka volcanism (Milner *et al*., 1995; Miller, 2008b). Apart from the obvious spatial association, the intrusive suite has been shown to be contemporaneous with the Etendeka event, although encompassing a wider age range of between 140 and 123 Ma (dating by $^{40}Ar/^{39}Ar$ methods: Renne *et al*., 1996, Stewart *et al*. 1996; Schmitt *et al*. 2000; $^{40}Ar/^{39}Ar$ and U-Pb zircon: Wigand, 2005; Rb-Sr: Milner *et al*., 1995). There are also common compositional and isotopic characteristics (Ewart *et al*., 1998a; Le Roex & Lanyon, 1998; Trumbull *et al*., 2000). The Damaraland intrusions are in general interpreted to represent the eroded roots of Etendeka volcanoes, from remnants of preserved lavas and evidence of cauldron subsidence (Marsh *et al*., 2001;

Bauer *et al*., 2003; Miller, 2008b). However, the Messum Complex (Fig. 1.2) is the only Damaraland intrusion yet to have been confirmed as the eruptive site of a specific Etendeka lava formation, by compositional correlation (Milner & Ewart, 1989; Milner *et al*., 1995; Miller, 2008b).

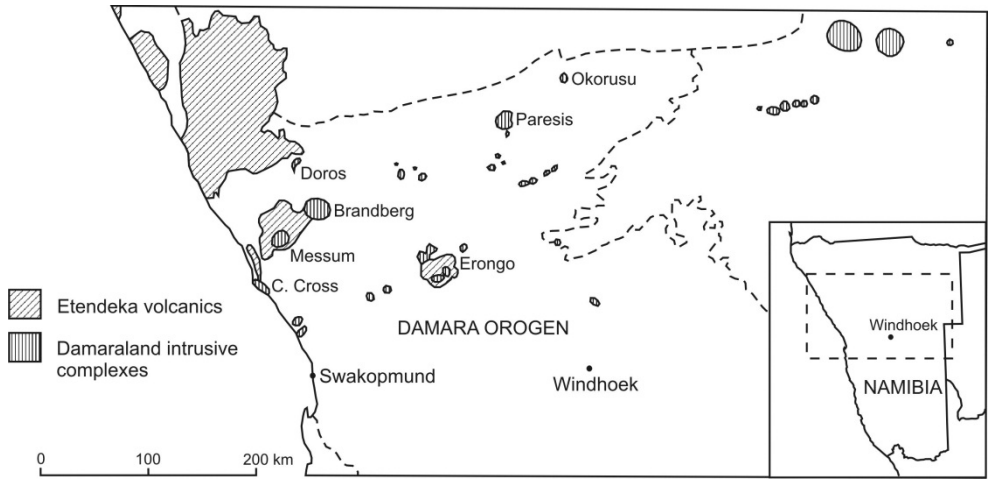


Figure 1.2: Distribution of the early Cretaceous Damaraland Intrusive Suite, including the Doros intrusion, and the present outcrop of the Etendeka volcanic rocks (after Miller, 2008b).

1.1.2 The Tristan mantle plume and rifting of the South Atlantic Ocean

The greater Paraná-Etendeka magmatic event has been attributed to the impingement of the Tristan mantle plume (Fig. 1.3) on the lithosphere and the associated opening of the South Atlantic Ocean, during the early Cretaceous breakup of West Gondwana (e.g. Milner *et al*., 1995; Le Roex & Lanyon, 1998; Ewart *et al*., 1998a, 2004a; Miller, 2008c). Evidence to support this interpretation includes close isotopic and trace element compositional similarities between some of the Paraná-Etendeka magma types and the plume, as identified from modern Tristan volcanic products (Hawkesworth *et al*., 1992; Le Roex & Lanyon, 1998; Ewart *et al*., 1998a, 2004a); the distribution of lavas about the original rift, on either side of the Atlantic Ocean (Peate *et al*., 1990); and the progression of ages and palaeomagnetic plate reconstructions that show the fit of the African and South American plates at the time of magmatism (Fig. 1.3), and their subsequent separation (O'Connor & Duncan, 1990; Gallagher & Hawkesworth, 1994; Torsvik *et al*., 2009). The Walvis Ridge and Rio Grande Rise link the Paraná and Etendeka with the present-day position of the plume, beneath the Tristan da Cunha island group (Fig. 1.1; O'Connor & Duncan, 1990; Ewart *et al*., 2004a; Miller, 2008b).



Figure 1.3: Reconstructed palaeopositions of South America, Africa and the Tristan Plume (T) at 130 Ma from Torsvik *et al*. (2009). P indicates the Paraná Province and E the Etendeka Province.

Although the geochemistry of the Paraná and Etendeka volcanic rocks has been extensively studied, there is still little agreement on the exact role of the mantle plume in the production of the magma types observed (Trumbull *et al*., 2000). This is largely because the majority of the lavas do not show a recognisable plume signature (Marques *et al*., 1999; Ernesto *et al*., 2002; Trumbull *et al*., 2000), since their primary compositions have been obscured by crustal contamination (Trumbull *et al*., 2003). There is also much controversy over the relative involvement of subcontinental lithospheric mantle (SCLM) and the source of the more evolved rock types. Some workers propose that much of the observed compositional variation derives from heterogeneous lithosphere (e.g. Peate & Hawkesworth, 1996; Marques *et al*., 1999; Gibson *et al*., 1999, 2006). Other workers argue that no SCLM involvement is required and that all compositions can be explained by differing mantle components (plume, N-MORB, subducted material) and variable degrees of crustal contamination (e.g. Ewart *et al*., 1998a, 2004a).

The Damaraland Intrusive Suite offers an alternative means to approach to the problem. The suite encompasses a wider range of rock types and therefore a greater compositional spectrum for which to investigate magma sources (Trumbull *et al*., 2000). The mafic and alkaline rock types of the intrusions are particularly well-suited to the assessment of mantle source components, since these consistently show O-, Sr- and Nd-isotopic compositions that have not been affected by significant crustal contamination (Trumbull *et al*., 2000, 2003). Also, unlike for the lavas, the sites of magmatism in the Damaraland intrusions are accurately spatially located. This allows for the examination of changing source

compositions with location, with respect to the plume, as well as to the crust through which the magmas were emplaced (Trumbull *et al*., 2000).

1.1.3 The Doros Complex

The Doros Gabbroic Complex (Fig. 1.4) is a relatively small (~8 km x 4 km) layered mafic intrusion that forms part of the Damaraland Intrusive Suite (Hodgson & Botha, 1974; Marsh & Duncan, 2008). It intrudes the contact between the Doros Salem-type granite-syenite pluton (~530 Ma; Schmitt *et al*., 2012) and strongly-folded, steeply-dipping, middle to upper greenschist facies rocks of the Zerrissene Group metaturbidite sequence (630 - 700 Ma), in the Southern Kaoko Zone of the Damara Orogenic Belt (Hodgson & Botha, 1974; Passchier *et al*., 2007; Marsh & Duncan, 2008; Miller, 2008). The Damaran rocks were originally overlain by Karoo Supergroup strata, and thin remnants of near-horizontal upper Dwyka and lower Ecca sandstones and shales (~300 Ma) are preserved below the gabbros on the Doros rim (Reuning & Martin, 1957; Hodgson & Botha, 1974; Miller, 2008d). The distinctive teardrop-shaped geometry of the Doros intrusion (Fig. 1.4) has been noted to correspond with pre-existing regional fold and foliation structures in the Damara Belt (Hodgson & Botha, 1974). The intrusion consists of several gabbroic units with varying textures, mineralogy and compositions, cut by syenitic (so-called "bostonite") dykes (Marsh & Duncan, 2008).

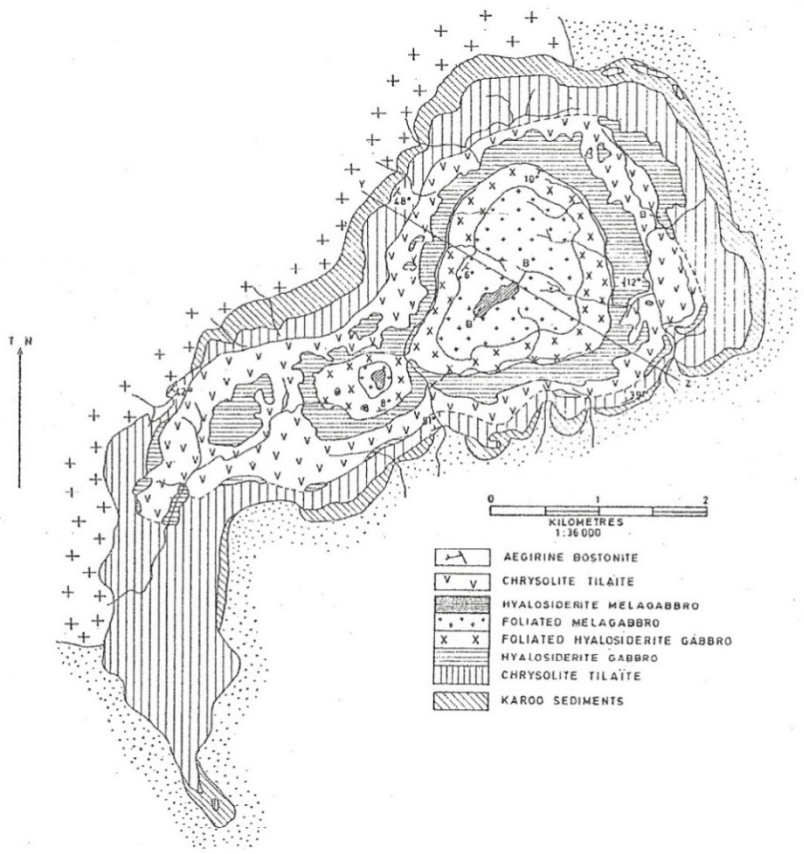


Figure 1.4: Geological map of the Doros Complex from Hodgson & Botha (1974), showing their lithological nomenclature.

Previous geochronology of the intrusion is limited to the dating by K-Ar methods of a single gabbro sample (whole-rock and mineral separates) by Siedner & Mitchell (1976), yielding ages of 134 - 124 Ma. An isochron produced from these gave an age of 134.2 ± 0.9 Ma. This confirms contemporaneity with the Paraná-Etendeka event.

The nature of any mineralisation in the complex is largely unknown, although reports of traces of native copper in the upper gabbro units by Reuning & Martin (1957) have since inspired small-scale prospecting in the area.

1.2 Previous research

1.2.1 Doros and its emplacement and crystallisation history

The Doros Complex has received little academic attention compared to some of the other Damaraland intrusions. The earliest, rudimentary descriptions of the Doros geology come from Reuning & Martin (1957). Subsequent research by Hodgson & Botha (1974) and Marsh & Duncan (2008) described and classified the rock types of the intrusion, based on field observations, petrographic analysis, a small number of whole-rock major element and selected trace element analyses, and optically-determined mineral compositions. No rare earth element or isotopic analyses have previously been obtained, nor has any investigation of geophysical properties been conducted.

Hodgson & Botha (1974) identified seven major lithological units in the Doros package (Fig. 1.4). At the base is an olivine-rich gabbro termed **chrysolite tilaïte**, bordered by a chilled **gabbro aplite**. This is overlain by a second layer of **chrysolite tilaïte**, which was interpreted as a later intrusion of magma into the complex. Above this is a more plagioclase-rich **hyalosiderite gabbro**. This is followed by a **foliated hyalosiderite gabbro**, a **foliated melagabbro** and finally a **hyalosiderite melagabbro** unit, that caps the intrusion. Lenses of **gabbro pegmatite** and felsic dykes, classified as **aegerine bostonite,** were documented to cut the upper units. Marsh & Duncan (2008) called for this classification and its generally out-dated terminology to be revised, and hence this is revisited in Chapter 3.

Hodgson & Botha (1974) further attempted to interpret the emplacement dynamics and crystallisation of the Doros magmas based on their field evidence and the major element compositions of seven samples. These authors proposed five periods of magma intrusion in the Doros Complex, as follows: The first pulse of gabbroic magma produced the chrysolite tilaïte to hyalosiderite gabbro units. The marginal chilled layer was interpreted as approximately representing the composition of the original magma. A second injection of gabbroic magma, inferred from a slight interruption to the differentiation trend, gave rise to the upper sequence of foliated gabbro units. A third injection was intruded into the existing package to form the second chrysolite tilaïte. The final phase was the injection of residual magma to form the gabbro pegmatite and, lastly, the aegerine bostonite dykes, interpreted as the alkaline end-product of differentiation. Each layer in the complex was proposed to correspond to a crystallisation cycle with the

sequence magnetite, to olivine, to pyroxene and plagioclase, with interludes marked by sharp interlayer contacts (Hodgson & Botha, 1974).

While this is clearly an insufficient database for a comprehensive analysis of fractionation, Hodgson & Botha (1974) bring to attention the fact that the Doros intrusion may have formed from multiple pulses of magma, and that this may be recognisable both in the field and with geochemical parameters. An evaluation of this hypothesis is central to the discussion of emplacement dynamics in Chapter 10.

Marsh *et al*. (2001) and Marsh & Duncan (2008) recognised two main geochemical trends in the Doros gabbros. They noted that a group of samples from the basal and upper units showed very little variation in the incompatible elements TiO_2, K_2O, Zr and Y with respect to MgO, and these were thus recognised as orthocumulates, having retained a relatively large and constant fraction of the residual liquid. A smaller group of samples was observed to show an increase in these components with decreased MgO, and were thus termed meso- and adcumulates, although no textural evidence was reported. The orthocumulate gabbros were proposed by Marsh and Duncan (2008) to approximately represent the composition of the original Doros magma.

While inferring magma compositions from cumulate rocks is highly problematic, and this distinction in geochemical trends is tenuous at best, the interpretations of Marsh and Duncan (2008) have proved instrumental in proposed correlations with the Etendeka volcanic succession, as will be discussed.

1.2.2 Source of Doros magmatism and the Tafelkop connection

No attempt has previously been made to investigate the mantle source of the Doros magmatism or its relation to the Tristan mantle plume. Early studies (Reuning & Martin, 1957; Hodgson & Botha, 1974) considered it part of the Karoo magmatic event, although genetic links with other Namibian alkaline intrusions (now the Damaraland Suite) and apparent affinities with nearby Etendeka "melaphyres" were suggested. This association with Etendeka volcanism was only actively investigated by Marsh *et al*. in 2001. These authors proposed that the Doros Complex may be the eruptive source of the Tafelkop Formation lavas of the Etendeka (Fig. 1.4). This is based on the spatial proximity of Doros to the present outcrop of the Tafelkop lavas, the apparent thickening of these lavas towards Doros and the suggested similarities between the Tafelkop basalts and Doros 'orthocumulate' group in terms of selected trace element ratios and unpublished Sr- and Nd- isotopic data (Marsh *et al*., 2001).

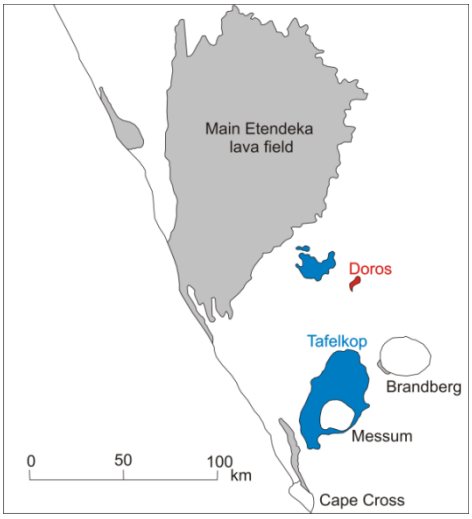


Figure 1.5: Simplified map showing the present-day outcrop of the Tafelkop lavas in relation to the Doros intrusion (after Miller, 2008c).

The Tafelkop suite itself represents an important magma group within the Paraná-Etendeka LIP. The Tafelkop olivine basalts are found at the very base of the volcanic succession in the southern Etendeka lava field (Miller, 2008c). They directly overlie, and in some places are intercalated with, the dune sands onto which the Etendeka was erupted (Miller, 2008c). One such flow has been dated at 132.0 ± 0.7 Ma ($^{40}Ar/^{39}Ar$; Renne *et al*., 1997 in Tuff *et al*., 2005). These lavas, and their associated doleritic feeders, have particularly high MgO (5 - 16 wt. %) and FeO_{Total} (10 - 16 wt. %; Ewart *et al*., 1998a; Jerram *et al*., 1999; Gibson *et al*., 2000; Thompson *et al*., 2001), and were thus classified by Gibson *et al*. (2000) and Thompson *et al*. (2001) as ferropicrites. They are distinct within the Etendeka Province due to their high and variable Ti/Y, Ti/Zr and Zr/Y, relatively low heavy rare earth element concentrations, and near-Bulk Silicate Earth initial Sr ratios (mean of 0.704857), with positive ε_{Nd} (mean of +1.6; Ewart *et al*., 1998a; Gibson *et al*., 2000; Thompson *et al*., 2001; Marsh *et al*., 2001; Miller, 2008c). There is no compositional equivalent in the Paraná Province (Ewart *et al.*, 1998a). Importantly, this magma group shows a clear, dominant Tristan plume signature, with relatively little crustal contamination or fractionation (Milner & Le Roex, 1996; Ewart *et al.* 1998a, 2004a; Gibson *et al.*, 2000). Ewart *et al*. (2004a) interpreted these magmas as plume melts, with minor entrained N-MORB and subducted sediments. Gibson *et al.* (2000) proposed early melting of iron-rich veins in the Tristan plume head, corresponding with the initial impingement of the plume on the base of the lithosphere.

Problems have already been raised here regarding the interpretation of the so-called Doros 'orthocumulate' group of Marsh & Duncan (2008) as representing a parental magma. Furthermore, Marsh *et al.* (2001) rely on minimal trace element data and a comparison of element trends between cumulate plutonic and volcanic rocks, a method which is arguably insufficient. Nevertheless, this suggested link between Doros and the Tafelkop basalts has important implications, including for the original extent of the lavas and the spatial location of the source of the Tafelkop magmas, particularly in relation to the plume. If the Doros Intrusion is indeed the source of the Tafelkop basalts, this would provide a more

complete magma system to investigate, from plutonic cumulates through to their volcanic products, and provide additional information on the earliest stage of plume impingement and continental flood basalt volcanism. This is therefore a crucial aspect for further investigation, but a different approach needs to be taken. It is proposed that isotopic tracers, no data for which have previously been published, will be a more robust method of detecting common magmatic origins. Isotopic data produced in this study, and the implications of these, are discussed in Chapters 7 and 11.

1.2.3 Large Igneous Provinces and mantle plumes

LIPs are areally-extensive magmatic provinces, comprising large volumes of magma (> $0.1x10^6$ km^3), in the form of dyke swarms, sill provinces, intrusive complexes and flood volcanic suites, emplaced over a relatively short period of time (< 5 m. y.; Bryan & Ernst, 2008). They are the most volumetrically-significant form of magmatism that is apparently unrelated to plate tectonics (Campbell, 2005). It is this latter property that has made their origins so intriguing and the subject of several decades of focussed research.

While some dissenters remain (e.g. Sheth, 1999; Foulger, 2002; Jones *et al*., 2002; Anderson, 2005), the general consensus is that LIP magmatism is generated by mantle plumes (Ernst & Buchan, 2003; Campbell, 2005), as the only hypothesis that can adequately account for all the features observed. However, there is less agreement on the exact role of plumes in producing the range of magmatic products, their relation to tectonic events, specifically uplift and rifting, their evolution over time and the nature of the plumes themselves, i.e. their source regions, their structure and the form they take (Coffin & Edholm, 1992; Ernst & Buchan, 2003; Ernst *et al*., 2005; Saunders *et al*., 2007). Each of these aspects has fundamental implications for our understanding of LIPs.

Plumes provide an essential link with the interior of the Earth, and more specifically, valuable insight into mantle dynamics and chemical heterogeneities. However, a major challenge is that they cannot be observed directly. Studies of plume dynamics thus rely largely on geophysical means, or on the interpretation of the products of plume magmatism at or near the surface, a large component of which are the LIPs (Ernst *et al*., 2005; Hawkesworth & Scherstén, 2007). Geochemistry is an essential tool here, for its role in elucidating the source components of LIP magmatism, specifically the relative contributions of asthenosphere, mantle lithosphere and crust, the conditions of melt generation, and the structure and evolution of the plume itself (Chesley & Ruiz, 1998; Ernst *et al*., 2005; Hawkesworth & Scherstén, 2007). As discussed in the previous sections, the Doros intrusion provides an important opportunity to investigate the role of the Tristan mantle plume in the Paraná-Etendeka LIP, due to the potential link with the Tafelkop lavas, which have a clear plume signature and are well-constrained in time.

Much of the controversy surrounding LIP genesis may be resolved to some extent by better characterisation of individual LIPs, i.e. determining their original extent, quantifying the rate of melt production, characterising the composition and distribution of the magma source regions and describing the geometry of their feeder systems (Ernst *et al*., 2005). This is crucial for understanding their origin,

geodynamic setting, evolution and implications for major tectonic events, such as continental break-up, and global climate and extinction events (Ernst *et al*., 2005). This study can also make an important contribution here.

1.2.4 Layered mafic intrusions and magma dynamics

Layered Mafic Intrusions (LMIs) have been the focus of many decades of research, since they preserve a unique record of the processes operating in magma systems – specifically those pertaining to magma crystallisation and differentiation – and provide a vital link between melt generation at depth and eruption on surface. They are also host to many of the world's largest and richest ore deposits and therefore a greater understanding of their formation has significant economic value. Despite the attention they have received and the progress that has been made, there are still many fundamental questions concerning the origin of such intrusions that remain unanswered, or at least, lack consensus. What is the nature of the input material? How are such large magma bodies emplaced, i.e. by what mechanism and in what time sequence? What are the processes responsible for the formation of the distinctive layering? I outline some of the current thinking here.

1.2.4.1 The origin of the layering in layered mafic intrusions

Almost all mafic intrusions show some form of layering, although the characteristics of this layering vary greatly (Naslund & McBirney, 1996). Interpreting the origin of this layering is central to understanding the emplacement and evolution of the magma body. This has therefore been a major focus of past research and will form a key aspect of investigation in this study.

The layering and fabrics observed in igneous intrusions are suggested to have been produced by three main sets of processes (Barbey, 2009):

- *Injection processes:* Primary features relating to magma emplacement and associated flow and mixing;
- *Magma chamber processes:* Secondary features relating to convection, crystallisation and compaction after emplacement; and
- *Tectonic processes:* Features produced by tectonic forces acting on the magma body during and after emplacement.

Specifically, these processes have been proposed to include (for more detail consult Naslund & McBirney, 1996):

- *Gravity-driven crystal settling and sorting:* Crystals form and sink (or float) through the magma at different velocities due to different densities (e.g. Marsh, 1989; Ariskin & Yaroshevsky, 2006);

- *Compaction:* Due to the pressure of the overlying cumulate pile, intercumulus melt is expelled and interacts with the magma above (e.g. Meurer & Boudreau, 1996; Philpotts *et al*., 1996; Boudreau & McBirney, 1997);
- *In-situ crystallisation:* Crystals nucleate progressively at the margins of a magma chamber under a thermal gradient (e.g. Mangan & Marsh, 1992; Tait & Jaupart, 1996);
- *Oscillations across a cotectic:* Periodic changes in conditions, such as temperature, pressure and oxygen fugacity, destabilise the system and induce crystallisation (e.g. Hort *et al*., 1993; Boudreau & McBirney, 1997; Morse, 2008);
- *Immiscibility:* Extreme fractionation may produce immiscible liquids that segregate (e.g. McBirney & Nakamura, 1974; Veksler *et al*., 2007);
- *Double-diffusive convection*: Material migrates due to a diffusivity gradient (e.g. Huppert & Sparks, 1984);
- *Multiple different magma injections:* Each layer forms from a new magma influx of a different composition or crystal content (e.g. Husch, 1990; Gibb & Henderson, 1992; Tegner *et al*., 1993);
- *Flow segregation:* Suspended crystals in a flowing magma are concentrated in areas of lower shear stress (e.g. McBirney & Nicolas, 1997; Bédard *et al*., 2007); and
- *Tectonic deformation:* Tectonic stresses deform the cumulate pile and induce flow and melt-migration along pre-existing foliations (e.g. McBirney & Nicolas, 1997).

Such is the variation in layering styles, i.e. in the thickness, textures, mineralogy, compositions, internal variations, contact relations, etc., that no single one of these processes can adequately explain all the features observed in LMIs, and it is possible that many if not all of these processes are operational in any intrusion (Naslund & McBirney, 1996).

While early research focussed mainly on processes of gravity-driven crystal settling, more recently there has been a shift in favour of *in situ* processes (Naslund & McBirney, 1996). Furthermore, previous interpretations and modelling of the origins of the layering in mafic intrusions have been largely predicated on the assumption of formation by emplacement of a single batch of crystal-free melt, and hence have centred on magma chamber processes (Glazner *et al*., 2004; Annen, 2011). However, a growing body of literature suggests that this initial assumption is not, in fact, the norm and that injection processes have a far greater role to play than previously supposed.

1.2.4.2 Single-pulse vs. multiple-pulse magma emplacement

There is increasing consensus that large magma bodies, at least in the upper crust, grow from multiple incremental, small-volume, sill-like emplacements of magma, and not from a single instantaneous, large-volume emplacement (Glazner *et al*., 2004; Annen, 2011; Menand, 2011; Miller *et al*., 2011). This is based on:

- *Geophysical evidence*: Seismic and electrical data show no evidence of significant volumes of melt (> 50% liquid) present anywhere in the crust today, as would be expected for an instantaneously-emplaced, large, completely liquid magma chamber, but rather only evidence of dispersed small-volume melt, or localised minor melt in dykes and veins (Glazner *et al*., 2004);
- *Geochronological evidence*: Precise dating reveals several discrete ages for different layers within one intrusion, age ranges implying time periods of formation greater than is thermally possible for a single-batch magma intrusion, and populations of crystals with different ages (e.g. Tuolumne Intrusive Suite, Torres del Paine Laccolith, Colorado River plutons; Coleman *et al*., 2004; Glazner *et al*., 2004; Michel *et al*., 2008; Miller *et al*., 2011);
- *Geochemical and petrographic evidence*: Many intrusions show abrupt changes in rock composition, mineralogy, grain size and texture, crystal populations with different isotopic characteristics, and zoned crystals that record multiple heating and cooling events (e.g. Sept Isles Intrusion, Palisades Sill, Bushveld Complex; Bishop Tuff magma system, Colorado River plutons; Gorring & Naslund, 1995; Glazner *et al*., 2004; Namur *et al*., 2010; Michaut & Jaupart, 2011; Miller *et al*., 2011; Roelofse & Ashwal, 2012); and
- *Field evidence*: Physical features such as intrusive internal contacts, with or without chill margins, and magmatic foliation, record magma intrusion and mingling (e.g. Shiant Isles Main Sill, Tuolumne Intrusive Suite, McDoogle Pluton; Henderson *et al*., 2000; Glazner *et al*., 2004; Annen, 2011; Miller *et al*., 2011; Saint-Blanquat *et al*., 2011).

This is also analogous to the processes observed on surface, where volcanic systems are fed by many small-volume lava eruptions and large-volume 'super eruptions' are rare (Glazner *et al*., 2004).

This new hypothesis has profound implications for our understanding of the differentiation, emplacement rates, thermal evolution and propensity for eruption of large magma bodies, and also for their relation to regional tectonics, the associated deformation and assimilation of country rocks, and for crust-building processes in general (Glazner *et al*., 2004; Annen, 2011). Most importantly, this implies that the classic idea of a magma chamber as a large, long-lived body of melt is an improbable simplification, with the exception perhaps of impact-generated melts (Glazner *et al*., 2004). Indeed, it may be unrealistic to view a LMI or magma chamber as a closed system. Glazner *et al*. (2004) argue further that, since many of the magma chamber processes described above require a large body of liquid to function, these consequently may not play as significant a role as previously thought. That is, once a magma is emplaced, it may fractionate by crystal settling, inward crystallisation, etc., but these may not be the dominant or primary processes responsible for the formation of igneous layering. This would suggest that a complete revision of our interpretation of magmatic systems is necessary.

This hypothesis of multiple incremental magma emplacement has become widely accepted in the granitic literature, and there are many supporting examples (see Miller, 2008; Saint-Blanquat *et al*., 2011), but it is still not readily applied to mafic systems. One reason is because evidence for multiple influxes of magma may be difficult to detect. Field evidence, as described above, provides the strongest indication, but this is

rarely present (Miller *et al*., 2011). This is because new influxes of magma, particularly in mafic systems, may have similar compositions and crystal contents to the magma into which they are emplaced, so there is not sufficient contrast, or these contacts may be thermally eroded or obscured by secondary tectonic and magma chamber processes (Miller *et al*., 2011; Saint-Blanquat *et al*., 2011). Compositional trends produced by *in situ* fractional crystallisation in a mafic magma chamber can also appear very similar to those produced by an amalgamation of magmas differentiated in a lower chamber prior to emplacement (Barbey, 2009). Recognition of multiple intrusions also depends on recently-attained sufficiently precise dating methods and isotopic analyses to distinguish different pulses of magma (Miller, 2008). However, there are several mafic intrusions where multiple magma injections have been documented, e.g. the Bushveld Complex (Ashwal *et al*., 2005; Kruger, 2005), Beacon Sill (Zieg & Marsh, 2012), Palisades Sill (Gorring & Naslund, 1995), Rum Layered Intrusion (Holness, 2005), Shiant Isles Main Sill (Gibb & Henderson, 2006) and Sept Isles Layered Intrusion (Namur *et al*., 2010). This study of the Doros intrusion provides a further opportunity to investigate the role of multiple magma emplacements in a mafic system.

1.2.4.3 Mode of emplacement and the construction of LMI

The small-volume magma replenishments that create thick intrusive bodies largely take the form of sills (Menand, 2011). Sills form where magma is halted in its ascent by some discontinuity that prevents it from continuing to propagate vertically, upon which it begins to spread laterally (Miller *et al*., 2011; Menand, 2011; Gudmundsson, 2011). This occurs mainly where there is: 1) a rheology contrast (a brittle layer over a more ductile one, e.g. a crystal-rich layer over a crystal-poor layer); 2) a rigidity contrast (an inelastic layer over an elastic layer); or 3) a change in stress regime (Menand, 2011).

Sills combine to form larger magma bodies by under-accretion, over-accretion, or intra-accretion (Annen, 2011). The first two geometries occur when the pre-existing sill is already solid (Cawthorn, 2012). This forms a series of separate, stacked sills. However, if the pre-existing sill has not completely crystallised at the time that the new magma intrudes, this magma will be emplaced into the melt-rich central zone at the cumulate-mush-liquid interface (Miller *et al*., 2011; Cawthorn, 2012). The liquid here is too weak to propagate a vertical fracture and effectively traps the rising magma (Miller *et al*., 2011). There may still be too great a temperature contrast between the new magma and this central melt zone and a composite sill will form, showing internal chill margins (Cawthorn, 2012). However, if the central zone is still sufficiently hot and liquid, i.e. less than 50% crystallised and with a temperature difference of less than 100°C, the new magma will be incorporated into and inflate the sill (Cawthorn, 2012). Several successive magma injections of this nature will form a thick layered intrusion that may retain a significant melt body (Cawthorn, 2012).

The propensity for a large magma body to develop in this way depends on the cooling rate, particularly relating to the volume of magma emplaced, the depth of emplacement, the conductivity of the host-rock, and the time interval between successive injections (Cawthorn & Walraven, 1998; Cawthorn, 2012;

Gudmundsson, 2011). Cawthorn (2012) calculates, for example, that a liquid sill 100 m thick, intruded into cold country rock, takes approximately 37 years to cool to the threshold of solidification. If the magma is convecting, contains significant fluids, or is already carrying a load of solid crystals, this would shorten the time window further (Cawthorn, 2012). Calculated average magma production rates show that such closely-spaced pulses of magmatism are not normal, but particularly high frequencies may occur for short periods in Large Igneous Provinces (Cawthorn, 2012). Only a short period of intense magma flux is necessary, because once a melt layer initially acts as a sill trap, it continues to do so, and with increasing ease, since the thicker body created will take longer to cool (Gudmundsson, 2011; Cawthorn, 2012).

1.2.4.4 Liquids vs. mushes and the magmatic mush column hypothesis

The shift in thinking from single-pulse to multiple-pulse emplacement models exposes an additional alleged misconception of the traditional magma chamber model. The traditional model, with its emphasis on magma chamber processes over injection processes, sees the layered intrusion itself as the locus of all fractional crystallisation, mixing and other magma differentiation processes. Marsh (2004, 2006, 2013) has pioneered the idea that there is a complex magmatic system of staging chambers and conduits from source to surface, all actively processing and crystallising magma, at overlapping times. The resulting material erupted on surface, or observed in a high-level intrusion, therefore has a complex, multi-stage, multi-depth history of differentiation (Marsh , 2004). This further implies that most of the magmas travelling through the system carry some type of crystal load (up to 55%; Marsh, 2013), i.e. are magma mushes in the general sense, and are not the pure liquids assumed in many models of magma evolution (Marsh , 2004). This is consistent with what is observed in the volcanic system, where there are multiple episodic eruptions of lavas, of different compositions and carrying different phenocryst loads, over a period of time (Gibb & Henderson, 2006; Shervais *et al*., 2006).

While plausible in theory, evidence of mush emplacement may be hard to detect, as primary rock textures and mineral chemical characteristics are typically obscured by re-equilibration during cooling (Bédard *et al*., 2007). The series of chambers that make up the system, and their interconnections, are never exposed in entirety and may only be detected by geophysical means (e.g. for the Snake River Plain; Shervais *et al*., 2006). Much of the available evidence can be interpreted in several ways, inciting vigorous debate in LMI research in recent years.

If this hypothesis applies, the physical and dynamic properties of magma mushes become very important to consider. By this model, both the new injection of magma and the material into which it is emplaced are crystal mushes. The proportion of liquid to crystals in magma has a profound influence on how it behaves (Bachmann & Bergantz, 2008). This affects the mobility of the magma and its response to flow, and therefore influences the modes of magma emplacement and processes of differentiation, as well as its propensity for eruption (Marsh, 2006; Bachmann & Bergantz, 2008).

As a corollary to his magma mush hypothesis, Marsh goes so far as to say that the presence of phenocrysts is necessary for any layering to form in an intrusion and, to a greater extreme, that

phenocryst-free intrusions are essentially undifferentiated (e.g. Mangan & Marsh, 1992; Marsh, 2006, 2013). This statement has come under attack (Latypov, 2009), specifically for its alleged narrow concept of differentiation (essentially, fractionation to granite), its focus on a single mechanism of differentiation (inward crystallisation) to the exclusion of all others, and its apparent disregard for convection processes. However, the underlying premise, that intrusions are built by multiple injections of crystal-bearing magma, is not specifically contested, although it is considered by Latypov (2009) to be the exception and not the rule.

The magma mush concept has somewhat polarised the LMI community into the pro-mush (no phenocrysts, no post-emplacement differentiation; each layer represents a new mush; e.g. Marsh, 2013) and anti-mush (classic Bowen-style fractional crystallisation of a cooling crystal-free liquid, e.g. Latypov, 2009) camps, largely without an alternative voice. A major challenge of either theory is that it is required to explain a vast range of features and types of intrusive bodies. In such circumstances, the moderately-sized (hundreds of metres) differentiated intrusions, like the Doros Complex, may provide a vital link between the small (tens of metres) mafic sills and dykes at one end of the spectrum, where the nature and timing of emplacement may be well-known but there is generally little layering and differentiation, and the large (kilometre-scale) layered intrusions, where there is extensive differentiation and well-developed layering but the emplacement and solidification history is obscure. This study therefore provides an important opportunity to evaluate the nature of magma input and the potential role of phenocryst-bearing magmas in the evolution of a relatively small layered mafic intrusion and potentially provide insight to the debate.

Hodgson & Botha (1974) have already raised the possibility that the Doros intrusion may have formed from multiple inputs of magma, but a comprehensive geochemical assessment of this was lacking, and no investigation of the form this material took was made. This study will examine the Doros field, petrographic and geochemical evidence in detail and attempt to resolve the magma dynamics of this system.

Latypov (2009) summarises what would be expected geochemically of a single-pulse liquid magma emplacement, based largely on observations of the impact-generated Sudbury Intrusion. This includes: 1) a progressive crystallisation trend defined by the sequential appearance of liquidus phases as cumulus minerals, which is reflected in the trends in associated major and compatible trace element concentrations; 2) a progressive change in composition of solid solution minerals, such as olivine and plagioclase, towards their low-temperature end members; 3) a systematic increase in the concentrations of incompatible trace elements (REE, Zr, Y etc.) while maintaining overall similarities in REE patterns; and 4) consistent incompatible trace element ratios and radiogenic and stable isotopic compositions. This forms the basis of a geochemical test for single pulse versus multiple-pulse magma emplacement that will be used in this study.

1.3 Aims and objectives of the project

A review of previous research has identified a number of gaps in our understanding of the Doros Complex and its relation to regional tectonomagmatic events in the early Cretaceous. In particular, it identifies the need for:

- A comprehensive analysis of the mineralogy, petrography and geochemistry of the Doros rock types, including rare earth elements and isotopes;
- A thorough investigation into the magma emplacement dynamics and crystallisation processes involved in the formation of the intrusion;
- A detailed investigation into the source of the Doros magmas, particularly with respect to the role of the putative mantle plume; and
- An evaluation of the suggested affinities of the Doros gabbros with the Tafelkop lavas of the Etendeka.

Specifically, the research in this thesis aims to:

1) Document and characterise the geology of the Doros Complex via fieldwork, **mapping** and sample collection, to provide a context for interpretation;
2) Examine the mineralogy, mineral abundances and textures of each of the units in the Doros intrusive package, via **petrographic analysis**, in order to refine the current lithologic classification, make inferences about crystallisation processes, and contextualise geochemical analyses;
3) Assess compositional changes through the units in the sequence, via whole-rock and mineral **geochemical analysis**, for interpretation of magma processes (number, nature and timing of magma pulses, mixing, contamination, differentiation);
4) Conduct a comprehensive Sr-, Nd- and Pb- **isotopic analysis** of the Doros rock types, for insight into magmatic source components, and the recognition of new magma influxes and possible crustal contamination;
5) Investigate the composition of a possible Doros parental liquid, via a **melt inclusion study**; and
6) Perform a **geophysical analysis** of the intrusion, by aeromagnetic and ground gravity surveys, to investigate the nature of the intrusion at depth and identify other associated subsurface features.

Essentially, the doctoral thesis is a petrographic, geochemical and geophysical study of the Doros Complex, with the aim of better understanding the petrogenesis and evolution of this intrusion and its relation to regional tectonomagmatic events.

Chapter 2: Analytical Methods

A total of 97 samples was collected from the Doros Complex and surrounding area on two field expeditions in 2009 and 2012. A selection of these was analysed for whole-rock, mineral and melt inclusion chemical compositions in the course of the study. Details of geophysical data acquisition are reported in Chapter 8.

2.1 Major and trace element analyses

Major element (Si, Al, Ti, Fe, Mn, Mg, Ca, Na, K, P, Ni, Cr, S) compositions of 39 samples (Tables C.1, C.2) were determined by X-ray fluorescence (XRF) using a Philips PW1480 wavelength-dispersive XRF spectrometer at the Department of Geological Sciences, University of Cape Town. Powdered samples were prepared as fusion disks, using a LiT/LiM flux and LiBr as a releasing agent, according to the method of Norrish & Hutton (1969). Analyses were made with a dual target Mo/Sc X-ray tube at 50 kV and 50 mA. The detection limit (DL) and the square root of the mean of the squares of the deviations (RMS) for each element are as in Table 2.1.

Table 2.1: Detection limits (wt. % oxide) and RMS deviations for major element analyses by XRF

	RMS	DL
Si	0.215	0.052
Ti	0.022	0.023
Al	0.084	0.074
Fe^{3+}	0.069	0.019
Mn	0.004	0.014
Mg	0.141	0.102
Ca	0.102	0.004
Na	0.065	0.17
K	0.037	0.003
P	0.011	0.008
Ni	0.003	0.004
Cr	0.011	0.008
S	0.112	0.1

Trace elements were analysed by inductively-coupled plasma emission-mass spectroscopy (ICP-MS) using a Thermo-Fisher X SeriesII quadropole instrument at the University of Cape Town. The analytical procedure is as follows: 50 mg of sample powder were dissolved in a 4:1 HF/HNO_3 acid mixture in sealed Savillex beakers on a hotplate for 48 hours. The mixture was then evaporated to incipient dryness and treated with 2 ml concentrated HNO_3. This was then taken up in a 5% HNO_3 solution containing 10

ppb Rh, Re, In and Bi as internal standards. Standardisation was against USGS artificial multi-element standard BHVO-2 (see Table 2.2 for a comparison in terms of rare earth elements with published values). Relative standard deviation for most samples was less than 5%.

Table 2.2: Within-run REE analyses (ppm) of BHVO-2 compared to published reference values

	This study					Published values			
	Run 1	Run 2	Run 3	Run 4	Run 5	1	2	3	4
La	14.42	14.58	14.55	14.65	14.43	15.2	15	14.8	15.25
Ce	36.39	36.94	36.32	36.09	35.64	37.5	38	38.8	37.84
Pr	5.082	5.096	5.044	5.116	5.034	5.29			5.351
Nd	23.67	23.6	23.97	23.74	23.44	24.5	25.0	24.6	24.39
Sm	5.870	5.891	5.858	5.828	5.938	6.07	6.2	6.0	6.03
Eu	2.007	2.015	2.051	2.069	1.973	2.07		2.01	2.036
Gd	6.252	6.229	6.268	6.377	6.137	6.24	6.3		6.229
Tb	0.907	0.913	0.929	0.946	0.893	0.936	0.9	0.88	
Dy	5.224	5.158	5.259	5.276	5.068	5.31			5.3
Ho	0.952	0.961	0.984	0.997	0.968	0.972	1.04		
Er	2.477	2.46	2.579	2.541	2.519	2.54			2.547
Tm	0.328	0.342	0.367	0.378	0.334	0.341			
Yb	1.950	1.935	1.980	2.004	1.998	2	2	1.89	1.955
Lu	0.278	0.284	0.315	0.322	0.294	0.274	0.28	0.275	0.2709

1 = Raczek *et al*. (2001); 2 = Wilson (1997); 3 = Ila & Frey (2000); 4 = Kent *et al*. (2004)

2.2 Radiogenic isotope analyses

Sr, Nd and Pb isotopes and relevant elemental concentrations were analysed in solution using a NuPlasma 51 multi collector-ICP-MS instrument at the University of Cape Town (Table C.4). Chromatographic separation of Sr and Nd was performed according to the method of Míková & Denková (2007). Pb was extracted with standard HBr-HCl anion exchange chemistry. Instrumental mass fractionation was corrected by normalisation to $^{86}Sr/^{88}Sr = 0.1194$ and $^{146}Nd/^{144}Nd = 0.7219$, and for Pb, by normalisation of the measured ratios of international standards. The standards used were NIST987 for Sr analyses, JNdi-1 for Nd analyses and NIST981 for Pb analyses. These yielded values during the session of NIST987: $^{87}Sr/^{86}Sr = 0.710247 \pm 40$ (2σ external; n = 8), JNdi-1: $^{143}Nd/^{144}Nd = 0.512102 \pm 16$ (2σ external; n = 8), NIST981: $^{208}Pb/^{204}Pb = 36.7165 \pm 0.0103$; $^{206}Pb/^{204}Pb = 15.5004 \pm 0.0038$; $^{207}Pb/^{204}Pb = 16.9454 \pm 0.0066$ (2σ internal; n = 8).

Decay constants used for age corrections are: $\lambda^{87}Rb = 1.395x10^{-11}$ yr^{-1} (Kossert, 2003), $\lambda^{147}Sm = 6.54x10^{-12}$ yr^{-1} (Lugmair & Marti, 1978), $\lambda^{238}U = 1.55125x10^{-10}$ yr^{-1}, $\lambda^{235}U = 9.8485x10^{-10}$ yr^{-1}, $\lambda^{232}Th = 4.9475x10^{-11}$ yr^{-1} (Steiger & Jäger, 1977). Epsilon values have been calculated using the CHUR parameters $^{147}Sm/^{144}Nd = 0.1967$ (Peucat *et al*., 1989) and $^{143}Nd/^{144}Nd = 0.512638$ (Goldstein *et al*., 1984).

2.3 Electron microprobe mineral analyses

Wavelength-dispersive electron microprobe analysis was performed on selected olivines, pyroxenes, feldspars, Fe-Ti oxides, amphiboles and glass from 12 samples at the central analytical facilities (Spectrau) of the University of Johannesburg, using a Cameca SX-100 instrument (Tables D.1-5 and 4.2). Measurements were made at an accelerating voltage of 20 kV, and a beam current of 30 nA for the silicate minerals or 40 nA for the oxides. All elements were analysed on their Kα lines, apart from Ba, which was analysed on Lα1. Reference materials include both natural and synthetic silicate and oxide minerals and metals. Detection limits were monitored using Cameca's Peak Sight software and are typically well below 0.2 mass %.

All Fe was assumed to be ferrous iron in analyses – ferrous and ferric components in pyroxenes and Fe-Ti oxides were recalculated assuming perfect stoichiometry. The ilmenite lamellae and titanomagnetite host phase of oxy-exsolved Fe-Ti oxides were probed separately.

2.4 Melt inclusion analyses

A set of olivine-hosted melt inclusions was analysed at the GeoForschungsZentrum (GFZ), Potsdam, Germany. The inclusions were homogenised before analysis by remelting them at approximately 1200 °C in a 1 atm reducing furnace for 30 minutes, followed by quenching in air. Measurements were also made of the daughter products of unhomogenised inclusions (Table F.1). Major element analyses were made by electron microprobe (with a Cameca SX100 instrument, at 15 kv and 10 nA) and trace element analyses were made by ion microprobe (Cameca IMS 6f at 12.5 kV, 8 nA). Further details of the homogenisation and analysis procedures may be found in Keiding *et al*. (2011).

The homogenised inclusions give Fe-Mg exchange coefficients between the olivine and liquid ($K_D = (FeO/MgO)_{Ol}/(0.88FeO_T/MgO)_{Liq}$) of 0.29 ± 0.10 (1σ), within the expected K_D range of 0.30 ± 0.03 for a normal basaltic system at shallow crustal pressures (Putirka, 2008). However, there is some scatter of values below and above this (Table F.2), which may be due to the single heating temperature for homogenisation (some inclusions may have been overheated, dissolving part of the host olivine) and potential imperfect quenching in air (some crystallisation may have occurred on the inclusion walls; Schiano, 2003). Thus the melt analyses have been corrected for post-entrapment crystallisation of olivine on the host walls by iteratively adding (or subtracting) increments of the host olivine (on average approximately 11%) to the co-existing melt composition until equilibrium was established (until K_D = 0.31 in this case; Thompson & Gibson, 2000). Analyses with unrealistically high K_D's, i.e. requiring unacceptably large amounts of olivine to be added, have been excluded from the study.

Chapter 3: Mapping and Field Relations

3.1 Introduction

A combination of field observations, sampling and aerial photograph and satellite image interpretation was used to construct a detailed geological map of the Doros Complex and to compile a stratigraphy of the units exposed. Mapping was previously conducted by Hodgson & Botha (1974), who also provided layer thickness, orientation estimates and rock descriptions. This chapter does not aim to replace this work, but serves to update and refine the earlier mapping, and form a platform for the comprehensive petrological and geochemical analysis that is the focus of the project.

3.2 Mapping

The study area was mapped during two field excursions in 2009 and 2012. Figure 3.1 shows sites of observation, measurement and sampling during these surveys (coordinates in Table A.1). The resulting geological map is included in the Appendix (Fig. A.1) and summarised in Figure 3.2.

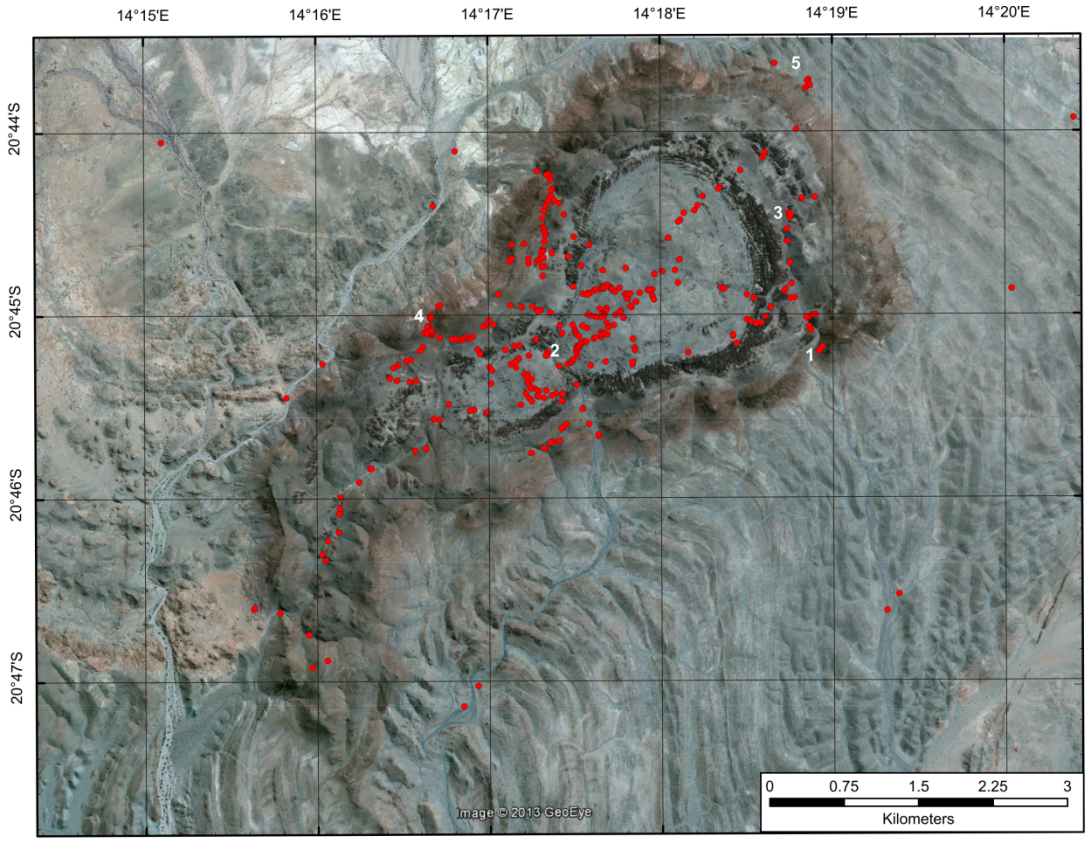


Figure 3.1: Georeferenced satellite image (Google Earth Pro 7.0.2, 2010) of the Doros intrusion showing observation and sampling sites from this study (red points). Localities specifically referred to in the text are numbered.

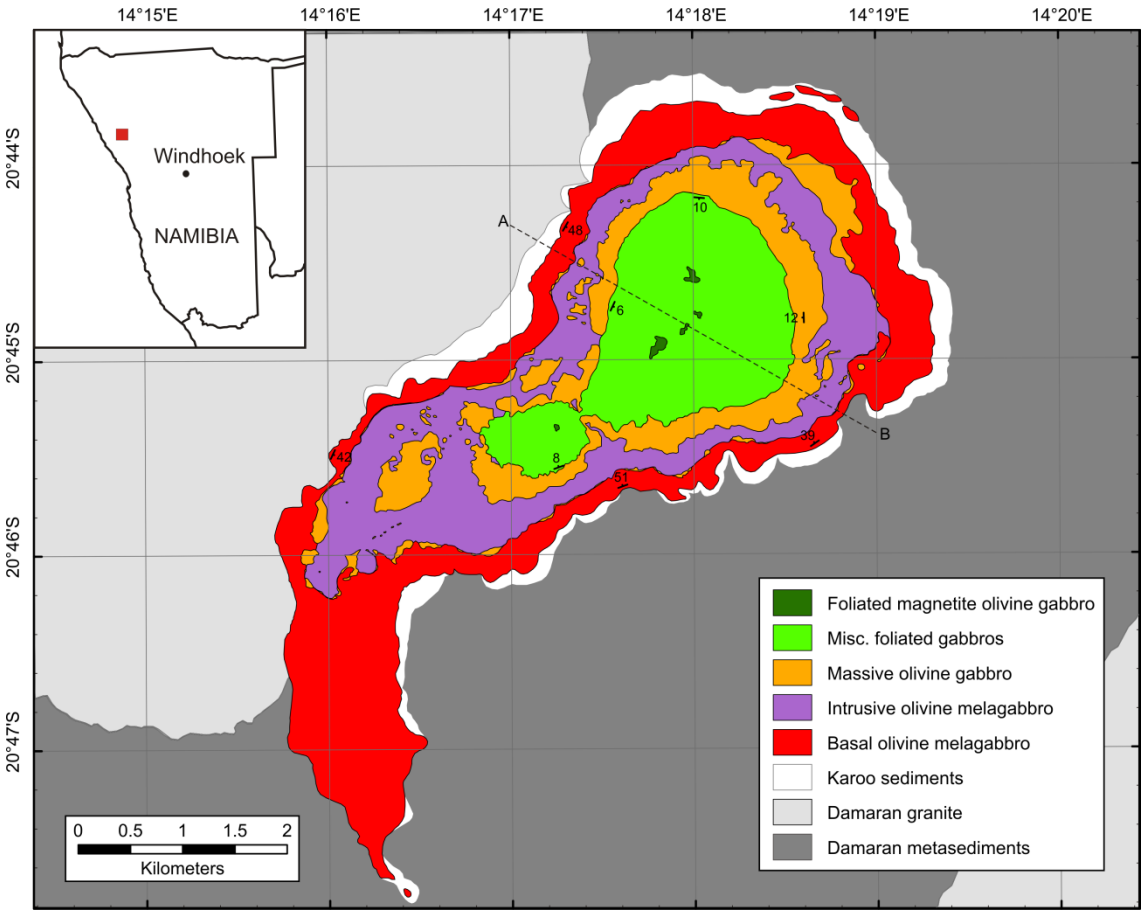


Figure 3.2: Simplified geological map of the Doros Intrusion, depicting the main lithological units identified in this study. Minor units and dykes are not shown here due to scale, but a more detailed map is available in the Appendix (Fig. A.1). Structural data are from Hodgson & Botha (1974). The section A-B corresponds to the cross-section in Figure 3.4. The red square on the inset shows the location of the mapped area within Namibia.

The Doros Intrusion appears in aerial photographs and satellite imagery as a prominent dark-coloured, concentrically-ringed, teardrop-shaped body within the deformed Neoproterozoic metasediments of the Damara Belt (Fig. 3.1). It is approximately 7.5 km in length and 3.5 km at its maximum diameter, with a surface area of ~17.4 km^2. The wider 'head' of the intrusion lies to the north-east and the 'tail' tapers towards the south-west. The outer rim stands at a higher elevation than the surrounding country rocks, hence its common name – the Doros Crater. Despite its prominence from the air, mapping is challenging, since extensive mechanical weathering means that *in situ* outcrop is generally isolated and of poor quality.

As described in Chapter 1, the complex intrudes a thin remnant of near-horizontal Karoo sedimentary strata (preserved as scattered outcrop and debris on the slopes of the rim of the intrusion; Fig. 3.5a), which overlie Damaran granitoids (to the north-west) and folded, steeply-dipping Damaran metasedimentary rocks (to the south-east; Hodgson & Botha, 1974; Passchier *et al*., 2007; Fig. 3.3). Due to poor outcrop and extensive scree cover, the contact between Doros and the Karoo sandstones and shales, and that between the Karoo and Damaran lithologies, is rarely observed (these boundaries on the

map are predominantly inferred). However, contact relations between Doros and the Damaran granites and schists, below the level of the Karoo, are preserved where river valleys exit the complex. The basal contact of the gabbro generally dips at 39° to 51° towards the centre of the intrusion, but becomes near-horizontal in the southernmost part of the tail (Hodgson & Botha, 1974). Small outliers of basal gabbro on the north-eastern margin of the complex (Locality 5, Fig. 3.1) are further evidence of the undulatory nature of the contact. Minor sub-vertical displacement of sections of the Karoo strata on the northern and eastern flanks of the complex indicate faulting associated with the emplacement of the gabbro.

The main body of the intrusion consists of a ±300 m-thick sequence of roughly concordant, sill-like gabbro layers, each dipping progressively more gently (between 12° and 6°; Hodgson & Botha, 1974) towards the centre of the intrusion (Fig. A.1). A simplified interpretation of this is shown in cross-section in Figure 3.3. It is evident that the uppermost parts of the original complex have been removed by erosion, likely predominantly during the early Cretaceous denudation period that occurred in response to continental-break-up (Goudie & Eckardt, 1999). The subsurface structure of the intrusion will be investigated using geophysical methods in Chapter 8.

Regional tectonic activity during and subsequent to the emplacement of the Damaraland intrusions was limited to minor reactivation of Damaran thrusts during the early Cretaceous continental break-up (Miller, 2008). Unlike many of the Damaraland complexes (e.g. Otjohorongo, Paresis, Erongo), Doros is not situated close to a Damaran lineament or fault, and as such the complex is undeformed and unmetamorphosed.

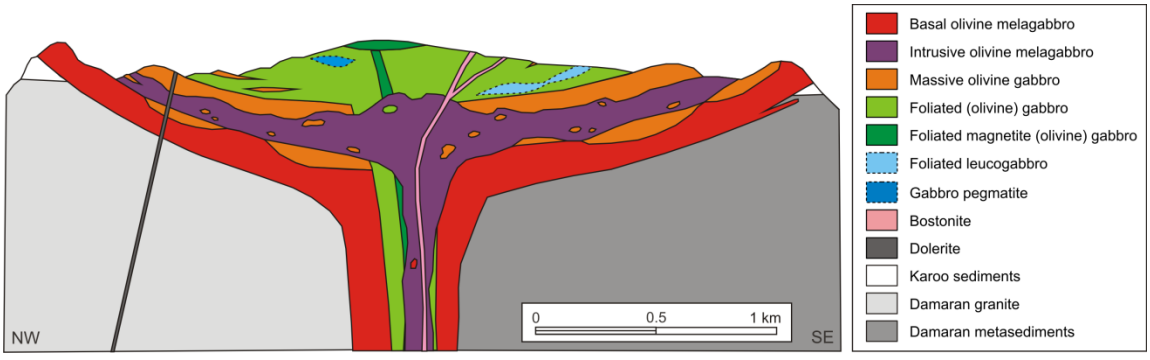


Figure 3.3: Inferred schematic cross-section from north-west to south-east through the widest part of the Doros intrusion (approximately A-B in Fig. 3.2), modified from Hodgson & Botha (1974). Dykes and xenoliths are not to scale.

3.3 Stratigraphy and field relations

Figure 3.4 shows the generalised stratigraphy for the observable section through the complex. A true, to-scale stratigraphic section is unobtainable without borehole core, since outcrop is so sparse.

In the field and in aerial and satellite imagery it is clear that there are three general ‘packages’ that make up the main body of the intrusion, and that define a broad stratigraphic subdivision (Figs. 3.1, 3.4):

1) A thick sequence of distinctively red-coloured olivine melagabbros in immediate contact with the country rock, forming an outer ring of rounded hills with scree-covered slopes, that constitute the **Lower Zone**;
2) A prominent inner ring of dark-coloured, radially-jointed olivine gabbros, mainly occurring as steep boulder piles – the **Intermediate Zone**; and
3) A sequence of highly variable, paler-coloured foliated gabbros in the central parts of the 'head' and 'tail' regions of the complex that constitute the **Upper Foliated Series**.

The characteristics of each of these packages, and the units and sub-units within them, will be examined in detail in the sections to follow.

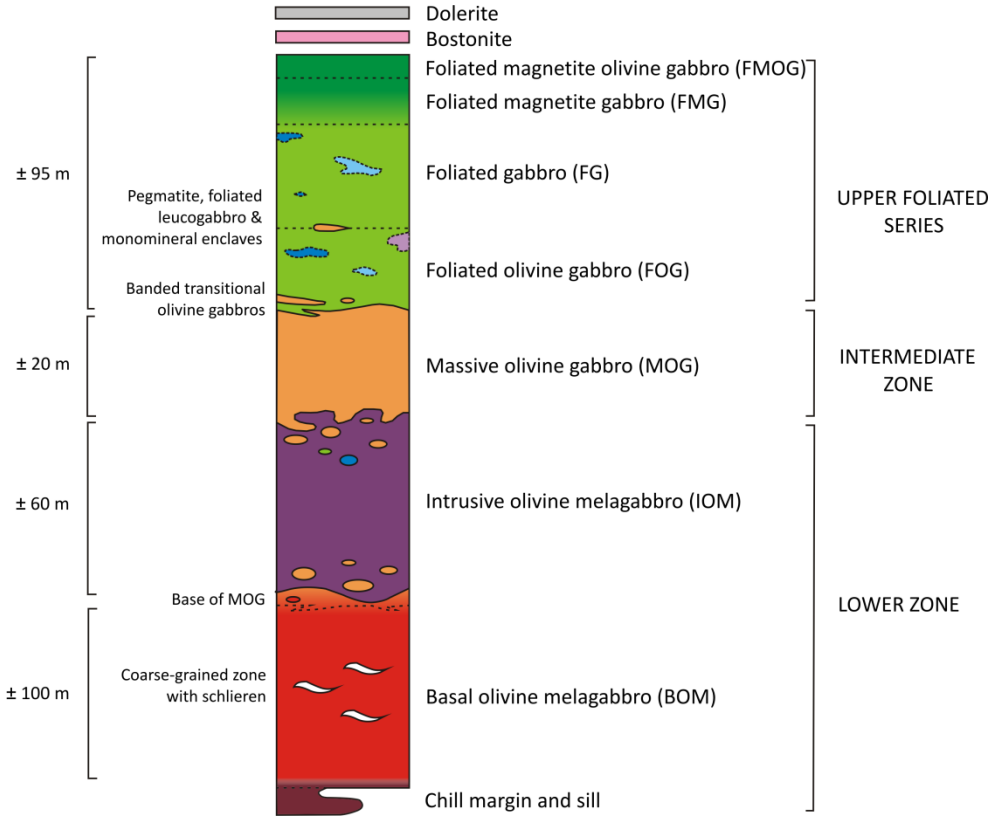


Figure 3.4: Generalised schematic stratigraphic section through the Doros Complex showing the main lithological units described in the text. Average layer thicknesses are from Hodgson & Botha (1974).

3.3.1 Lower Zone

The basal unit of the Doros Intrusion is in intrusive contact with the host Damaran or Karoo rocks (Fig. 3.2). The contact itself is sharp (Figs. 3.5b, 3.6), with a variably thick, red-brown, aphanitic to glassy **chill margin** that is highly vesicular. Sparse pipe vesicles do not show significant flow deformation. This grades over a few centimetres into a fine-grained, green-grey, less vesicular chilled gabbro. Where in contact with Damaran metasedimentary rocks, the marginal gabbros and aureole are brecciated and riddled with calcite veins and the vesicles are filled by calcite (Fig. 3.5c). Apart from this brecciation, and

the minor fault displacement described above, the host rocks show no obvious deformation associated with the emplacement of the intrusion. Contact metamorphic effects are limited to a thin purple-grey baked aureole in the Damaran and Karoo sedimentary host rocks.

Several thin (centimetre-scale) apophyses of gabbro extend from the contact into the host metasediments. On the south-eastern side of the complex (Locality 1; Fig. 3.1), an approximately 3 m-thick, entirely chilled, sill-like body of gabbro protrudes into the Damaran metasedimentary rocks, below the main contact of the basal gabbros. This **chilled gabbroic sill** appears as a fine-grained, grey, friable material containing calcite-filled vesicles. Entrained fragments of Damaran schist are evident within the sill (Fig. 3.5d).

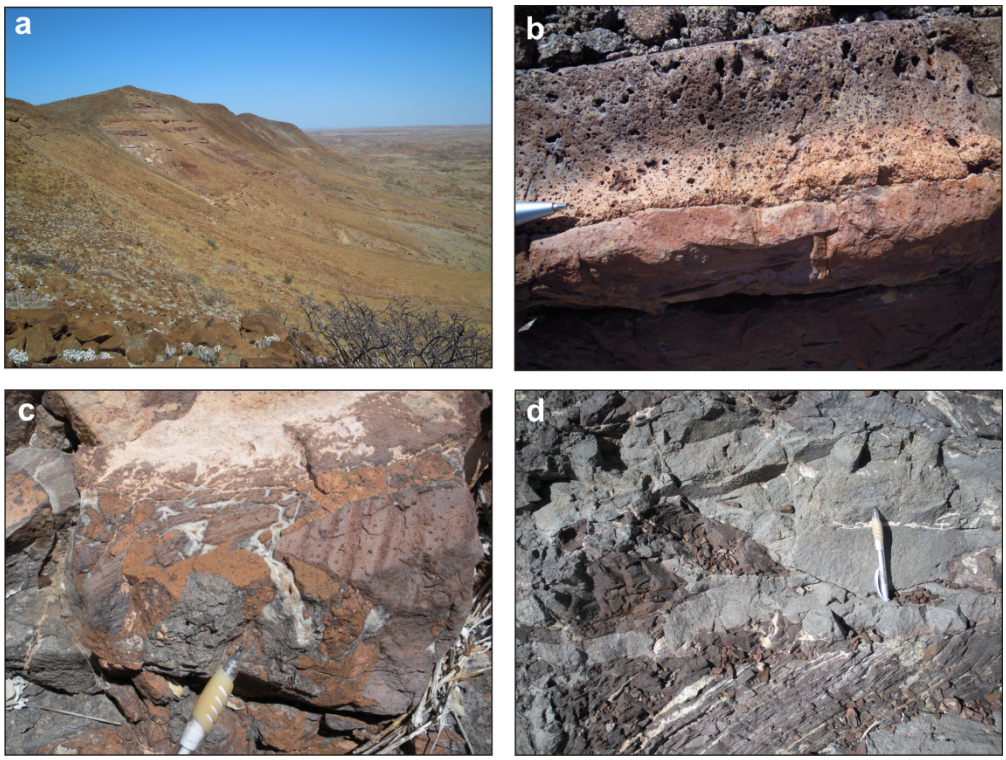


Figure 3.5: a) Remnants of Karoo sedimentary strata on the northern flank of the complex. b) Sharp contact between Karoo sandstone (bottom) and chilled vesicular basal gabbro (top). The brown-red zone is the glassy part of the chill margin. Waypoint 374.5, Fig. A.1. c) Brecciation and calcite infill in the contact zone, from Locality 1, Fig. 3.1 (Waypt. 123, Fig. A.1), on the south-east side of the complex. d) Fragments of Damaran metasedimentary wall-rock entrained in the chilled gabbroic sill (Locality 1/Waypt. 123).

The **basal olivine melagabbro (BOM)** unit is the lowermost layer exposed in the complex. It forms rounded hills with scree-covered slopes, constituting the outer rim of the 'crater'. Outcrop is generally sparse except in river sections and on ridge scarps, where it is strongly jointed and weathers to form characteristic sheets or small elongate blocks. The BOM is medium- to coarse-grained (1 - 4 mm) and has a characteristic dark red colouring, due to abundant haematised olivine (30% - 60%; Table 4.1).

The BOM contains numerous discontinuous, wispy feldspathic 'schlieren' (Fig. 3.6a). These appear as irregular enclaves or linear concentrations of plagioclase, within a pyroxene-olivine framework. The

schlieren increase in number and thickness upwards to the central parts of the unit, where zones of coarse-grained material (round cumulus clinopyroxene grains up to 10 mm) and enclaves of moderately foliated plagioclase tens of cm thick may be observed (Fig. 3.6b).

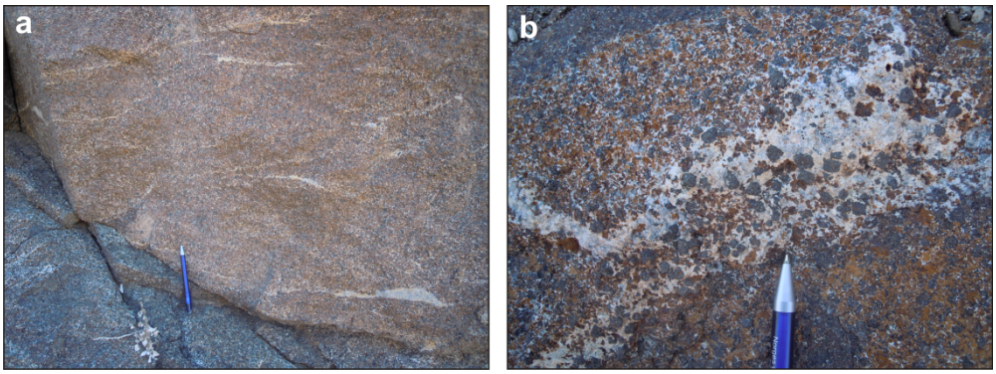


Figure 3.6: a) Basal olivine melagabbro with feldpsathic schlieren. b) Close-up of feldspathic schlieren within coarse-grained BOM. Note the large rounded clinopyroxene grains (dark grey). Both localities in the tail of the complex, close to Waypt. 254.

At the top of the unit, the basal olivine melagabbro transitions over a relatively short distance (typically a few meters), by means of a zone of patchy intermingling (Fig. 3.7a), into a more leucocratic gabbro, which in all respects resembles the massive olivine gabbro unit higher up in the stratigraphy and has therefore been classified as such (Fig. 3.4). Rounded, dark red **olivine-rich xenoliths** are common within this gabbro near the lower contact (Fig. 3.7a, b).

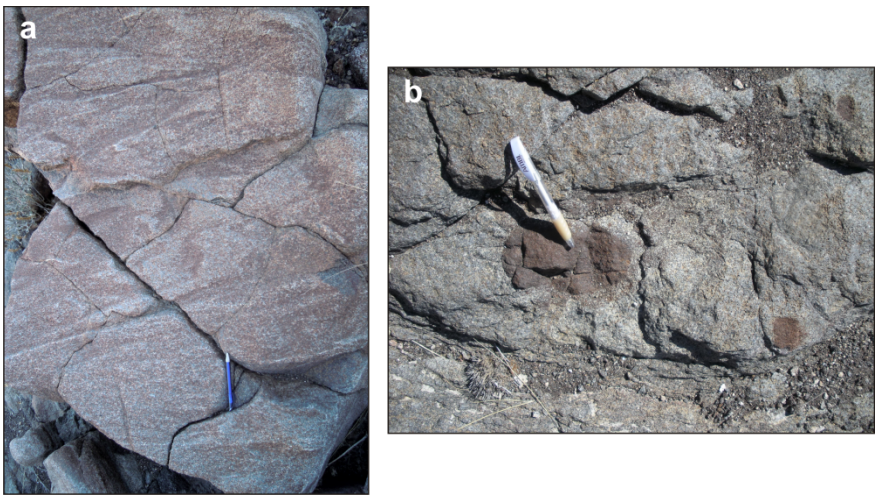


Figure 3.7: a) Intermingling of magmas in the basal olivine melagabbro-massive olivine gabbro transition zone (Waypt. 248). b) Rounded xenoliths of olivine-rich material enclosed in massive olivine gabbro near the MOG lower contact in the tail of the complex.

This transition is truncated by the **intrusive olivine melagabbro (IOM)** unit. This intrusive contact is sharp but irregular, such that in some parts of the complex it is at a lower stratigraphic level and the base of the massive olivine gabbro is not present, and in other parts a thick massive olivine gabbro unit is

evident below the intrusive layer (Fig. 3.3). The IOM is inferred to have intruded into and displaced (and partially replaced) the lower parts of the original massive olivine gabbro layer.

The intrusive olivine melagabbro is almost identical to the basal olivine melagabbro in terms of mineralogy and modal proportions. However, while the clinopyroxene in the BOM is characteristically equant, in the IOM it is more elongate. This unit appears to weather more easily than the BOM, forming the valley between the rim and rocky inner ring of the complex, and is commonly riddled with calcrete veins. There are no zones of coarse-grained material as were noted in the BOM. However, there are feldspathic schlieren. In a zone 15 to 20 m wide in the 'neck' of the complex (Locality 2; Fig. 3.1), there is a set of semi-continuous, sub-parallel, planar concentrations of plagioclase (Figure 3.8a), trending at a high angle to the local magmatic layering (bearing 260° - 300°) and with a variable apparent dip of 50° to 75° to both the north and south. These appear as channelised concentrations of plagioclase, rather than distinct layers or graded layer tops, as the material between these features is massive and relatively homogeneous.

The lower and upper levels of the IOM are host to pale-coloured elliptical xenoliths, increasing in abundance and size (up to 2 m in diameter) towards the respective contacts (Fig. 3.8b). While the xenoliths are predominantly of the massive olivine gabbro into which the IOM intrudes, xenoliths of foliated leucogabbro and gabbro pegmatite may also be observed (Fig. 3.8c). Sparse, small olivine-rich xenoliths, similar to those in the MOG, also occur.

The contact between the intrusive olivine melagabbro and massive olivine gabbro layer above is distinct in outcrop and highly undulatory. In parts, tongues of IOM extend into the massive olivine gabbro, as in Figure 3.8d.



Figure 3.8: a) Linear sub-parallel concentrations of plagioclase in intrusive olivine melagabbro, Locality 2 (Waypt. 34). b) Aligned elongate massive olivine gabbro xenoliths (paler coloured) within intrusive olivine melagabbro in the contact zone (Waypt. 127). c) Large partially-digested raft of gabbro pegmatite within IOM (Waypt. 261). d) Fingered extension of IOM (darker) in massive olivine gabbro (paler) in the contact zone (Waypt. 138).

3.3.2 Intermediate Zone

The next major unit in the succession is the **massive olivine gabbro (MOG)**. Apart from the thin sliver preserved between the BOM and IOM layers, this is exposed as a prominent ring of dark-coloured, steep-sided boulder piles, with a radial joint set trending towards the centre of the complex that is clearly visible on aerial photographs (Fig. 3.9a). These boulders exhibit a characteristic dark weathering patina, commonly display a 'ribbed' surface and produce a distinctive metallic sound when struck. Fresh surfaces appear grey – paler than the basal olivine melagabbro and lacking its distinctive red hue – due to greater proportions of plagioclase.

The upper contact of the MOG is not easily observed due to lack of outcrop, but where present takes the form of a wide transition zone of interfingering magmas, commonly appearing as grain-size banded gabbros such as in Figure 3.9c, or with elongate xenoliths of MOG entrained in the foliated gabbro unit above (Fig. 3.9b).



Figure 3.9: a) Typical massive olivine gabbro boulder piles in the inner ring of the complex. b) MOG xenolith in foliated olivine gabbro in the contact zone (Waypt. 64). c) Small-scale interlayering of massive and foliated olivine gabbros in the contact zone (near Waypt. 142).

3.3.3 Upper Foliated Series

Overlying the massive olivine gabbro is a series of layered, mineralogically-variable foliated gabbros in the central parts of the 'head' and 'tail' regions of the complex. All show a moderate to strong magmatic foliation, usually parallel to the layer bottom. Outcrop is generally very poor except along the central ridge and in river sections.

Although four distinct sub-units may be distinguished within the foliated gabbro series from their geochemistry, these are not easily recognised and located in the field. However, several rings of sparse outcrop may be detected on the slopes of the central core to the complex. This is best observed in aerial photographs (Fig. 3.1). These correspond roughly to the sub-unit tops – thus a simplified stratigraphy of the core may be inferred as in Figure 3.10. The sub-units are presumed to have gradational contacts (though not clearly observed) and are thus mainly a result of varying mineral proportions.

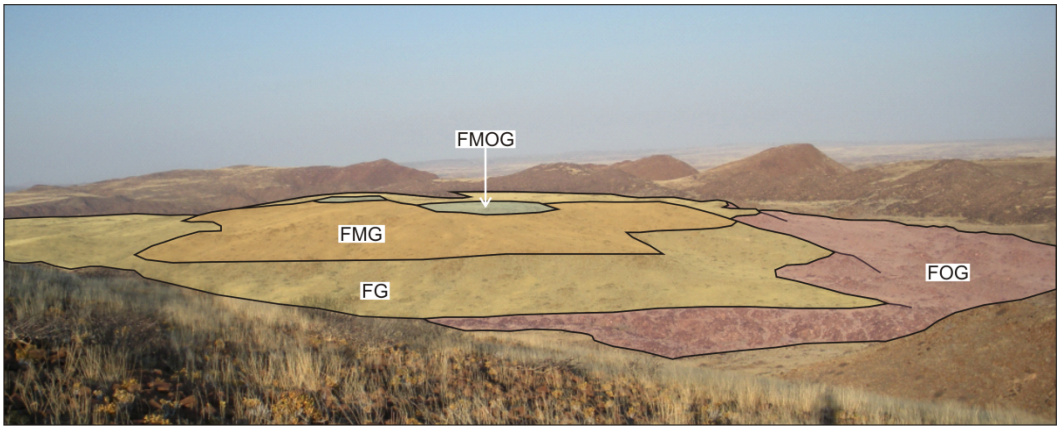


Figure 3.10: Inferred approximate locations of the foliated gabbro units in the core of the 'head' of the complex (viewed towards the south). The ring of dark boulders behind the core is the massive olivine gabbro layer, while the red hills behind these are the basal olivine melagabbros.

The **foliated olivine gabbro (FOG)** unit is found predominantly at the base of the Upper Foliated Series, where it is commonly interlayered with MOG (this zone henceforth referred to as the banded transitional olivine gabbros; Fig. 3.9b, c). The mineral proportions are roughly equivalent to the MOG, but the rock is significantly more coarse-grained (typically 2 - 5 mm), with characteristically platy plagioclase grains and a distinctive greenish colour, from the serpentinisation of olivine. The FOG has a 'knobbly' weathering style and readily disintegrates to form a regolith of small speckled pebbles. This rock typically shows a strong layer-parallel foliation, but this diminishes where the gabbro becomes coarser grained (Fig. 3.11a). The foliation curves around xenoliths and protrusions of MOG and intensifies between them. The rock becomes more leucocratic with stratigraphic height.

The layer above the FOG is a much finer grained (typically 1 - 3 mm) **foliated gabbro (FG)**, which is characterised by the near absence of olivine and greater proportions of magnetite. It weathers to a light-coloured pebbly material similar to the FOG. In parts of the FG, flecks of malachite are present, associated with nearby gabbro pegmatite lenses.

The proportion of magnetite increases significantly as the foliated gabbro grades into the **foliated magnetite gabbro (FMG)** above and these rocks are therefore noticeably darker in colour. The magnetite in this unit is in the form of elongate cumulus grains, aligned with the foliation. At the base of this layer, roughly corresponding to the second ring of outcrop in the core of the complex, large (up to 3 cm long), haematised, coin-shaped magnetite grains are present, lying within the plane of foliation (Fig. 3.11a, b). These weather negatively to form a characteristic pock-marked surface. The grain size increases upwards though the layer.

The uppermost unit is markedly darker in colour and forms the crest to the central ridge in the 'head' of the complex. This **foliated magnetite olivine gabbro (FMOG)** is relatively coarse-grained (2 - 6 mm) and characterised by significant proportions of elongate, aligned olivine, as well as significant cumulus magnetite. The rock is stained pink by haematite alteration of the magnetite and olivine.

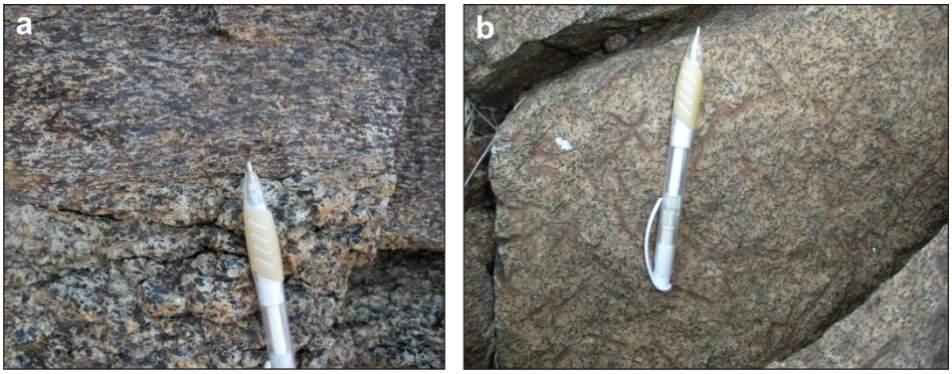


Figure 3.11: a) Foliated olivine gabbro demonstrating the disappearance of the magmatic foliation where the rock becomes coarser grained (Waypt. 60). b) Foliated magnetite gabbro containing large coin-shaped haematised magnetite, viewed in the plane of foliation (Waypt. 59).

In some parts of the Upper Series, the foliated gabbros become very leucocratic, with a distinctive poikilitic texture of aligned platy cumulus plagioclase and 'rosettes' of interstitial mafic minerals (pyroxene and magnetite; Fig. 3.12a). Where the proportion of plagioclase exceeds 60%, this is classified as **foliated leucogabbro (FL)**. Enclaves and veins of > 80% plagioclase are present within the FG unit in the core of the complex, associated with local disruptions to the foliation (Fig. 3.12b-d).



Figure 3.12: a) Foliated leucogabbro showing a poikilitic texture of aligned platy plagioclase and interstitial clinopyroxene and magnetite (Waypt. 141). b) Plagioclase vein intruding coarse-grained foliated olivine gabbro (near Waypt. 105). c) Interlayering of foliated gabbro and foliated leucogabbro (Waypt. 368). d) Plagioclase vein displacing the adjacent foliation in the direction of movement (Waypt. 106).

Several relatively small-volume features are present within the core of the complex. Irregular zones of coarse-grained, dark grey, very pyroxene-rich gabbro are common, in some parts also exhibiting sparse red patches of haematised magnetite (Fig. 3.13a). These represent localised accumulations of cumulus pyroxene crystals, i.e. **clinopyroxene cumulate enclaves**. Similarly, although less common, **magnetite cumulate enclaves** (Fig. 3.13b) and **olivine cumulate enclaves** are evident (Fig. 3.13c). The olivine-rich enclaves differ from other olivine-rich gabbros in the complex in that they are foliated and the olivine grains are characteristically elongate.

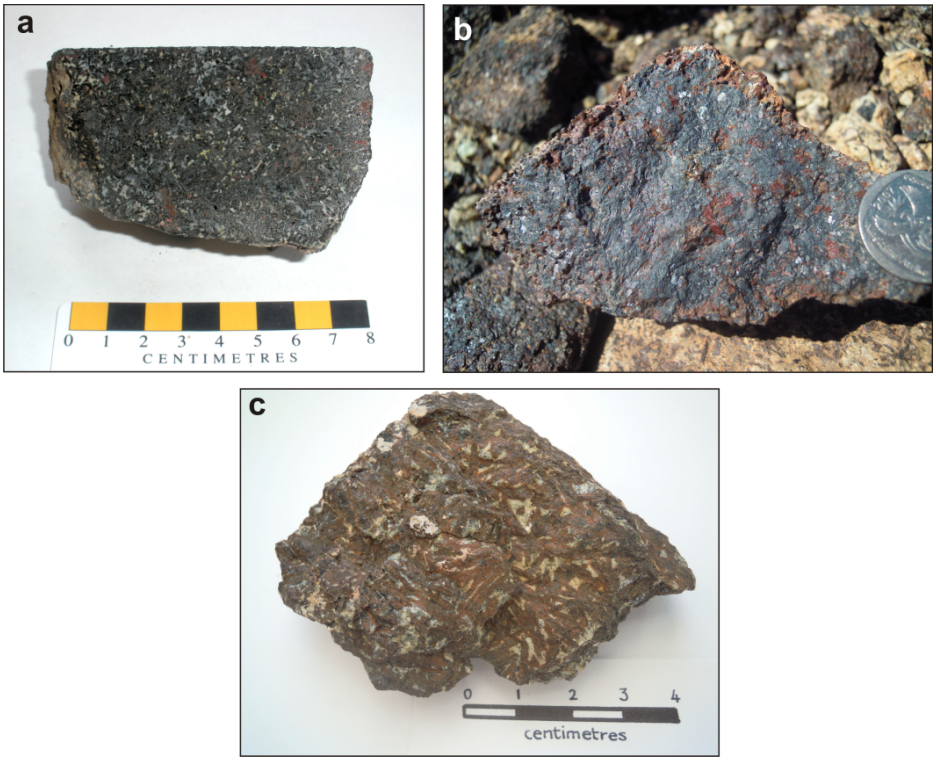


Figure 3.13: a) Clinopyroxene cumulate with minor interstitial plagioclase and magnetite (red patches), from Waypt. 149. b) Magnetite cumulate, from rubble at Waypt. 210. c) Olivine cumulate viewed perpendicular to the plane of foliation (from Waypt. 365). The red colour of the prismatic olivine grains is due to intense haematite alteration.

Irregular enclaves or lenses (up to 1 m wide) of **gabbro pegmatite (GP)** are abundant in the core of the complex, most commonly hosted in coarse-grained FOG, but also observed within FG and clinopyroxene cumulate enclaves (Fig. 3.14). These consist predominantly of plagioclase laths (up to 5 cm long) with interstitial clinopyroxene, but commonly show secondary malachite, botryoidal prehnite and chlorite.

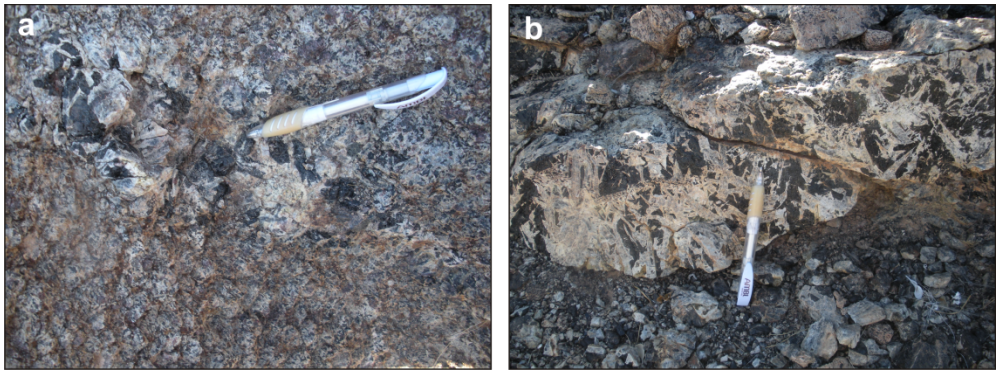


Figure 3.14: a) Pegmatitic lens within coarse-grained gabbro (near Waypt. 105). b) Dyke-like body of gabbro pegmatite (Waypt. 114).

The gabbro pegmatite material in the core of the complex also commonly hosts a central zone of coarse-grained (up to 13 mm) feldspathic material that in its most extreme form may be classified as **bostonite**[1] (Fig. 3.15). The feldspars occur as euhedral laths, with a characteristic pale pink colour, and are inferred to be alkali feldpsars. The enclaves are zoned such that the grain size increases and the proportion of mafic minerals decreases towards the centre. Although in the form of a xenolith, Figure 3.8c is also a good example of gabbro pegmatite transitional to bostonitic material.

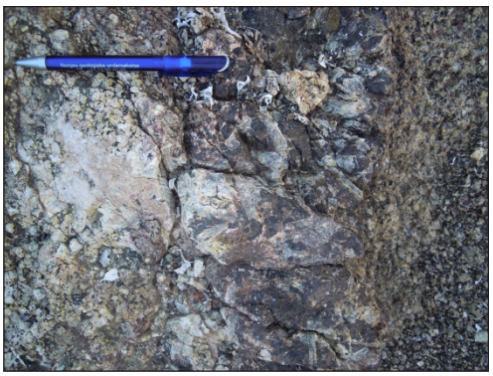


Figure 3.15: A bostonitic enclave (on the left) showing a typical pyroxene-rich pegmatite margin, and a feldspathic centre (Waypt. 356).

3.3.4 Discordant features

In addition to the enclaves described in the core of the complex, dykes of **bostonite** (with a consistent width of between 20 and 60 cm) are observed cross-cutting the gabbros in the Lower and Intermediate Zones (Figs. 3.16a, A.1). These are also zoned, with darker, relatively more pyroxene-rich margins that resemble the coarse-grained gabbro found elsewhere (FOG), followed by a fine-grained feldspathic zone and, depending on the width of the dyke, with a pegmatitic alkali feldspathic centre (Fig. 3.16b). These rocks are heavily altered to prehnite, sericite and epidote.

Dolerite dykes cross-cut the Doros gabbros in several localities (e.g. Figs. 3.16c, A.1). Abundant dolerite rubble is also evidence of dykes not preserved in outcrop. The dykes generally trend north to north-west, vary in thickness from 20 cm to 2 m wide and are in sharp contact with the surrounding gabbros, with no evidence of deformation. They typically display a thick (> 5 cm) chilled margin and are very fine-grained, with prominent phenocrysts of yellow-green olivine (up to 7 mm). In all respects they resemble the dolerite dykes that cross-cut the Damaran granite and schists to the north and west of the complex. A slightly coarser-grained (~ 1 mm) plagioclase-phyric variety is observed cross-cutting the basal gabbros in the tail of the complex (Waypoint 256, Fig. A.1).

[1] In the sense of an alkali feldspar-dominated hypabyssal intrusive rock; essentially monzodioritic to syenitic in composition. This term may be considered archaic, but is used here to be consistent with the Doros literature.

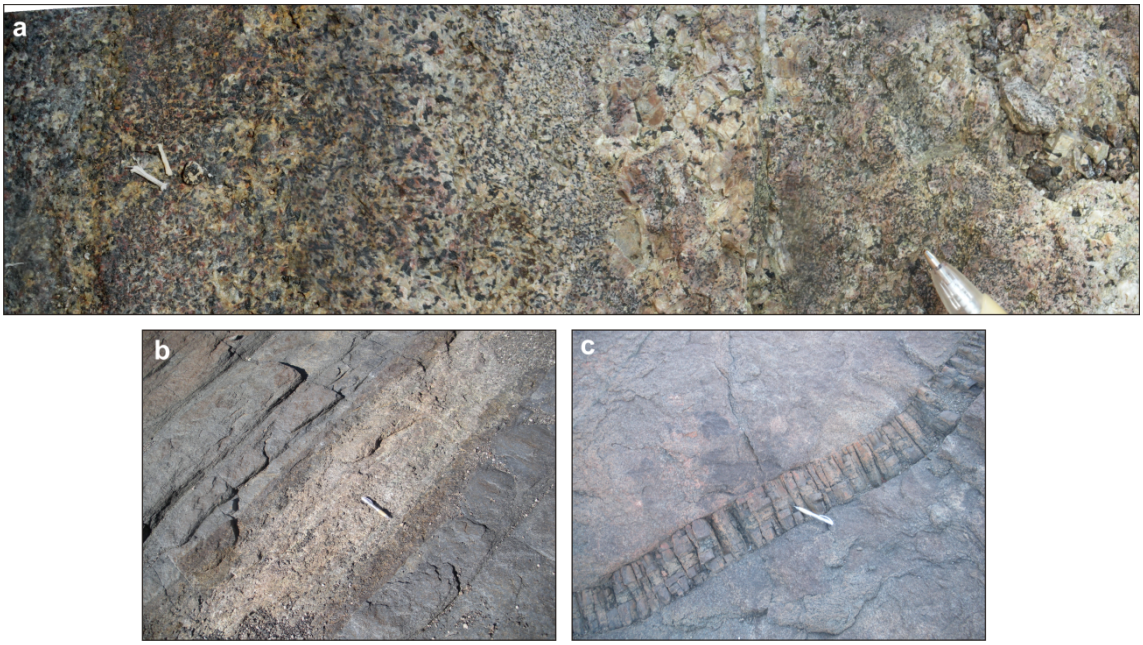


Figure 3.16: a) Close-up section of a bostonitic dyke, from the coarse-grained pyroxene-rich margin (on the left), through the fine-grained feldspathic intermediate zone, to the altered pegmatitic feldspathic centre (on the right). b) Bostonite dyke (~40 cm thick) intruding massive olivine gabbro at Locality 3 (Waypt. 129). c) Dolerite dyke intruding MOG (Waypt. 36).

On the north-western rim of the complex (Locality 4, Fig. 3.1; Fig. A.1), and extending outwards through the Karoo remnants and into Damaran granite, is a **breccia pipe** - a roughly north-west-trending zone of brecciated gabbro and wall-rock up to 60 m wide. The breccia consists of a fine-grained matrix (on average 70% of the rock) with the composition of the local material, i.e. basaltic where the pipe extends into the basal gabbro and siliceous or calcareous where it is hosted in the Karoo sedimentary layers (e.g. Fig. 3.17a). This contains angular to sub-rounded fragments (up to 60 cm in size) of Doros gabbros (basal olivine melagabbro, foliated olivine gabbro), wall-rock (Karoo sandstones and shales, Damaran granite) and Etendeka quartz latite. The only sidewall contact observed is a sharp, but irregular, contact with a coarse-grained foliated gabbro resembling the FOG unit (Fig. 3.17). This feature was recorded by Reuning & Martin (1957) to be at its widest within the Karoo strata and to thin and likely pinch out within the Damaran granite.

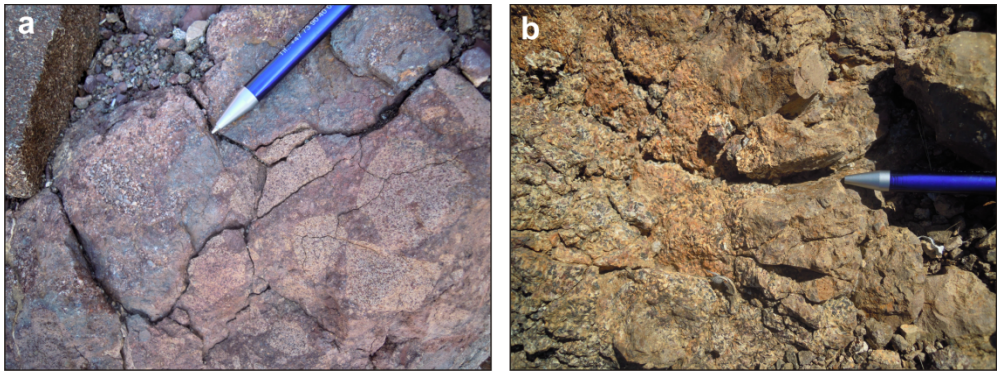


Figure 3.17: a) Brecciated fragments of basaltic material within a red siliceous matrix derived from local Karoo sandstone (Locality 4/ Waypt 397). b) Contact between the breccia pipe (here with a basaltic matrix) and coarse-grained olivine gabbro (on the left; Locality 4/Waypt. 401).

While the gabbros in the main body of the intrusion are clearly comagmatic, their relation to the dykes must be established. The sharp contacts and thick glassy chill margins of the dolerite dykes indicate intrusion quite some time after the emplacement of the host gabbros, after these had cooled significantly and were perhaps already solid. The presence of similar dykes within the Damaran rocks outside the complex (Fig. A.1) suggests that these are part of a larger suite that relates to a later magmatic event. While further evidence of distinct source characteristics will be presented in later chapters, it is important to note that the dolerites will not be considered to be part of the Doros intrusive suite. This is contrary to the suggestion of Hodgson & Botha (1974) that the dykes may be derived from the Doros gabbros. The bostonite dykes also show sharp contacts and distinct cross-cutting relations with the Doros gabbros. They do not have quenched margins, but the finer grain size of the outer portions of the dykes is testament to some cooling at the contact. They were clearly emplaced after the BOM and MOG that they intrude. However, the presence of bostonitic material in isolated enclaves in the core of the complex, gradational to the pegmatite, suggests that this material is closely related to the formation of the intrusion and may therefore be interpreted as part of the Doros suite. However, this will be investigated further in Chapters 7 and 11.

3.4 Comparison with the literature

As outlined in Figure 3.4, 10 major lithological units have been identified in the Doros stratigraphy. Table 3.1 demonstrates how this new classification scheme correlates with those of the previous studies of the Doros intrusion by Hodgson & Botha (1974) and Marsh & Duncan (2008).

Table 3.1: Comparison of lithological classification systems for the Doros Complex

	This work	Marsh & Duncan (2008)	Hodgson & Botha (1974)
Dykes & enclaves	Bostonite	Aegerine bostonite	Aegerine bostonite
	Gabbro pegmatite	Gabbro pegmatite	Gabbro pegmatite
	Pyroxene, olivine and magnetite cumulates		
	Foliated leucogabbro		
Layered sequence	Foliated magnetite olivine gabbro	Upper Foliated gabbros	Hyalosiderite melagabbro (Dr 7)
	Foliated magnetite gabbro		
	Foliated gabbro		Foliated melagabbro (Dr 6)
	Foliated olivine gabbro		Foliated hyalosiderite gabbro (Dr 5)
	Massive olivine gabbro	Layer 3 gabbro	Hyalosiderite gabbro (Dr 4)
	Intrusive olivine melagabbro	Layer 2 gabbro	Intrusive chrysolite tilaïte (Dr 3)
	Basal olivine melagabbro	Basal gabbro	Chrysolite tilaïte (Dr 2)
	Chill margin & chilled gabbroic sill		Aplite (Dr 1)

The classification scheme for this study is essentially equivalent to that of Hodgson & Botha (1974), although with simplified terminology. Additions to the scheme are the separation of the olivine-bearing and olivine-free magnetite gabbros and the recognition of the chilled gabbroic sill and cumulus crystal enclaves as distinct lithological entities.

3.5 Comparison with other layered mafic intrusions

Doros is undoubtedly a layered mafic intrusion (LMI). With its estimated preserved thickness of ~300 m (and original thickness of perhaps ~500 m) and surface area of ~17 km^2, it may be considered relatively small in the scheme of layered mafic intrusions that includes the famous Bushveld Complex (up to 9 km thick; 65 000 km^2 in surface area; Namur *et al*., 2010), the Kiglapait Intrusion (up to 8.5 km thick, 560 km^2 in area; Namur *et al*., 2010), the Skaergaard Intrusion (3.5 km x 90 km^2; Namur *et al*., 2010), and the Stillwater Igneous Complex (6.5 km x 4400 km^2; Namur *et al*., 2010). But it is of a similar scale to, for example, the Fedorivka Layered Intrusion (300 m x 3 km^2; Namur *et al*., 2010), the Palisades Sill (300 m thick; Gorring & Naslund, 1995), and the Graveyard Point Intrusion (up to 160 m thick, 24 km^2; White, 2007), each of which has made an important contribution to our understanding of emplacement and differentiation processes in mafic magma systems. In fact, as argued in Chapter 1, such moderately-sized intrusions may have advantages over their larger and smaller (single sill) counterparts in this regard.

The layering in the Doros Intrusion is generally modal and/or grain-size layering, as is present in all LMIs, although this is generally irregular, and the spectacular fine-scale rhythmic or cyclic layering characteristic of the larger LMIs (e.g. Bushveld, Skaergaard, Stillwater) is not evident.

LMIs typically consist of a sequence of pyroxene- or olivine-rich ultramafic rocks at the base, followed by a sequence of layered, more plagioclase-rich mafic rocks, and a series of intermediate to felsic rocks at the top (Blatt & Tracy, 1996). The Bushveld Complex is a spectacular example of this, with a thick basal sequence of dunite, harzburgite and pyroxenite, followed by an extensive layered series of predominantly gabbronorites and norites, capped by ferrodiorite (Cawthorn *et al*., 2006). However, this complete package is not always present, or at least, exposed. Doros lacks a basal ultramafic series, although the most olivine-rich of the basal melagabbros approach wehrlite compositions. The main body of the intrusion also does not show a highly-fractionated intermediate or felsic upper sequence, such as in the Sept Iles intrusion (Namur *et al*., 2011), or an internal 'Sandwich Horizon', as in the Skaergaard intrusion (McBirney, 1989). However, if the bostonite dykes are indeed comagmatic with the main Doros suite, as the field evidence suggests, they may represent feeders to an upper-level evolved, syenitic phase that has since been eroded.

3.6 Summary of findings

Field observations and mapping show that the Doros Intrusion consists of a series of roughly concordant, sill-like gabbro layers dipping at between 51 and 6° towards the centre of the intrusion, cross-cut by dolerite and bostonite dykes. The exposed portion of the intrusion is approximately 300 m thick, with an areal extent of ~17.4 km^2. The main body of the intrusion broadly comprises the Lower Zone, consisting of olivine-rich melagabbros complete with basal chill margin, the Intermediate Zone of more plagioclase-rich olivine gabbros, and the Upper Foliated Series, consisting of variable, layered, foliated gabbros.

Chapter 4: Petrography and Mineral Chemistry

4.1 Introduction

The field observations and mapping (Chapter 3) have led to the identification of 10 major units and several sub-units within the Doros Complex, as well as cross-cutting dykes, giving a total of 17 distinct lithological components that will be examined and characterised in this chapter. These are as follows:

1) Chill margin
2) Chilled gabbroic sill
3) Basal olivine melagabbro
4) Intrusive olivine melagabbro
5) Massive olivine gabbro (and xenoliths thereof)
6) Foliated olivine gabbro
7) Foliated gabbro
8) Foliated magnetite gabbro
9) Foliated magnetite olivine gabbro
10) Foliated leucogabbro and feldspathic enclaves
11) Olivine-rich xenoliths
12) Pyroxene cumulate enclaves
13) Magnetite cumulate enclaves
14) Olivine cumulate enclaves
15) Gabbro pegmatite and coarse-grained enclaves
16) Bostonite dykes and enclaves
17) Dolerite dykes

4.2 Petrography

The complete range of materials sampled within the Doros Complex and details of the hand samples and thin sections that represent them are presented in Table B.1 of the Appendix. The typical ranges of mineral modal abundances (from visual hand sample and thin section estimates and CPIW norm calculations) are summarised in Table 4.1 below. The full set of norm calculations may be found in Table C.3.

Table 4.1: Approximate visually-estimated modal abundances for each of the Doros lithological components

Lithological unit	Plag	Cpx	Ol	Ox	Alk fsp	Accessory
Chill margin	50-70%	~10%	0-20%	<5%	-	
Chilled gabbroic sill	~50%	10-30%	0-20%	~10%	-	ap, chpy
Basal olivine melagabbro	10-30%	20-35%	30-60%	<5%	-	bi
Intrusive olivine melagabbro	10-40%	25-40%	30-50%	<5%	-	ap, bi
Olivine-rich xenoliths	<10%	~25%	60-70%	<5%	-	
Massive olivine gabbro	45-60%	20-40%	5-25%	<5%	-	ap, bi
Foliated olivine gabbro	45-50%	15-40%	10-25%	3-6%	-	ap, bi
Foliated gabbro	45-55%	30-45%	<5%	<10%	-	ap, bi
Foliated magnetite gabbro	40-50%	30-40%	<10%	10-15%	-	ap, bi
Foliated magnetite olivine gabbro	30-40%	25-30%	15-30%	10-15%	-	
Foliated leucogabbro	55-90%	5-30%	<5%	<10%	-	ap, chpy
Pyroxene cumulate	~30%	~60%	<5%	<5%	-	
Magnetite cumulate	<15%	-	<10%	75-90%	-	
Olivine cumulate	~25%	~25%	~50%	<5%	-	ap, bi
Gabbro pegmatite	~50%	45-50%	-	<5%	-	ap
Bostonite	30-60%	10-15%	<5%	~5%	15-45%	ap, amph
Dolerite	~45%	20-40%	5-15%	5-10%	-	py, chpy

Plag = plagioclase; cpx = clinopyroxene; ol = olivine; ox = Fe-Ti oxides; alk fsp = alkali feldspar; ap = apatite; bi = biotite; amph = amphibole; py = pyrite; chpy = chalcopyrite

Mineral chemical analyses are presented in Tables D.1-6 of the Appendix. Major element compositions of the feldspars, pyroxenes, olivines and Fe-Ti oxides are shown in Figure 4.1 below. Microprobe data are limited to one sample per major lithological unit, so mineral chemistry may be considered as a representative example, rather than depicting the full range of variation of the material concerned. It is clear that many of the mineral analyses in the dataset, particularly for the feldspars, are problematic, with high or low totals, but this does not affect mineral classification, An content (An # = 100 x molar Ca /(Ca + Na)) or Mg number (Mg # = 100 x molar Mg /(Mg + Fe)).

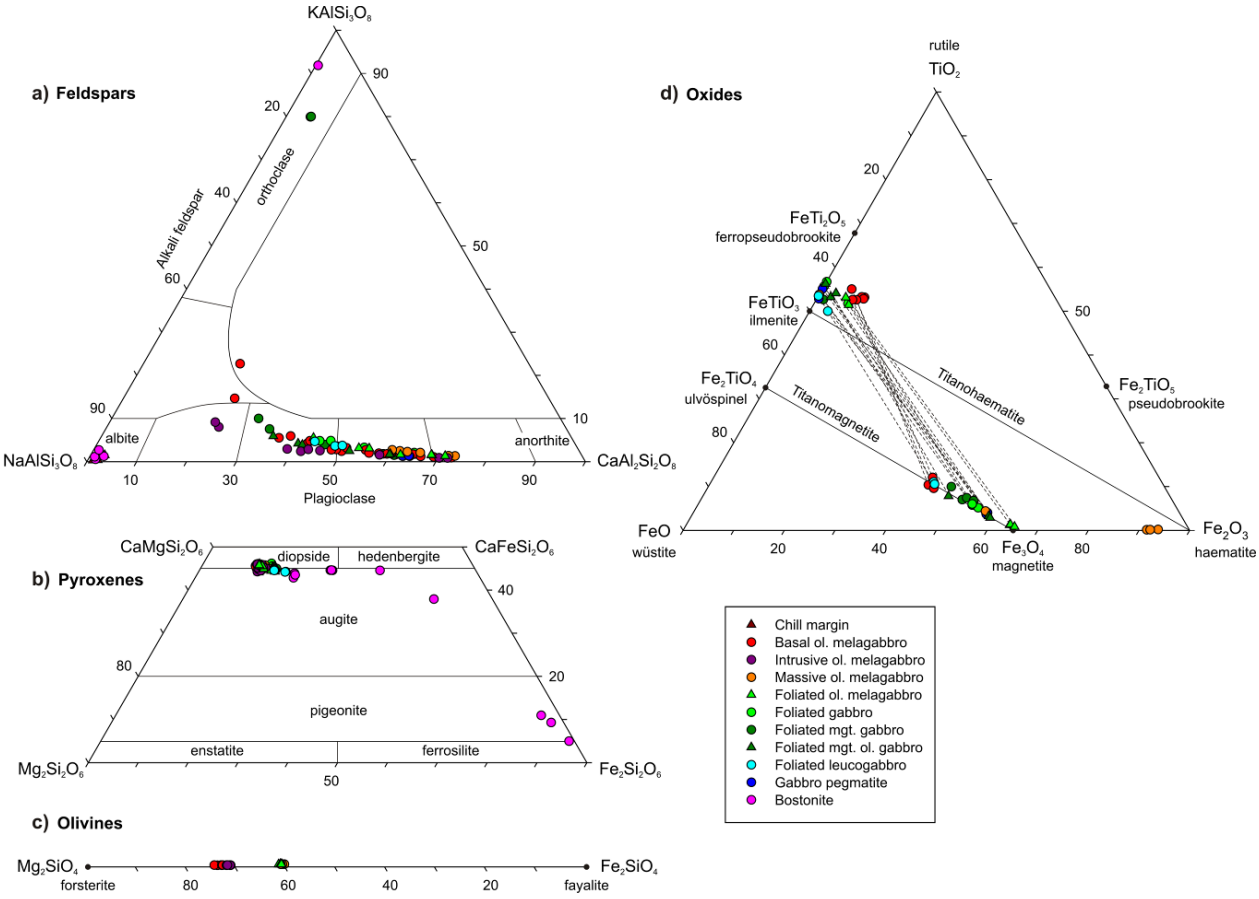


Figure 4.1: Compositions, from mineral spot analyses, of selected a) feldspars, b) pyroxenes, c) olivines and d) Fe-Ti oxides in the Doros rocks. Tie lines connect co-existing titanomagnetite host-ilmenite lamella pairs in the Fe-Ti oxides.

4.2.1 Chill margin and chilled gabbroic sill

In thin section, the contact between the Doros gabbros and host rocks is sharp but irregular (Fig. 4.2a). Apart from a slight shearing of the foliation in the Damaran metasediments in some places, there is no evidence of mineral-scale deformation at the contact. The host Damaran metasedimentary rocks are intensely altered (predominantly to clay minerals), so contact metamorphic effects are difficult to detect. No index minerals are evident. However, polycrystalline calcite veins and calcite-filled vugs are common in these rocks, indicating remobilisation of calcareous material.

The chilled gabbros at the margins of the intrusion are glassy to aphanitic, and micro-porphyritic. Although the glass is heavily altered (mainly to calcite) and totals are poor, compositions suggest abundant normative plagioclase, with minor clinopyroxene, olivine and oxide components (Table 4.2). Phenocrysts (~20% of the rock) are predominantly of euhedral altered sodic plagioclase (close to pure albite at $An_{1\text{-}3}$; Fig. 4.1), with minor fragmented clinopyroxene (Mg# ~78), typically occurring as plagioclase-pyroxene agglomerates (as in Fig. 4.2a). There is also sparse relict euhedral olivine, almost completely replaced by Ti-magnetite, serpentine, calcite and clay minerals, and therefore no longer

identifiable by chemistry (probed remnants show high concentrations of Ca and Ti, but very little Fe and Mg; Table D.1), but still recognisable by shape and texture (Fig. 4.2b). These are typically surrounded by diffusion haloes in the matrix (Fig. 4.2b), which are very Ca-rich (Table 4.2) and are thus inferred to be predominantly calcite. Large vugs and vesicles are filled by calcite or rimmed by recrystallised plagioclase. The groundmass progresses from glass to cryptocrystalline altered plagioclase (fringed tabular and acicular crystals), homogeneous Fe-Ti oxides and clinopyroxene. The chill margin to the gabbroic sill (TOD59) contains abundant, well-developed (although heavily altered) plagioclase and clinopyroxene phenocrysts, whereas in the margin to the basal olivine melagabbro (TOD3), these are relatively rare.

Table 4.2: Microprobe analyses (unnormalised) and CIPW normative abundances of glass in the Doros chill margin

Sample	TOD59 Chill margin		
Point	4/20	4/21	7/25
Comment	Glass	Glass	Diffusion halo
SiO_2	62.98	60.05	4.11
TiO_2	2.89	2.48	3.30
Al_2O_3	17.88	16.99	0.48
FeO_T	7.80	13.32	6.18
MnO	0.10	0.12	0.18
MgO	0.18	0.07	0.81
CaO	1.01	1.23	47.60
Na_2O	10.68	10.79	0.22
K_2O	0.10	0.10	0.01
Cr_2O_3	0.03	0.02	0.01
NiO	0.00	0.04	0.01
Total	103.65	105.22	62.89
Mg#	3.95	0.93	18.94
Normative mineral abundance (wt. %)			
Orthoclase	0.59	0.59	
Albite	84.21	69.84	
Anorthite	0.55		
Nepheline	3.34	9.21	
Diopside	3.93	5.43	
Olivine	3.75	10.41	
Magnetite	1.89	1.25	
Ilmenite	5.49	4.71	
Acmite		3.94	

The chilled sill is fine-grained (< 1 mm) and consists of sericitised plagioclase, skeletal crystals of unexsolved Fe-Ti oxide (indicating quenching; Fig. 4.2c), pale brown, Ti-rich, concentrically-zoned clinopyroxene and minor olivine, which is heavily altered to serpentine and haematite. Apatite needles are common and traces of chalcopyrite may be present.

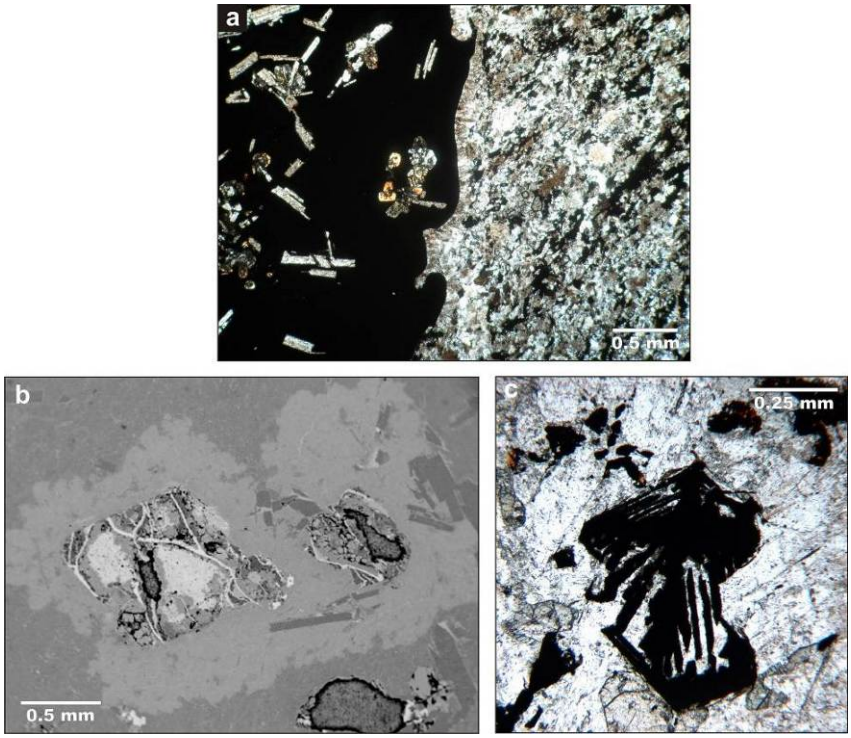


Figure 4.2: a) Cross-polarised light (XPL) photomicrograph showing the sharp contact between glassy chilled gabbro at the margin of the gabbroic sill (on the left), containing small phenocrysts of euhedral plagioclase and clusters of plagioclase with pyroxene, and siliceous Damaran metasediments (on the right; TOD59). b) Back-scattered electron (BSE) image of calcic diffusion haloes surrounding relict olivine phenocrysts, completely replaced by serpentine, calcite and oxides (TOD59). c) Photomicrograph of skeletal magnetite in the chilled gabbroic sill (plane-polarised light; PPL; TOD58).

4.2.2 Basal olivine melagabbro

The basal olivine melagabbro consists predominantly of rounded subhedral cumulus olivine (Fo_{72-75}; 30% - 60%), which is heavily haematised, giving this material its characteristic dark red colouring (Fig. 4.3a). Interstitial to the olivine are calcic clinopyroxene, plagioclase, minor irregular Fe-Ti oxides and accessory red-brown biotite as rims to the oxides. The clinopyroxene is pale olive-brown and occurs as large equant grains (up to 5 mm) that appear sector-zoned in thin section, but this zoning is less easily discernible in BSE imagery and compositions show only a small decrease in Mg content from core to rim (Mg# 78-80; Table D.3). Pyroxene grains commonly contain many small inclusions (plagioclase, oxides) and appear resorbed where in contact with plagioclase. The plagioclase exhibits patchy zonation, becoming increasingly more sodic (and potassic) from core to rim (Table D.2). Compositions are typically between An_{40} and An_{73}, but some grains show K-rich rims as low as An_{25}, suggesting extreme fractionation of trapped interstitial melt. The olivine commonly contains fine, beaded, haematised melt inclusions, particularly in the upper reaches of the unit (discussed in detail in Chapter 7). The oxide phase is typically ilmenite containing small titanomagnetite sectors (composite type oxy-exsolution), such as in Figure 4.3b below, although trellis type oxy-exsolution of ilmenite lamellae within titanomagnetite may also be

present. Fe-Ti oxide grains are commonly surrounded by oxide-filled fractures. The plagioclase is mildly altered to sericite and prehnite.

At the margins of the feldspathic schlieren in the central zone of the BOM unit, the olivine has identical characteristics to elsewhere in the layer (rounded, subhedral, haematised, with melt inclusions; Fo_{73-75}), but clinopyroxene grains are significantly larger, at 8 to 10 mm in diameter. The plagioclase laths in the enclaves are moderately aligned parallel to schlieren contacts and are normally-zoned (An_{39-73}).

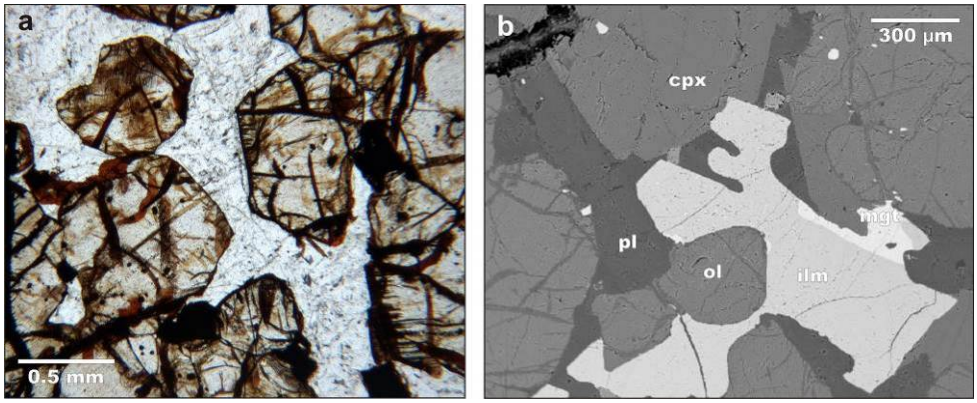


Figure 4.3: a) Photomicrograph of haematised subhedral olivine with interstitial plagioclase in basal olivine melagabbro (PPL; TOD40). b) BSE image of interstitial ilmenite with remnant magnetite sectors (sandwich oxy-exsolution; TOD40).

4.2.3 Intrusive olivine melagabbro

The intrusive olivine melagabbro is equivalent to the basal olivine melagabbro in terms of mineralogy, modal proportions and mineral textures. The rock consists of haematised cumulus subhedral olivine (Fo_{71-74}), large interstitial zoned brown clinopyroxene (Mg# 76-80), interstitial normally-zoned plagioclase (An_{23-73}) and minor Fe-Ti oxides, with accessory apatite. The olivine grains vary greatly in size, from 0.1 mm to 3 mm in diameter (Fig. 4.4), and contain abundant melt inclusions.

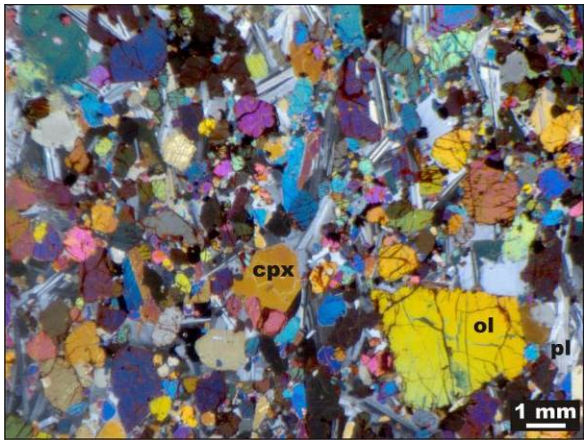


Figure 4.4: Typical intrusive olivine melagabbro, showing the variation in size of the cumulus olivine grains (XPL; TOD21).

4.2.4 Olivine-rich xenoliths

The xenoliths within the lower massive olivine gabbro are similar to the BOM in texture and character, but with greater proportions of subhedral haematised cumulus olivine (> 60%), a smaller grain size (< 1 mm) and significantly less interstitial plagioclase (< 10%; Fig. 4.5).

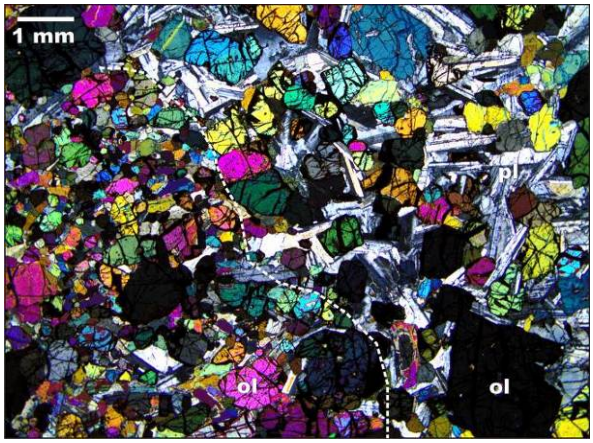


Figure 4.5: Boundary between a finer-grained, more olivine-rich xenolith (bottom left) and coarser-grained olivine gabbro host (XPL; TOD35B).

4.2.5 Massive olivine gabbro

The massive olivine gabbro is characterised by the first appearance of cumulus plagioclase (normally-zoned; An_{45-72}), which comprises 45 to 60% of the rock (Fig. 4.6a). In contrast to the basal olivine melagabbro, this material is relatively olivine-poor (less than 25%), while the proportions of clinopyroxene and magnetite remain similar. Like in the BOM, the olivine (Fo_{61}) is heavily altered to haematite, but also serpentine and iddingsite. Olivine grains are smaller in size than those in the BOM and are typically fragmented and resorbed. The clinopyroxene is similarly brown in colour and in thin section

appears strongly zoned (Fig. 4.6b; Mg # 73-79). Pyroxene grains are relatively large (up to 5 mm), with a sub-ophitic texture. Anhedral Fe-Ti oxides display trellis and minor composite oxy-exsolution, as in Figure 4.6c, and haematite alteration. Minor biotite and apatite are present.

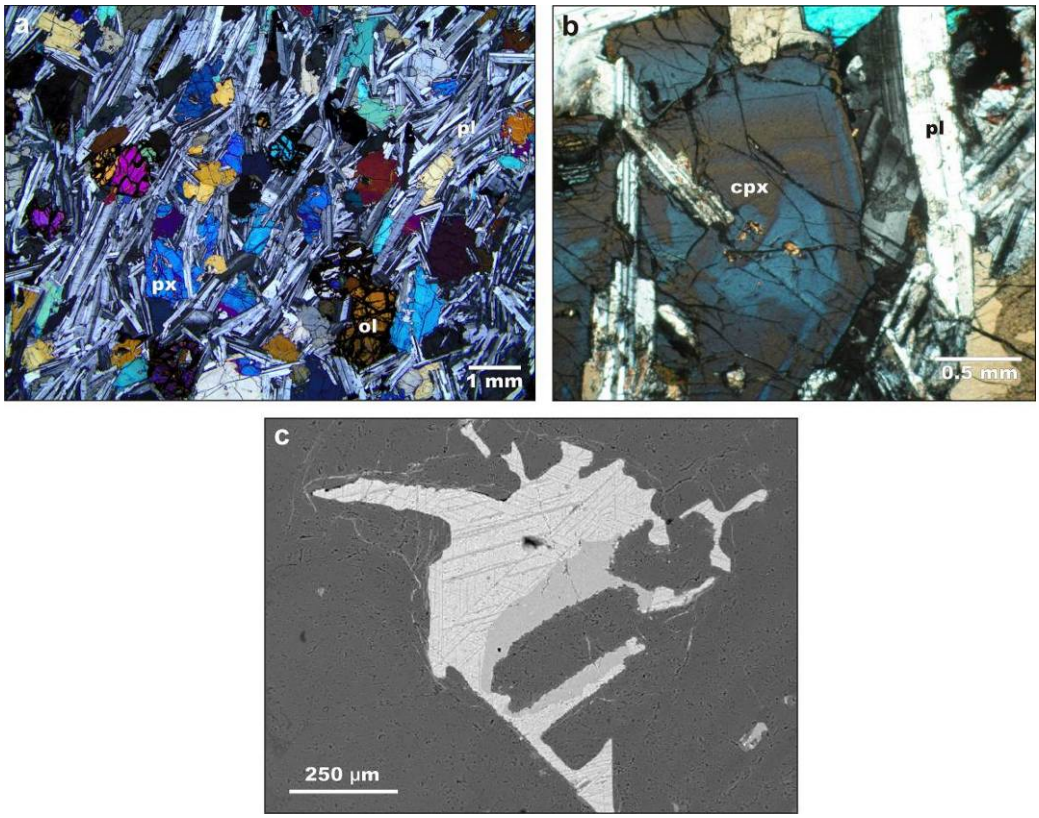


Figure 4.6: a) Typical massive olivine gabbro, showing significant subhedral cumulus plagioclase with interstitial altered and resorbed olivine, clinopyroxene and Fe-Ti oxides (XPL; TOD43). b) Ti-rich zoned clinopyroxene in MOG xenolith TOD68A (XPL). c) BSE image of both trellis-type (fine, crystallographically-controlled) and composite-type (coarse, unoriented) oxy-exsolution of ilmenite lamellae (darker grey) within titanomagnetite (TOD45).

4.2.6 Foliated olivine gabbro

The foliated olivine gabbro unit is characterised by the strong planar alignment of laths of normally-zoned cumulus plagioclase (up to 7 mm in length; An_{45-72}; Fig. 4.7). Unlike in the units below this, the euhedral cumulus olivine grains here are elongate and aligned in the plane of foliation. The olivine (Fo_{61-62}) is strongly haematised and serpentinised. Olivine and plagioclase crystals are typically hosted by large (up to 15 mm) oikocrysts of brown clinopyroxene (Mg# 73-79), which are commonly sector-zoned. Interstitial Fe-Ti oxides show both trellis and composite oxy-exsolution textures and haematite alteration. Minor red-brown biotite and apatite may be observed. The proportions of minerals in the FOG are equivalent to those in the MOG, but the strong foliation and sub-ophitic to ophitic textures are distinctive.



Figure 4.7: Aligned plagioclase laths and elongate altered olivine hosted in large clinopyroxene oikocrysts in foliated olivine gabbro (XPL; TOD22).

4.2.7 Foliated gabbro

The foliated gabbro is mineralogically equivalent to the foliated olivine gabbro, but contains less than 5% olivine. Where minor olivine is present, it is completely replaced by serpentine and iddingsite. Interstitial clinopyroxene (Mg # 74-77) grains are smaller, more elongate and not oikocrystic (Fig. 4.8). Aligned, subhedral, normally-zoned plagioclase (An_{47-67}) is typically heavily sericitised. Fe-Ti oxides are interstitial, with dominant trellis- and minor composite-type oxy-exsolution and strongly haematised margins. Cumulate textures are less easy to discern.

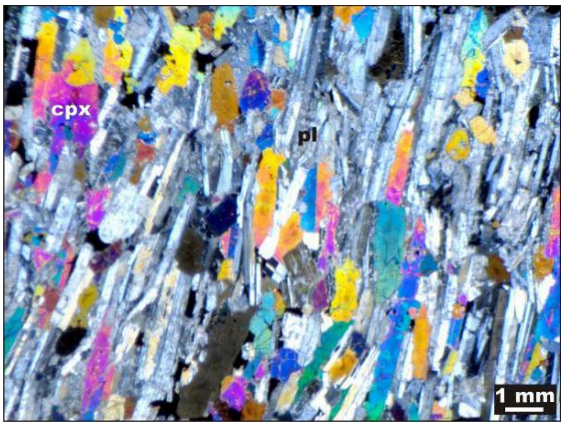


Figure 4.8: Photomicrograph of typical foliated gabbro, showing aligned sericitised plagioclase and elongate clinopyroxene with interstitial Fe-Ti oxides (XPL; TOD15).

4.2.8 Foliated magnetite gabbro

The foliated magnetite gabbro unit is marked by a distinct increase in the proportion of Fe-Ti oxides (up to 15%), which make their first appearance at this level as a cumulus phase. The oxides occur as equant

rounded or subhedral grains, with trellis titanomagnetite-ilmenite oxy-exsolution textures and are typically surrounded by oxide-filled fractures (Fig. 4.9). The phenocrystic coin-shaped magnetite grains noted at the base of this layer in the field were not observed in thin section, but are clearly euhedral and strongly haematised. Elongate subhedral clinopyroxene (Mg # 75-77) crystals define the foliation. These are characteristically inclusion-riddled (mainly plagioclase and oxides) and show sector zoning. Some pyroxenes have fine-grained haematite alteration. The cumulus plagioclase (An_{24-62}) is subhedral to euhedral and shows strong normal zonation. Sparse K-rich feldspars (orthoclase) are present in interstices between plagioclase grains (Fig. 4.9c). Plagioclase grains are typically 1.5 mm long, but phenocrystic laths up to 6 mm in length may be present (Fig. 4.9d). There is accessory red-brown biotite and apatite.

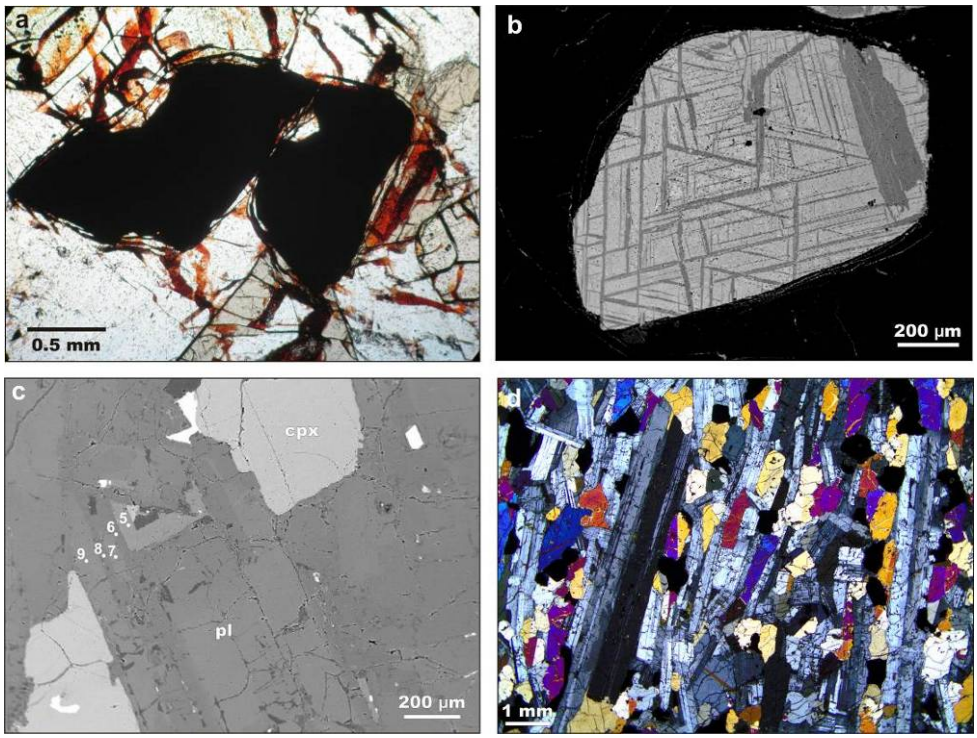


Figure 4.9: Rounded cumulus Fe-Ti oxides in foliated magnetite gabbro, a) surrounded by haematised fractures (PPL; TOD13B), and b) showing trellis-type oxy-exsolution textures of variable coarseness with ilmenite lamellae in titanomagnetite (BSE; TOD13C). c) Zoned plagioclase (numbers represent locations of microprobe analyses, i.e. probed points 6 to 9 of grain 4 in Table D.2) with a K-feldspar-filled interstice (point 5; BSE; TOD13C). d) FMG from the base of the unit containing aligned plagioclase laths (some phenocrystic) with subhedral clinopyroxene and Fe-Ti oxides (XPL; TOD23).

4.2.9 Foliated magnetite olivine gabbro

This unit marks the reappearance of cumulus olivine in the stratigraphy (up to 30%). This is present as distinctly elongate grains in the plane of foliation (in contrast to the rounded olivines of the melagabbros). The olivine (Fo_{61-62}) is commonly altered to serpentine, haematite and magnetite. In all other respects these gabbros resemble the foliated magnetite gabbro below, with aligned subhedral, normally-zoned plagioclase (An_{37-61}), zoned inclusion-riddled brown clinopyroxene (Mg# 73-74) and rounded, equant

cumulus Fe-Ti oxides with more than one generation of trellis oxy-exsolution, surrounded by fractures (Fig. 4.9).

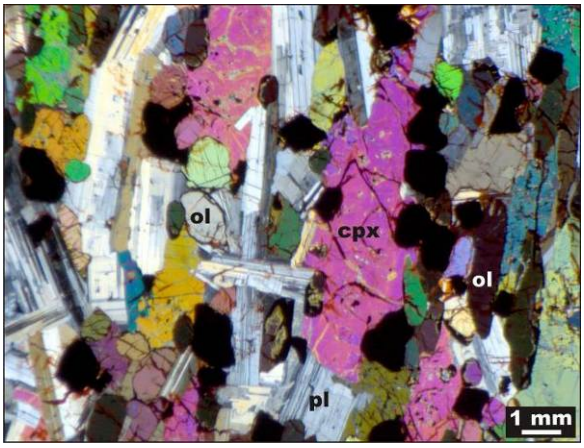


Figure 4.10: Photomicrograph showing typical foliated magnetite olivine gabbro, with aligned elongate olivine, clinopyroxene and plagioclase and rounded cumulus Fe-Ti oxides (XPL; TOD53).

4.2.10 Foliated leucogabbro

The foliated leucogabbro is the most plagioclase-rich unit in the Doros suite. These rocks consist of 55% to 90% strongly-aligned euhedral plagioclase laths (An_{46-51}), hosted in large oikocrysts of zoned brown clinopyroxene (Mg# 69-73), with patches of interstitial oxy-exsolved (trellis- and composite-type) Fe-Ti oxide and sparse interstitial olivine (Fig. 4.11). This sub-ophitic texture gives the rocks their characteristic mottled appearance. Apatite occurs as relatively large euhedral grains within pyroxene. If present, olivine is heavily altered to serpentine and haematite, and rarely, green hornblende. The feldspar is typically altered to sericite and clay minerals and, in some cases, prehnite. Sparse, fine-grained chalcopyrite may be present. This rock type is essentially a plagioclase-rich variant of the foliated gabbro.



Figure 4.11: Whole thin section view of a typical foliated leucogabbro with aligned cumulus plagioclase and interstitial oikocrystic brown clinopyroxene and Fe-Ti oxides (TOD34).

4.2.11 Pyroxene cumulate

The enclaves of pyroxene-rich gabbro consist of approximately 60% euhedral prismatic calcic clinopyroxene (2 - 6 mm), hosted within large oikocrysts of sericitised plagioclase and lesser haematised Fe-Ti oxide (Fig. 4.12). The pyroxene is paler in colour than that found elsewhere in the complex and typically shows fine-grained haematite alteration.

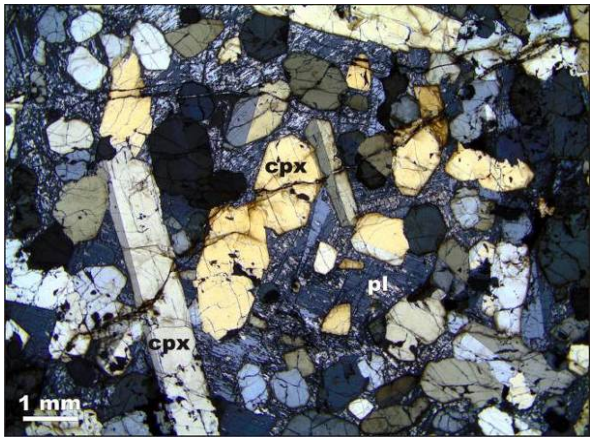


Figure 4.12: Pyroxene-rich gabbro TOD77 showing haematised euhedral clinopyroxene with interstitial altered plagioclase (XPL; slide thin).

4.2.12 Olivine cumulate

The olivine-rich gabbro enclaves consist of approximately 50% weakly-aligned euhedral, elongate magnesian olivine (up to 8 mm in length), with zoned, subhedral plagioclase (~An_{73}), large interstitial, zoned brown clinopyroxene and minor oxides (Fig. 4.13a). The olivine is strongly haematised, and also shows serpentine, iddingsite and biotite alteration. Several olivine grains contain large round inclusions (up to 1 mm), filled with plagioclase and minor apatite, in some cases with secondary oxides or serpentine (Fig. 4.13b). The oxide phase is secondary or interstitial, and in the latter is predominantly ilmenite with small titanomagnetite sector-lamellae, as in the BOM. Apatite needles are common, and are associated with plagioclase. This is essentially an olivine-rich variety of the FOG.

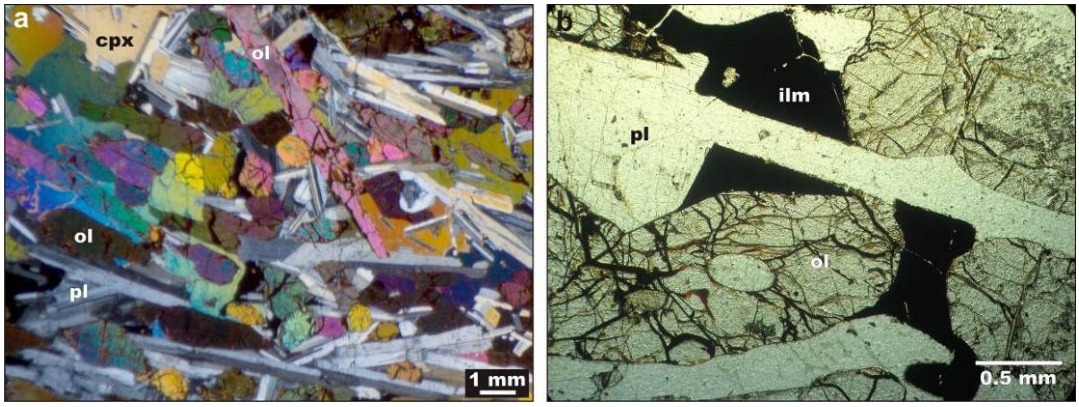


Figure 4.13: a) Weakly foliated olivine-rich gabbro showing prismatic cumulus olivine grains (XPL; TOD83). b) Haematised olivine grain with elliptical plagioclase inclusion (PPL; TOD83).

4.2.13 Magnetite cumulate

Although no thin sections are available for this material, it is clear from hand samples that it consists primarily (75 - 90%) of equant subhedral cumulus Fe-Ti oxides (~1 mm), associated with intense haematite alteration. The interstitial material is primarily plagioclase.

4.2.14 Gabbro pegmatite

The gabbro pegmatite consists predominantly of euhedral plagioclase laths (up to 5 cm long) with large oikocrysts of yellow-brown clinopyroxene (Mg# 76-78), in roughly equal proportions. The plagioclase is unzoned and has compositions of An_{63-65}. Also present are minor rounded Fe-Ti oxides with more than one generation of trellis-type oxy-exsolution and accessory euhedral apatite, commonly as inclusions in pyroxene. This material is typically heavily altered, in parts extensively replaced by prehnite, as well as clay minerals, sericite and haematite.

4.2.15 Bostonite

The bostonite consists predominantly of large euhedral grains of orthoclase (in parts perthitic) and albite (An_{1-3}). The ratio of alkali feldspar to plagioclase increases towards the pegmatitic centre of the dykes or enclaves. All the feldspars are heavily and ubiquitously altered (sericite, clay minerals) and thus original chemistry is almost impossible to obtain. The rock also contains small subhedral to euhedral grains of clinopyroxene, which is strongly concentrically zoned, from colourless augite cores to bottle-green aegerine rims (Mg# 1-65; Fig. 4.14a, b). Clinopyroxene also occurs as radial symplectitic intergrowths with feldspar (Fig. 4.14c). These are not restricted to interstices and do not appear to nucleate from grain boundaries, but from the feldspar grain centre, and are therefore unlike reaction or non-reaction intergrowths reported in other mafic intrusions (e.g. Skaergaard, Holness *et al*., 2011). Nevertheless, they likely indicate the final stages of crystallisation of the magma in the presence of a fluid phase. Fe-Ti oxides in the finer-grained margins of the dykes consist of ilmenite with haematite lamellae, where the

host phase is preferentially altered to clay minerals (Fig. 4.14d). Elsewhere these occur as small secondary subhedral grains associated with pyroxene. Olivine is rare, and where present is almost completely altered to serpentine, magnetite and iddingsite (Fo_{18-32} from the norm). Accessory apatite occurs as needles up to 0.6 mm long. Chlorite, serpentine, aegerine, purple sodic amphibole, brown sodic-calcic amphibole (replacing cpx) and prehnite are common in interstices between the feldspars in the pegmatitic central zone.

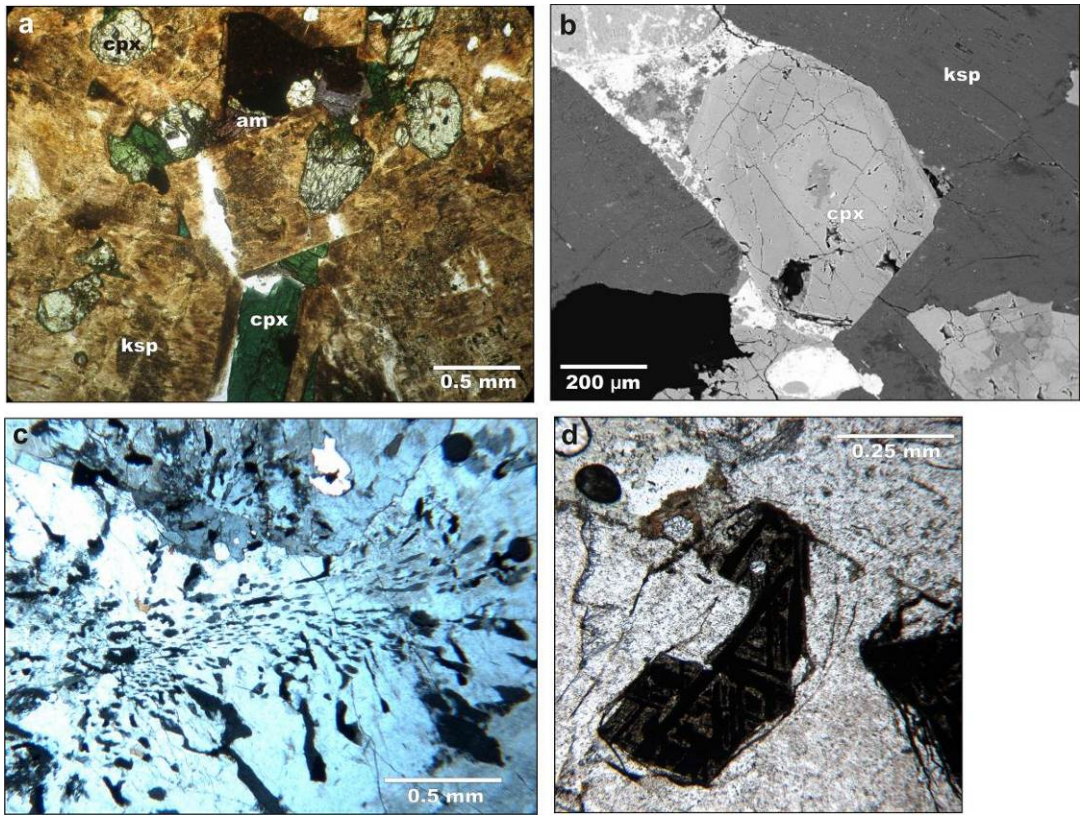


Figure 4.14: a) The central pegmatitic zone of a bostonite dyke showing heavily altered tabular alkali feldspar, subhedral colourless to bottle-green clinopyroxene and interstitial purple amphibole and oxides (PPL; TOD84). b) BSE image of zoned euhedral clinopyroxene (aegerine-augite to aegerine; TOD84). c) Symplectitic radial clinopyroxene lamellae (with secondary magnetite) in feldspar (PPL; TOD64). d) Exsolved Fe-Ti oxides showing preferential alteration of the host phase, in the bostonite marginal zone (PPL; TOD66).

4.2.16 Porphyritic dolerite

The dolerite typically consists of phenocrysts of large euhedral prismatic or equant olivine, with aggregates of phenocrystic pale green calcic clinopyroxene and plagioclase laths (~An_{46}), within an altered fine-grained matrix of similar composition (Fig. 4.15). Some of the olivine contains clusters of melt inclusions of variable size. The olivine may be mildly serpentinised, but shows no haematite alteration. The coarser-grained dolerite in the tail of the complex shows sparse clinopyroxene phenocrysts (up to 5 mm) and plagioclase aggregates, but no olivine phenocrysts. The matrix here consists of plagioclase laths, pale green clinopyroxene, heavily altered remnant olivine, skeletal magnetite and secondary sulphides (pyrite, chalcopyrite).

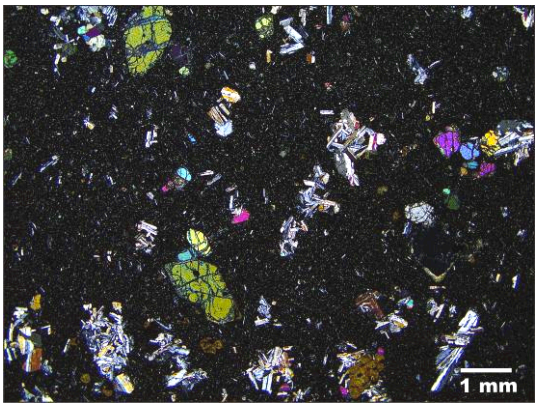


Figure 4.15: Typical porphyritic dolerite showing olivine phenocrysts and plagioclase-clinopyroxene aggregates in a fine-grained plagioclase-rich matrix (XPL; TOD10).

The petrographic features of the dolerite dykes support a disparate origin to the main Doros intrusion. The olivine does not show the ubiquitous haematisation that is characteristic of the Doros rocks. The green colouring of the pyroxenes is atypical, as is the relative abundance of sulphide minerals in these rocks.

4.3 Rock classification

The mineralogy of the Doros gabbros is relatively simple, with all major units essentially consisting of the same four basic minerals – plagioclase, clinopyroxene, olivine and Fe-Ti oxides. However, the modal proportions of these minerals, mineral and rock textures and mineral compositions make each of these units distinctive.

Lithological classification is based predominantly on mineral proportions, from hand sample and thin section modal abundance estimates and CIPW normative calculations (Fig. 4.16), but also takes textural characteristics into account. Modal abundance estimates may represent the actual mineral proportions in the rock, but determination is subjective, not volumetric, and impossible in very fine-grained material such as the chill margin. On the other hand, the norm calculations tend to underestimate olivine contents, in particular. The method of Morse *et al*. (2004), using oxygen norms, is more representative, but relatively few chemical analyses are available. Hence all of these methods are used in combination. Not reflected in these diagrams is that other minerals have also proved significant in classification – particularly magnetite, in the foliated gabbro, and alkali feldspar in the bostonites. In addition, textural characteristics and stratigraphic location have served to link samples, hence the apparent discrepancies in nomenclature in the basal olivine melagabbros and foliated leucogabbros. This is also the basis for the separation of the massive olivine gabbro and foliated gabbro units, which otherwise show similar modal mineralogy. Furthermore, major and trace element geochemical characteristics have assisted in the subdivision of the foliated gabbros in particular.

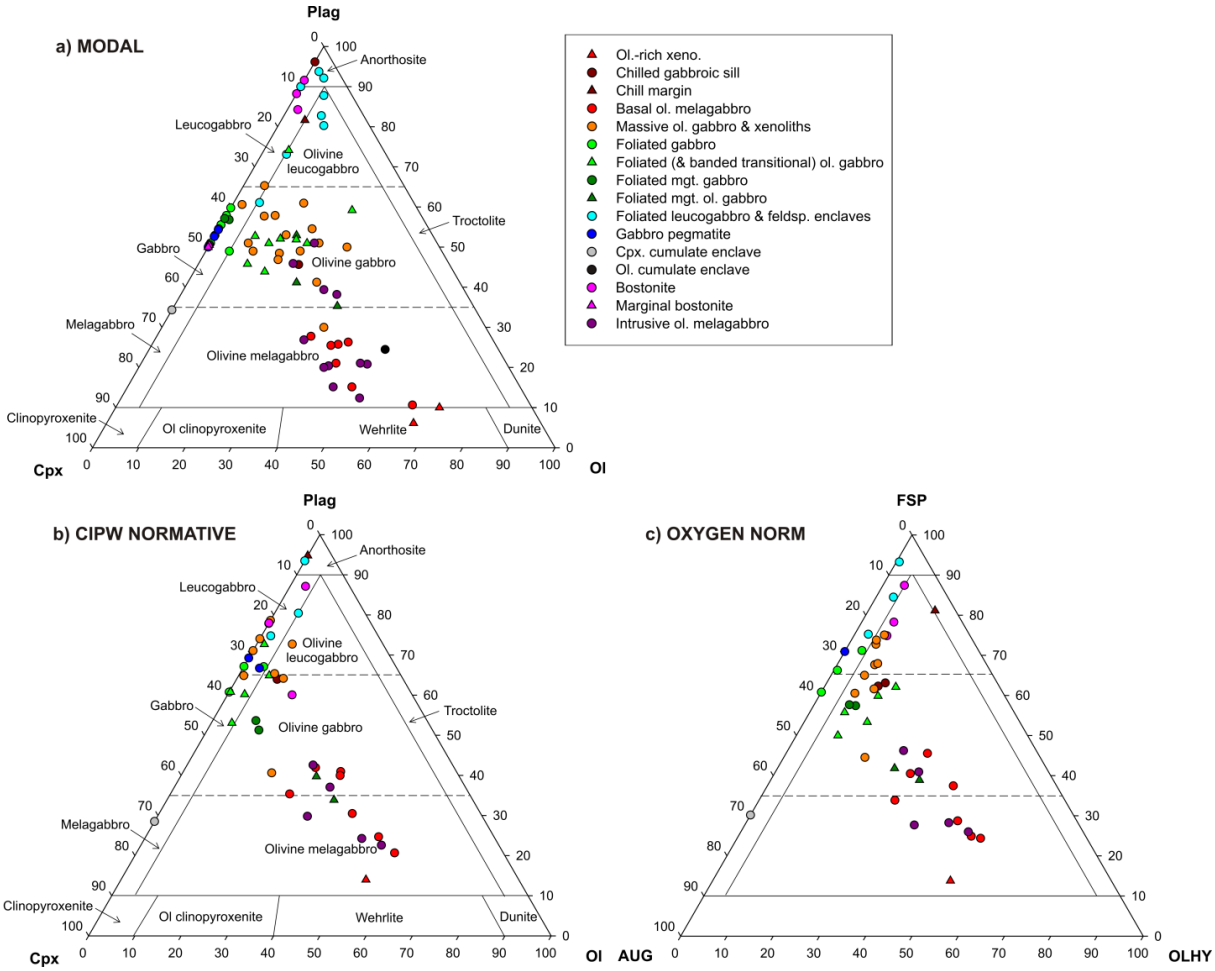


Figure 4.16: a) Modal plagioclase, olivine and clinopyroxene abundances (from thin section and hand sample estimates) for all Doros samples in this study. Classification from Streckeisen (1976) and Le Maitre *et al*. (1989). In the case of the bostonites, the plagioclase end member represents all feldspar present, since these are not readily distinguishable. b) Normative mineral abundances (calculated using the scheme of Kelsey, 1965) for Doros materials from this study and that of Marsh & Duncan (2008). Here the plagioclase end member represents normative anorthite + albite. c) Oxygen norm for the end members total feldspar (FSP), clinopyroxene (AUG) and olivine (OLHY) taking into account excess 'hyalosiderite' in the norm, according to the method of Morse *et al*. (2004).

Samples from the earlier studies of Hodgson & Botha (1974) and Marsh & Duncan (2008) have been reclassified on this same basis and included in many of the diagrams presented here, to supplement the database.

4.4 Layering and mineral stratigraphy

The Doros lithologies are clearly cumulate rocks and, while extensive recrystallisation and post-cumulus growth has obscured primary textures in many cases, the cumulus mineralogy is still discernible to a large extent. Figure 4.17 summarises the characteristics (cumulus phases; mineral major element compositions) of the main lithological units discussed in the preceding section. The petrography thus provides better delineation of the phase, modal and grain-size layering in the intrusion inferred in the field (Chapter 3). The BOM/IOM-MOG interface is defined by the appearance of cumulus plagioclase, while the FG-FMG

boundary marks the transition from intercumulus to cumulus magnetite, and the base of the FMOG sees the reappearance of cumulus olivine. Clinopyroxene textures are difficult to discern and, while this is not noted as a cumulus phase, apart from in isolated enclaves, it is only unambiguously interstitial in the poikilitic foliated olivine gabbros and leucogabbros.

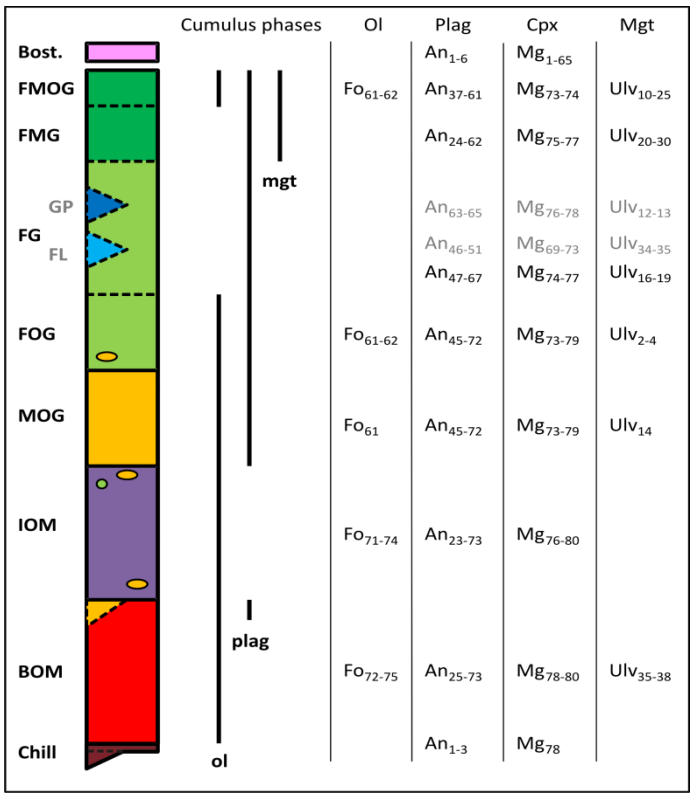


Figure 4.17: Trends in mineralogy and representative mineral chemistry (olivine forsterite content, plagioclase anorthite content, pyroxene Mg # and ulvöspinel mole fraction in titanomagnetite) through the stratigraphic succession. Not to scale. Lithological unit abbreviations are as in the text.

Although an accurate stratigraphic section through the intrusion is not obtainable due to the paucity of outcrop, changes in mineral abundances and compositions with height may be assessed in more detail by reconstructing the stratigraphy from estimates of height relative to layer contacts. In Figure 4.18, and other diagrams of a similar nature, the relative position of each sample within the unit, i.e. the true thickness from the basal contact of the layer, is calculated using the overland distance between the sample and the contact, the difference in elevation, and the approximate dip of the layer (from Hodgson & Botha, 1974). Since layer thicknesses vary, the maximum thickness is indicated in the plot (hence the seemingly incongruous total thickness of the section).

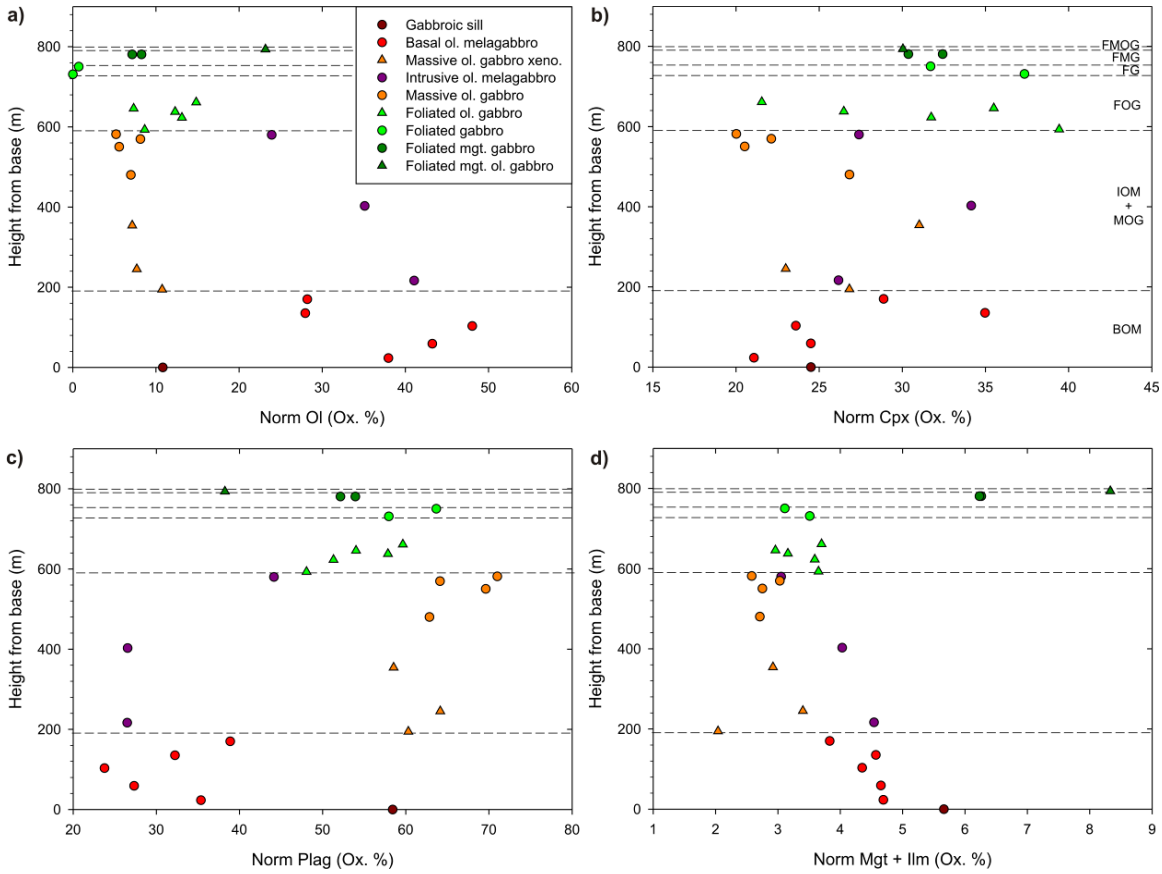


Figure 4.18: Reconstructed stratigraphic profiles through the Doros intrusion showing changes in mineral abundances (from oxygen norms) with relative height. a) Olivine (OLHY of Morse *et al*., 2004); b) clinopyroxene (AUG); c) plagioclase (FSP) and d) magnetite and ilmenite. Dashed lines indicate approximate layer boundaries.

Although semi-quantitative, the profiles of mineral normative abundances in Figure 4.18 highlight the sharp contrasts in mineral proportions across the BOM-MOG, MOG-FOG and FG-FMG interfaces, defining the modal layering. The chilled gabbroic sill is distinct from the BOM, with high normative plagioclase and very little olivine. The BOM is characteristically olivine-rich, and shows an apparent increase in olivine and decrease in plagioclase towards the centre of the layer. The IOM shows similar mineralogy to the BOM, with a trend of decreasing olivine and increasing plagioclase with height. The IOM may have intruded and displaced the lower section of the MOG unit, but xenoliths of MOG entrained within it record the composition of the original MOG. The high plagioclase content of this layer marks it as distinct from the melagabbros below. There is a subtle upward increase in plagioclase and decrease in clinopyroxene with relatively constant olivine through the MOG. The MOG-FOG interface is denoted by an abrupt decrease in plagioclase and increase in clinopyroxene. Within the FOG, there is a decrease in clinopyroxene proportions and a lesser increase in plagioclase with height. An abrupt increase in the proportions of magnetite defines the base of the FMG. Samples are sparse in the FMOG and FMG units, but there is an overall trend of increasing olivine and magnetite.

Changes in the anorthite content (An #) of plagioclase, the magnesium number (Mg #) of olivine and clinopyroxene and the ulvöspinel proportion of magnetite with stratigraphic height are shown in Figure

4.19, with the equivalent whole-rock variations for comparison. Although the mineral data reflect analyses of, in most cases, grains within a single representative sample for each of the rock units, they give some indication of overall trends through the intrusion.

In general, the plagioclase throughout the intrusion is strongly zoned, with a wide range of compositions (Figs. 4.1, 4.17, 4.19a). This indicates substantial *in situ* fractionation, both as an intercumulus phase and as overgrowths on cumulus plagioclase. The extremely sodic composition of the intensely altered feldspar in the chill margin is markedly different to that in the rest of the Doros intrusion (Fig. 4.1). Compositions for the BOM, IOM, MOG and FOG are fairly similar, but the plagioclase becomes slightly less calcic from the FG upward (Fig. 4.19a). The bostonite is characterised by sodic or potassic alkali feldspars (Fig. 4.1). The Doros feldspars also contain small amounts of Fe (FeO_T = 0.03 - 0.71%; Fig. 4.20) and Ti (TiO_2 ≤ 0.24%). Fe contents decrease upward from the BOM, increase at the level of the MOG, decrease once more, and then increase from the level of the FMG (Fig. 4.20). The small shift in plagioclase compositions at the level of the MOG may be associated with the appearance of plagioclase as a cumulus phase.

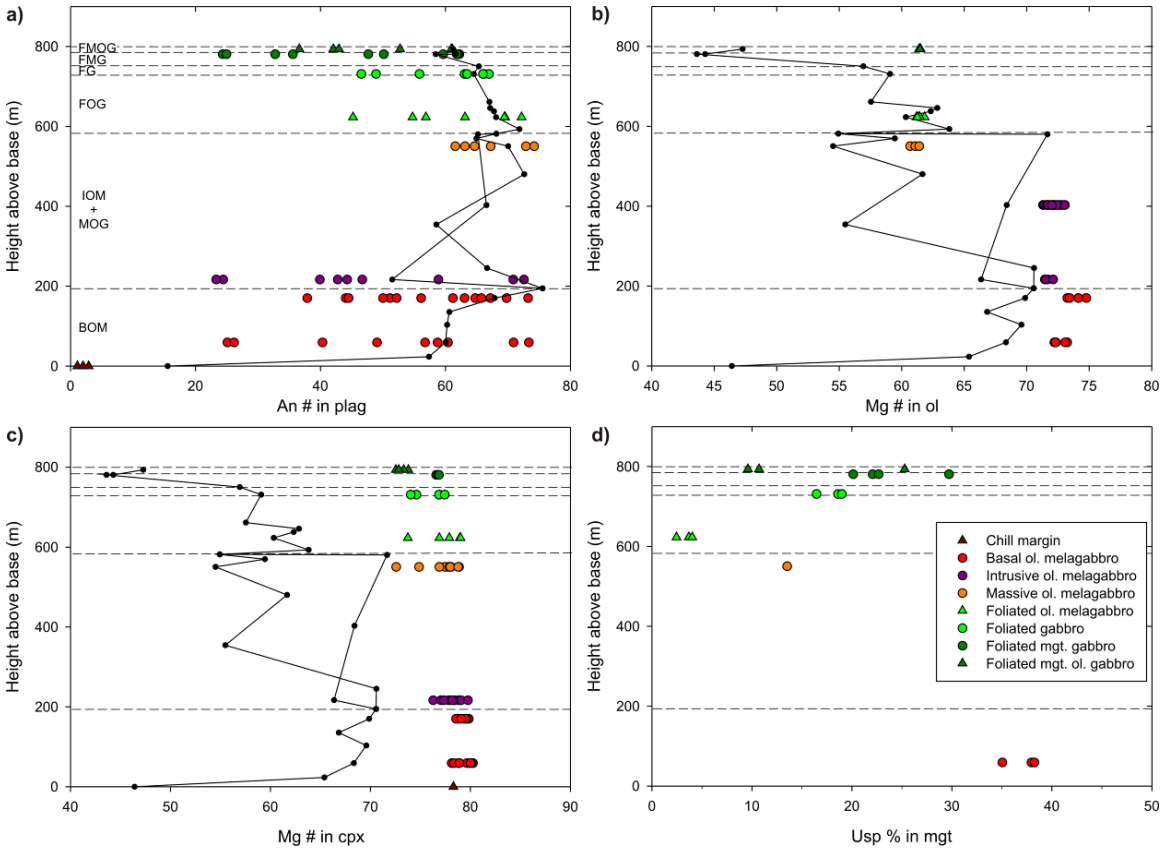


Figure 4.19: Changes in mineral chemistry with reconstructed stratigraphic height. a) Spot analyses of anorthite content of zoned cumulus and intercumulus plagioclase grains. Whole-rock An content is shown for reference (black line; split for IOM and MOG). b) Magnesium number of single olivine grains, relative to whole-rock Mg #. c) Mg # of clinopyroxenes relative to the whole-rock. d) Mole fraction of ulvöspinel in host titanomagnetites of the Fe-Ti oxide phase.

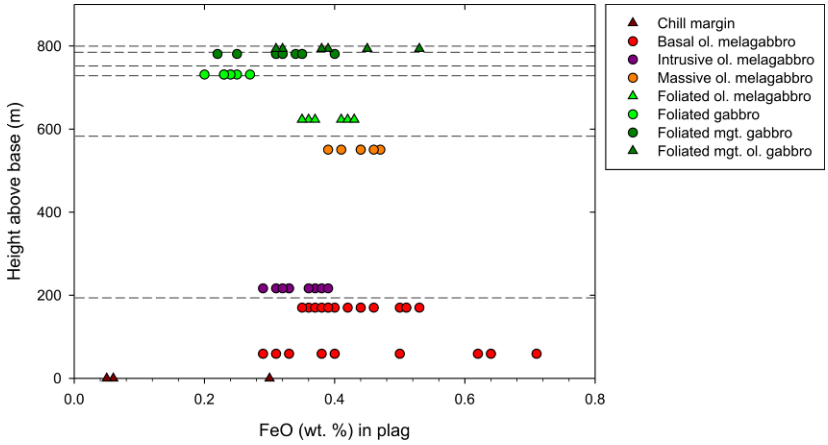


Figure 4.20: Variations in Fe contents of cumulus and intercumulus plagioclase with stratigraphic height, from spot analyses of zoned plagioclase grains from the Doros intrusion.

Olivine is consistently a cumulus phase in the intrusion. Olivines in the main body of the intrusion define two distinct, homogeneous populations in terms of magnesium content (Figs. 4.1, 4.19b). Those in the BOM and IOM have very similar, Mg-rich compositions (Fo_{71-75}), while those in the MOG, FOG and FMOG are markedly less magnesian (Fo_{61-62}). Overall, from the base to the top of the intrusion, there is a slight decrease in olivine Mg # (Fig. 4.19b). The Doros olivines are moderately Ni-rich (1491 - 1916 ppm; Fig. 4.21). In terms of Ni concentrations, three distinct clusters are evident. The BOM and IOM contain the most Ni, the FOG and MOG have intermediate compositions, and the FMOG has the lowest Ni content. This clustering of olivine compositions and lack of significant zonation suggests extensive homogenisation of olivine compositions. Maximum Mg # for clinopyroxene is consistently higher than for olivine in the same layer (Fig. 4.19).

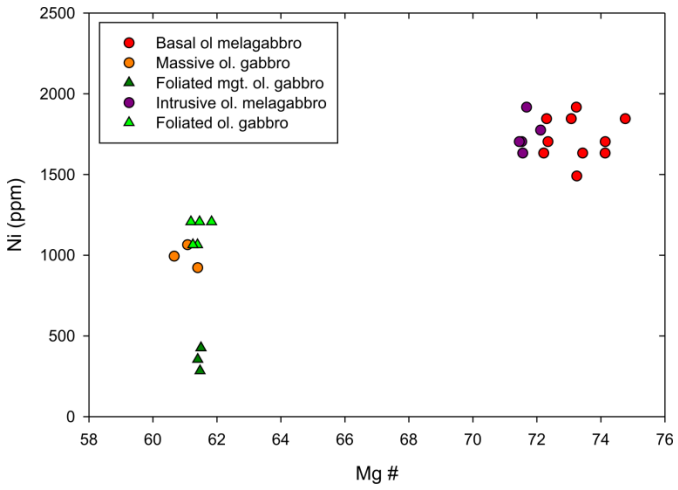


Figure 4.21: Ni contents against magnesium number in olivine in the olivine-bearing units of the Doros intrusion.

Major element compositions of clinopyroxene are very consistent throughout the main body of the intrusion, at Mg# 73-80, with only marginally raised Fe contents in the foliated leucogabbro enclaves (Figs. 4.1, 4.17, 4.19c). Pyroxenes in the bostonite, however, show a marked trend from equivalent

compositions to very Na- and Fe-rich compositions (Fig. 4.1; Table D.3). The trace elements reveal greater compositional variability. There is a subtle intra-grain zonation and cryptic trend in Cr contents, which generally decrease upwards through the main body of the intrusion (Fig. 4.22). Overall, the BOM pyroxenes are the most Cr-rich, and the foliated leucogabbro and bostonite pyroxenes are the least Cr-rich in the intrusion (Fig. 4.22, Table D.3).

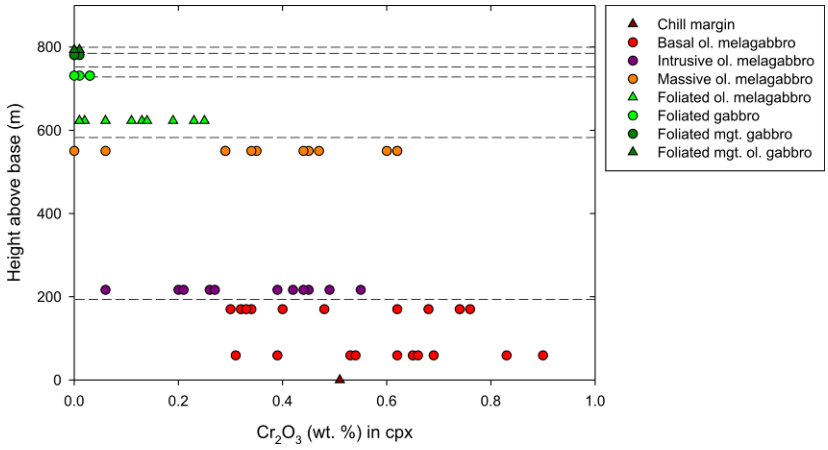


Figure 4.22: Variations in Cr contents of clinopyroxene with stratigraphic height in the Doros intrusion.

The oxidation exsolution textures documented in the Fe-Ti oxides formed due to the separation of ilmenite lamellae from titanomagnetite under subsolidus conditions, during slow cooling of the intrusion (Buddington & Lindsley, 1964). This style of oxy-exsolution, i.e. relatively Ti-poor magnetite with abundant ilmenite lamellae, indicates that oxidation has progressed to the C3 stage of Haggerty (1991; moderate to complete oxidation of ulvöspinel). The titanomagnetite host component in the Fe-Ti oxides shows a distinct decrease in the proportion of Ti (represented by the mole fraction of ulvöspinel) from the basal gabbros to the FOG, followed by an increase through the FG and FMG, and a slight decrease once more thereafter (Figs. 4.17, 4.19d). Overall, the magnetite hosts of the Fe-Ti oxides show a positive correlation between Ti and Fe^{2+} content (Fig. 4.23a). This roughly corresponds with the degree of oxy-exsolution – with increased oxidation, more Ti is incorporated into exsolved ilmenite lamellae. Titanomagnetites in the foliated leucogabbro have relatively high Ti-contents, on a par with the MOG.

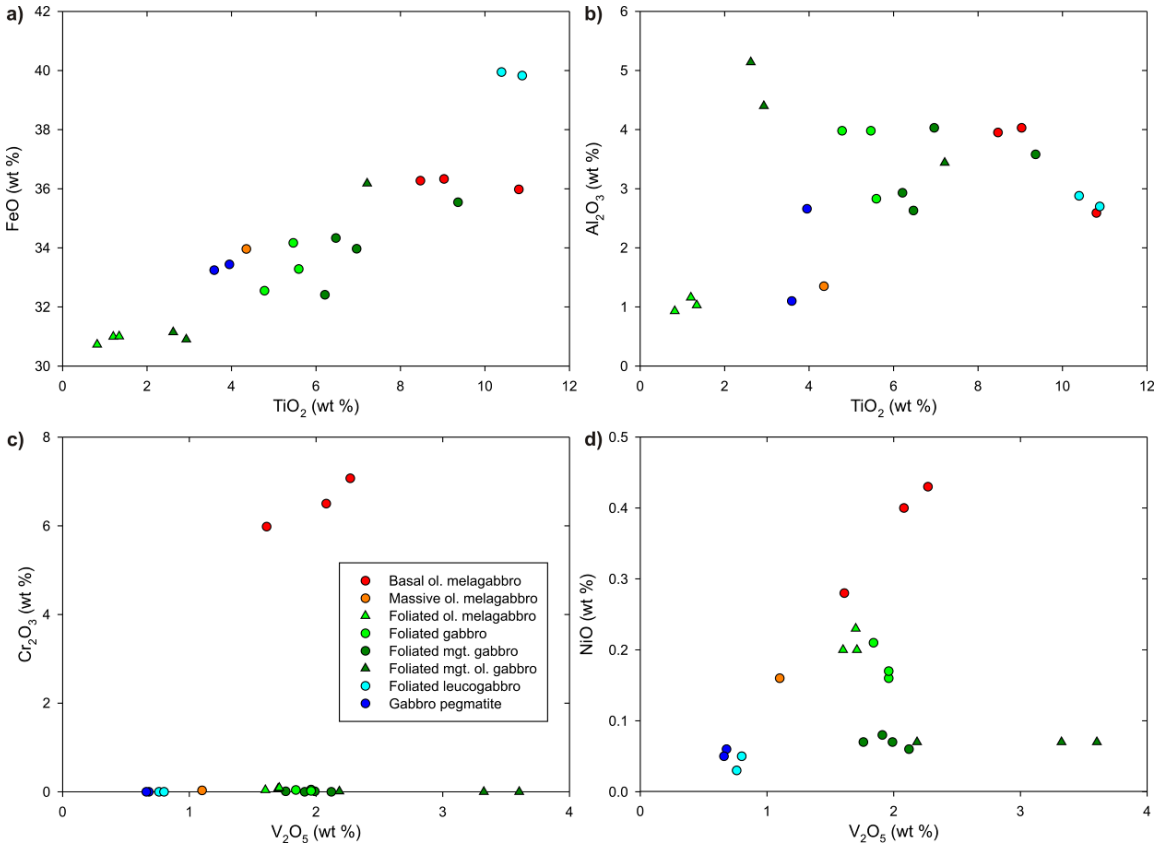


Figure 4.23: TiO_2, FeO (recalculated from perfect stoichiometry), Al_2O_3, Cr_2O_3, V_2O_3 and NiO contents of spot analyses of the titanomagnetite host phase of Fe-Ti oxide grains in the Doros intrusion.

The Fe-Ti oxides also contain appreciable amounts of Al, Mg, Mn, Cr and V (Fig. 4.23). The trends in concentration of these elements in the oxide phase are obscured to some extent by differing degrees of oxy-exsolution, which redistributes these constituents between the host magnetite and ilmenite lamellae. While bulk compositions would be more representative, these are notoriously difficult to calculate and require extensive modal data to quantify the proportions of phases, which are not available. Nevertheless, these concentration data give some indication of overall compositional trends. Al_2O_3 is highest in the titanomagnetite hosts of the foliated magnetite gabbro and lowest in the foliated olivine gabbro (Fig. 4.23b). The titanomagnetites of the basal olivine melagabbro are distinctly more enriched in Cr_2O_3 (up to 7 wt. %) compared to the rest of the suite (Fig. 4.23c). This is not coupled with V contents. V_2O_5 decreases from the BOM to the MOG, then increases upward in the stratigraphy from the MOG to the FMOG (up to 3.6 wt. %). Enrichment in V in magnetite where this mineral first appears in the stratigraphy as a cumulus phase is typical of layered mafic intrusions (Frost & Lindsley, 1991). Ni contents in titanomagnetite decrease upward from the BOM to MOG, return to higher levels in the FOG, and decrease again towards the FMG, remaining constant thereafter (Fig. 4.23d). In general, the oxides in the foliated leucogabbro and pegmatite show the lowest abundances of trace components.

The ilmenite lamellae of the Fe-Ti oxide phase are relatively rich in MgO (up to 7 wt. %). When compared with MnO contents, there are distinct clusters of compositions and not a linear trend (Fig.

4.24). However, the basal olivine gabbro lies at the high-Mg, low-Mn end of the range and the pegmatite and foliated leucogabbro generally fall at the opposite end of the range.

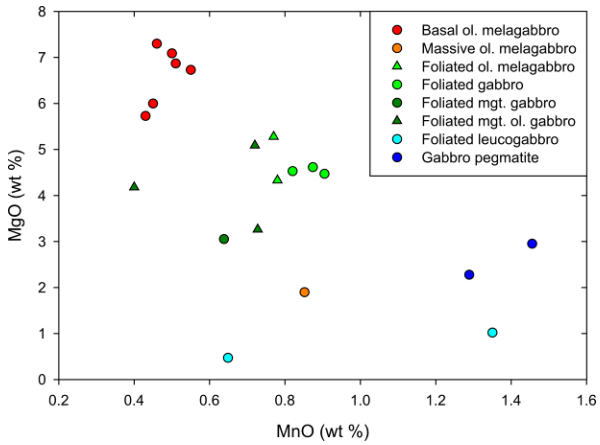


Figure 4.24: Concentrations of MgO vs. MnO in ilmenite lamellae of Fe-Ti oxides in the Doros intrusion.

The Fe-Ti oxides provide information on the conditions of crystallisation. That is, not of primary magmatic crystallisation, as in such plutonic rocks this has been obscured by subsolidus recrystallisation, but of equilibrium conditions at the time of oxy-exsolution, in the later stages of cooling and crystallisation of the Doros magma (Buddington & Lindsley, 1964; Frost, 1991). Equilibrium temperatures and oxygen fugacities were calculated here using the chemical data for co-existing Fe-Ti oxide phases in oxy-exsolved grains, using the program ILMAT (Lepage, 2003) and the methods of Stormer (1983) and Andersen & Lindsley (1985), which consider the influence of all minor element components. The results (Table D.6) are shown graphically in Figure 4.25.

Most of the analysed magnetite-ilmenite pairs indicate conditions near the QFM (quartz-fayalite-magnetite) buffer, as in most layered mafic intrusions. The basal olivine gabbro shows the highest temperature of equilibration, at 734 to 788°C, and the highest oxygen fugacity. This is followed by the foliated gabbro, foliated leucogabbro, foliated olivine gabbro, and with a trend to more reducing conditions, the foliated magnetite olivine gabbro, foliated magnetite gabbro and gabbro pegmatite. The FMG and pegmatite approach the MW buffer. The pegmatite is the least oxidised and began to exsolve at temperatures close to 370°C. Clearly oxidation exsolution for each unit occurred over a range of temperatures.

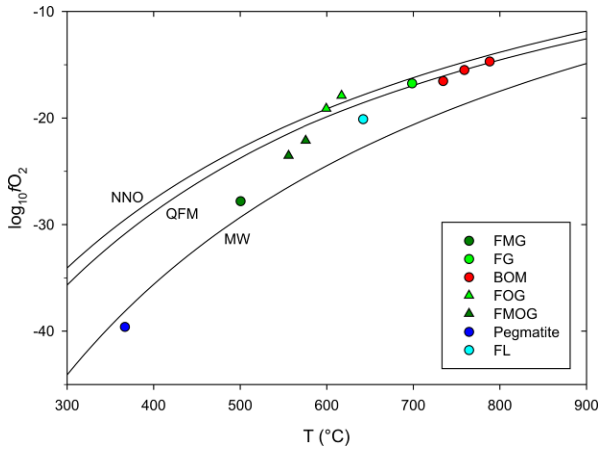


Figure 4.25: Equilibrium temperatures and oxygen fugacities calculated from co-existing magnetite-ilmenite pairs. Curves represent the quartz-fayalite-magnetite (QFM), Ni-NiO (NNO) and magnetite-wüstite (MW) buffers (all at 1 kbar), for reference (Frost, 1991).

Despite the uniformity of olivine and clinopyroxene compositions through the intrusion, the whole-rock Mg # varies significantly (Fig. 4.19b, c). This confirms that whole-rock chemistry is dominantly an effect of the proportion of minerals, rather than variations in mineral chemistry. Overall, the change in plagioclase maximum An content with stratigraphic height correlates well with that of the co-existing clinopyroxene maximum Mg #, although at a differential rate of approximately 3 times more efficient plagioclase fractionation. There is no good correlation with olivine Mg #.

The overall decrease in plagioclase An content, Mg # of the mafic minerals and mineral trace constituents through the Doros stratigraphy is consistent with fractionation. However, the irregular changes in Usp content of titanomagnetite and reversals in mineral trace element components, particularly at the levels of the MOG and FOG, allude to complexities on a smaller scale.

4.5 Hydrothermal alteration and oxidation

The Doros rocks show evidence of hydrothermal alteration, both at high and low temperature stages of their evolution. The ubiquitous haematisation of the olivine in the Doros gabbros indicates high temperature (> 600°C), deuteric alteration under oxidising conditions (Haggerty & Baker, 1967). This is also reflected in the oxy-exsolution of the associated Fe-Ti oxides, which I have shown suggests conditions close to the QFM buffer. The Doros magmas thus experienced oxidising conditions, in the presence of a fluid phase, during the late stages of crystallisation.

The chill margin rocks show intense alteration of the glassy matrix to low temperature hydrous minerals, such as calcite and clay minerals, and of the phenocrysts to serpentine, oxides, sericite and haematite. The abundance of calcite infilling vesicles suggests interaction with a CO_2-rich fluid. The chilled gabbroic sill shows similar, but milder alteration. The extremely sodic composition of the plagioclase in the chill margin indicates that this rock is essentially spilitised. The high contents of Ca and Ti in the olivine show intensive replacement by calcite and Fe-Ti oxides. These minerals clearly do not reflect their original

compositions. Only the clinopyroxene appears largely unaffected, with characteristics equivalent to that in the BOM, IOM and MOG. The fluids responsible for alteration were likely derived from the metasedimentary wall rocks to the intrusion. The Zerrissene Group, which abuts the southern and eastern contacts, contains metacarbonates (Miller, 2008d) that are a likely source for the CO_2. The baked aureole shows that the dehydration contact metamorphism did not extend further than a few metres into the wall-rock.

In the gabbro pegmatite enclaves and bostonite dykes, there is abundant prehnite, chlorite, malachite, serpentine, epidote, amphiboles, sericite and clay minerals replacing the primary feldspar and mafic minerals. This is indicative of late-stage hydrothermal alteration. The prehnite in particular indicates temperatures between 200 and 400°C, pressures less than 3 kbar, and a CO_2-poor fluid (Liou, 1971; Deer *et al*., 1992).

The foliated leucogabbro shows extensive prehnite and clay mineral alteration of plagioclase. Minor prehnite, calcite, chlorite, serpentine and clay mineral alteration is also present in some samples of the Upper Foliated Series. Thus, while fluids were concentrated in the pegmatitic and bostonitic enclaves, they were also circulating through the core rocks.

The presence of malachite in the pegmatite, bostonite and foliated gabbro , and the small amounts of disseminated native copper observed in the massive olivine gabbro and foliated gabbro (Reuning & Martin, 1957; Hodgson & Botha, 1974; Marsh & Duncan, 2008) are a strong indication that the fluids circulating through the intrusion during this late stage of crystallisation were relatively copper-rich. These are not primary magmatic ores, and there is no association with sulphides, as in other LMIs. It is suggested that the copper originated from the Doros magma – plume-derived basaltic magmas are known to contain moderate concentrations of Cu (Sawkins, 1976) – but, in the absence of a sulphide component (S content is low, generally < 200 ppm; Chapter 5), this incompatible element was concentrated in the final excluded, fluid-rich melt fraction that contributed to pegmatite formation. The copper was then redistributed through the core rocks by circulating low-temperature fluids.

4.6 Comparison with other layered mafic intrusions

The major mineralogy of the Doros intrusion, i.e. olivine, plagioclase, calcic clinopyroxene (no orthopyroxene or pigeonite) and titanomagnetite (no primary ilmenite, only oxy-exsolved), is somewhat unusual for a layered mafic intrusion. Most of the well-known LMIs have two-pyroxene assemblages, e.g. Bushveld (ol + plag + cpx + opx + mgt + chr; Cawthorn *et al*., 2006), Stillwater (ol + plag + cpx + opx + chr + mgt + ilm; McCallum *et al*., 1980), Skaergaard (ol + plag + cpx + opx + mgt + ilm; McBirney, 1989), Dufek (plag + opx + cpx + ilm + mgt; Himmelberg & Ford, 1977). In this regard it may be comparable with the Kiglapait intrusion, which is dominated by olivine, augite and plagioclase, with minor magnetite and ilmenite, and orthopyroxene occurs only in trace amounts as rims on olivine or augite (Morse, 1979b). This indicates a basaltic parental magma with relatively low silica activity (Morse,

1980) and suggests negligible crustal contamination. It is also consistent with crystallisation at a relatively shallow depth (< 15 km; Green & Ringwood, 1967). Most mafic intrusions also contain primary ilmenite as a dominant or minor oxide phase (Frost & Lindsley, 1991), with a notable exception in the Bushveld Complex, where discrete ilmenite is rare (Molyneux, 1972; Cawthorn *et al*., 2006). This may indicate relatively low Ti in the original magma.

The apparent disappearance of olivine at the level of the FOG and return at the FMOG is important to note. The stratigraphic disappearance and reappearance of cumulus olivine in LMIs is commonly attributed to an olivine-melt reaction forming enstatite, followed by Fe-rich olivine crystallisation (e.g. in the Stillwater intrusion; Raedeke & McCallum, 1984). However, there is no orthopyroxene associated with this interval of the Doros stratigraphy, or indeed anywhere in the intrusion, and the olivine that crystallises at the FMOG is still relatively Mg-rich (Fo_{61-62}). This suggests that the Doros layering is not solely derived from simple fractional crystallisation processes.

The range of mineral compositions reported for the Doros intrusion is not as great as in the classic LMIs. Primitive compositions are not evident, since an ultramafic series is absent. The most magnesian olivine is Fo_{75} and the most calcic plagioclase is An_{73}, compared to Fo_{89} and An_{80} in the Bushveld Complex (Cawthorn *et al*., 2006) and Fo_{90}, An_{88} in the Stillwater Complex (Raedeke & McCallum, 1984). However, in this respect it is comparable to the Kiglapait (Fo_{74}, An_{70}; Morse, 1979a) and Sept Iles (Fo_{75}, An_{72}; Namur *et al*., 2010) intrusions. Similarly, the main body of the Doros intrusion does not obtain the highly evolved mineral compositions present, for example, in the Kiglapait (Fo_{0}, An_{12}; Morse, 1979a), Skaergaard ($Fo_{0.3}$, An_{30}), or Bushveld (Fo_{5}, An_{7}). However, comparable Fe-rich pyroxenes and alkali feldspars are present in the bostonite phase, suggesting that this may represent a late-stage differentiate of the Doros magma.

4.7 Summary of findings

The Doros Intrusion consists predominantly of a modal or grain-size layered sequence of gabbros and olivine gabbros. The fundamental mineralogy is plagioclase + calcic clinopyroxene + oxy-exsolved Fe-Ti oxides ± olivine. Variations in the modal proportions of these minerals, mineral and rock textures, and compositions define 17 distinct lithological units which have been described in detail here. In summary, the main body of the intrusion consists of a lower sequence of massive olivine cumulates, with a basal chill margin, followed by a massive plagioclase-cumulate layer, and topped by a series of variable, strongly foliated, plagioclase-, olivine- or magnetite-cumulate layers. A syenitic phase occurs as dykes or enclaves within the gabbros. The stratigraphic order of appearance of cumulus minerals and trends in mineral chemistry are consistent with overall fractional crystallisation. However, subtle disruptions to these trends suggest a more complex history.

Chapter 5: Whole-rock Chemical Compositions

5.1 Introduction

The previous chapter documented the mineral and textural characteristics of the Doros intrusion. Here I examine the chemical characteristics of the rock units. Whole-rock major and trace element compositions for the set of Doros samples analysed in this study are presented in Table C.1 of the Appendix. CIPW norm calculations are presented in Table C.3. Geochemical data from previous studies by Hodgson & Botha (1974) and Marsh & Duncan (2008) are included in many of the diagrams for a more complete sample set. While LOI is generally less than 2%, all data in figures are renormalised volatile-free, for effective comparison.

5.2 Whole-rock major element compositions

As the total alkalis versus silica plot (Fig. 5.1) shows, the main Doros layered suite consists of gabbros, with typical gabbro chemistry (48 – 51% SiO_2; 2 - 4% alkalis), and 'peridotgabbros' (picritic gabbros), which contain less silica (down to 40% SiO_2), in line with their higher olivine (and in some cases magnetite) contents. There is a trend towards more felsic, monzonitic to syenitic compositions in the foliated leucogabbro and feldspathic enclaves, chill margin and bostonite dykes (up to 60% SiO_2; 11% alkalis). The suite straddles the alkaline-subalkaline divide.

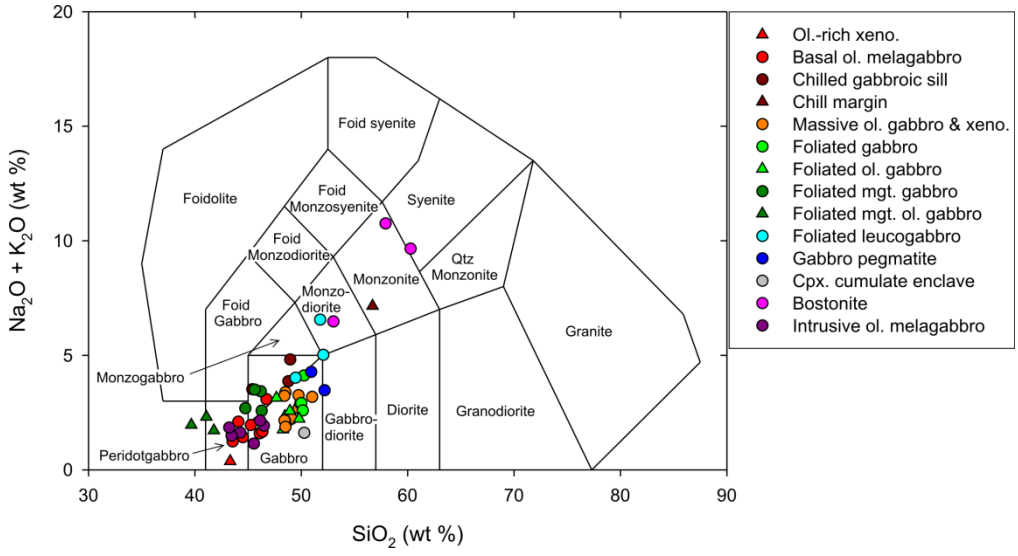


Figure 5.1: Classification of all Doros samples (this study; Marsh & Duncan, 2008) using the total alkalis versus silica diagram for plutonic rocks of Middlemost (1994).

In terms of CIPW normative compositions (Fig. 5.2, Table C.3), the suite is predominantly olivine-normative (0 - 43%), although a few samples show minor normative quartz (< 2%), while other samples show minor normative nepheline (< 4%). This apparent crossing of the albite-olivine thermal divide is clearly an artifact of the norm – the rocks show neither modal quartz nor nepheline, and several quartz-normative samples in fact have significant modal olivine. There is also normative hypersthene (up to 18%) in some rocks, although no modal orthopyroxene is present in the suite. A similar problem was encountered in the orthopyroxene-absent Kiglapait intrusion and was attributed by Morse *et al*. (2004) to small excesses in SiO_2 in analyses. A more representative, modified oxygen normative system was devised to account for this, and was presented for the Doros lithologies in Figure 4.16. Thus, although the CIPW normative compositions in the standard Ne-Di-Ol-Hy-Qz diagram (Fig. 5.2) indicate great scatter between silica-undersaturated to saturated to oversaturated compositions, the modal assemblage is more in line with mildly alkaline basalt.

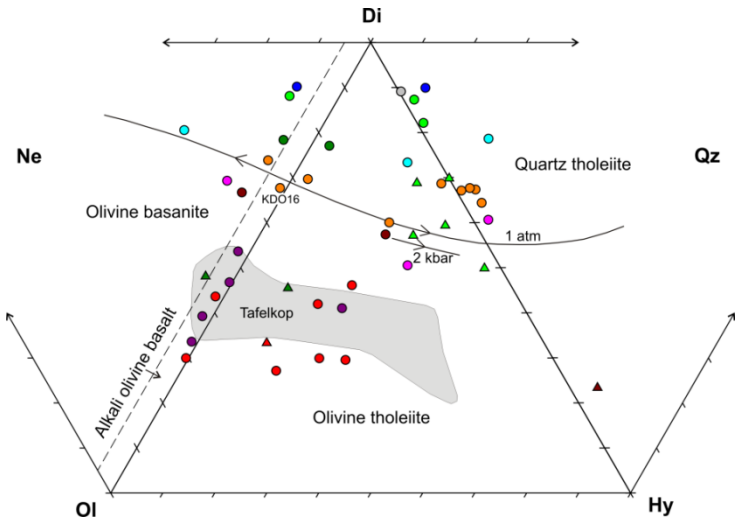


Figure 5.2: CIPW normative diopside, olivine, hypersthene, nepheline and quartz in the Doros rocks (this study; Marsh & Duncan, 2008). Symbols are as in Figure 5.1 above. The experimentally-determined cotectics for olivine + plagioclase + clinopyroxene + basaltic liquid at 1 atm (from Thompson *et al*., 2005) and 2 kbar (from Grove *et al*., 1992, in Thompson *et al*., 2007) are also shown (solid arrow lines). The grey field represents the Tafelkop Group basalts from the Etendeka Province (Ewart *et al*., 1998a; Jerram *et al*., 1999; Gibson *et al*., 2000; Thompson *et al*., 2001), which will prove important for later discussion.

Overall, the suite shows a trend from the most primitive rocks (basal olivine melagabbro, intrusive olivine melagabbro), through the massive olivine gabbro and foliated gabbro, to the most evolved rocks, the foliated leucogabbro and bostonite (Figs. 5.3, 5.4). The highest MgO contents (15 - 25 wt. %) in the BOM and IOM reflect high proportions of olivine, as supported by the petrography. The magnetite (olivine) gabbro samples have high TiO_2 (3 - 4 wt. %) and FeO (12 - 21 wt. %) contents, this being incorporated into Fe-Ti oxides (Fig. 5.4c, d). In this respect, they define a separate trend from the main suite (e.g. Figs. 5.3a, 5.4c, d). The relatively higher Al_2O_3 and Na_2O contents in the MOG, foliated (olivine) gabbro and foliated leucogabbro (Fig. 5.4a, e) are in line with the abundant plagioclase documented in these rocks. The bostonite dykes are distinct from the main suite, particularly in their low CaO (Fig. 5.4b), high Na_2O

(Fig. 5.4e), very high K_2O contents (up to 6 wt. %; Fig. 5.4f) and divergent trajectory of FeO contents (Fig. 5.3b). This is evident in the predominance of sodic and potassic feldspar and Na-Fe pyroxenes in these rocks (Chapter 4). The chilled gabbroic sill samples have distinct characteristics to the other Doros units, although there are some affinities with the foliated magnetite gabbros with respect to MgO, FeO, TiO_2 and Al_2O_3 contents. The intensely altered chill margin (to the sill) shows anomalous chemistry, with particularly high Na_2O (6.9 wt. %) and low CaO (3.4 wt. %) contents (Fig. 5.4b, e).

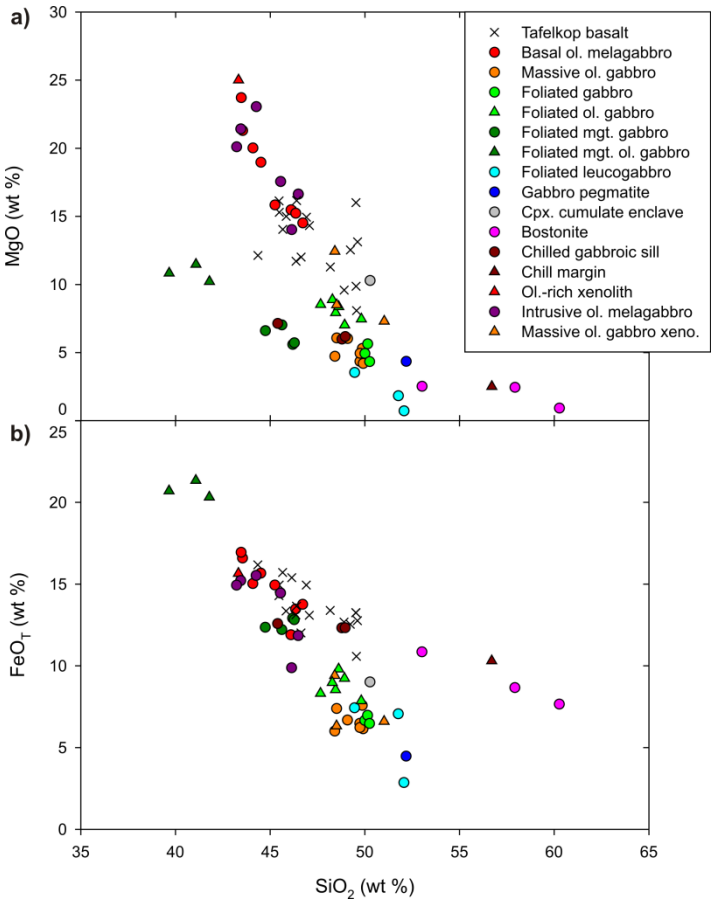


Figure 5.3: Whole-rock SiO_2 vs. a) MgO and b) total Fe as FeO, for the complete Doros suite (this study; Hodgson & Botha, 1974; Marsh & Duncan, 2008). Also shown are compositions of Tafelkop Group basalts from the Etendeka Province (Ewart *et al*., 1998a; Jerram *et al*., 1999; Gibson *et al*., 2000; Thompson *et al*., 2001), which will prove important for later discussion.

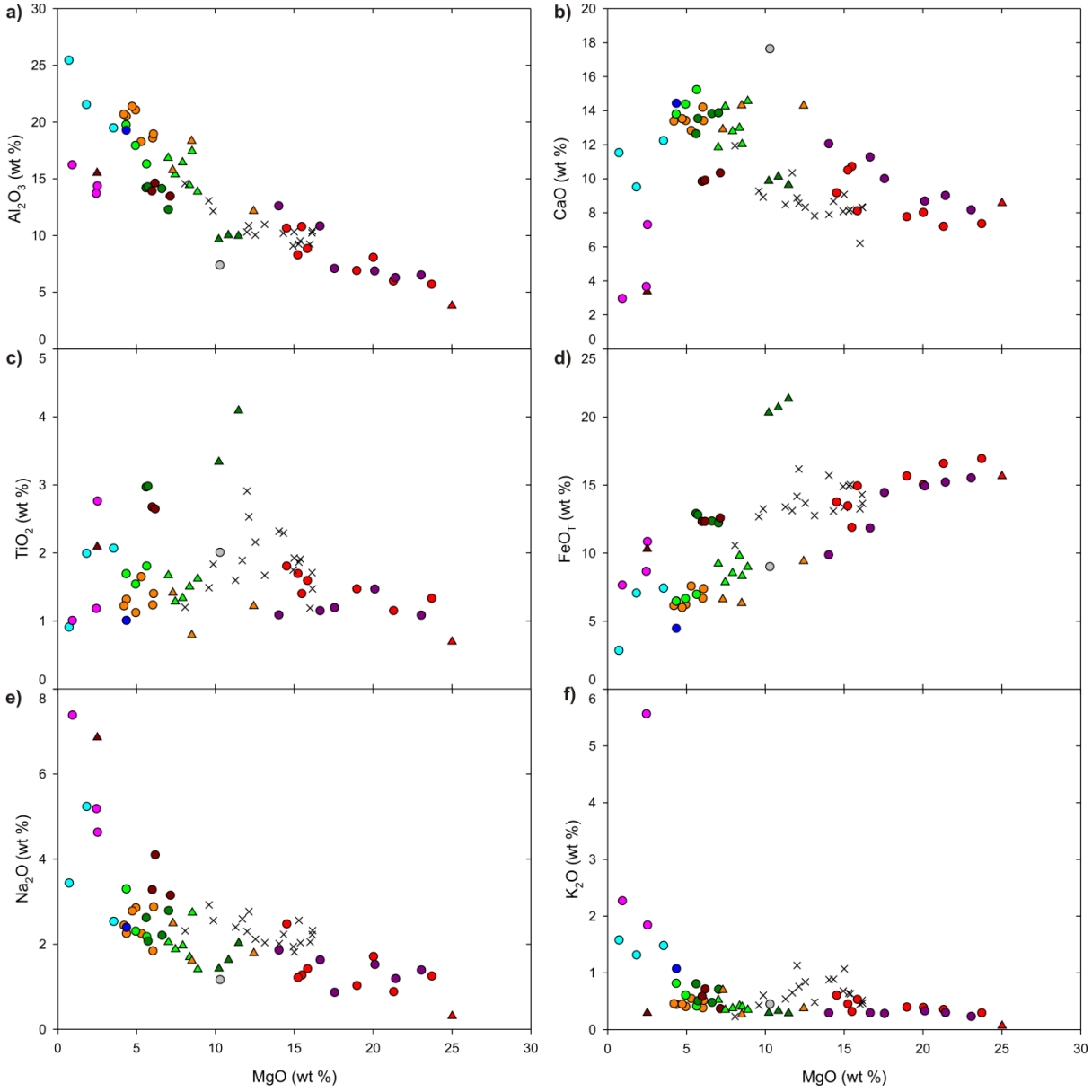


Figure 5.4: Whole-rock MgO against a) Al_2O_3, b) CaO, c) TiO_2, d) total FeO, e) Na_2O and f) K_2O, for the complete Doros suite (this study; Hodgson & Botha, 1974; Marsh & Duncan, 2008) and Tafelkop basalts (Ewart *et al*., 1998a; Jerram *et al*., 1999; Gibson *et al*., 2000; Thompson *et al*., 2001). Symbols are as in Figure 5.3.

Compositional trends with stratigraphic height may be assessed by reconstructing the stratigraphy (Fig. 5.5), as was done for mineral abundances and compositions in Chapter 4. Mg contents mimic the trends of olivine abundances observed in the rocks, while Na contents reflect plagioclase abundances. There is an overall trend of decreasing magnesium number with stratigraphic height. However, clear distinctions in chemistry can be seen across the Sill-BOM, BOM-MOG, MOG-FOG and FG-FMG contacts.

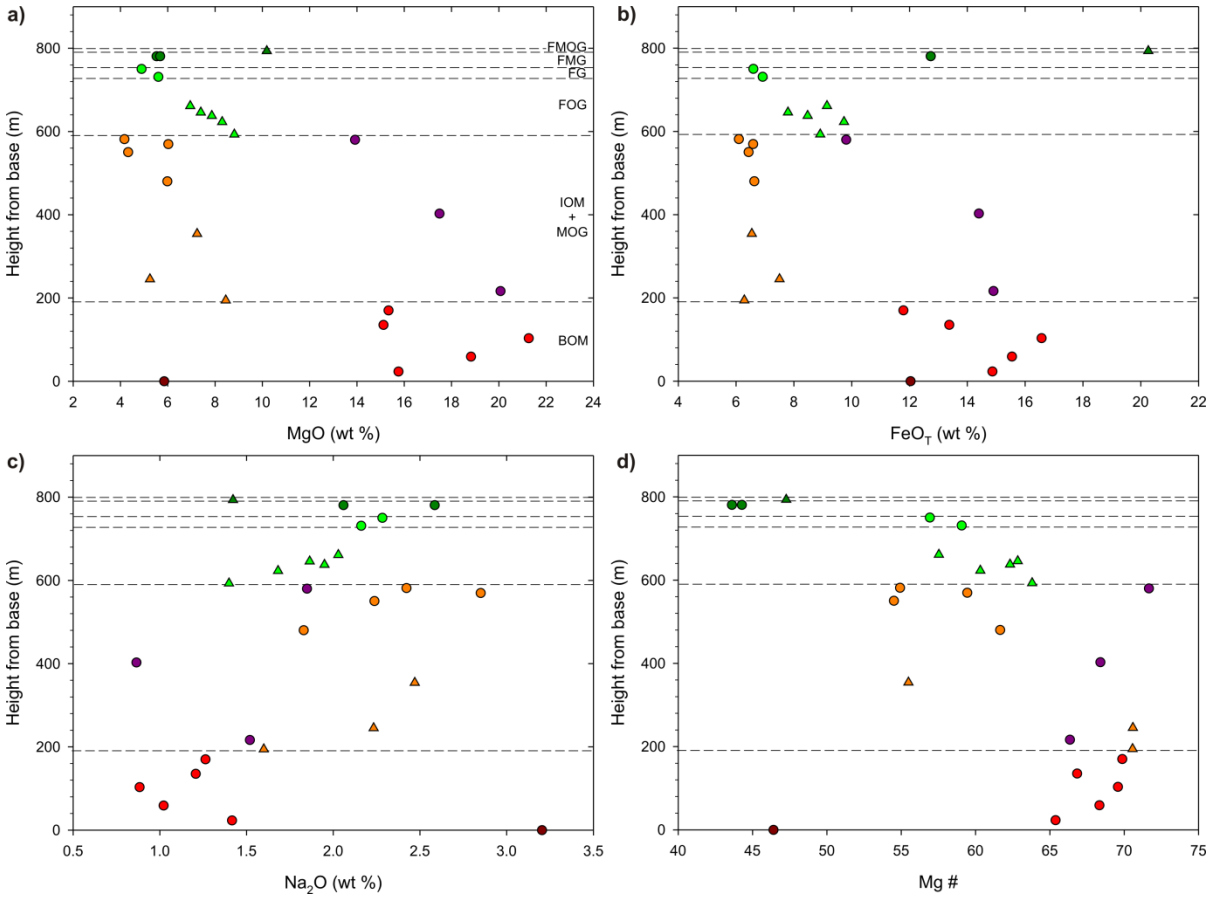


Figure 5.5: Reconstructed stratigraphic profiles through the main body of the Doros intrusion showing changes in major element contents. a) MgO, b) total FeO, c) Na_2O and d) magnesium number. Dashed lines indicate approximate layer boundaries. Symbols are as in Figure 5.3.

5.3 Rare earth element abundances

The majority of the Doros samples show similar, gently sloping, linear rare earth element (REE) patterns, with mild light REE enrichment and no Eu anomalies (Fig. 5.6). All the major units in the main body of the intrusion, i.e. the BOM, IOM, FOG, FG, FMG and FMOG, show overlapping REE patterns with concentrations between 3 and 67 times chondrite. The foliated leucogabbro, chilled sill and chill margin are slightly more enriched in REE than the major units, but with the same pattern. The bostonite dykes are the most enriched samples in the suite, at up to 608 times chondrite, and with negative Eu anomalies, but show the same slope of enrichment.

An exception is the olivine-rich xenolith, which shows the lowest overall REE abundances and relative depletion in the lightest REE. This rock is dominated by olivine, which largely excludes REE, hence the low concentrations, and the only other significant mineral is clinopyroxene, in which the lightest REE are incompatible (Philpotts & Ague, 2009). The pyroxene cumulate enclave shows a similar effect, although diluted, where the slight flattening at the LREE end is due to the high proportions of clinopyroxene. The gabbro pegmatite and a repeat analysis of the same sample show patterns both equivalent to the major

units and to this enriched sub-set. This reflects inhomogeneities in the proportion of minerals sampled, due to the large grain size.

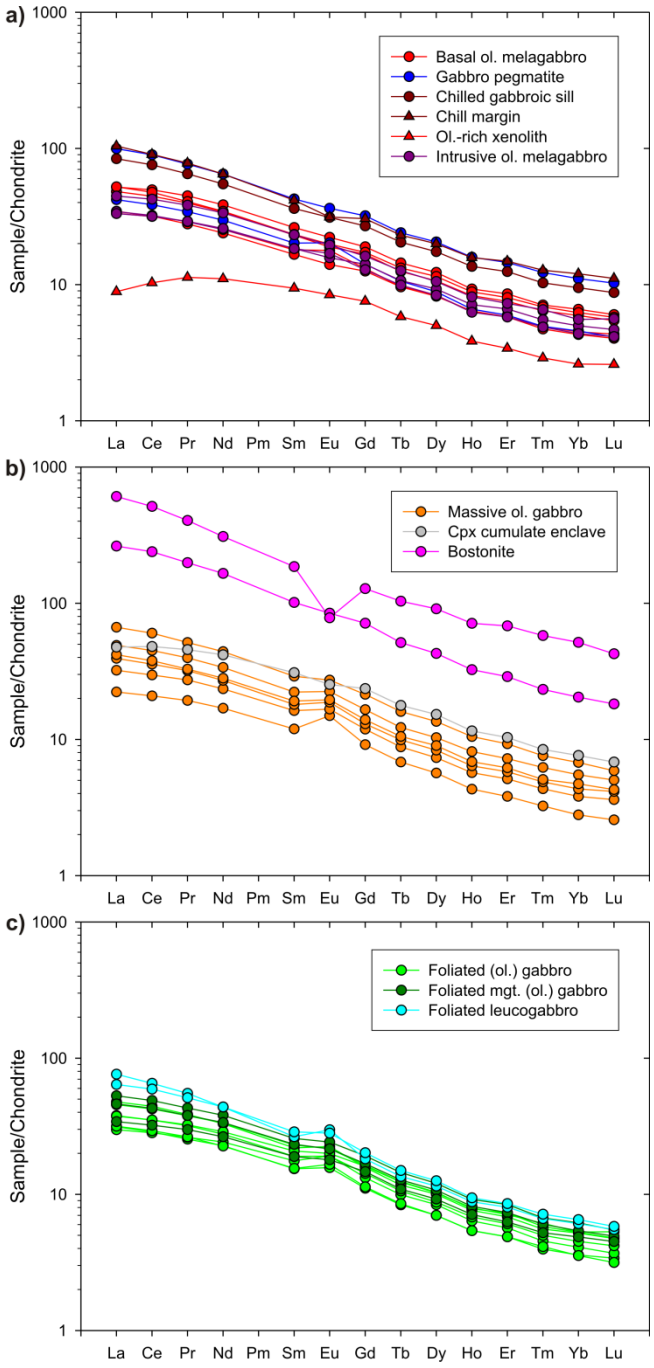


Figure 5.6: Rare earth element abundances for the Doros intrusive suite, normalised to CI chondrite of Anders & Grevesse (1989). a) Basal olivine gabbro, intrusive olivine gabbro, gabbro pegmatite, chilled gabbroic sill and chill margin samples. b) Massive olivine gabbro, bostonite and pyroxene cumulate enclave. c) Foliated gabbro and foliated olivine gabbro, foliated magnetite and foliated magnetite olivine gabbro, and foliated leucogabbro.

Eu anomalies vary from strongly negative ($\frac{Eu}{Eu*} = \frac{Eu_N}{\sqrt{Sm_N \times Gd_N}}$ = 0.51) in the bostonite (TOD84) to moderately positive (Eu/Eu* = 1.43) in massive olivine gabbro xenolith TOD37. The magnitude of the europium anomaly corresponds well with plagioclase abundances in the rocks - specifically anorthitic plagioclase (Fig. 5.7). In general, the basal and intrusive olivine melagabbros show no Eu anomalies, while the massive olivine gabbros and foliated gabbro series show slight positive anomalies. This is in line with the significant cumulus plagioclase documented in the latter group. Basal olivine melagabbro TOD39 is an exception, with a minor positive anomaly, which is due to the small feldspathic enclaves in this sample. The gabbro pegmatite lies off the trend, as it contains significant plagioclase, yet shows no Eu anomaly. However, the repeat analysis of this sample shows a positive anomaly and corresponds well with the rest of the suite. There is a small negative anomaly in the chill margin. One of the two bostonite samples has no anomaly and lies on the trend, but the other displays a strong negative Eu anomaly (not shown in Fig. 5.7).

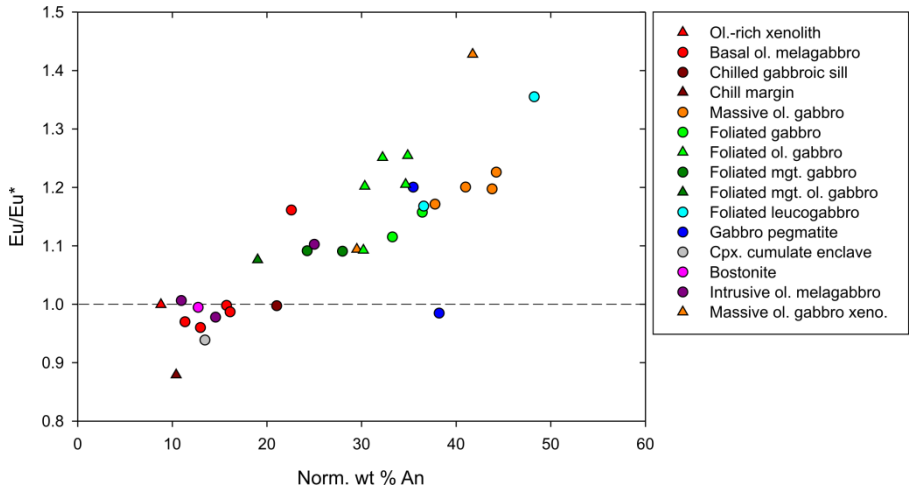


Figure 5.7: Normative anorthite abundances against the magnitude of the europium anomaly. Samples below the dashed line have negative Eu anomalies. Bostonite TOD84 is omitted from this plot, but would lie at 0% An; 0.51 Eu/Eu*.

5.4 Multiple trace element variations

All the major units (BOM, IOM, MOG, FOG, FG, FMG, FMOG) in the intrusion have similar patterns of trace element abundances, defining a tight array between 1 and 49 times primordial mantle (Fig. 5.8). The foliated leucogabbro, gabbro pegmatite, chill margin and sill are relatively more enriched than this main suite, although, apart from the chill margin, they have a similar pattern of abundances. As in the REE, the olivine-rich xenolith shows low levels of enrichment relative to primordial mantle. The bostonite dykes show high trace element concentrations (up to 222 times primordial mantle), in contrast with the rest of the suite.

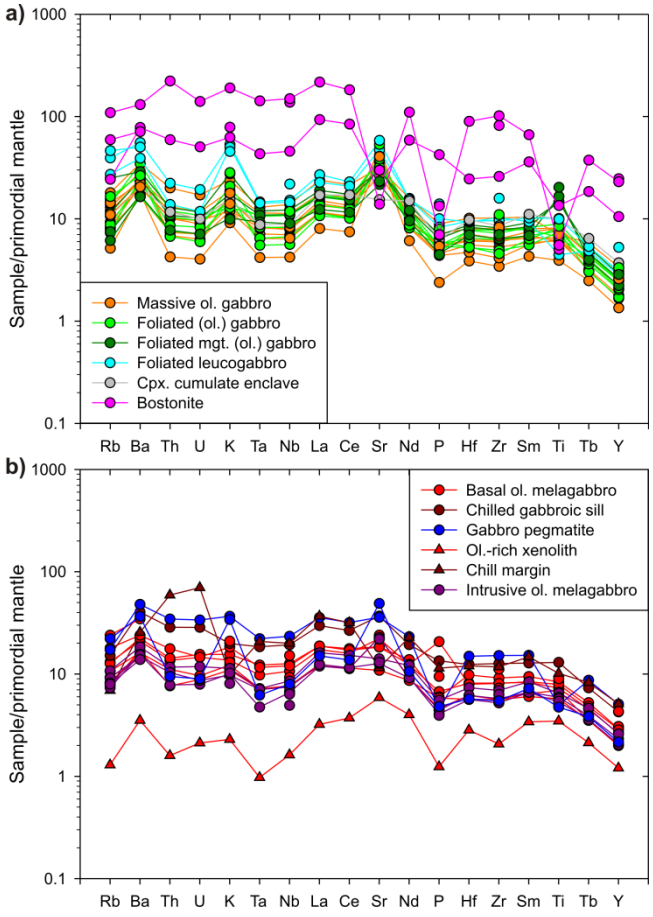


Figure 5.8: Primordial mantle-normalised multi-element diagram for a) the Upper Foliated Series, massive olivine gabbro, pyroxene cumulate enclave and bostonite dykes, and b) the Lower Zone units, chill margin and sill, gabbro pegmatite and olivine-rich xenoliths of the Doros suite. Unjoined data points are from the limited trace element analyses of Marsh & Duncan (2008). Normalising values are from McDonough & Sun (1995).

Prominent positive Sr spikes in the massive olivine gabbro, foliated gabbro series and pegmatite reflect relatively high plagioclase contents in these samples. Sr concentrations correlate well with the magnitudes of Eu anomalies across the suite. Overall, there is an increase in Sr contents upward through the intrusion (Fig. 5.9a) that mimics increasing plagioclase abundances. Relatively low Sr in the bostonite dykes and chill margin reflect the dominance of sodic, rather than calcic, feldspar in these rocks.

There is a strong correlation in Ni and other olivine-compatible trace element contents (Co, Mn) with MgO in the BOM and IOM units (Fig. 5.9b). Since the Ni content of olivines in these units is very uniform (Chapter 4), this trend roughly correlates with the changing proportions of olivine in these units.

The foliated magnetite gabbro samples display strong relative enrichment in Ti and, in most cases, V, reflecting their high proportions of titanomagnetite (Figs. 5.8a, 5.9d). With respect to V, sample KDO19 from Marsh & Duncan (2008) is anomalous, but as this is the only geochemical deviation from its counterparts and significantly so, this is suggested to be analytical error due to overlap with Ti spectral

peaks. Trends in Cr abundances track changes in titanomagnetite proportions in the basal units (Fig. 5.9c), where the oxide phase is noted to be relatively Cr-rich (Chapter 4).

The two samples of gabbro pegmatite either show a trace element pattern resembling the main suite, but with prominent spikes in Sr and K, similar to the leucogabbros, or relatively more enriched, similar to the chilled gabbroic sill, but with lower P and Ti concentrations (Fig. 5.8b). Again, this is a result of inhomogeneities in the sample material.

High Sc concentrations in the clinopyroxene cumulate enclave (Table C.1) are in line with the high proportions of clinopyroxene in this sample.

The chill margin is similar in most respects to the chilled gabbroic sill, but shows a strong relative enrichment in U, Th and Pb and comparatively less of the mobile elements Sr, K, Rb and Ba (Fig. 5.8b). This is despite high proportions of plagioclase (50 - 60%). The effects of potential alteration will be discussed in Section 5.5. The similarities in trace element compositions of the chilled sill with the pegmatite and chill margin are contrary to what is observed in the major elements.

The bostonite shows overall enrichment to a similar high degree in all incompatible trace elements, apart from Sr, P and Ti (Fig. 5.8a).

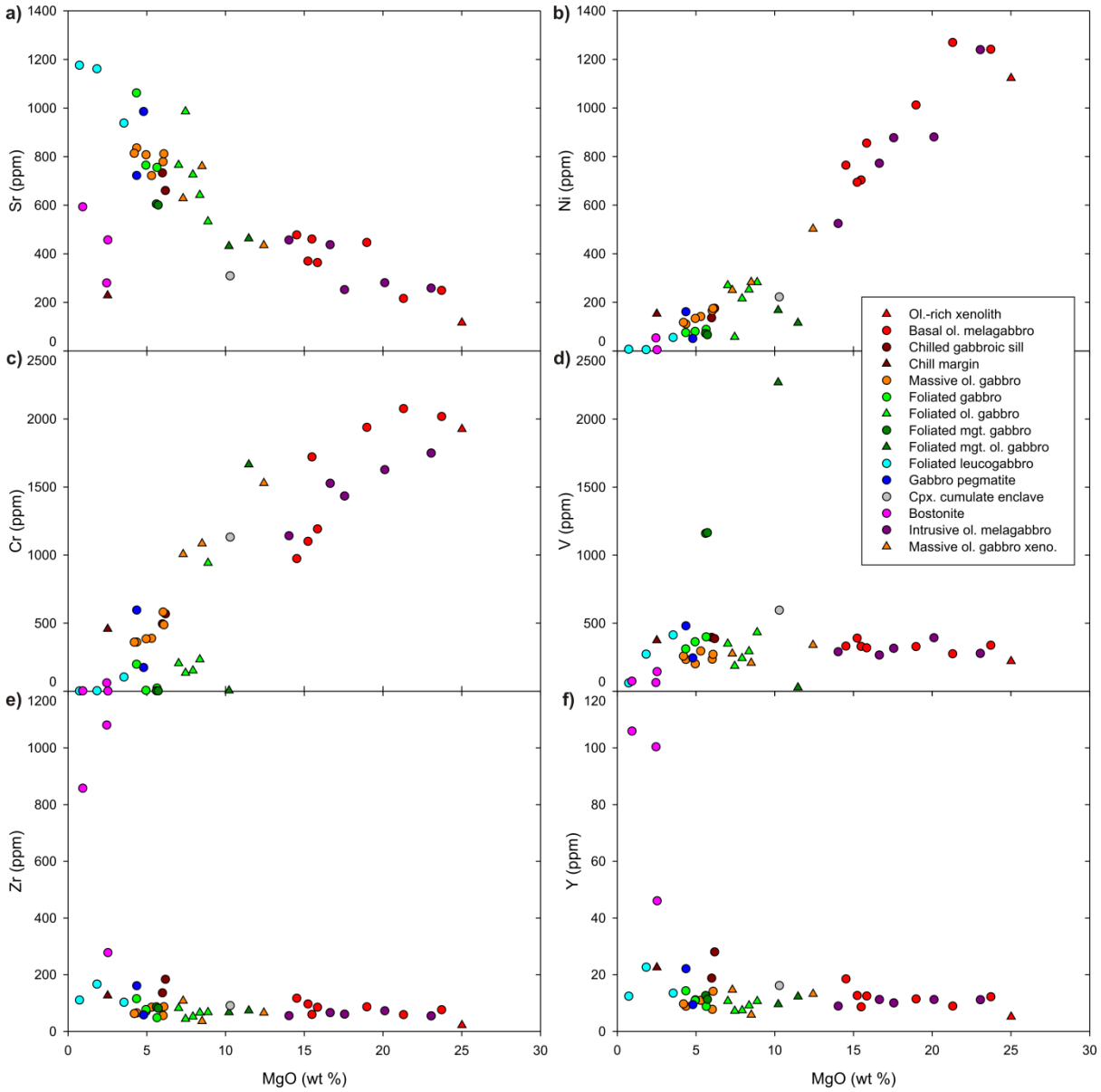


Figure 5.9: Whole-rock trace element compositions for the complete Doros suite (this study; Marsh & Duncan, 2008) plotted against MgO content. a) Sr, b) Ni, c) Cr, d) V, e) Zr, and f) Y.

In the main body of the intrusion, there is no overall trend in incompatible trace element concentrations (e.g. Y, Zr) with height (Fig. 5.10).

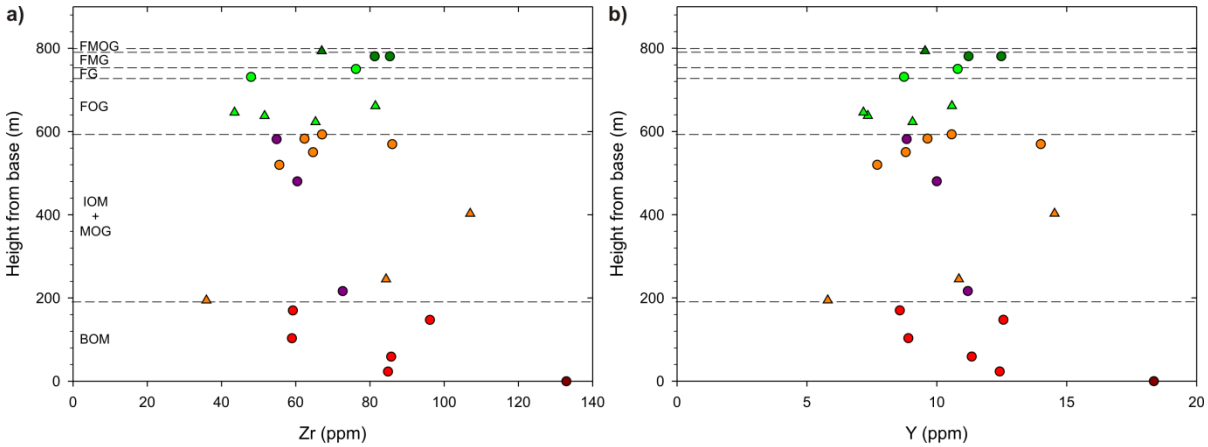


Figure 5.10: Reconstructed stratigraphic profiles through the main body of the Doros intrusion showing changes in selected incompatible trace element concentrations. Dashed lines indicate approximate layer boundaries. Symbols are as in Fig. 5.8.

5.5 Hydrothermal alteration

The presence and implications of particular alteration minerals and mineral compositions in the Doros rocks were discussed in detail in Chapter 4. While great care was taken to sample the least altered rocks for geochemical analysis, this was not always possible. Thus there are also geochemical indications of alteration in some of the Doros samples. These are important to consider during interpretation.

The chill margin shows geochemical evidence of intense hydrothermal alteration. Depletions in whole-rock Ba, K, Rb and Sr (Fig. 5.8b) suggest selective removal of these mobile elements by fluids. The sodic composition of the plagioclase in the chill margin (Chapter 4), coupled with relatively low whole-rock CaO (Fig. 5.4b), indicates intense spilitisation – Ca was removed from plagioclase by fluids and replaced by Na. The Ca then combined with CO_2 to precipitate the abundant calcite observed in vesicles and fractures. A similar, although considerably milder, effect may also be argued for the chilled sill.

Li concentrations in the Doros gabbros are generally very low (< 10 ppm). However, one analysis of gabbro pegmatite, the gabbroic sill and Foliated magnetite gabbro sample TOD13B are distinct outliers, at 17.8 - 21.3 ppm Li (Fig. 5.11b). Li concentrations may be affected by olivine abundances (Ryan & Langmuir, 1987), but this is clearly not the case here – neither the pegmatite nor magnetite gabbro contains any olivine. Li is soluble in hydrothermal fluids and enrichment commonly takes place during alteration, where it resides in clay minerals (Horstman, 1957; Ryan & Langmuir, 1987). The petrography confirms that these samples show minor clay mineral alteration.

Evidence of Cu-bearing minerals in the Doros intrusion, associated with hydrothermal alteration, was documented in Chapter 4. While Reuning & Martin (1957) recorded 1800 ppm Cu in one sample, the analyses from this study do not show similar levels of Cu enrichment, likely because of preferential sampling for fresh material. Most of the Doros rocks show less than 200 ppm Cu (Fig. 5.11a), apart from

massive olivine gabbro xenolith sample TOD68 (254 ppm) and bostonite sample TOD66 (557 ppm Cu). Both these samples show petrographic evidence of alteration.

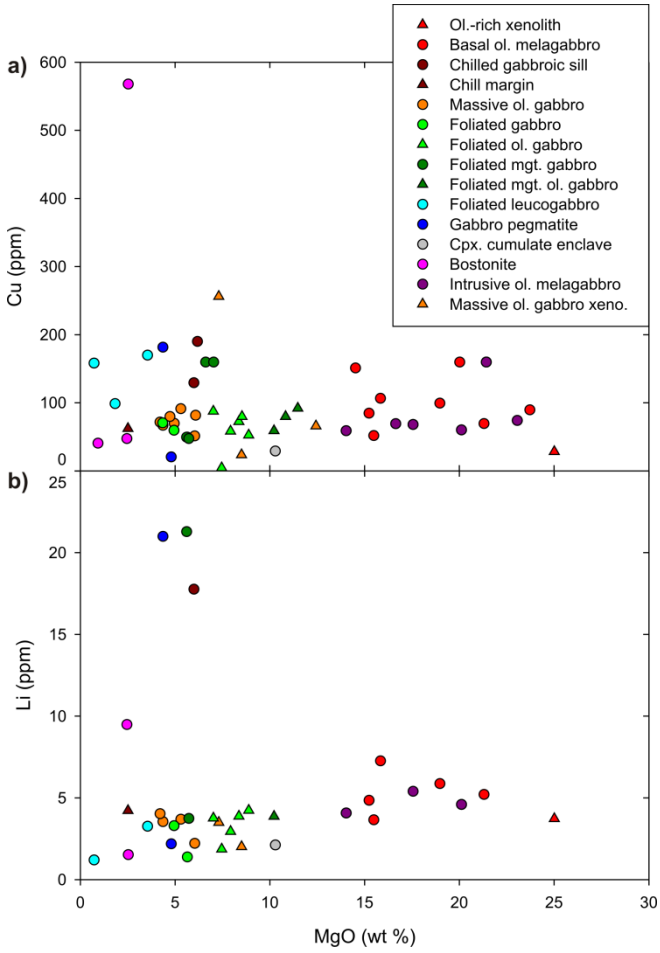


Figure 5.11: a) Cu and b) Li concentrations for the Doros suite, shown against MgO (this study; Marsh & Duncan, 2008).

The degree of alteration may be assessed to some extent by the proportion of volatiles in the rock, since there are no significant hydrous minerals in the Doros assemblage. An additional accepted method of evaluating alteration is the Chemical Index of Alteration of Nesbitt & Young (1982), where CIA = $100xAl_2O_3/(Al_2O_3 + CaO^* + Na_2O_3 + K_2O)$ in molecular proportions and CaO* is for the silicate proportion of the rock only (Fedo *et al*., 1995). This documents the progressive loss of Na^+, K^+ and Ca^{2+} from feldspars during alteration, while the immobile Al^{3+} stays constant. Plotting these factors against each other (Fig. 5.12), it is clear that the bostonite, foliated leucogabbro, chill margin and chilled sill are the most altered rock types in the Doros suite. This is supported by the secondary minerals recorded in these rocks.

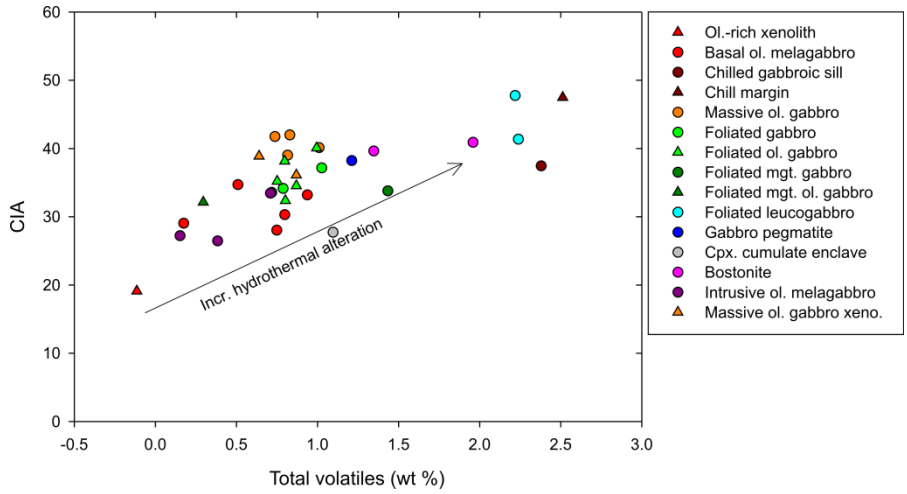


Figure 5.12: Total volatile content (LOI + SO_3 + H_2O) plotted against the Chemical Index of Alteration (CAI; Nesbitt & Young, 1982) for the Doros suite. The arrow indicates the suggested trend of progressive alteration.

5.6 Fractional crystallisation and evolution of the Doros magma(s)

A key aspect in describing the evolution of the intrusion is deciphering its crystallisation history. However, it is clear from the petrography described in Chapter 4 that these are cumulate rocks, and their compositions thus reflect a complex record of both fractionation and accumulation.

As will be discussed in more detail in Chapter 10, Doros is a shallow-level intrusion, likely emplaced within a few kilometres of the surface. Experimental phase relations for such low pressures are difficult to determine, due to the problem of maintaining long runs, but Morse *et al*. (2004) demonstrated that pressure has very little effect on cotectic positions below 15 kbar. Their experimentally-determined 5 kbar cotectic was deemed appropriate for the Kiglapait intrusion (emplaced at ~2.5 kbar), and should therefore be suitable here. However, both Figure 5.2 and Figure 5.13 below show that very few of the Doros rock samples lie on the cotectic trace, i.e. they do not represent plausible liquid compositions. Thus almost all these rocks show some degree of accumulation. The BOM, IOM and FMOG lie in the forsterite stability field (Fig. 5.13) and therefore show olivine accumulation. The MOG, FG, FL and pegmatite are dominated by plagioclase accumulation. The FOG and FMG are intermediate between these two groups. The composition of the pyroxene cumulate enclave, in the diopside stability field, indicates significant clinopyroxene accumulation.

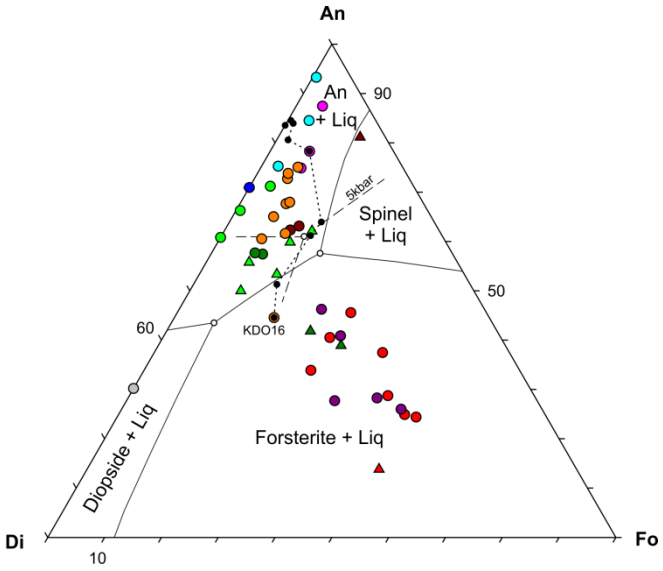


Figure 5.13: Modified version of the Fo-Di-An ternary system using oxygen norms (calculated from the method of Morse *et al*., 2004). The solid lines represent the 1 atm cotectic trace determined by Osborn & Tait (1952). The spinel field is shown here for completeness, but note that this is projected and not ternary. The dashed lines indicate the experimentally-determined 5 kbar olivine-clinopyroxene-plagioclase cotectic trace of Morse *et al*. (2004). The dotted line is the path of a fractionating hypothetical liquid equivalent to sample KDO16 of Marsh & Duncan (2008), modelled with MELTS (see text for details).

The effect of fractionating and accumulating mineral phases is also seen in the trends of major and trace element compositions across the suite. The divergent trend in the FMG and FMOG, particularly in terms of FeO and V contents (Figs. 5.3b, 5.9d), is indicative of accumulation of magnetite in these units. Positive Eu anomalies in the FL, FG, FOG, MOG and pegmatite (Fig. 5.7) show plagioclase accumulation, while negative Eu anomalies in the chill margin and bostonite point to plagioclase removal. Relative depletions in P and Ti in the bostonite (Fig. 5.8a) suggest prior crystallisation of the minerals apatite and titanomagnetite.

It must be noted that the so-called "orthocumulate" versus "adcumulate/mesocumulate" trends identified by Marsh *et al*. (2001) and Marsh & Duncan (2008; see Section 1.2.3) are not evident at all in this larger dataset (Fig. 5.14). Not only is there no grouping of Doros samples following the "orthocumulate" trend, but the Tafelkop Group basalt samples do not appear to follow this trend either (Fig. 5.4). Furthermore, contrary to the interpretation of Marsh & Duncan (2008), none of the "orthocumulate" basal and foliated gabbros shows cotectic mineral proportions (Fig. 4.15c) and so these cannot reflect equivalent liquid compositions.

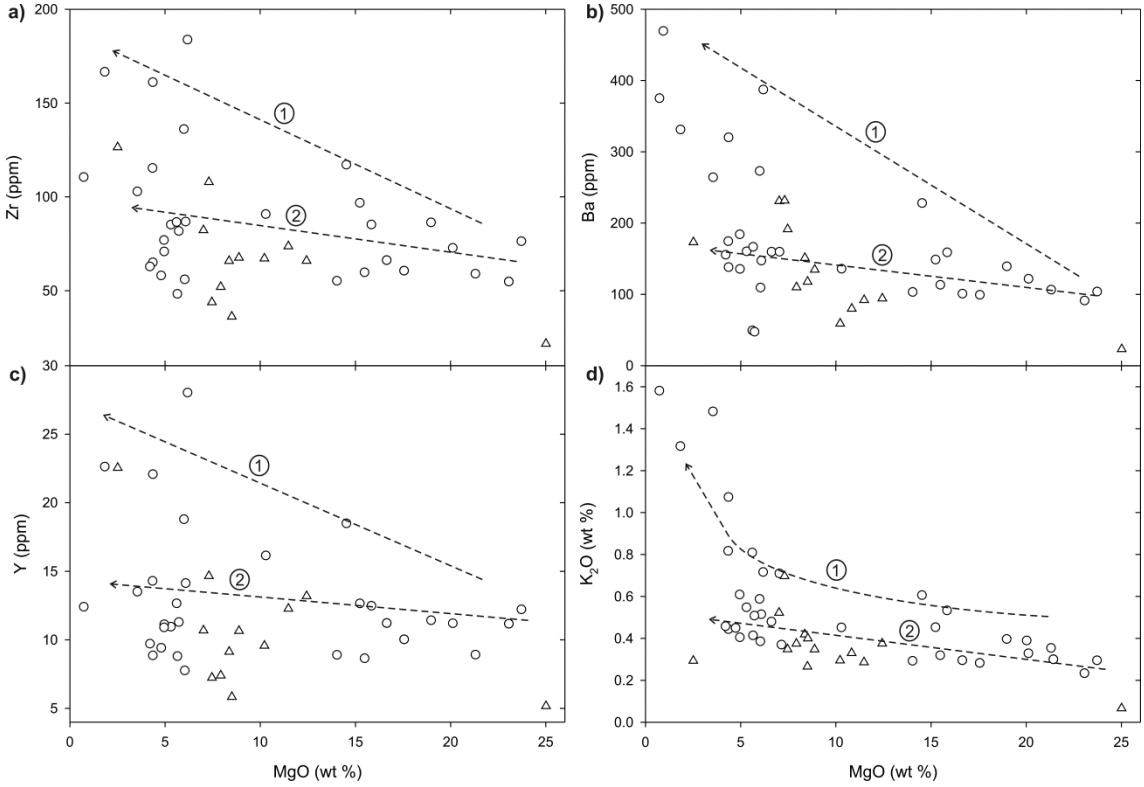


Figure 5.14: Selected major and trace elements against MgO showing the Doros samples (as in Figs 5.4 and 5.9 above) alongside the trends identified by Marsh *et al*. (2001) and Marsh & Duncan (2008; numbered arrows). According to these authors, Trend 1 delineates the orthocumulate group, while Trend 2 rocks are meso- and adcumulates. However, these trends are not easily distinguished in this larger dataset.

In such circumstances, the evolution of the Doros liquid is difficult to infer. To perform any form of quantitative modelling, the composition of the parental magma is required. This is notoriously challenging to obtain – the nature of the parental magma(s) to the Bushveld Complex, for example, has been hotly debated for decades without complete consensus (Wilson, 2012).

One method is to obtain this starting composition from appropriate fine-grained rocks associated with the intrusion (chilled margins or feeder dykes or sills). However, there is no fine-grained material in the Doros suite that may be considered equivalent to a parental liquid. As is evident from its evolved and intensely altered chemistry, the chill margin is clearly not a suitable candidate, contrary to the interpretation of Hodgson & Botha (1974). The chilled gabbroic sill is marginally less altered and has approximately cotectic normative mineral proportions, but also shows compositions too evolved to represent parental material. In any case, there is no assurance that a dyke or chilled phase is representative of the parental magma for an intrusion as a whole (Godel *et al*., 2011; Wilson, 2012). While the Tafelkop lavas of the Etendeka could potentially represent derivative liquids from the Doros intrusion (see discussion in Chapter 11), these are almost all sparsely to highly porphyritic (olivine, plagioclase, clinopyroxene, Ti-magnetite; Miller, 2008c) and thus also do not have cotectic mineral proportions (Fig. 5.2).

An estimate of the parental liquid composition may also be obtained by back-calculating cumulate rock compositions based on the premise of an equilibrium state between the melt and crystals (Godel *et al*., 2011). This is a process fraught with assumptions and several different approaches have been proposed to deal with this, depending on the data available (see for example Godel *et al*., 2011). The major element composition of the starting magma can only be feasibly derived from a suite of volcanic rocks, i.e. where the subsequent liquid path is reasonably well-constrained. In lieu of this, trace elements offer a more robust tool, since partition coefficients depend less on temperature, magma composition, and element interactions and more on the properties of host minerals (Albarède, 1996).

In this regard, I have chosen to use the REE (and Y) as a basis for calculation of liquid compositions, given their relative immobility. I have back-calculated the concentrations of these elements in the original liquids of each of the major units in the Doros intrusion (Fig. 5.15, Table E.2), following the procedure outlined by Godel *et al*. (2011; Method 2). This uses whole-rock and cumulus mineral compositions to reconstitute the liquid, assuming that intercumulus phases represent the interstitial melt and no melt migration has taken place. This has been shown to be a valid means of parental magma estimation for the Bushveld Complex (Godel *et al*., 2011). Partition coefficients for clinopyroxene in basaltic liquid for this calculation are taken from McKenzie & O'Nions (1991) and Irving & Frey (1984), for magnetite from the compilation of Bédard (2006b), for plagioclase determined using the method of Bédard (2006a), based on An content (Table E.3), and for olivine determined using the method of Bédard (2005), based on melt MgO content (Table E.4). While there are several assumptions made here, specifically regarding the equilibrium state of the system and the proportion of interstitial liquid, and there may be sources of error, for example in the estimation of mineral proportions (from the CIPW norm) and the choice or calculation of partition coefficients, this estimation is considered sufficient as a means of comparison.

The resulting calculated liquids (Fig. 5.15) are surprisingly evolved, equivalent to the upper range of the main Doros suite. In fact, in terms of REE, they are very similar to the chilled gabbroic sill (also shown in Fig. 5.15). This suggests that the magma(s) emplaced into the Doros complex was already a derivative of a more primitive precursor. Although the major element composition of the sill has clearly been disturbed by alteration, modelling with the MELTS algorithm (Ghiorso & Sack, 1995; Asimow & Ghiorso, 1998) indicates that a liquid of this composition would crystallise in the spinel field and the olivine, clinopyroxene and plagioclase produced subsequently would have more evolved compositions than are observed in the Doros cumulate rocks.

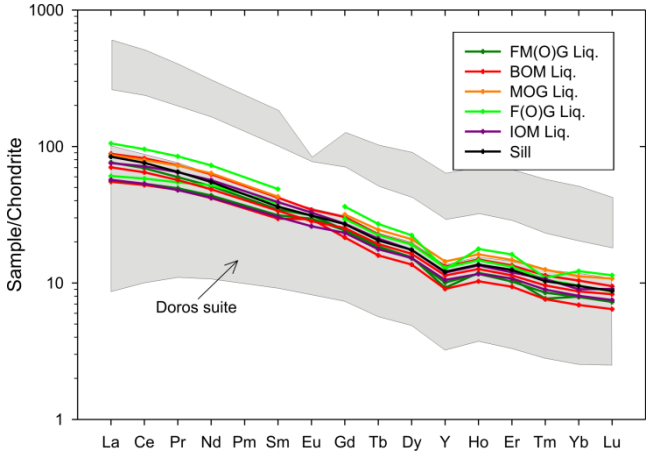


Figure 5.15: Calculated trace element compositions (after Godel *et al*., 2011) of the original liquids of each of the major units in the Doros intrusion, in comparison to the complete Doros cumulate suite and bostonites (grey fields). Also indicated is the chilled gabbroic sill (black).

In the absence of a suitable fine-grained or calculated candidate for the parental magma, an alternative is to consider the most primitive rock in the suite that has a cotectic composition. Thus I select massive olivine gabbro sample KDO16 (of Marsh & Duncan, 2008) from the base of the MOG unit as a proxy for the liquid at some early stage in its evolution. This material is a borderline olivine tholeiite and mildly alkaline basalt, like the Doros suite as a whole, and has roughly cotectic mineral proportions (Figs. 5.2, 5.13).

Since the proportions of liquids and accumulated minerals cannot confidently be assessed, a quantitative model is difficult to constrain. Nevertheless, a semi-quantitative model can to some extent account for the compositional diversity and major element trends observed. To separate the effects of fractionation from accumulation, and thus describe the differentiation history of the system, at least semi-quantitatively, major element modelling has been performed using the MELTS algorithm (Ghiorso & Sack, 1995; Asimow & Ghiorso, 1998). Although this is a shallow level intrusion (see discussion in Chapter 10), crystallisation may have occurred at a range of crustal levels, so the pressure is difficult to infer. For these purposes, a constant pressure of 1 kbar is used, but it is noted that a difference of 1 kbar either way makes little difference to the model. The oxygen fugacity is fixed at QFM, as this is what is suggested by oxide geothermometry to be the approximate fugacity for crystallisation (see Chapter 4).

The liquidus temperature of the initial magma is estimated to be 1272 °C. The modelled liquid line of descent is produced by the crystallisation of, initially, olivine and clinopyroxene, joined by plagioclase, then by magnetite and apatite, and finally by K-feldspar (Table E.1; Figure 5.16). The total proportions of each are 11% olivine, 49% clinopyroxene, 29% plagioclase, 5% magnetite, 1.5% K-feldspar and 0.2% apatite. The modelled liquid roughly follows the predicted path in Figure 5.13, but departs the cotectic after the onset of crystallisation of magnetite, followed by apatite. This modelling has several important implications. Firstly, it is evident that magmas of bostonitic composition may plausibly be produced by fractionation of a basaltic liquid. This is not sensitive to the chosen starting composition. This supports an

origin for this rock type as a late-stage, evolved liquid in the Doros intrusion, as posited by Hodgson & Botha (1974). The chilled gabbroic sill samples also lie on the modelled liquid evolution path (e.g. Fig. 5.16a), suggesting an origin as a relatively more evolved liquid that was quenched on emplacement. The remainder of the suite may be adequately explained by an evolving basaltic liquid with accumulation of various combinations of three basic minerals: olivine, plagioclase and magnetite. The specific compositions of the responsible cumulus minerals are approximated by the most primitive measured compositions in the rock types concerned (shown in large symbols in the figure). In this regard, four major groups of rock types may be identified in the intrusion, as follows:

1) The basal and intermediate olivine gabbros represent olivine cumulates (approximately Fo_{75}) from an early stage liquid.
2) The massive olivine gabbro unit and foliated olivine gabbro to foliated gabbro sequence represent cumulates of early plagioclase (~An_{74}) and minor olivine (~Fo_{62}; predominantly in the lower reaches of each of these units), from a relatively more evolved liquid.
3) The foliated leucogabbro is a plagioclase cumulate (~An_{51}) from an intermediate liquid.
4) The foliated magnetite gabbro to foliated magnetite olivine gabbro is a sequence of cumulates of early magnetite (~Ulv_{30}), followed by intermediate olivine (~Fo_{62}) in the upper reaches, from an intermediate liquid.

These interpretations are in line with the petrographic evidence of accumulation and the major and trace element characteristics discussed above.

While the major element modelling shows that overall the Doros suite is consistent with the fractionation of a basaltic system, in detail this history is more complex. When placed in a stratigraphic context, it is clear that there is not a simple progressive differentiation trend from the base to the top of the intrusion. There are several disruptions to the trend, marked by abrupt changes in mineralogy and mineral composition (discussed in Chapter 4), as well as whole-rock major and trace element concentrations (Figs. 5.5, 5.10).

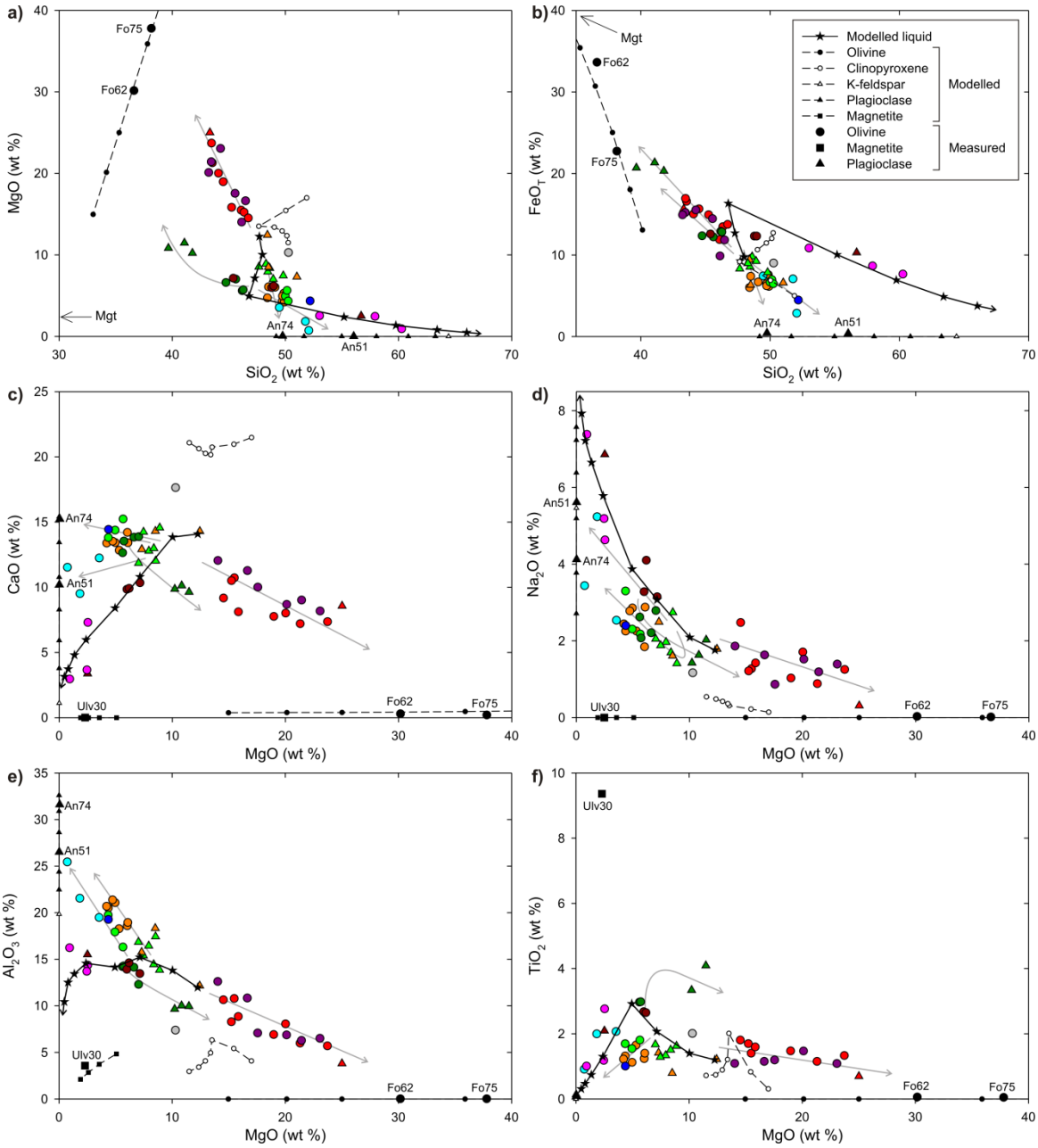


Figure 5.16: Results of MELTS major element modelling shown with the complete Doros suite (this work; Hodgson & Botha, 1974; Marsh & Duncan, 2008). Symbols are as in Figure 5.12. The solid black line represents the path of the fractionating liquid from a hypothetical starting composition equivalent to massive olivine gabbro KDO16 (Marsh & Duncan, 2008). The calculated compositions of minerals crystallising to produce this trend are also shown (small symbols). The grey arrows indicate the four major trends of accumulation evident in the suite (see text for explanation). Actual measured compositions of the cumulus minerals in each group are indicated as larger symbols with composition specified.

The chilled gabbroic sill has been shown to represent a relatively evolved liquid, yet is emplaced below the basal olivine melagabbro, the most primitive unit in the intrusion. This transition, therefore, represents a significant reversal in compositions (Fig. 5.5). As described above, the BOM reflects a primitive magma, with significant olivine accumulation. This is followed by the massive olivine gabbro, which shows a shift to the accumulation of plagioclase. This is consistent with the modelled liquid line of

descent. However, the intrusive olivine melagabbro, which from cross-cutting relations clearly post-dates the MOG, shows a return to olivine accumulation, with almost identical whole-rock compositions and mineral chemical characteristics to the BOM. This is clearly evident in the trends of all major elements (see for example Fig. 5.5, 5.16). Above the plagioclase-rich MOG, the FOG-FG sequence shows renewed accumulation of olivine and plagioclase, marked at the contact by an abrupt increase in MgO and FeO and decrease in Na_2O (Fig. 5.5) and reversals in whole-rock Ni (Fig. 5.9b). This is essentially a repetition of the MOG trend. The changes at the FG-FMG contact are associated with the onset of magnetite crystallisation and accumulation, as predicted by the MELTS model. However, there is a further pulse of olivine accumulation, and corresponding return to more primitive compositions, at the level of the FMOG, evident in major element trends (Figs. 5.5, 5.16). The implications of these complexities to the Doros fractionation path will be discussed in Chapter 10.

5.7 Summary of findings

The chemical characteristics of the Doros suite reflect a complex history of fractionation and accumulation. Major element modelling shows that overall the spectrum of rock types in the suite may be described by the fractional crystallisation of a basaltic parental magma, specifically crystallising olivine, clinopyroxene, plagioclase, magnetite, K-feldspar and apatite, accompanied by variable accumulation, predominantly of olivine, plagioclase and magnetite. However, the stratigraphic succession does not correspond to a simple progressive differentiation trend. Instead, a series of punctuated trends of differentiation are identified, each separated by a compositional reversal or hiatus.

Chapter 6: Radiogenic Isotope Compositions

6.1 Introduction

No radiogenic isotope data have previously been published for the Doros intrusion. Sr-, Nd- and Pb-isotopic analyses for the Doros suite are presented in Table C.4, along with the relevant trace element concentrations. In addition, the sample set includes an analysis of a dolerite dyke cross-cutting the complex, undertaken as part of this study.

6.2 Sr- and Nd-isotopic compositions

Initial Sr- and Nd-isotopic compositions for each of the Doros samples, calculated at 132 Ma, are shown in Figure 6.1. The Doros samples have high ε_{Nd} values in the range of +3.67 to +6.46 and low to moderate initial Sr ratios of 0.703970 - 0.709525. There is a clustering of samples around ε_{Nd} = +5 and $(^{87}Sr/^{86}Sr)_{132}$ = 0.704 and the suite is therefore depleted in Nd relative to Bulk Silicate Earth (BSE). There are not sufficient samples per rock type to establish relative isotopic variations within each unit. However, the massive olivine gabbro samples, gabbro pegmatite, chilled gabbroic sill and bostonite have ε_{Nd} values at the lower end of the range.

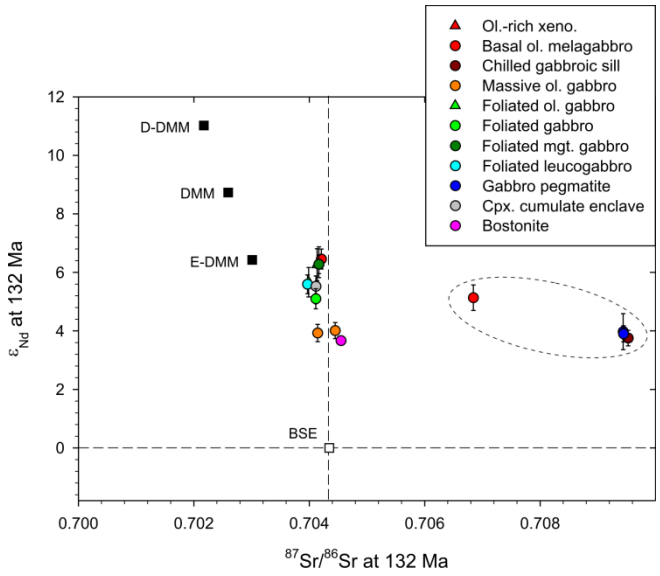


Figure 6.1: Initial Sr- and Nd-isotopic compositions for the Doros intrusive suite, relative to approximate compositions of the mantle reservoirs. D-DMM, DMM and E-DMM are depleted-, average- and enriched-depleted MORB mantle of Workman & Hart (2005); BSE is Bulk Silicate Earth (Allègre *et al*., 1988; Faure & Mensing, 2005). The outlying samples within the dashed ellipse are identified as altered material (see discussion in text). Error bars indicate 2σ error (smaller than symbol size for I_{Sr}).

Three samples – TOD40 (basal olivine melagabbro), TOD58 (chilled gabbroic sill) and TOD55 (gabbro pegmatite) – plot as clear outliers (circled in Fig. 6.1). The ε_{Nd} values of these samples are similar to the

main Doros cluster, but the initial Sr ratios are displaced to significantly higher values. These samples are not anomalous in their Pb isotopic compositions (Section 6.3 to follow) or major and trace element chemistry (Chapter 5) and comprise three different rock types, so this is a Rb- or Sr-specific effect that is not restricted to stratigraphic level or lithology. There are three possible explanations for this displacement.

It may firstly be considered that this is a result of analytical error, due to the fact that trace element concentrations and isotope ratios were measured on different aliquots of material and not by isotope dilution. However, it is clear that it is the measured Sr-isotopic ratios of these samples that are anomalous and not the Rb or Sr elemental concentrations, or as a result, the parent-daughter ratios. A repeat analysis of TOD55 produces near equivalent $^{87}Rb/^{86}Sr$. The outlying samples are not within error of the main cluster, nor are they analyses with relatively high standard deviations on the isotopic ratio measurements. Analytical error is not a factor here.

It may also be proposed that these samples have selectively assimilated small amounts of a very ^{87}Sr-enriched contaminant. A more detailed discussion of possible contamination for the Doros Complex as a whole will take place in Chapter 10; however, for the moment these samples are considered in isolation. Potential crustal contaminants are restricted to the rocks through which the Doros magma was emplaced, i.e. 1) the Karoo metasedimentary strata, 2) the Damaran metasedimentary and granitoid rocks, 3) the underlying Archaean basement, or partial melts of these. The Karoo strata here are part of the Huab Basin, with provenance to the north-west (Miller, 2008d). Therefore they were derived largely from Damaran schists and granites and can be expected to have similar isotopic signatures. The Damaran lithologies do have the high initial $^{87}Sr/^{86}Sr$ ratios at 132 Ma that would be required: 0.709913 - 0.871072 for the Damaran metasediments (McDermott & Hawkesworth, 1990; Thompson *et al.*, 2007) and 0.712729 - 0.914894 for the Damaran granites (McDermott *et al*., 1996; Jung *et al*., 1998; Thompson *et al*., 2007). However, ε_{Nd} values at 132 Ma for these sources are correspondingly low (between -4 and -24). Since Sr/Nd ratios are greater in the Doros mafic parental magma than in these potential contaminants, contamination has a greater effect on Nd than Sr, and thus this should result in significant displacement of these compositions to more enriched ε_{Nd}, which is not the case. The Archaean crust below the Damara typically has even lower ε_{Nd} values at 132 Ma (-21 to -24; Mingram *et al.*, 2000), so poses a similar problem. Pb isotopes are discussed in more detail in the following section, but it must be noted that these are very sensitive indicators of contamination and the lack of an equivalent displacement towards radiogenic Pb-isotopic compositions for these specific samples argues strongly against crustal contamination. The absence of orthopyroxene in the Doros assemblage (Chapter 4) further precludes significant contamination of any of the Doros magmas. Selective contamination of these particular outlying samples is also implausible. While the sill and basal gabbro may have entrained wall-rock material on emplacement, given their marginal positions in the intrusion and suggested petrogenesis (see Chapter 9), the pegmatite is unlikely to have done so. There are also no other geochemical differences between the supposedly-contaminated BOM TOD40 and other samples from the same unit that show 'normal' Sr-isotopic ratios.

An alternative proposition is that these samples have been affected by low temperature hydrothermal alteration. The effects of this process on certain of the Doros rock types have already been discussed in Chapters 4 and 5. Sr is a relatively mobile element and may be preferentially removed (or added) during the interaction of the rock with circulating fluids, leading to increased (or decreased) $^{87}Sr/^{86}Sr$ ratios. Alteration is difficult to quantify in such rocks, and although samples TOD58 and TOD55 are observed to contain significant sericite, clay minerals and hematite, and in the case of the pegmatite, prehnite, melagabbro sample TOD40 does not. If fluids have interacted with the rock, a similar effect may be expected for mobile U, but these samples do not show significant U loss. However, there does appear to be a correlation with Li concentrations (Fig. 6.2). As discussed previously, Li is known to reside in clay minerals and increased concentrations of this element may be an indication of low temperature weathering or late magmatic fluid alteration (Horstman, 1956; Ryan & Langmuir, 1987). Samples TOD58 and TOD55 have anomalously high Li (> 17 ppm) and although sample TOD40 is not enriched to the same extent, it nevertheless has higher Li concentrations than the main suite. This would suggest that alteration of these rocks predominantly affected feldspar, leading to its breakdown and the formation of clay minerals. During this process some Sr may have been lost, but U was negligibly affected. It is noted that foliated magnetite gabbro TOD13B also has high Li levels, yet does not show raised initial Sr values (Fig. 6.2). In this case, although the plagioclase was altered, Sr was not removed from the system.

Since these outlying samples do not reflect their original compositions, they have been omitted from subsequent discussions relating Sr-isotopic compositions to magma source.

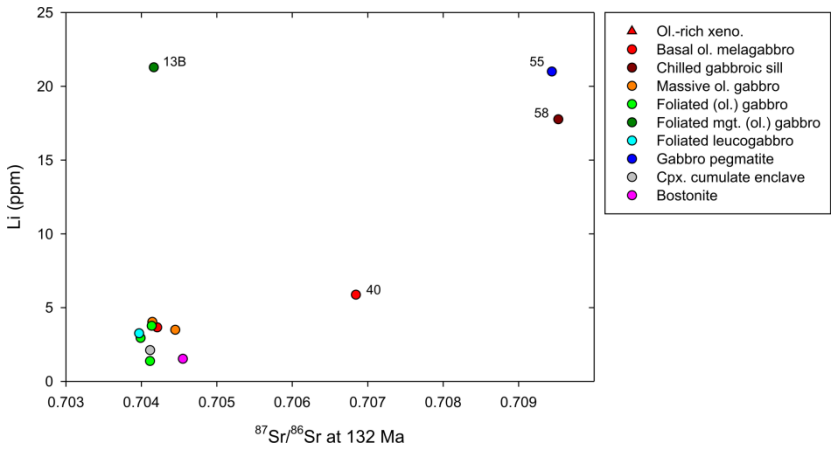


Figure 6.2: Initial Sr ratios against Li concentrations for the Doros units analysed in this study. Raised Li levels indicate clay mineral alteration, which may be responsible for the high initial Sr ratios in certain samples.

Figure 6.3 shows the Sr- and Nd- isotopic compositions of the Doros suite in relation to contemporaneous mafic magmatism in the Paraná-Etendeka Large Igneous Province (the Tafelkop, Tafelberg, Horingbaai, Esmeralda, Khumib, Kuidas and Albin groups of the Etendeka, and their Paraná equivalents), as well as the Tristan mantle plume, at 132 Ma. The isotopic composition of the material produced by the Tristan plume is inferred to have stayed relatively constant over time (Milner & Le Roex, 1996) and thus modern basalts from the islands of Tristan da Cunha, Gough and Inaccessible, the products of the present Tristan

plume tail, are considered a good proxy for the plume component in the Paraná-Etendeka magmas. Trumbull *et al.* (2003) have used these modern basalts to calculate the likely range of compositions for the plume source at 130 Ma and this is also indicated in the Fig. 6.3.

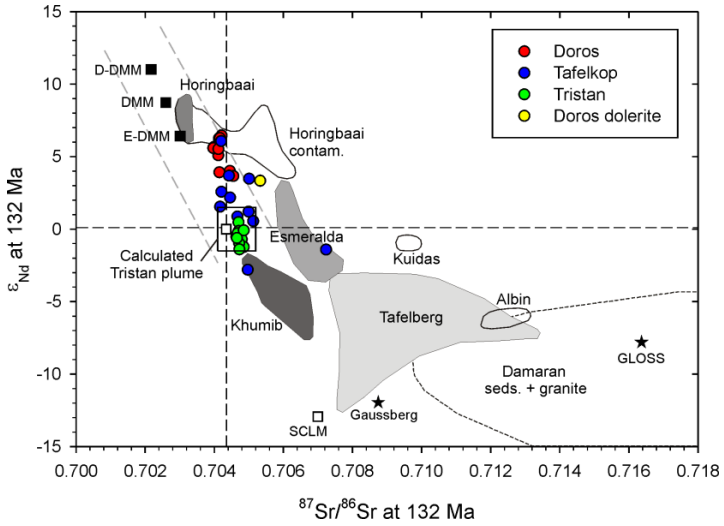


Figure 6.3: Initial Sr- and Nd-isotopic compositions of the Doros intrusive suite, compared with representative fields for the Tafelkop lavas (Ewart *et al*., 1998a; Gibson *et al*., 2000; Thompson *et al*., 2001), other Paraná-Etendeka mafic magma groups (Tafelberg, Khumib, Esmeralda, Horingbaai, Kuidas, Albin; Peate & Hawkesworth, 1996; Peate *et al*., 1999; Thompson *et al*., 2001; Ewart *et al*., 2004a) and modern-day Tristan group lavas (Tristan da Cunha and Inaccessible Islands; Cohen & O'Nions, 1982; Newsom *et al*., 1986; Le Roex *et al*., 1990; Cliff *et al*., 1991). The calculated composition of original Tristan plume material is from Trumbull *et al*. (2003). Dashed grey lines approximately indicate the mantle array. Potential contaminants are represented by global subducting sediment (GLOSS; Plank & Langmuir, 1998), Damaran metasediments and granites (McDermott & Hawkesworth, 1990); Jung *et al*., 1998), recycled subducted material (Gaussberg; Murphy *et al*., 2002) and the approximate composition of the local sub-continental lithospheric mantle (SCLM; Gibson *et al*., 1995). All initial ratios are calculated at 132 Ma. The Tafelkop basalts are emphasised because of their importance for later discussion.

The Doros suite shows isotopic compositions within the mantle array, between Tristan plume material and depleted mantle compositions. It is not as enriched as the Khumib, Esmeralda, Tafelberg, Kuidas or Albin mafic magma groups, but shows some overlap with the Tafelkop suite.

Neither Sr- nor Nd-isotopic compositions yield meaningful isochron ages for the Doros suite (MSWDs are excessive). This is not unexpected, since only whole-rock data are available, and the range of rock types, and therefore parent-daughter ratios, is small.

6.3 Pb-isotopic compositions

Measured Pb-isotopic ratios for the Doros suite are presented in Figure 6.4. These samples form a tight cluster in the range $^{206}Pb/^{204}Pb$ = 18.17 - 18.47, $^{207}Pb/^{204}Pb$ = 15.55 - 15.59 and $^{208}Pb/^{204}Pb$ = 37.93 - 38.42, sub-parallel to the Northern Hemisphere Reference Line (NHRL) of Hart (1984), above which lie the enriched, generally-Southern Hemisphere 'DUPAL' oceanic basalts. Only the olivine-rich xenolith TOD38 is a distinct outlier, with similar $^{207}Pb/^{204}Pb$ ratios, but lower $^{206}Pb/^{204}Pb$ and $^{208}Pb/^{204}Pb$. This may be attributed to the extremely low concentrations of U, Th and Pb in this sample (< 0.5 ppm; Table C.4),

causing greater sensitivity to errors in measurement, rather than a distinct magma source. Isotopic compositions of this sample must therefore be treated with caution.

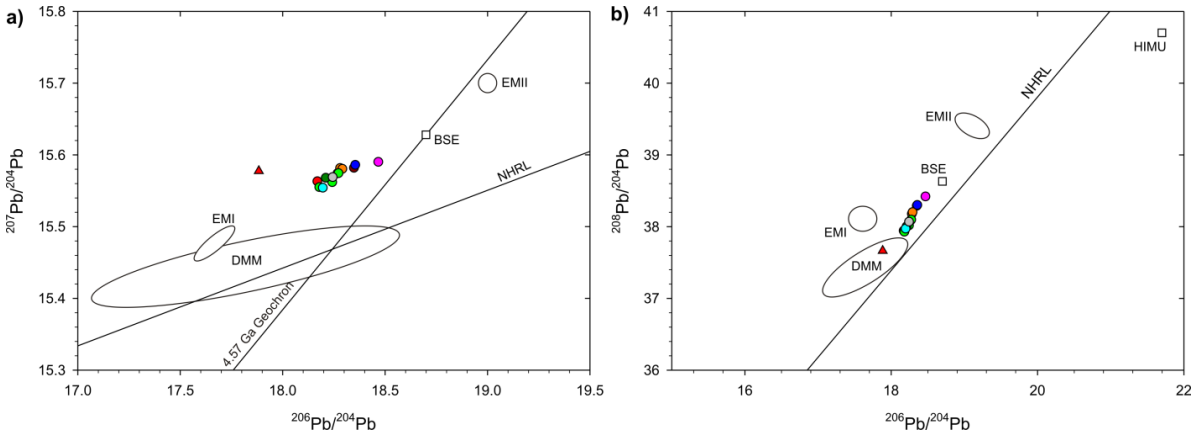


Figure 6.4: Measured Pb-isotopic compositions of the Doros gabbroic suite (symbols as in Fig. 6.1) in relation to the approximate compositions of the mantle end member components: BSE (Stacey & Kramers, 1975), DMM (Zindler & Hart, 1986; Ito *et al*., 1987; Allègre *et al*., 1988; Zartman & Haines, 1988; Kramers & Tolstikhin, 1997; Rehkämper & Hofmann, 1997; Workman & Hart, 2005), EMI (Zindler & Hart, 1986; Hart, 1988), EMII (Hart, 1988; Weaver, 1991) and HIMU (Hart, 1988; Salters & White, 1998). Northern Hemisphere Reference Line (NHRL) from Hart (1984). 2σ errors are smaller than symbol sizes.

All the Doros samples plot to the left of the geochron, indicating evolution from a depleted source (Fig. 6.5). $^{207}Pb/^{204}Pb$ and $^{206}Pb/^{204}Pb$ compositions lie between the 'Depleted Mantle' evolution curve of Kramers & Tolstikhin (1997) and the 'Lower Mantle' curve of Kamber & Collerson (1999; Fig. 6.5). $^{208}Pb/^{204}Pb$ compositions lie between the 'Lower Mantle' and 'Upper Mantle' curves of Kamber & Collerson (1999). This suggests mixing between depleted upper mantle and lower mantle components. The trend of the Doros suite (excluding the olivine-rich xenolith), gives a reservoir separation age of 2.265 Ga (Fig. 6.5).

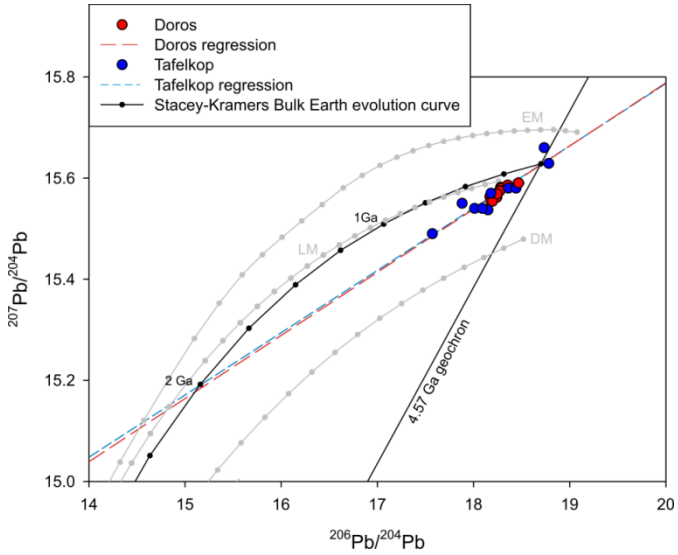


Figure 6.5: Measured Pb-isotopic compositions of the Doros and Tafelkop suites (Ewart *et al*., 1998a; Gibson, *et al*., 2000; Thompson *et al*., 2001). Grey Pb evolution curves are EM = Erosion Mix (essentially upper continental crust, considering the effects of erosion) and DM = Depleted Mantle of Kramers & Tolstikhin (1997) and LM = Lower Mantle of Kamber & Collerson (1999). 2σ errors are smaller than symbol sizes.

Figure 6.6 shows initial Pb-isotopic ratios for the Doros suite relative to the Etendeka mafic magma groups and Tristan plume material at 132 Ma. The tight clustering of initial ^{207}Pb ratios suggests a single-stage process followed by differentiation, supporting derivation from a single mantle-sourced magma. However, the trend in initial ^{208}Pb may indicate that the Pb isotopic systems are decoupled. The Doros samples show some overlap with Tristan group compositions, the Tafelkop suite and uncontaminated samples of the Horingbaai dyke suite.

Pb isotopes do not yield meaningful isochron ages for the Doros suite.

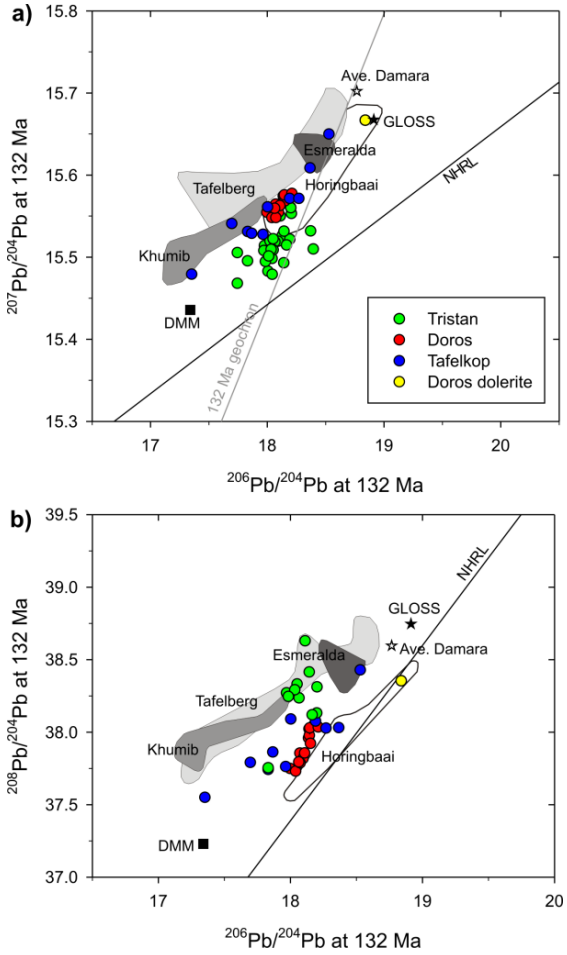


Figure 6.6: Initial (132 Ma) Pb-isotopic compositions of the Doros intrusive suite, in comparison with the main Etendeka mafic magma groups (Peate & Hawkesworth, 1996; Ewart *et al*., 1998a; Peate *et al*., 1999; Gibson *et al*., 2000; Thompson *et al*., 2001; Ewart *et al*., 2004a) and Tristan group lavas (Le Roex *et al*., 1990; Cliff *et al*., 1991; Ewart *et al*., 2004a). Average Nama and Etusis Formations (McDermott & Hawkesworth, 1990) represent a potential Damaran metasedimentary contaminant. GLOSS = global subducting sediment (Plank & Langmuir, 1998). DMM = average depleted MORB mantle of Allègre *et al*. (1988). NHRL = Northern Hemisphere Reference Line of Hart (1984).

6.4 Doros dolerite and bostonite dykes

To investigate whether the numerous dolerite dykes cross-cutting the Doros Complex are related to the same magmatic event, an isotopic analysis of one such dolerite is included in this study. This sample (TOD10) shows higher initial Sr and lower ε_{Nd} values than the main Doros suite (Fig. 6.3), and significantly more radiogenic initial $^{206}Pb/^{204}Pb$, $^{207}Pb/^{204}Pb$ and $^{208}Pb/^{204}Pb$ (Fig. 6.6). Further implications of this chemistry will be discussed in detail in Chapter 10.

6.5 Summary of findings

Samples from the main body of the Doros intrusion, as well as the bostonite dykes, form a relatively tight cluster in Sr- and Nd-, and Pb-isotopic space. Mean $I_{Sr} = 0.704182$, $\varepsilon_{Nd} = +5.12$, $^{206}Pb/^{204}Pb = 18.11$, $^{207}Pb/^{204}Pb = 15.56$ and $^{208}Pb/^{204}Pb = 37.89$ at 132 Ma. The Sr- and Nd- isotopic compositions lie within

the mantle array and the Pb-isotopic compositions fall to the left of the geochron, indicating a relatively depleted mantle source for the Doros magmas. Pb-isotopic ratios further suggest a single stage of melting and a source with both upper and lower mantle components.

Chapter 7: Melt Inclusion Mineralogy and Chemistry

7.1 Introduction

Chapter 4 alluded to the presence of melt inclusions (MIs) in the Doros rocks. Melt inclusions are small pockets of melt that become trapped inside crystals, due to some irregularity in growth conditions (Roedder, 1979; Lowenstern, 2003; Kent, 2008). In igneous rocks this usually takes the form of a silicate liquid, which can be preserved as glass, or be partially or completely crystallised. Analyses of MIs have the potential to provide valuable information on the nature and source of early magmas, as well as the processes of melt generation and evolution (Roedder, 1979; Schiano, 2003; Kent, 2008). Specifically, an investigation of these trapped melts can provide unique insight into the parental magma compositions and melt evolution of the Doros Complex, which are poorly constrained due to the cumulate origin of these rocks (see discussion in Chapter 5).

This aspect of the research was conducted in collaboration with Dr Jakob Keiding of the German Research Centre for Geosciences (GFZ), Potsdam, who also performed all analyses.

7.2 Melt inclusions

The value of melt inclusions lies in the fact that they ideally represent the actual melt present at the time of formation of the host crystals, which is trapped and preserved in isolation from the external evolving magma by a theoretically impermeable host (Sobolev, 1996; Danyushevsky *et al*., 2004; Kent, 2008). Therefore, they have the potential to retain vital information about the earliest magmas in the system, particularly features that may be destroyed or obscured by later processes of magma differentiation, contamination, devolatilisation and alteration (Kent, 2008). Several studies have shown that MIs can provide important constraints on liquid compositions in layered mafic intrusions, e.g. for the Greenhills Complex (Spandler *et al*., 2003), Bushveld Complex (Li *et al*., 2005), Sept Isles intrusion (Charlier *et al*., 2011) and the Skaergaard intrusion (Jakobsen *et al*., 2010).

Melt inclusions may be primary, i.e. they are cogenetic with the host phase, or secondary, if they are trapped after the host crystal is formed (Schiano, 2003). Primary MIs are typically larger than secondary inclusions, and isolated or randomly distributed (Roedder, 1979; Schiano, 2003).

In practice, the melt may be modified to some extent subsequent to entrapment, by crystallisation of the host mineral on the walls of the inclusion, or of daughter phases within the inclusion, or by diffusion through the host mineral (Roedder, 1979; Schiano, 2003; Danyushevsky *et al*., 2004; Kent, 2008). However, these effects can to some extent be reversed, or at least minimised. In the case of post-entrapment crystallisation, this is done by reheating the inclusions until they attain equilibrium and

correcting for any fractionation (Danyushevsky *et al*., 2004; Kent, 2008). Imperfect quenching may, however, cause some host-wall crystallisation even after homogenisation. The effects of diffusion can be quantified to some extent by an assessment of compositional profiles through the host (Danyushevsky *et al*., 2004; Kent, 2008). Elements that are compatible in the host phase are the most susceptible to equilibration with the host, and therefore their concentrations in the melt must be considered potentially less reliable (Kent, 2008). A suitable choice of host mineral is also important. For mantle-derived magmas, olivine is considered a relatively robust host mineral, since it is incompatible for most trace elements, is usually not in equilibrium with the surrounding melt and readily forms inclusions (Sobolev, 1996; Kent, 2008).

This study focuses on a set of olivine-hosted melt inclusions in the Doros rocks. All the inclusions have been homogenised by heating prior to analysis and post-entrapment crystallisation has been corrected for (see details of the procedure in Section 2.4).

7.3 Petrographic characteristics of the Doros inclusion suite

Melt inclusions are abundant within olivines of the melagabbro units (BOM and IOM) of the Doros suite, but are rare or non-existent in rocks from higher up in the stratigraphy. The MIs are generally round and between 20 and 40 μm in diameter (but can reach several 100 μm), and are commonly strongly oxidised. They appear randomly distributed through the host crystals. This, and the mineralogy, size and shape of the inclusions, suggest that they are primary MIs. Smaller, less abundant inclusions are also present in plagioclase in these rocks, but were not analysed here, since the more primitive olivine-hosted inclusion data were readily available.

All the Doros MIs contain crystalline phases. Major element analyses of unhomogenised inclusions (Table F.1) show that the daughter products include amphibole (kaersutite), clinopyroxene, orthopyroxene, titanomagnetite, ilmenite and apatite (Fig. 7.1a-f). In addition, the large size of certain of the ilmenite, titanomagnetite and clinopyroxene crystals, such as in Figure 7.1c, indicates that they were trapped as solid inclusions along with the melt, rather than crystallised as daughter phases. These crystals are always accompanied by glass of variable composition, which generally falls into two categories: relatively SiO_2- and Al_2O_3-rich, alkali-feldspar-like compositions, or SiO_2-poor, MgO- and FeO-rich, vermiculite-like compositions (Table F.1).

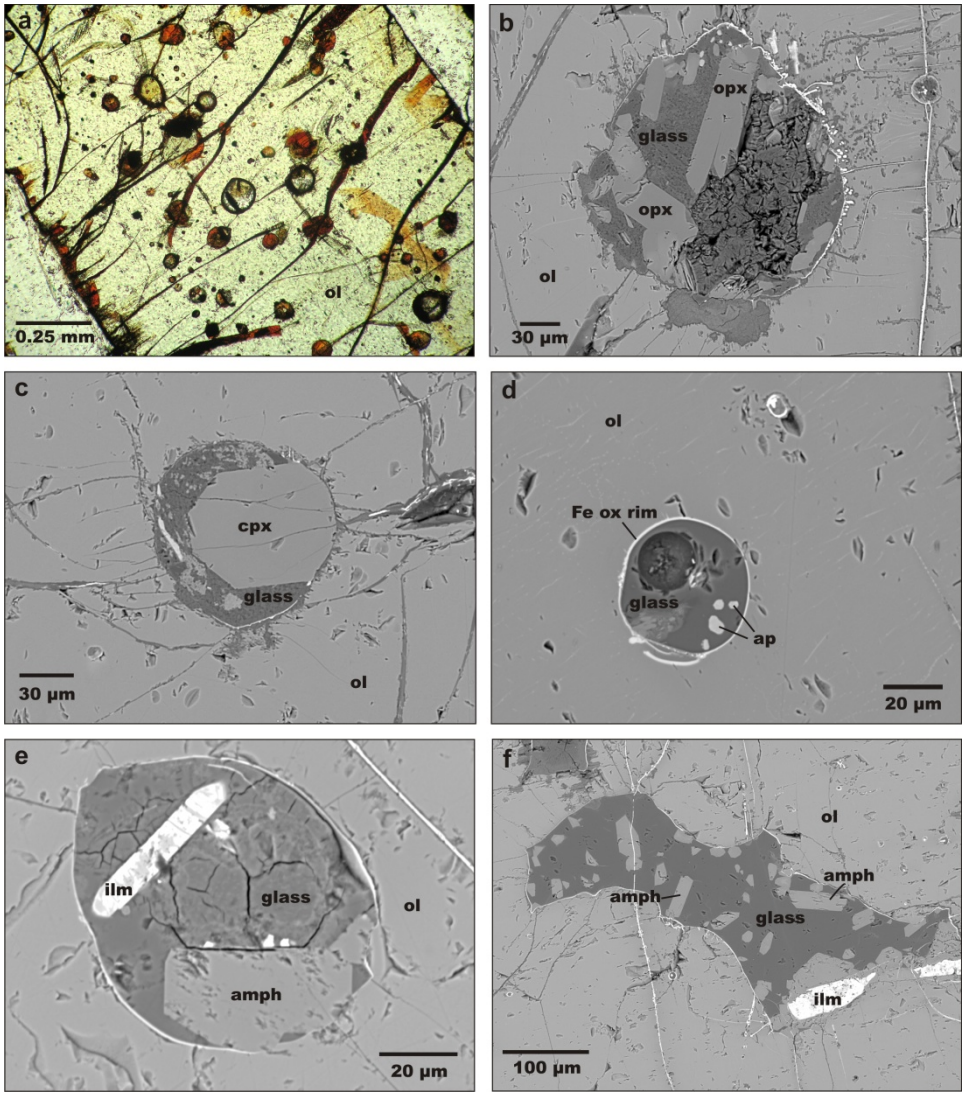


Figure 7.1: Photomicrographs (a) and backscattered electron (BSE) images (b-f) of unhomogenised olivine-hosted melt inclusions in the Doros melagabbros. a) Inclusion population in an olivine grain in intrusive olivine melagabbro TOD70 viewed in PPL. b) & c) Crystals of orthopyroxene (opx) and clinopyroxene (cpx) with glass in basal olivine melagabbro TOD63. The disproportionately large size of the cpx crystal in c suggests trapping as a solid inclusion. d) Crystals of apatite (ap) in a glassy inclusion, surrounded by a rim of iron oxide (BOM TOD39; BSE). e) & f) Crystals of ilmenite (ilm) and kaersutitic amphibole (amph) with glass in IOM TOD70 (BSE).

7.4 Melt inclusion chemistry

Olivine-corrected major and trace element data for the homogenised melt inclusions are presented in Tables G.3-4 of the Appendix. Compositions are variable, but mainly plot in the basalt to trachybasalt to basaltic trachyandesite fields of the total alkalis versus silica diagram (Fig. 7.2; Middlemost, 1994). Despite disparate host rock types and olivine Fo contents, compositions for inclusions in each of the 3 samples overlap extensively (Fig. 7.1). Hence, they are not distinguished in subsequent diagrams.

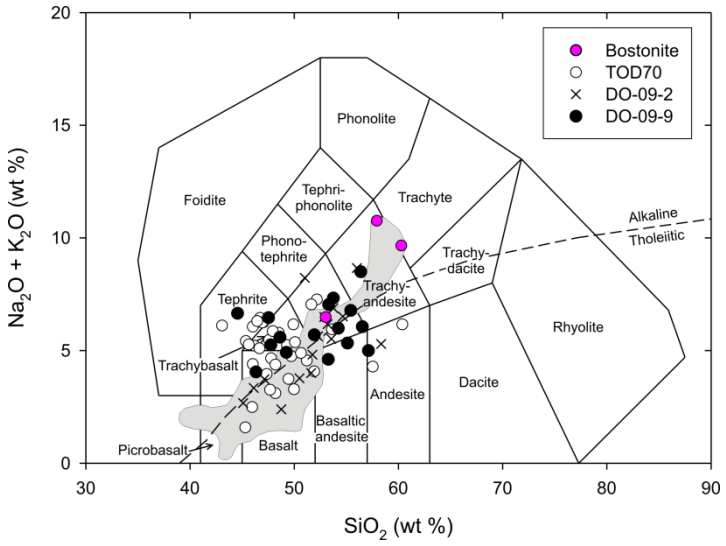


Figure 7.2: Total alkalis versus silica for olivine-hosted melt inclusions analysed in each of three samples, TOD70 (IOM), DO-09-2 (BOM) and DO-09-9 (not *in situ*, but inferred to be BOM), compared with the Doros whole-rock suite (grey field) and specifically, the bostonite dykes. The dashed line is the alkaline/sub-alkaline division of Philpotts & Ague (2009).

SiO_2 contents in the MIs range between 42% and 60% (Fig. 7.3a) – roughly equivalent to the range in the Doros whole-rock suite. MgO contents are between 3% and 11% (Mg # = 44 - 48) – more evolved than the host melagabbro cumulate rocks, but more primitive than the Doros chill margin. FeO contents are very variable (8 - 26%), and consistently higher for equivalent SiO_2 or MgO than the bulk rocks (Fig. 7.3b). Almost all inclusions show extremely low CaO contents (~3 wt. %; Fig. 7.4c). TiO_2 is highly variable, between 0.2 and 7.9 wt. % (Fig. 7.4b). The majority of inclusions are relatively enriched in alkalis and P_2O_5 (Fig. 7.4d-f). CIPW norm calculations indicate a wide range of quartz-, nepheline-, hypersthene- and olivine-normative compositions.

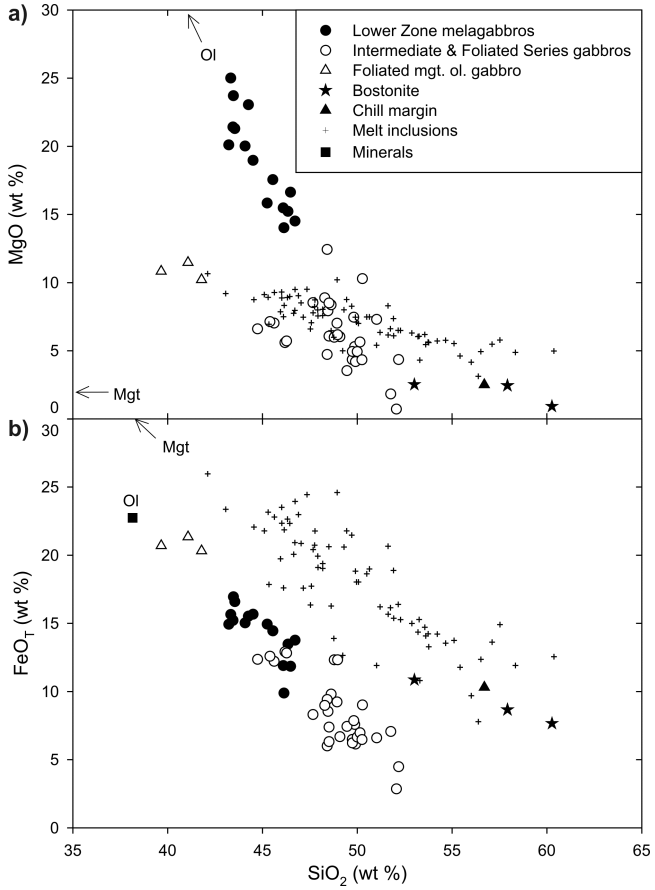


Figure 7.3: a) MgO and b) total FeO against SiO_2 for the Doros olivine-hosted melt inclusions, in relation to the whole-rock suite (this study; Hodgson & Botha, 1974; Marsh & Duncan, 2008). The most primitive measured olivine (Ol) and Fe-Ti oxide (Mgt) compositions for the BOM and IOM are also indicated.

The trace element and REE contents of the melt inclusions are distinctly enriched compared to the bulk host rock, on a par with the Doros bostonites (Fig. 7.5). This is despite the major element compositions of these inclusions covering a range of major element compositions, from relatively more primitive, to more evolved. The majority show a prominent negative Eu anomaly (Eu/Eu* = 0.19 - 0.72; Fig. 7.5a). No comparably large negative Eu anomalies are present in the Doros rocks. REE patterns are generally parallel, with moderate overall LREE enrichment similar to the whole-rock suite, but marginally steeper patterns in the HREE.

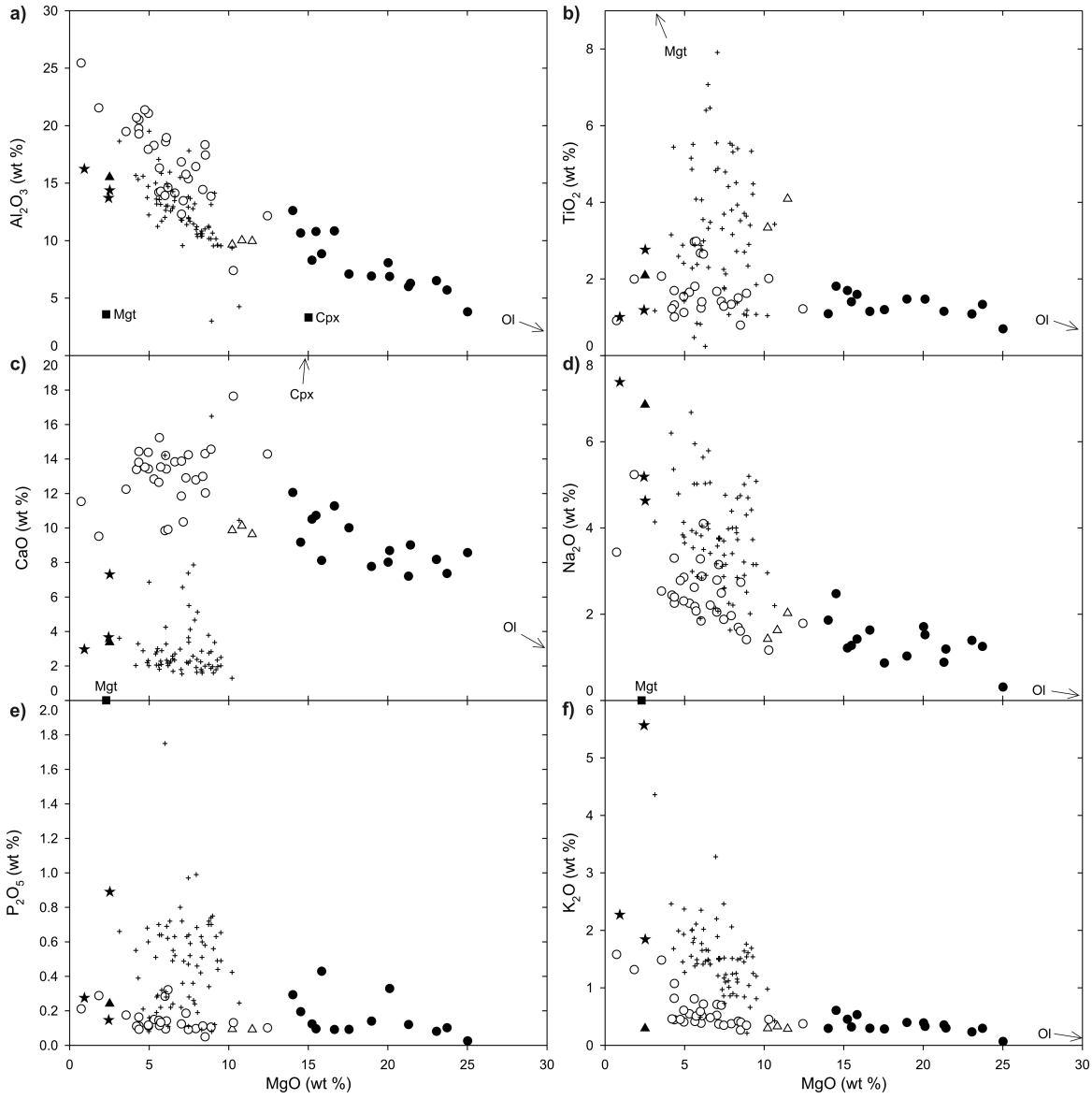


Figure 7.4: Major element compositions against MgO for the Doros olivine-hosted melt inclusions, in relation to the whole-rock suite (this study; Hodgson & Botha, 1974; Marsh & Duncan, 2008). Measured olivine (Ol), clinopyroxene (Cpx) and Fe-Ti oxide (Mgt) compositions for the BOM and IOM are also indicated. Symbols are as in Figure 7.3.

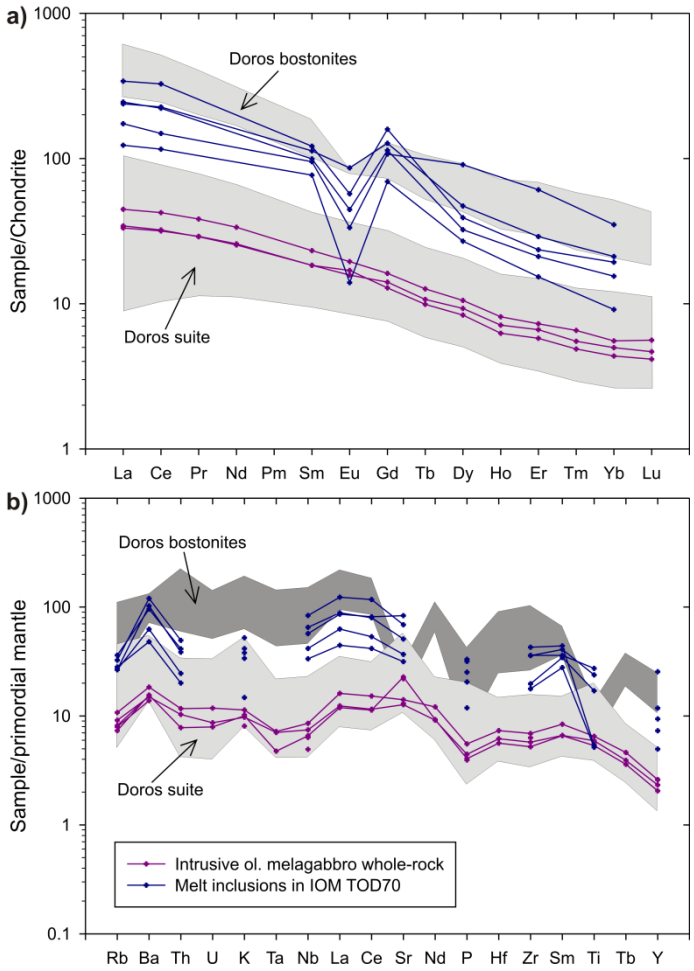


Figure 7.5: a) Rare earth element and b) mantle-normalised trace element abundances for olivine-hosted melt inclusions in intrusive olivine melagabbro sample TOD70, in relation to the Doros whole-rock suite. CI chondrite from Anders & Grevesse (1989); primitive mantle from McDonough & Sun (1995).

Incompatible trace elements are generally well correlated and show similar trends to the main Doros whole-rock suite, with the exception of Sr and Th (Fig. 7.6). The MIs are, however, significantly more enriched than the melagabbro host rocks, and indeed most of the whole-rock suite, and again show affinities in this regard with the bostonite dykes.

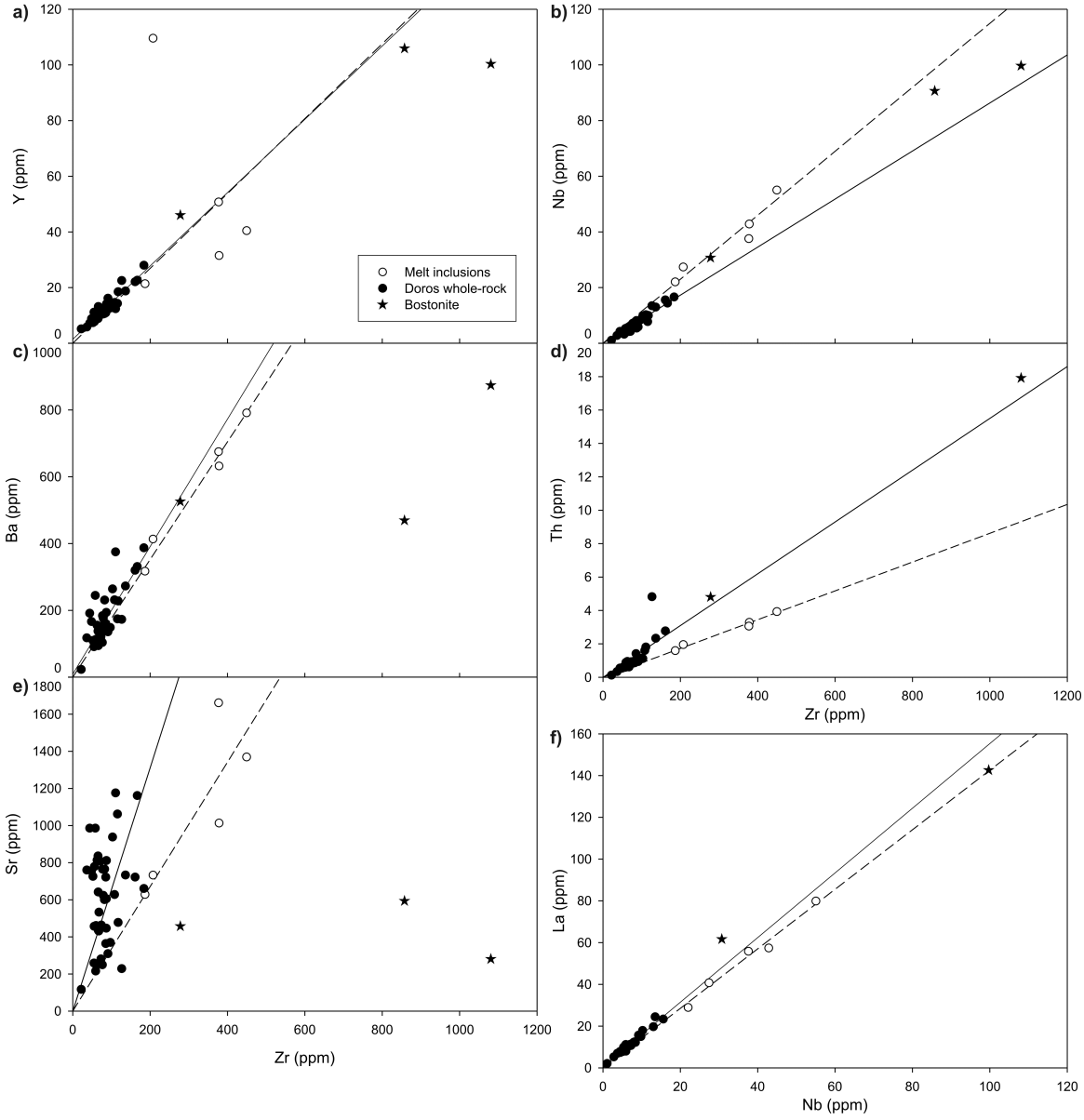


Figure 7.6: Incompatible trace element bivariate plots for the Doros melt inclusions (sample TOD70), shown with the whole-rock suite (this study; Marsh & Duncan, 2008). The dashed line is a regression through the MI data; the solid line a regression through the main Doros suite (excluding the bostonites).

7.5 Origin of Doros melt inclusions: Identification of magmas and their relation to the host rocks

The Doros MI presented here have highly variable chemical compositions (Figs. 7.2, 7.3, 7.4, 7.6), even within the same host crystal. Strong diversity of both compatible and incompatible elements seems to be a common feature of melt inclusions and can reflect a wide range of igneous processes, such as fractional crystallisation, melt mixing, assimilation/contamination, source heterogeneity and liquid immiscibility (e.g. Sobolev *et al*., 1993; Kent *et al*., 2002; Jakobsen *et al*., 2005; Keiding *et al*., 2011; Moune *et al*., 2012). A further complication can arise from geochemical features that are related to entrapment or post-entrapment processes in the MIs and that therefore do not reflect primary magmatic processes.

A first order observation is that the compositional variability observed in the MIs cannot readily be explained by fractional crystallisation, since there is little correlation between highly incompatible oxides such as P_2O_5, TiO_2 or K_2O and the MgO content of the melt inclusions (Fig. 7.4). Furthermore, the inclusion compositions are not what would be expected for a plausible parental liquid, nor are they similar to bulk compositions of rocks in the Doros suite that may be considered to approach derivative liquid compositions, such as the chill margin, chilled gabbroic sill, or gabbro KDO16 (see discussion in Chapter 5). Neither do they plot on mineral control lines related to these compositions, as would indicate accumulation or fractionation of olivine or other cumulate phases. While MIs in general typically show a wide range of compositions, even the average of this range does not correspond with a predicted early melt composition (CaO contents are too low; FeO and incompatible elements too high; Figs. 7.3, 7.4). This is also supported by petrographic observations. The daughter phases in the inclusions include orthopyroxene, which is not present anywhere in the whole-rock suite, and alkali amphibole, which occurs only in minor amounts in the bostonite dykes.

Although the MI compositions are highly variable, there is a suggestion in both the major and trace elements of a mixing trend between two components: one possibly basaltic – similar in some aspects to the foliated gabbros, but very Fe-rich – and one much more enriched, similar to the bostonite phase. In order to quantify this, the major elements are plotted together such that the mixing trends can be projected to obtain plausible mixing end members, as in Figure 7.7. This constrains the primitive end member to have a composition similar to or more primitive than A (corresponding to the most magnesium-rich or silica-poor inclusion in the suite), and the evolved end member to have a composition similar to or more enriched than B (the most magnesium-poor, silica-rich end of the range). The inferred approximate compositions of A and B are given in Table 7.1 below. The trends are plotted relative to both MgO and SiO_2 as indicators of differentiation since, as an olivine-compatible element, Mg compositions are relatively less well-constrained – but the results are similar.

Table 7.1: Approximate compositions (in wt. %) of melt inclusion mixing components, based on either MgO or SiO_2 contents

	Component A		Component B	
	Mg-rich	Si-poor	Mg-poor	Si-rich
SiO_2	43.07	43.06	58.29	60.42
TiO_2	3.24	4.09	3.37	2.24
Al_2O_3	8.01	10.67	17.42	15.58
FeO_T	26.7	23.5	7.72	9.07
MnO	0.31	0.32	0.14	0.11
MgO	10.67	9.38	3.14	3.79
CaO	3.74	4.09	2.81	1.98
Na_2O	2.91	3.27	4.67	4.46
K_2O	0.67	1.05	2.44	2.24
P_2O_5	0.51	0.58	0.51	0.43

The enriched component B is in many aspects remarkably similar to the measured Doros bostonites (see Table C.1 for comparative chemistry). Trends in incompatible trace elements (Zr, Nb, La, Y; Fig. 7.6), in particular, suggest a progression, both in the whole-rock and MI compositions, towards a bostonitic end member. It must also be considered, from the silica-rich compositions, that this may be a trend towards a crustal component. However, in terms of trace elements, the inclusions are significantly more enriched than the local Damaran crust (McDermott & Hawkesworth, 1990; Schmitt *et al*., 2012), so this is unlikely. While the bostonite phase has been suggested in previous chapters to represent an extreme fractionation product of the Doros magma, the melt inclusions do not simply reflect progressive fractionation, otherwise trends would be expected to mimic, at least in part, those in the bulk suite.

The more magnesian end member A is similar to an alkali basalt composition, but has distinctly higher FeO than expected, and to some extent TiO_2, markedly lower CaO, and possibly lower MgO. It is noted that, as olivine-compatible elements, Fe and Mg may have undergone some equilibration with the host, affecting their concentrations in the melt. However, diffusion of this nature would result in a decrease in melt Fe contents – the Fe-loss problem of Danyushevsky *et al*. (2000) – and therefore cannot explain the high FeO observed. Host-wall crystallisation of olivine could raise FeO contents in the melt, but would also significantly increase MgO (Rowe *et al*., 2006). The correction for post-entrapment crystallisation itself may be a source of potential error (Kent, 2008). However, the addition of forsteritic olivine raises MgO contents relative to FeO in the MI (see Tables G.2 and G.3 for a comparison of uncorrected and corrected data) and therefore cannot explain the unusually high FeO contents.

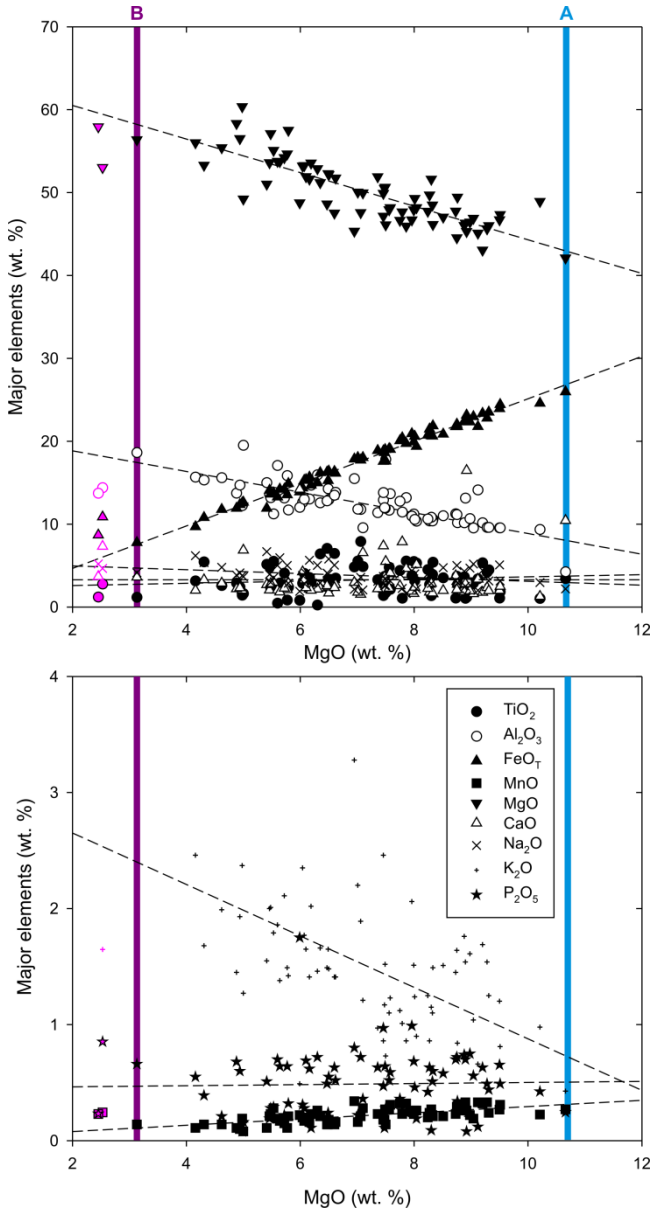


Figure 7.7: Major element trends in the Doros melt inclusion suite, suggesting mixing between an Mg-rich component A and Mg-poor component B. Doros bostonites TOD66 and TOD84 (pink symbols) are also shown for reference.

It is notable that TiO_2 contents are high and variable across the MI spectrum (Fig. 7.4b). There is some evidence from the crystalline phases present in the inclusions, which include magnetite and ilmenite, that heterogeneous entrapment has occurred, i.e. small crystals were trapped as solids along with the melt on formation. These would have been incorporated into the melt upon heating and homogenisation. The high TiO_2 and FeO contents of the MIs can thus be explained by the incorporation of small Fe-Ti oxide crystals with the melt. This has been proposed for high-Fe MIs in alkalic lavas elsewhere (Rowe *et al*., 2006). Similarly, entrapment of small clinopyroxene crystals can explain the high CaO (and CaO/Al_2O_3 ratios) in a few of the Doros inclusions (Fig. 7.8).

However, heterogeneous entrapment cannot explain the anomalously low CaO contents observed throughout the suite. CaO/Al_2O_3 ratios in the MI suite cluster around 0.34, and extend as low as 0.12 (Fig. 7.8). There are few cases of such low CaO/Al_2O_3 ratios in melt inclusions reported in the literature and these are usually associated with boninitic, adakitic or lamproitic melts (e.g. Defant & Drummond, 1990; Kamenetsky *et al*., 2002; Salvioli-Mariani *et al*., 2004). This ratio is not affected by olivine host wall crystallisation. Diffusion of CaO into the host olivine may have occurred, but Ca diffusion is very slow and could not account for the extent of Ca-loss required (Petry *et al*., 2004). In any case, re-equilibration would be expected to lead to an increase in melt Ca contents (Gaetani *et al*., 2002). The Eu anomalies of variable magnitude in the inclusions across the mixing spectrum (Fig. 7.5a) are evidence that some plagioclase fractionation from the melt has occurred. However, while this may deplete CaO, it would increase CaO/Al_2O_3 ratios (Fig. 7.8). Low or decreasing CaO/Al_2O_3 ratios are commonly attributed to clinopyroxene removal (Fig. 7.8). However, such low ratios are inconsistent with the normal extent of clinopyroxene fractionation. Considering a range of possible parent materials, including typical ocean island basalt, primary Tristan plume melts, mid-ocean ridge basalt and early Doros liquid KDO16 (see Chapter 5), it is estimated that a ratio of 0.34 would require 25 - 40% crystallisation of end-member diopside, and for a ratio of 0.12 as much as 30 - 50%. This is unrealistic for a magma that was clearly still crystallising significant primitive olivine. There is also no good correlation between CaO/Al_2O_3 and melt Mg #, Al_2O_3 or incompatible trace element concentrations (e.g. Fig. 7.8).

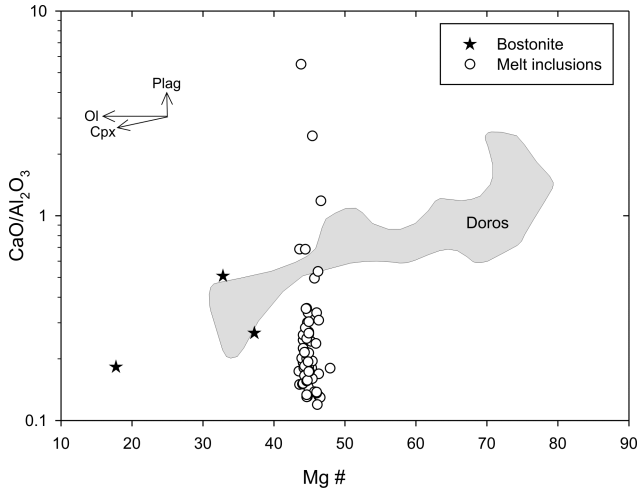


Figure 7.8: CaO/Al_2O_3 versus Mg # for the Doros melt inclusions, compared to the whole-rock suite (grey field) and bostonite dykes. The majority of inclusions, across the mixing spectrum, show CaO/Al_2O_3 ratios less than 0.5. Arrows indicate the approximate vectors of crystallisation for plagioclase, olivine or clinopyroxene.

Crustal contamination may decrease CaO/Al_2O_3 ratios, due to the incongruent melting of alkali feldspar (Kamenetsky & Gurenko, 2007). This has been proposed for unusual melt compositions in plagioclase-hosted inclusions in the Goboboseb quartz latites of the Etendeka succession (Ewart *et al*., 1998b). However, these melts characteristically show elevated SiO_2 contents, which are not present here. Furthermore, incompatible trace element ratios for the Doros MIs, such as in Figure 7.9, are not

consistent with the incorporation of crustal material. The MIs clearly lie on the mantle array and are not displaced towards crustal compositions (Fig. 7.9).

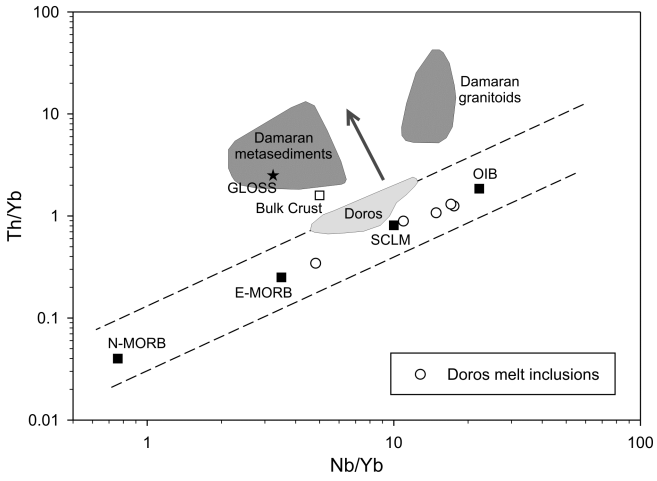


Figure 7.9: Th/Yb and Nb/Yb for melt inclusions (sample TOD70) alongside the Doros whole-rock suite, Damaran country rock (McDermott & Hawkesworth, 1990; Schmitt *et al*., 2012) and representative mantle and crustal components. Mid-ocean ridge basalt (MORB) and ocean island basalt (OIB) from Sun & McDonough (1989); sub-continental lithospheric mantle (SCLM) from McDonough (1990); global subducting sediment (GLOSS) from Plank & Langmuir (1998); bulk continental crust from Taylor & McLennan, 1995. The dashed lines delineate the mantle array. Crustal contamination would be expected to displace compositions off the array in the direction of the arrow.

Alternatively, the low CaO/Al_2O_3 may be a characteristic inherited from the mantle source, with or without subsequent clinopyroxene fractionation. The MIs show some chemical similarities, particularly depletion in the HREE, with a set of hypersthene-normative inclusions (CaO/Al_2O_3 = 0.05 - 0.04) in volcanic rocks from the Indonesian arc from the study of Elburg *et al*. (2006). These were interpreted as originating from a garnet-bearing source, either from melting at depth (> 90 km), or at shallower levels of the mantle in the presence of a water-rich fluid phase. REE ratios for the Doros MI (Fig. 7.10) support the presence of both residual garnet and clinopyroxene in the source. Low CaO/Al_2O_3 ratios may also reflect incongruent melting of an amphibole-bearing source, but this should correspond with relatively high Al_2O_3 contents and a depletion in K relative to Th, neither of which are evident here (Fig. 7.5b). Thermodynamic mantle melting models have shown that low CaO/Al_2O_3 ratios (and low CaO) are consistent with low degrees of partial melting and/or a fertile source (Hirschmann *et al*., 1999). The EMI end member characteristically shows low CaO/Al_2O_3 (and high K_2O/TiO_2; Jackson & Dasgupta, 2008). While the contributions of each of these factors cannot be further constrained here, it is suggested that a clinopyroxene- and garnet-bearing source and/or low degrees of partial melting may be plausible for the Doros MIs.

Thus, if a Doros parental melt is represented in the inclusion suite, it is likely a mildly enriched, low-Ca melt with alkali basalt affinities. However, compositions are obscured by heterogeneous entrapment and extensive mixing with a highly enriched melt of a bostonitic character.

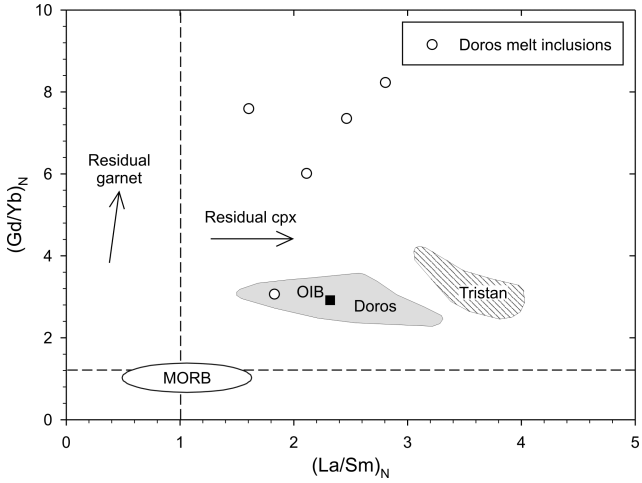


Figure 7.10: Chondrite-normalised (Anders & Grevesse, 1989) rare earth element ratios for the Doros melt inclusions (sample TOD70), in comparison to the whole-rock suite, typical MORB and OIB (Sun & McDonough, 1989), and modern-day Tristan plume basalts (Le Roex *et al*., 1990; Cliff *et al*., 1991).

A fundamental question to melt inclusion studies is, how representative are analysed melts of the bulk magma composition of the system? Inclusion suites commonly show a much wider range of compositions than is represented in the bulk rock suite (Kent, 2008). Unusual or unexpected MI compositions have been documented in several studies (e.g. Schiano *et al*., 2000; Danyushevsky *et al*., 2004; Elburg *et al*., 2006). It is also not uncommon for inclusions to show these anomalous compositions in greater abundance than 'normal' compositions. Danyushevsky *et al*. (2004) argue that these do not necessarily indicate significant new magmas in the system, but instead reflect minor boundary melts that are preferentially sampled. Interaction between a newly-emplaced primitive magma and the wall rock or a pre-existing mush layer at the margins of the body can induce small-scale dissolution and incongruent melting of this material, which is then incorporated into the magma. This mechanism was argued for the contaminated melts of the Goboboseb discussed previously (Ewart *et al*., 1998b). Early-formed crystals, typically primitive olivines (Fo >85), may trap these anomalous melts before sufficient mixing of the magma homogenises compositions (Danyushevsky *et al*., 2004). Because these crystals predominantly nucleate at the rapidly-cooling margins of the magma body, they preferentially trap melts in this region. Rapid nucleation also promotes the preservation of melt inclusions (Roedder 1979; Kent 2008). Thus, crystals forming in the centre of the magma body, where there is potential to trap 'normal' melts, are unlikely to preserve melt inclusions. Sampling may also be biased towards larger melt inclusions, which are easier to analyse, but which are more likely to have formed in the heterogeneous boundary layer (Danyushevsky *et al*., 2004).

The Doros olivine hosts are not as primitive as in other studies of anomalous compositions, but the abundance of melt inclusions strongly suggests rapid growth in a boundary layer. It is proposed that the Doros parental magma interacted with a pre-existing bostonitic unit at the margins of the chamber.

While a useable Doros parental magma composition cannot be isolated here, it is suggested that further work with more trace element analyses, and potentially isotopic data, for these melts could shed more light on a potential mantle source and the processes contributing to these unusual melt compositions.

7.6 Summary of findings

A set of olivine-hosted melt inclusions from the Doros melagabbro units was analysed for major and trace elements. Compositions are highly variable, but are generally relatively evolved. High TiO_2 and FeO contents in the homogenised inclusions indicate significant heterogeneous trapping of Fe-Ti oxide crystals. The origin of unusually low CaO/Al_2O_3 ratios across the suite is uncertain, but we speculate that these may indicate low degrees of melting and/or a clinopyroxene and garnet-bearing mantle source. Overall chemical trends in the MI suite suggest mixing between a derivative basaltic melt, possibly representing an early magma emplaced into the Doros chamber, and a highly enriched melt that shows affinities with the Doros bostonites, likely reflecting interactions in the magma boundary layer.

Chapter 8: Geophysical Analysis

8.1 Introduction and geological model

The previous chapters have documented the cross-cutting relations, orientations, rock textures, mineralogy and chemistry of the portion of the Doros intrusion that is presently exposed on surface. These features suggested a series of gently inward-dipping, sill-like gabbroic units and an exposed section approximately 300 m thick. The lowermost unit exposed – the basal olivine melagabbro (BOM) – was inferred to represent the base of the intrusive package. On this basis, a shallow-level intrusion with a funnel-like geometry was proposed, as in Figure 3.3. However, this subsurface geometry is not well constrained. There is no information about potential changes in the dip or thickness of layers with depth or the geometry of the feeder conduit. Furthermore, the presence of the partially-exposed, chilled gabbroic sill observed below the level of the BOM near the south-eastern margin of the body, and the apparent absence of an ultramafic zone typical of layered intrusions, suggests that there may be a lower-level component of the intrusion that is not exposed. In the absence of drilling, this proposed geometry can be investigated by geophysical means. Better knowledge of the sub-surface geometry and geology of the intrusion will also prove important for the understanding of magma emplacement processes and the overall petrogenesis of the complex.

8.2 Previous geophysical research of this nature

While no geophysical study has previously been conducted for the Doros intrusion, geophysical imaging (reflection and refraction seismic, gravity and aeromagnetic data) has been used to investigate the nearby Messum, Cape Cross and Brandberg Complexes of the Damaraland Intrusive Suite (Bauer *et al*., 2003; Vietor *et al*., 2001), to which Doros belongs (Chapter 1; Fig. 1.2). Each of these complexes is characterised by strong magnetic and gravity highs (Bauer *et al*., 2003; Vietor *et al*., 2001). In the case of the Messum and Cape Cross Complexes, both composite ring complexes, a reflection seismically-transparent crust up to 20 km depth and steep-sided gravity and magnetic anomalies were interpreted to indicate sub-vertical zones of mafic intrusions extending deep into the lower crust (Bauer *et al*., 2003). Brandberg is predominantly granitic on surface, but modelling of aeromagnetic data over the complex, in combination with gravity and seismic interpretation, identified a significant sub-surface mafic body that is wider than the granite and dips outwards, although the absolute depth is not well constrained (Vietor *et al*., 2001). These studies show that geophysical methods are effective for investigating the 3D geometries of the Damaraland intrusions, and also provide opportunities for comparison with the Doros Complex.

Magnetic methods have also been applied to the study of layered mafic intrusions elsewhere, for example for the Dufek intrusion (Ferris *et al*., 1998), the Sept Isles intrusion (Loncarevic *et al*., 1990) and the

Bjerkreim-Sokndal intrusion (McEnroe *et al*., 2009). However, in most cases the aeromagnetic data have been used largely to identify the extents and overall geometries of these intrusions at depth, and little attention has been paid to relating specific components to their magnetic responses, as will be done in this study.

8.3 Objectives of the geophysical study

The original objective of this aspect of the study was to obtain information on the subsurface geology using two potential-field geophysical methods: by magnetic survey (providing information on changes in magnetic susceptibility) and by gravity survey (providing information on changes in density). High-resolution aeromagnetic data are readily available from the Namibian regional airborne geophysical database, provided by the Geological Survey of Namibia. However, no gravity data (either airborne or ground) of sufficiently high resolution were available for this area at the time of the study. Hence, a local ground gravity survey of Doros and surrounds was commissioned and conducted by the Geological Survey, in collaboration with the author. Unfortunately the survey was hampered by instrumentational problems and the gravity data could not be made available at the time of publication of the thesis. However, forward modelling from the planning stages has been incorporated here and suggests that a gravity study will make an important contribution to future research.

While correlation between two geophysical parameters, at different resolutions, would have been optimal, the magnetic data alone can still provide important insights into the Doros surface and sub-surface geology.

The study aims to address several important questions in what is essentially an evaluation of the proposed geological model:

- How does the dip of the body change with depth?
- How does the thickness change with depth?
- What is the overall depth extent of the intrusion?
- What is the geometry and relative location of the feeder conduit?
- What is the nature of the host wall contact?
- Do the data require features that are not documented in the surface geology?
- What do the data imply about the temporal extent of emplacement?

8.4 Details of the aeromagnetic survey and data processing

The aeromagnetic data are derived from the Fransfontein Survey, conducted in 2006-2007 with a fixed-wing aircraft and a caesium vapour magnetometer. The draped survey was flown with a nominal height of 80 m above the terrain. Flight lines run north-south, at a spacing of 200 m, and tie lines run east-west, at a spacing of 2 500 m. Magnetic data were collected at a sampling rate of 20 Hz. Subsequent to acquisition, the data were levelled and gridded at 50 m. Corrections include the subtraction of the International Geomagnetic Reference Field (IGRF; 2005 Model), based on the acquisition time and elevation.

For interpretation, pole reduction was applied. These data were then further processed by generating the first vertical derivative, to emphasise shallow features and thereby assist in their identification; the second vertical derivative, to enhance feature boundaries; the analytical signal, to further enhance contacts; and by upward continuation, to reveal deeper structures. For details of the mathematics behind these routines, refer to Milligan & Gunn (1997).

The data used in this study cover a section of the survey between 20.86 S 14.20 E and 20.70 S 14.38 E – an area of approximately 330 km^2.

8.5 Data images

The gridded total magnetic intensity (TMI) data are shown in Figure 8.1 below. The image shows a strong tadpole-shaped magnetic low, coupled with a magnetic high on the southern margin, in the area of the Doros intrusion. The lowest intensities are less than -1 700 nT, slightly south of the centre of the feature. A small zone of relatively higher magnetic intensity (up to -65 nT) appears in the centre of the widest part of the negative anomaly, while the highest intensities occupy a broad zone along the southern rim and exceed 400 nT in some places. To the south-east and north-west of these features are two roughly elliptical positive anomalies in the region of the Damaran-age Doros and Voetspoor granitoid plutons. Maximum magnetic intensities here exceed 600 nT. Several north- to north-west-trending linear features are present in in the south-western portion of the magnetic data area.

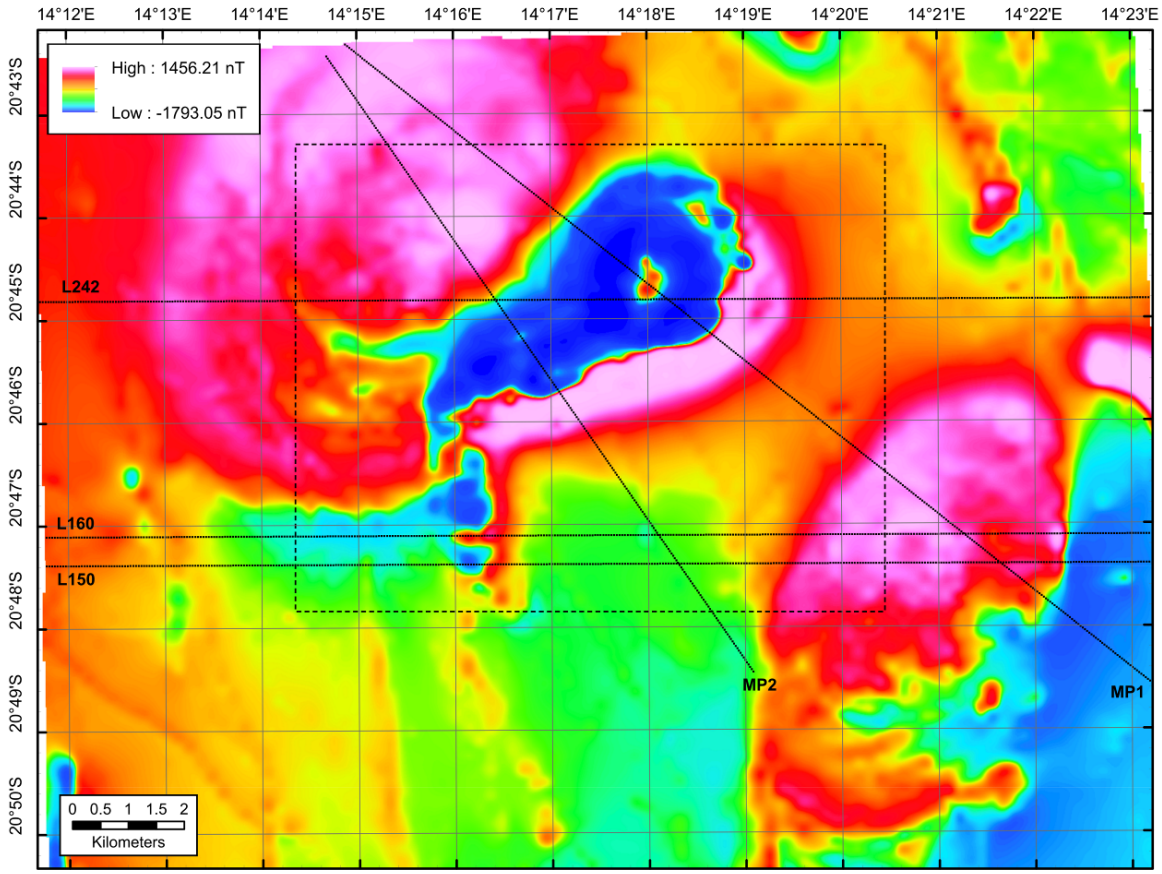


Figure 8.1: Gridded total magnetic intensity data (in nT) for the study area (IGRF removed). Section lines indicated are the modelled profiles discussed in Section 8.6. The dashed box indicates the mapped area (Chapter 3) and the extent of view in several of the processed images to follow.

Figure 8.2 shows the reduced-to-pole (RTP) magnetic data of a zoomed-in view of the surveyed region, centred on the Doros Complex (indicated by the boxed area in Fig. 8.1). This is overlain with the mapped surface geology of Chapter 3, based on outcrop. The image shows a magnetic low associated with the surface expression of the gabbro body, rimmed by higher intensities. Again, strong positive anomalies appear in the region of the two granitoid plutons. No linear features are evident in this image.

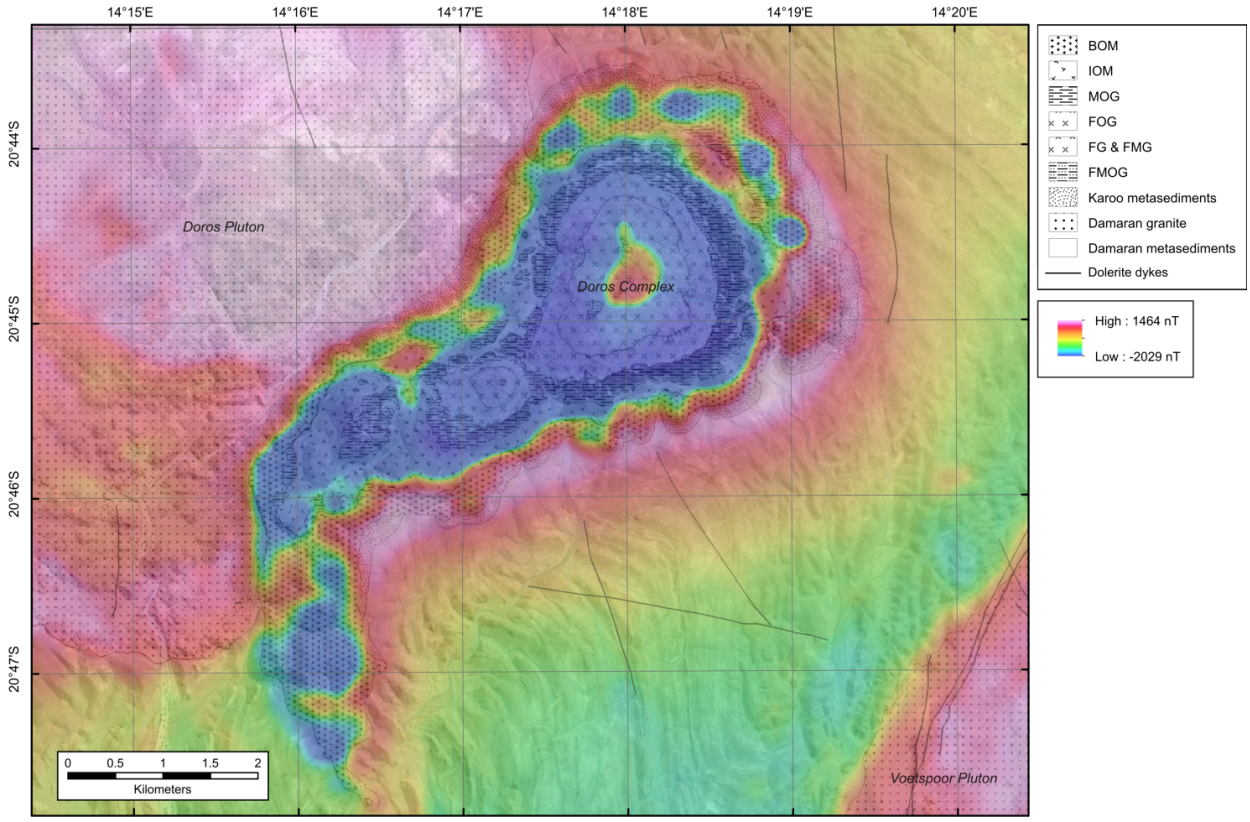


Figure 8.2: Map of reduced-to-pole magnetic anomaly data for the Doros gabbroic intrusion and surrounding Damaran granitoid plutons and schists, overlain with the mapped surface geology from this study (for unit abbreviations see Chapter 3) and satellite imagery (Google Earth Pro 7.0.2, 2010).

The first vertical derivative (1VD) of the RTP data (Fig. 8.3) shows strong gradients in intensity near the margins of the Doros intrusion and in parts of the complex interior. The signal in the region of the two granite bodies is variable. Several north- to north-west-trending linear features are present outside the complex and some appear to correspond with mapped dolerite dykes. It is not clear if these continue through the Doros region. The effect of the north-south survey flight lines is evident in the fragmentation of these linear anomalies.

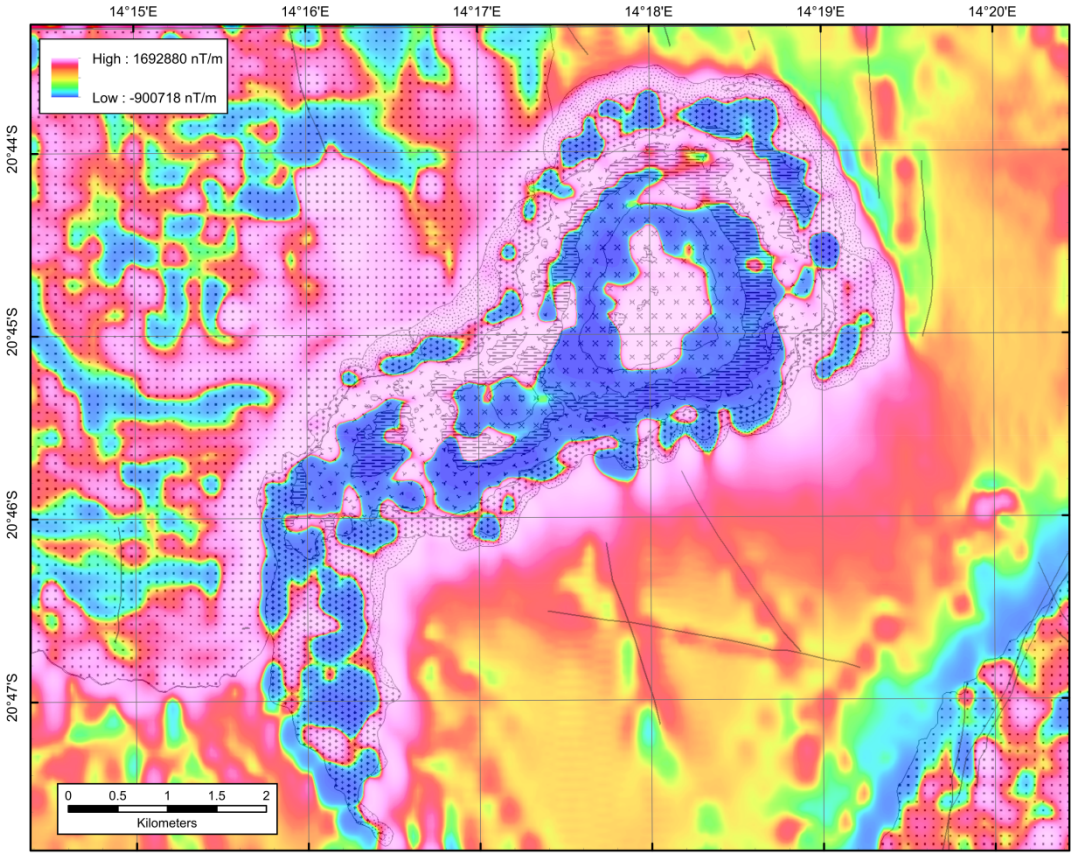


Figure 8.3: First vertical derivative of the pole-reduced aeromagnetic data over the Doros intrusion (in nT/m), overlain with the mapped surface geology (symbols in Fig. 8.2).

The second vertical derivative (2VD) of the RTP data (Fig. 8.4), shown here for the wider study area, further enhances some of the features observed in the previous image. High amplitude values coincide with the Doros intrusion and the two granitoid plutons. Several additional linear features are identified in the south and east of the image by their strong gradients. There is also evidence of noise in the data.

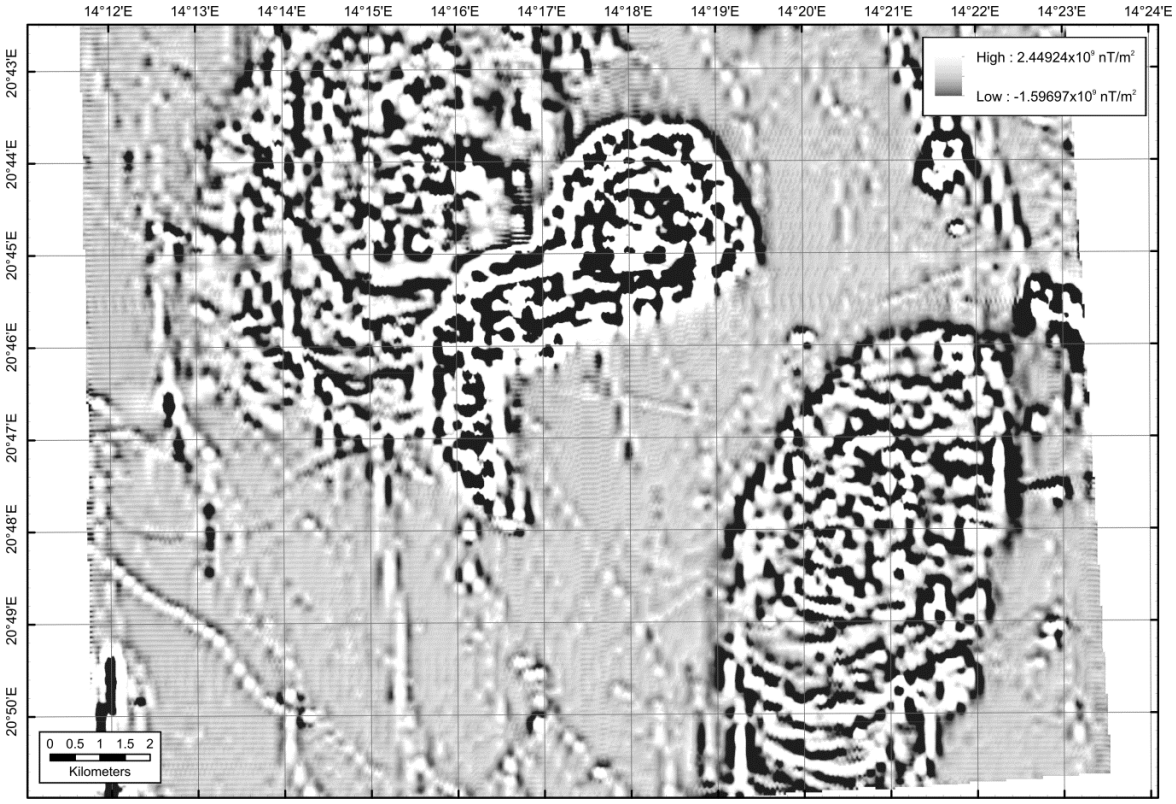


Figure 8.4: Second vertical derivative of the pole-reduced aeromagnetic data (nT/m^2) over the Doros intrusion and surrounding regions.

The analytical signal image (Fig. 8.5) shows a high amplitude feature coincident with the mapped Doros Complex. The peak of the anomaly exceeds 900 000 units. Highs of variable amplitude are also associated with the domain of the two granitoid plutons.

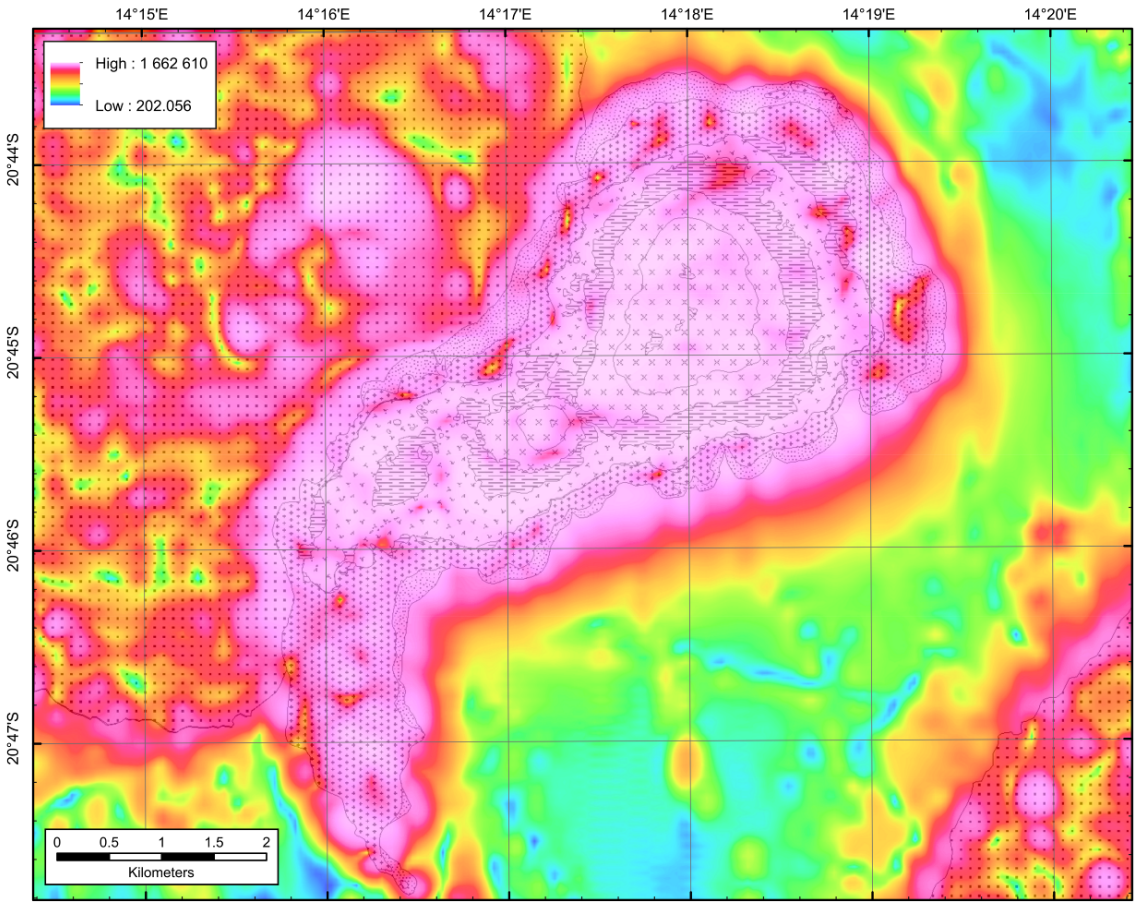


Figure 8.5: Analytical signal of the RTP data (unitless) over the Doros intrusion, with the mapped surface geology (symbols in Fig. 8.2).

The RTP data were upward-continued to an elevation of 3 000 m, at intervals of 500 m. Figure 8.6, for example, shows the data at an elevation of 2 000 m. In this image, the distinctive tadpole-like shape of the negative anomaly in the RTP data disappears and an elliptical low remains slightly south of the centre of the head of the complex. This feature decreases in diameter with apparent depth and is not evident in the data continued to greater than 2 500 m. This negative anomaly is bounded on either side by strong, low frequency highs.

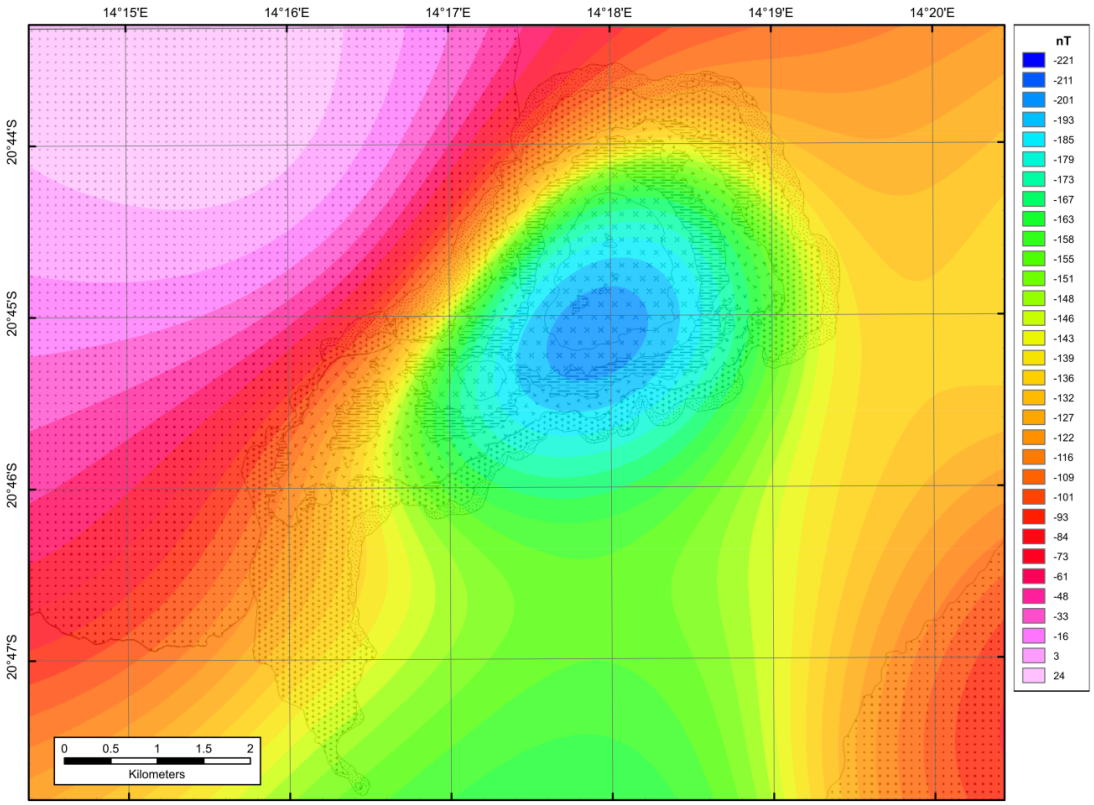


Figure 8.6: RTP magnetic data upward continued at an elevation of 2 000 m, overlain with the mapped surface geology.

8.6 Physical properties

Magnetic susceptibility (k) readings were taken for a selection of hand samples covering the range of Doros rock types, as well as local Damaran schists and dolerite dykes, using ZH SM-30 and GMS-2 hand-held susceptibility meters. The results of these measurements are shown in Table G.1 of the Appendix, and summarised in Table 8.1.

Most of the major units of the Doros intrusion have moderate to high magnetic susceptibilities (0.0026 - 0.015 SI). The majority of these rocks are documented to contain minor Fe-Ti oxides, as oxy-esolved titanomagnetite (up to 5 modal %; Chapter 4). However, the FMG and FMOG units are distinct, with susceptibilities of up to 0.039 SI. This strongly ferromagnetic character is clearly due to the high proportions of titanomagnetite in these rocks (10 - 15%). This is also the reason for the very high susceptibility values (up to 0.54 SI) for the magnetite cumulate, which contains up to 90% magnetite. Susceptibilities for the chilled gabbroic sill are also very high, at ~ 0.065 SI. While modal proportions for this fine-grained rock are not well-constrained, CIPW normative calculations indicate significant magnetite and ilmenite (Table C.3). The strongly magnetic properties suggest that Fe-Ti oxides likely comprise at least 10 % of this rock.

Table 8.1: Averages of measured magnetic susceptibilities (*k*) of selected rock types

Rock type	*n*	*k* (SI)
Basal ol. melagabbro	5	0.0096
Intrusive ol. melagabbro	2	0.0067
Massive ol. gabbro	3	0.0063
Foliated ol. gabbro	2	0.013
Foliated gabbro	2	0.0027
Foliated mgt. gabbro	4	0.024
Foliated mgt. ol. gabbro	2	0.024
Mgt. cumulate enclave	3	0.53
Cpx. cumulate enclave	1	0.0032
Bostonite	4	0.0088
Chilled gabbroic sill	3	0.065
Dolerite	2	0.058
Damaran schist	8	0.0077

Susceptibility values for the Damaran metasedimentary host rocks vary significantly (0.000054 - 0.018 SI), but are generally low. The samples taken in the Doros metamorphic aureole on the southern margin of the complex (TOD4, TOD61) have marginally higher susceptibilities than that taken far to the east (TOD2). This may be a consequence of magnetite formation during contact metamorphism by the intruding gabbro (Clark, 1997) or a coincidence of lithology (variations in magnetic properties with sedimentary facies). The dolerite dyke measured here shows contrastingly high magnetic susceptibilities (~0.058 SI).

No samples of the Damaran granitoids or Karoo metasediments in the region were taken in this study, but their susceptibilities may be inferred to some extent. The Doros and Voetspoor plutons consist of hornblende quartz syenite, clinopyroxene-hornblende quartz syenite, biotite granite and diorite (Schmitt *et al*., 2012). No ferromagnetic minerals are reported in their petrography (Schmitt *et al*., 2012), but the accessory mineral assemblage suggests that they may be in the magnetite series (Clark, 1999) and CIPW normative calculations indicate magnetite and ilmenite contents of up to 5%. Thus susceptibilities are expected to be moderately high for these rocks. It is noted that the Omangambo granitoid pluton, approximately 20 km to the north-east of Doros, has measured susceptibilities of ~0.011 SI (Rankin, pers. comm.).

There are no susceptibility data available in the literature for the Karoo strata in this region (the Huab Basin). The sandstones, shales and calcareous units preserved at the margins of the Doros intrusion are interpreted to correlate with the upper Dwyka and lower Ecca Group (Miller, 2008d). Mesosaurus-bearing bone breccias documented by Reuning & Martin (1957) indicate that the upper strata extend at least to the Rhino Wash Formation of the Ecca Group (Miller, 2008d). Measured susceptibilities for South African equivalents are low, ranging between 0.000011 and 0.00256 SI (Scheiber, pers. comm.). However, the red

colouring of some of the shale and siltstone units on the Doros rim suggests that they may be ferruginous and therefore have higher susceptibilities.

8.7 Image analysis

The magnetic data allow some first-order interpretations to be made regarding the geology of this region and the geometry of the Doros Complex.

In general, the Doros and Voetspoor granitoid plutons are correlated with strong magnetic highs in the TMI data (Fig. 8.1), consistent with their inferred high magnetic susceptibilities. The Damaran metasedimentary rocks coincide with intermediate magnetic intensities, in line with relatively low measured susceptibilities (Fig. 8.1). However, the apparent change in susceptibilities of the metasediments with distance from the Doros intrusion (Section 8.6) is not evident in the aeromagnetic data. While the TMI image (Fig. 8.1) does show raised magnetic intensities within the metasediments south of the Doros intrusion, these are not present on the western margin, as would be expected for a metamorphic aureole, nor are they correlated with the mapped strike of the Damaran strata, which is approximately orthogonal to the Doros contact in this region (Passchier *et al*., 2007). These intensities are also much higher than would be predicted for the measured susceptibilities. The measured variation in susceptibility is clearly negligible for the range of values in the image.

The Doros mafic intrusion is clearly the source of the strong magnetic low that stands out in sharp contrast to the rest of the TMI image (Fig. 8.1). However, the Doros gabbros have been shown to have relatively high magnetic susceptibilities (Table 8.1), and would be expected to produce high positive magnetic intensities in the aeromagnetic data, if only the induced field is considered. The observed negative anomaly is thus evidence that there must be a strong component of remanent magnetisation in these rocks, in the opposite direction to the current geomagnetic field.

Although pole-reduction assumes that there is no remanent magnetisation, the RTP image (Fig. 8.2) is useful for interpretation because it centres the anomalies over their sources, to some extent, allowing better correlation with the mapped surface geology. In Figure 8.2, the boundary of the negative anomaly coincides closely with the basal contact of the Doros intrusion mapped (or inferred) on surface. This suggests that the source of the anomaly, i.e. the main body of the intrusion, is relatively shallow and does not expand outwards below surface. However, there is a region of high magnetic intensity along the southern rim of the intrusion that extends into the domain of the Damaran schists, and therefore does not correlate with any lithologies in the mapped surface geology. There are also variations in amplitude in the magnetic signal around the margins of the body, largely within the BOM and IOM units. The lowest observed magnetic intensities correspond with the MOG, FOG and FG units, with a minimum in the neck of the complex. This is in agreement with an increase in depth extent of the intrusion, and therefore strengthening of the anomaly, towards the centre, as is suggested by the dip of the layers in the field (Chapter 3). The small, but strong magnetic high in the core of the complex is clearly associated with the

domain of the magnetite-bearing gabbros, which have been shown to have some of the highest magnetic susceptibilities in the intrusive suite. This gives a better indication of the extent of these units, which are otherwise poorly-exposed on surface.

The first vertical derivative of the RTP data (Fig. 8.3) better defines the outer boundary of the Doros intrusion and reveals concentric structures within the complex head, consistent with the mapped layering. It also highlights linear features within the granitoid plutons that correspond well with the fabrics and metasedimentary xenoliths mapped by Passchier *et al*. (2007). The linear features with high magnetic intensities and strong gradients within the metasediments are clearly caused by cross-cutting dolerite dykes, which have appropriate susceptibilities (Table 8.1) and are exposed on surface in several of these locations (Fig. 8.3). These dykes are best delineated in the second vertical derivative of the data (Fig. 8.4), where several unmapped dykes are also revealed. The majority of the dykes in the region trend north to north-west, but a set of north-east-trending dykes is evident in the vicinity of the Voetspoor pluton. It is not clear in the aeromagnetic data whether these regional dykes extend through, and therefore cross-cut, the Doros intrusion, although several dolerite dykes have been documented to intrude the Doros gabbros in the interior of the complex (Chapter 3).

The presence of remanence in addition to induced magnetisation complicates interpretation. However, the analytical signal of the RTP data (Fig. 8.5) removes the effects of the magnetisation direction, thereby reducing the distortion due to remanence (Foss, 2006). This allows the edges of the Doros body to be more clearly distinguished, particularly along the northern contact with the granite, which was previously partially obscured by interference between the adjacent granite and gabbro anomalies. The mafic body is clearly shallow and strongly magnetised.

Upward continuation of the RTP data (e.g. Fig. 8.6) is used to assess the depth extent of the intrusion, and better detect low frequency anomalies. The decrease in diameter of the Doros anomaly with apparent depth supports a narrowing of the intrusion below surface, and thus a lopolithic shape. This also indicates that the thickest part of the intrusion, potentially the location of the feeder conduit, is slightly offset to the south of the centre of the body. There is no distinct anomaly deeper than 2 500 m, suggesting that the main body of the intrusion is likely shallower than this.

8.8 Forward modelling

To more accurately relate the mapped surface geology and measured magnetic properties of these lithologies to their response in the aeromagnetic data, several profiles across the body have been selected for quantitative modelling (locations indicated in Fig. 8.1). The unfiltered, gridded TMI data are used for this purpose, so that both the induced and remanent components can be investigated.

The geology of the Doros Complex on surface is fairly well known, from the mapping and photo interpretation of Chapter 3. The layer orientations, at least near surface, are constrained by the strike and dip measurements of Hodgson & Botha (1974). The measured magnetic susceptibilities of these

lithologies are compiled in Table 8.1. The properties of the geomagnetic field at the time of the survey can be approximated (British Geological Survey, 2013). Therefore the unkowns in the modelling are the subsurface geometry and geology, and the component of remanent magnetisation, which may vary for different rock units. There are no published data for remanent magnetisation in these rocks. However, unpublished data in the posession of the author for the Etendeka volcanic succession, to which the Doros intrusion is interpreted to be related in petrogenesis, if not in time, suggest significant variability in remanence, including several magnetic reversals. Koenigsberger ratios (Q), the ratios of the intensity of remanent to induced magnetisation, are typically greater than 1 for these Etendeka lithologies.

Forward modelling is conducted with the Mag2dc software (Version 2.11; Cooper, 2004). A regional field equivalent to the average Damaran metasediments has been removed from the data, and departures from this baseline are modelled as contrasts in susceptibility and remanence, constrained by the surface geology and measured dips. For simplicity, the Doros intrusion is modelled as four major units, based on the susceptibility data in Table 8.1: the BOM + IOM + MOG, the FOG, the FG, and the FMG + FMOG. The Basal and Intermediate Zone gabbros have been grouped based on similar measured susceptibilities. The two magnetite gabbros are not distinguished due to the scale of the model.

Forward modelling is a method used to test the plausibility of various combinations of body geometries and magnetic properties and eliminate those that are invalid, and therefore many permutations are possible. However, it allows the previously proposed geological model to be evaluated in detail and for further constraints to be placed on this, according to the objectives laid out in Section 8.3.

The modelling takes the following approach: Initially, the simplest scenario is considered, i.e. a homogeneous mafic body, with consistent dips equivalent to those measured at surface. The first test evaluates the effect of varying inclinations and intensities of the component of remanent magnetisation for this body on the modelled response. The second test examines the effect of changing the dip of the lower contact, effectively changing the shape of the body from a pipe-like geometry, to a steep-sided lopolith, to a lopolith that shallows with depth. The third test varies the internal properties of the body, taking into account layering with different susceptibility properties. The fourth test considers variations in the dips of the layer contacts and/or the layer thicknesses. The fifth test introduces features in the country rock (granitoid plutons; Karoo strata; varying Damaran lithologies) and evaluates the effects of changing geometries and magnetic properties on the modelled response, as well as interference with the modelled Doros body. Finally, the modelling is used to evaluate additional features that are not exposed on surface, but that other evidence suggests may be present (a Doros ultramafic zone; an extension of the chilled gabbroic sill; dolerite dykes). Each of these tests is applied in isolation, as well as in combination with the other parameters.

Two modelled profiles are selected for display and discussion. Profile L150 (Fig. 8.7) shows the simplest section through the body, where only one major unit is present on surface (the BOM), and the mapped country rock consists only of Damaran schists, i.e. there is minimal interference from the Doros granitoid

pluton. The intrusion has a very shallow measured dip here (Hodgson & Botha, 1974). Profile MP1 (Fig. 8.8) is a section roughly perpendicular to the strike of the head of the complex, showing all the main gabbro units identified in the stratigraphy. The north-western rim of the intrusion is in contact with a thin layer of Karoo metasediments and the Doros granitoid pluton. The south-eastern contact is with Damaran metasediments, and less well-exposed.

While the models presented here are just a selection of many iterations of geometry, susceptibility and remanence in the solution space, they demonstrate several important principles that may be extracted from the modelling as a whole. These are as follows:

1) All the models show that contrasts in susceptibility play a minor role and it is the inclination and intensity of the remanent magnetisation that is the dominant factor responsible for the characteristic aeromagnetic response over the Doros intrusion.

2) To produce the required negative anomaly, the component of remanent magnetisation for at least part of the intrusion must be in the opposite direction to the induced field.

3) The measured aeromagnetic response over the Doros intrusion is consistent with a body that shallows to a round- or flat-bottomed lopolith (Fig. 8.8b or c). This is similar to what was proposed in the geological model (Chapter 3). A steepening of the outer contact with depth, i.e. a pipe-like geometry, or a constant dip with depth (as in Fig. 8.8a), produces a poor fit with the observed data.

4) The modelling suggests that the main body of the intrusion is likely to be at least 500 m thick. However, the absolute depth extent of the body is not well constrained, since features below approximately 1 000 m make little contribution to the magnetic response. The upward continuation of the data (Fig. 8.6) is the best indication that the intrusion is shallow, at least no more than 2 500 m thick. For this same reason, the lateral geometry of the feeder conduit cannot be accurately determined, but the data do not disallow an axial feeder conduit such as is suggested in the geological model.

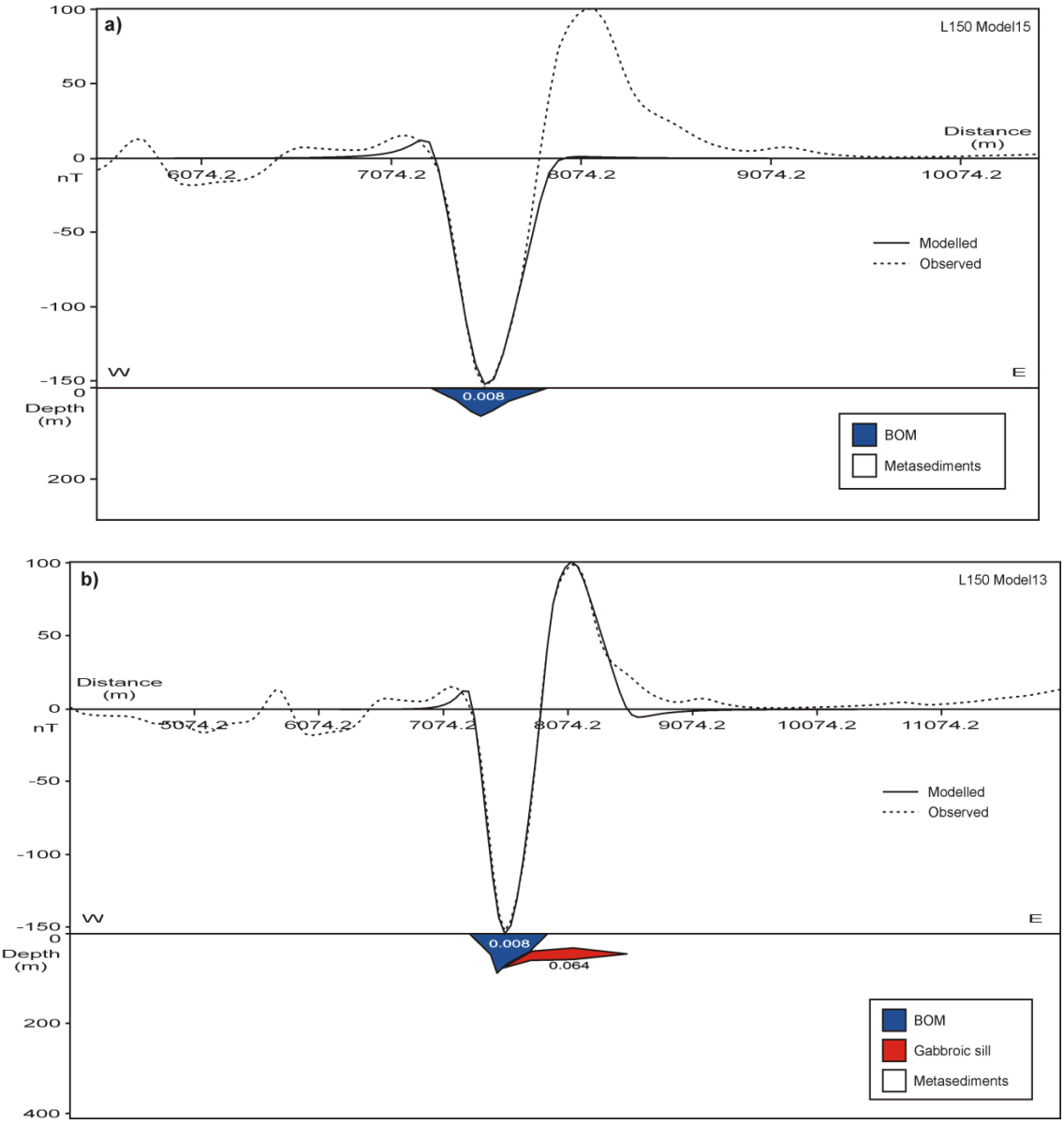
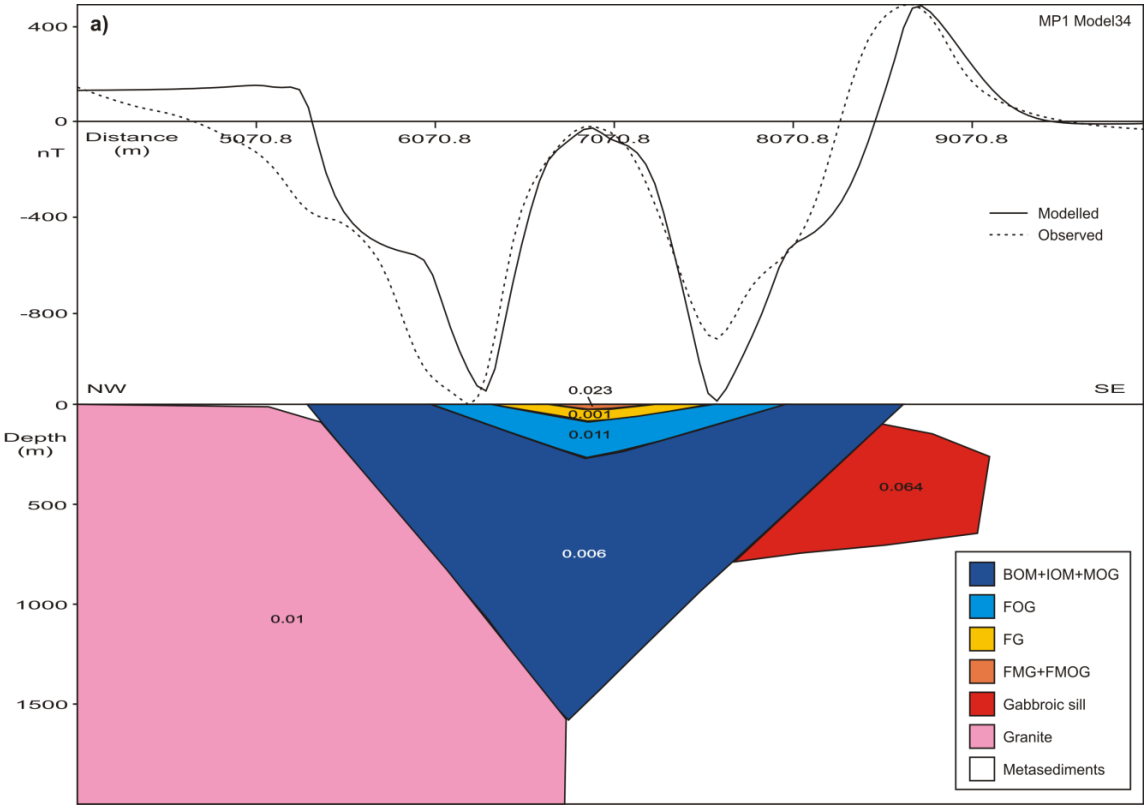
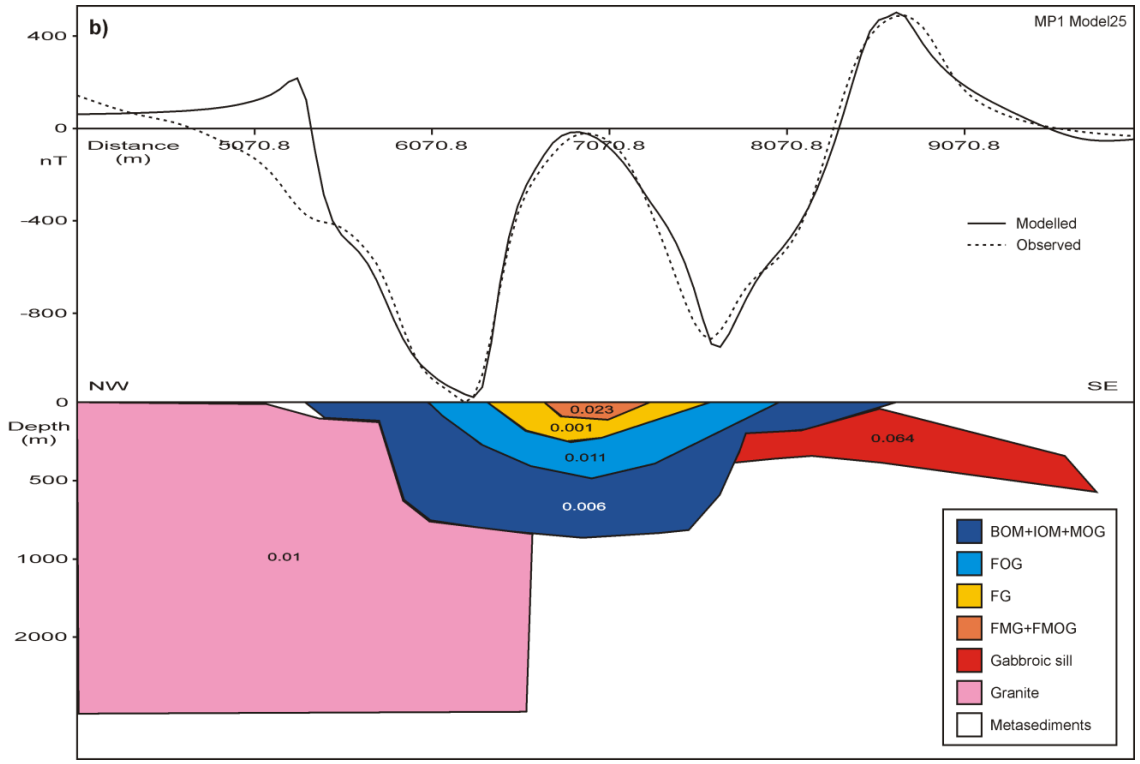


Figure 8.7: Two models for a section of profile L150 through the tail of the Doros Complex (see Fig. 8.1 for location). Distances are plotted with respect to the beginning of the section line. Susceptibility contrasts in SI (with reference to the Damaran metasediments) are indicated on each body. Bodies modelled with reverse remanent magnetisation are represented in cold colours and bodies with normal remanent magnetisation in warm colours. a) Model 15 considers only a simple, shallow, inwardly-dipping body of Doros gabbro (BOM). This model cannot explain the positive anomaly on the eastern margin of the intrusion in the observed data. b) Model 13 considers the same Doros body, with the addition of a mafic sill to the east that is not exposed on surface.


a)
MP1 Model34
400
0
-400
-800
nT
Distance (m)
5070.8
6070.8
7070.8
8070.8
9070.8
Modelled
Observed
NW
SE
0.023
0.001
0.011
0.064
0.006
0.01
Depth (m)
500
1000
1500
BOM+IOM+MOG
FOG
FG
FMG+FMOG
Gabbroic sill
Granite
Metasediments


b)
MP1 Model25
400
0
-400
-800
nT
Distance (m)
5070.8
6070.8
7070.8
8070.8
9070.8
Modelled
Observed
NW
SE
0.023
0.001
0.011
0.064
0.006
0.01
Depth (m)
500
1000
2000
BOM+IOM+MOG
FOG
FG
FMG+FMOG
Gabbroic sill
Granite
Metasediments

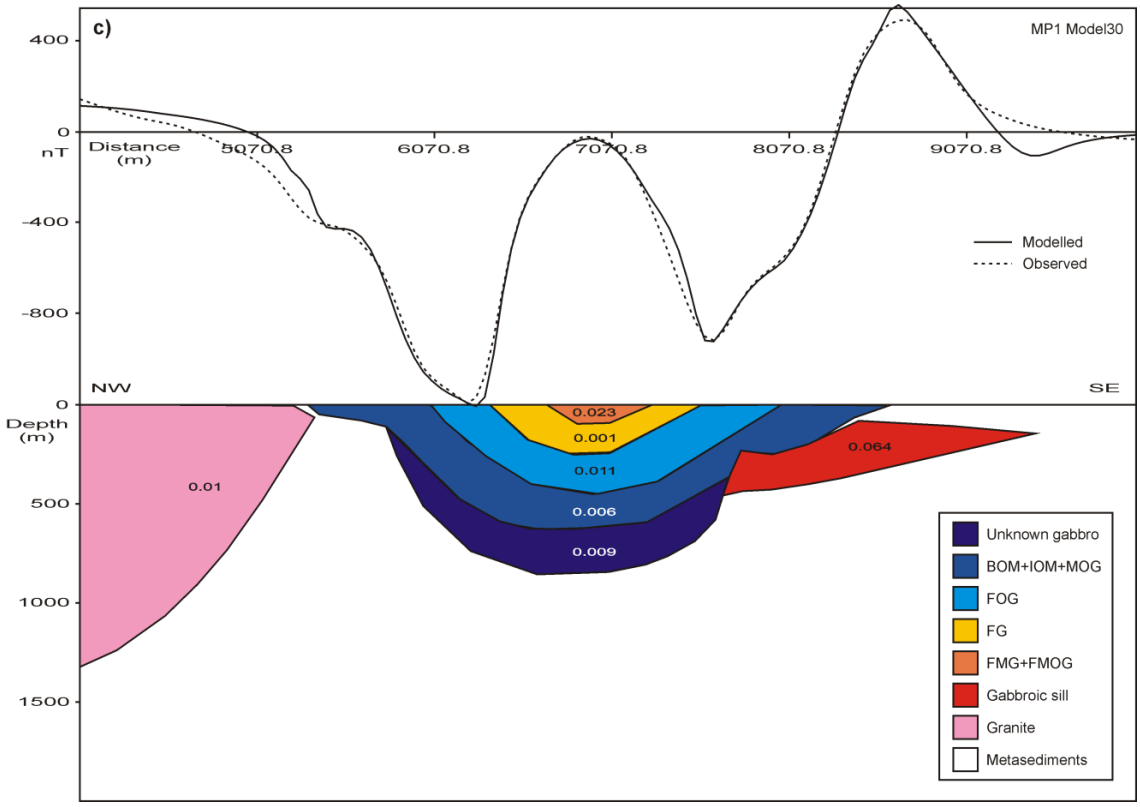


Figure 8.8: Three models for the center section of profile MP1 through the head of the Doros Complex (see Fig. 8.1 for location). a) Model 34 considers a layered Doros body (only those units mapped on surface) with a constant dip (approximately as measured). The model also comprises a granitoid pluton to the north-west of Doros and a sub-exposural mafic sill to the south-east. The shape of the modelled response is appropriate, but the fit with the observed data is poor. b) Model 25 considers a layered Doros body with a variable dip that flattens out at depth. The granitoid pluton extends southward under the Doros intrusion. The model fits the observed data well, but there is a noticeable departure in the vicinity of the granite contact. c) Model 30 considers the effect of an additional gabbro layer not exposed on surface that may represent an ultramafic zone, as well as a northward-dipping granite pluton. Compared to Model 25, the model correlates equally well with the observed response over the Doros intrusion, but better for the granite pluton.

5) The variations in magnetic response over the intrusion are consistent with the mapped layering of units with different measured susceptibilities, but only if there is also variation in the characteristics of the remanent magnetisation with the stratigraphy. The best-fit models require reverse remanent magnetisation for the BOM unit through to the FOG unit, but normal remanence for the FG to FMOG units (e.g. Fig. 8.8b, c). Low negative remanence or zero remanence for the FG to FMG does not fit the measured response. This indicates that there were at least two discrete pulses of magma emplaced into the intrusion, separated by a magnetic reversal. The magnitude of remanence varies, but the highest intensities are likely in the basal units. The modelling is consistent with, but not limited to, an inclination of magnetisation of approximately 40° in either direction.

6) While the geological model for the complex, with the parameters described above, adequately describes the negative anomaly over the intrusion and its central high, this alone cannot account for the significant positive anomaly (> 400 nT) that is ubiquitous along the southern and eastern margins

of the complex (Figs. 8.1, 8.7, 8.8). The simple scenario in Figure 8.7a shows this clearly. Several possibilities have been considered to explain this high intensity feature. The Karoo strata preserved along parts of the intrusion rim may be sufficiently magnetic, but are not vertically or laterally extensive enough to produce the required anomaly. There should also be an equivalent response on the northern margin of the intrusion, where the Karoo sequence is, in fact, better preserved. Relatively high susceptibilities were measured for the Damaran metasedimentary rocks near the southern margin (Section 8.6), but it has already been argued that these are not capable of producing sufficiently high magnetic intensities, with the right areal extent (Section 8.7), and the modelling confirms this. This anomaly can only be attributed to a feature that is not exposed on surface and was not considered in the geological model. There is some indication that there is an extension of the complex below the level of the BOM in the presence of the chilled gabbroic sill, documented in one locality at the southern margin, not far from profile MP1 (Waypoint 123, Fig. A.1). Since this rock type is only exposed in this locality and there were no indicators of its true extent, it was not previously considered a significant unit in the complex. This material is very strongly magnetic (~0.065 SI). The forward modelling shows that a sill-like body of this nature, with a component of positive remanent magnetisation, can plausibly explain the observed magnetic highs marginal to the Doros intrusion (Figs. 8.7b, 8.8a-c). This indicates that there is an additional episode of intrusion associated with the complex. Several different geometries for the sill fit the model (e.g. Figs. 8.8a-c), but these consistently indicate that this body extends to the south and east of the surface expression of the intrusion. Depending on the modelled remanence properties and profile section, the sill is between 50 and 700 m thick.

7) The modelling further shows that the variable amplitude of the magnetic response for the BOM and IOM units in the outermost parts of the intrusion (Fig. 8.2) can be attributed to irregularities in the basal topography, i.e. thickness, of the intrusion and/or in the chilled gabbroic sill unit, as is modelled in Figure 8.8b and c. The amplitude of these features is too large (~600 m) to be due to artefacts of the survey flight lines. Lateral variations in susceptibility are also unlikely, since this occurs within the same mapped units. The sill is inferred to be closest to surface under the south-eastern part of the intrusion, where this anomaly is most extensive, despite the overlying basal melagabbro. Less variation in the bottom topography may be required if an additional sub-exposural layer of gabbro is present, potentially representing an ultramafic basal zone of the complex, as in Model 30 (Fig. 8.8c), but this is not well constrained.

8) The parts of the intrusion in contact with the granite, where there is interference between anomalies, are challenging to model. While the magnetic properties of the granite are not well-constrained, modelling shows that the magnetic response is consistent with a moderately magnetic body (~0.01 - 0.02 SI) with a component of positive remanence (Fig. 8.8). Variations in the amplitude of the signal may be accurately modelled with small variations in granitoid lithology (granite versus diorite versus syenite, or sedimentary xenoliths) and/or depth. While the geological model indicated that the granite

may extend under the Doros intrusion, forward modelling suggests that a better fit with the field data is achieved if the granite dips shallowly towards the north, as in Model 30 (Fig. 8.8c), so as to minimise the positive feature associated with the Doros contact, evident in Model 25 (Fig. 8.8b). Since a component of future research will include a gravity survey of the area, a gravity forward model is constructed for this profile to test if the geometry of the granitoid pluton may be better constrained with gravity data (Fig. 8.9). While measured rock densities are not available for these rocks, reasonable estimates may be derived from the rock compositions and the literature (see Table G.2). The results in Figure 8.9 show that the modelled gravity responses for a southward-extending granite body (1) and northward-dipping granite (2) are very similar in shape, but show small differences in amplitude. This geometry may not easily be resolved in gravity field data.

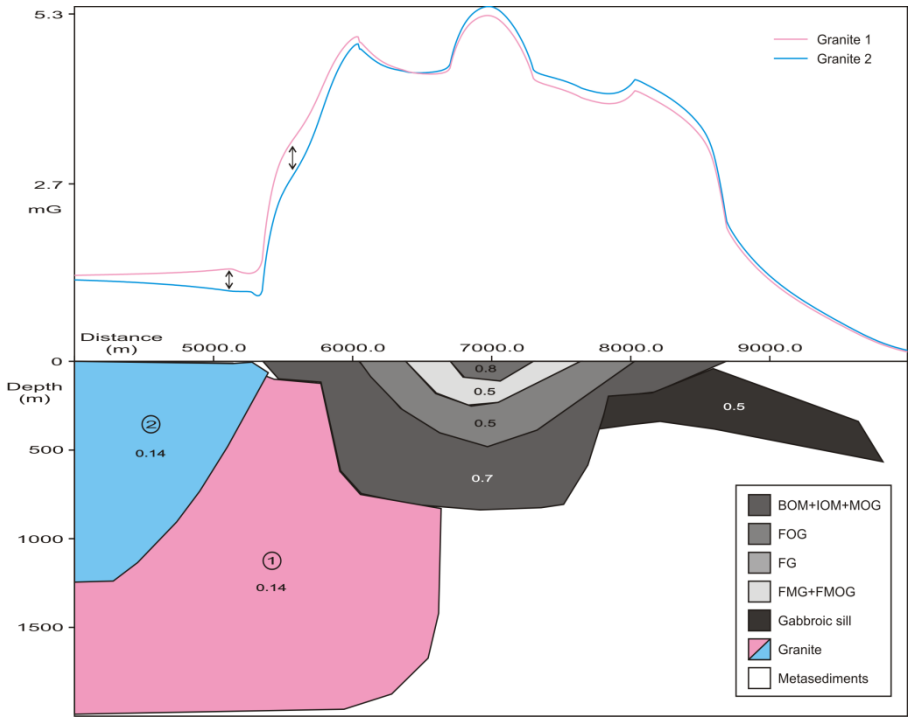


Figure 8.9: Modelled gravity response for a section of profile MP1, considering two different configurations for the Doros granitoid pluton. Granite 1 is the southward-extending granite of magnetic Model 25 above, and granite 2 the northward-dipping granite of Model 30 (Fig. 8.8). The difference in extent produces small changes in the amplitude of the modelled response, as indicated.

8.9 Implications of the study

The aeromagnetic image analysis and forward modelling show that the Doros Complex is a relatively shallow, layered, lopolithic body, consistent with the predicted geological model. However, the modelling also reveals the presence of a sill-like body, likely equivalent in mineralogy to the sampled chilled gabbroic sill, below the level of the BOM in the southern and eastern parts of the complex. Hence, an updated cross-section can be constructed as in Figure 8.10 below. The true thickness of the intrusion is

likely to be at least 500 m, but no more than 2 500 m – greater than originally anticipated from the exposed succession.

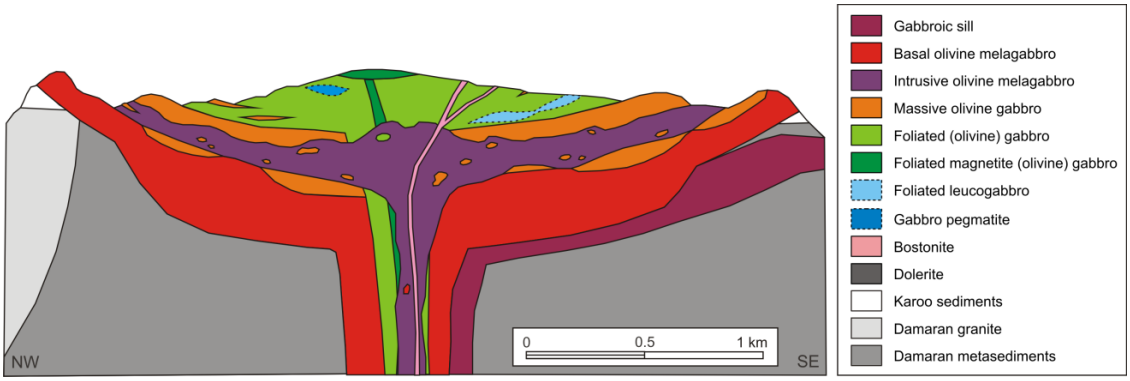


Figure 8.10: A revised schematic cross-section (roughly 1:1) through the widest part of the Doros intrusion (close to profile MP1), incorporating the findings of the aeromagnetic survey – specifically the presence of an additional gabbro layer below the level of the BOM in the south of the complex and a northward dip for the Damaran granite contact.

The intrusion has a strong component of remanent magnetisation that varies in intensity and inclination with stratigraphic height. Specifically, three distinct polarities of remanence are required: normal polarity (relative to the present-day field) for the chilled gabbroic sill unit, reversed polarity for the succession from the BOM to FOG, and normal polarity for the upper succession from the FG to FMOG. This implies a minimum of two episodes of mafic magma emplacement, separated by a magnetic reversal, if the units with normal polarity were emplaced at different stratigraphic levels at the same time. This is in line with the complex emplacement history suggested by petrographic and compositional trends in Chapters 4 and 5. A detailed palaeomagnetic study may be able to relate these reversals to the magnetic stratigraphy of the Etendeka volcanic succession (e.g. Renne *et al*., 1996), and thereby distinguish the number of episodes of emplacement and constrain these in time.

Most of the Doros intrusion is strongly reversely remanently magnetised, in contrast to the Messum, Cape Cross and Brandberg Complexes (Section 8.2). The emplacement of the Doros gabbros may therefore correspond to a different time period in the history of the Etendeka LIP. The presence of any deeper level intrusions or staging chambers below the Doros Complex cannot be assessed with the aeromagnetic data alone, but these previous studies of other Damaraland intrusions indicate that this may be resolved with the addition of a gravity (or seismic) study.

The image analysis also provides a refinement of the mapped surface geology, particularly with regard to the domain of the poorly-exposed magnetite-bearing gabbros and the overall lateral extent of the intrusion. Several unmapped dolerite dykes are also delineated outside the complex. A revised geological map incorporating the geophysical results is shown in Figure 8.11.

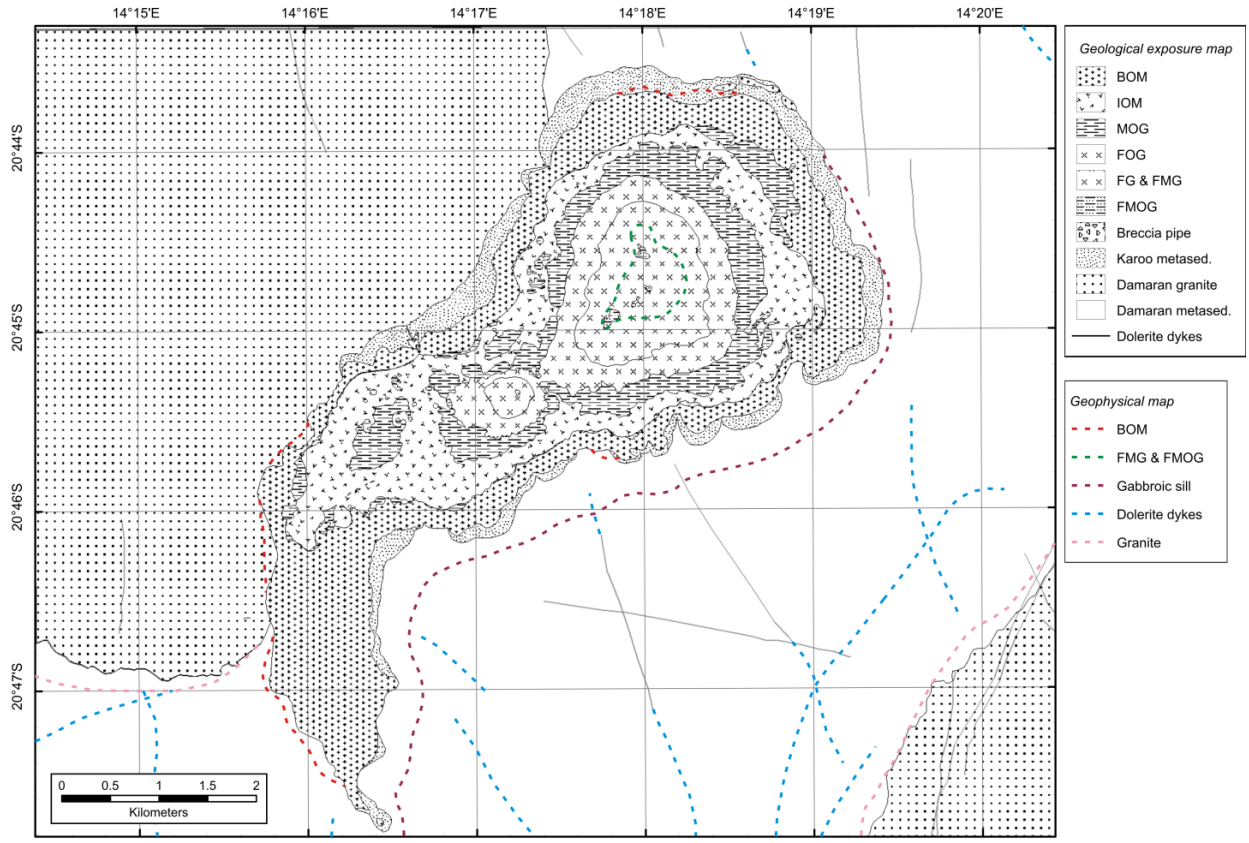


Figure 8.11: Map of the Doros intrusion showing the extents inferred from geophysics (not surface exposures) of the BOM outer contact, the chilled gabbroic sill, the magnetite-bearing gabbros, dolerite dykes outside the complex and the granite plutons.

8.10 Summary of findings

The aeromagnetic data analysis has allowed further constraints to be placed on the sub-surface geometry of the Doros mafic intrusion. The results of the study indicate that the shape of the body is consistent with a shallow-level, layered, lopolithic intrusion as predicted by the surface geology. However, it reveals that a component of the intrusion exists below the present level of exposure, at least in the southern and eastern parts of the complex, which is roughly equivalent in magnetic properties, and therefore likely in mineralogy, to the sampled chilled gabbroic sill. The data further indicate that there are at least two, and potentially three, discrete episodes of magma emplacement in the complex, separated by magnetic reversals. Future research is directed to a gravity and/or seismic study, to better resolve the nature of the Doros-granite contact and assess possible deeper level features.

Chapter 9: Emplacement Dynamics and Evolution of the Suite

9.1 Introduction

The previous chapters have shown that the Doros Complex is a shallow lopolith, consisting of a series of roughly concordant, sill-like gabbro layers dipping gently in towards the centre of the intrusion. As has been discussed, the petrography and chemistry of the gabbros is consistent with the differentiation of a basaltic parental magma, but suggests complexities in the nature of the magma emplacement and crystallisation processes. These are examined in more detail in this chapter.

9.2 Mode of emplacement

The sharp contact between the Doros intrusion and the host rock and the lack of significant assimilation and deformation of the host suggest emplacement along a pre-existing fracture. Given the position of the Doros intrusion, Hodgson & Botha (1974) proposed that it was the Damaran (Neoproterozoic) granite-metasediment contact that likely facilitated the passage of the ascending magma. However, the geophysical modelling in Chapter 8 has indicated that this contact may not extend under the Doros intrusion. Alternatively, pre-existing regional fold or foliation structures within the Damaran metasediments, with which the axis of the intrusion is observed to correspond (Hodgson & Botha, 1974), may have facilitated magma intrusion. Several of the other early Cretaceous Damaraland Complexes (e.g. Otjohorongo, Okenyenya, Erongo) are associated with structural lineaments and faults in the Damara Belt (Miller, 2008b). The relatively symmetrical nature of the intrusion, on surface and inferred at depth, points to a fissure-like feeder conduit axial to the complex, as depicted in the cross-section in Figure 3.3. The basal contact of the Palaeozoic Karoo metasedimentary rocks, or bedding planes within this unit, may have enabled the magma to spread laterally away from the feeder zone. This is supported by the near-concordant relationship of the basal gabbro with the Karoo strata in the “tail” of the complex (Hodgson & Botha, 1974). The new volume of material was likely accommodated by dilation of the host fractures and upward doming of the overlying sedimentary strata (since removed by erosion).

The overall saucer-like shape of the intrusion and gentle inward dip of the layers is typical of mafic layered intrusions (Petraske *et al*., 1978). This may be a primary feature of emplacement – several studies have shown that shallow-level, sill-like intrusions fundamentally show sub-horizontal centres and inclined rims (e.g. Malthe-Sørenssen *et al*., 2004; Galland *et al*., 2009). Alternatively, it may be a result of post-emplacement sag due to crustal flexure, on cooling, in response to the weight of the relatively more dense mafic magma (Petraske *et al.*, 1978; Watts, 2007). A detailed palaeomagnetic study may be able to resolve the relative timing of emplacement and sag, as has been done for the Bushveld Complex (Letts *et al.*, 2009).

9.3 Conditions of emplacement

The conditions of emplacement, i.e. the temperature of the Doros magma and depth at which it intruded, have important implications for the crystallisation process.

In several other layered intrusions, e.g. Kiglapait (Berg & Docka, 1983) and Rum (Holness & Isherwood, 2003), an estimate of the temperature and pressure of the incoming magma has been obtained from the nature of the contact metamorphism of the host rocks. However, the heavy alteration and absence of index minerals in the Doros contact metamorphic aureole disallows thermobarometric calculations of the conditions of emplacement by this means.

Alternatively, this information may be obtained from geothermobarometric calculations for the gabbros themselves. While ilmenite-titanomagnetite pairs have provided some information on oxide equilibration temperatures and fugacities (Chapter 4), these clearly do not reflect the primary crystallisation conditions of the magma. The Doros rocks lack the appropriate co-existing minerals for the standard geothermometers to be applied, e.g. the olivine-glass, two pyroxene or plagioclase-amphibole thermometers. Instead, the olivine-augite Mg-Fe exchange thermometer of Loucks (1996) is employed. Calculations using the most primitive olivine and clinopyroxene analyses in each sample (screened for low totals or non-stoichiometry), produce crystallisation temperatures of 915 to 1064 ± 6.1 °C (Table 9.1). The reliability of these values may be questionable, since the calculation assumes equilibrium between olivine and clinopyroxene crystals, which has not been demonstrated convincingly. However, although these temperatures are at the low end of the range expected for olivine-clinopyroxene co-crystallisation, they are not unreasonable. These results are used in conjunction with the clinopyroxene barometer of Nimis & Ulmer (1998), with the CpxBar program, to derive an estimate of the pressure on emplacement (Table 9.1). This yields values of between 0.69 and 7.93 ± 2.6 kbar (~2 - 26 km depth) using the barometer for hydrous basic magmas (BH), or between 2.19 and 7.93 ± 2.0 kbar (~7 - 26 km) for mildly alkaline magmas (MA). The Doros suite straddles these compositional boundaries (Fig. 5.1). The range of pressures is large and the errors are significant, and it must be noted that these are very sensitive to the input temperature, but this does suggest some possible constraints on depth. Interestingly, the MOG and FOG display the lowest calculated temperatures but highest pressures of crystallisation.

Alternatively, olivine-liquid thermometry may be peformed on the olivine-hosted melt inclusions in the Doros melagabbros described in Chapter 7, according to the methods of Putirka (2008). This yields temperatures between 1100 and 1398 °C (Table F.3), depending on the method of calculation, for the time of inclusion trapping. While the melt inclusion compositions may not accurately represent the bulk Doros magma (see discussion in Chapter 7), these results indicate that higher temperatures may be warranted for the onset of crystallisation of olivine. However, input into the clinopyroxene barometer of Nimis & Ulmer (1998) does not yield useable pressure values, likely because co-existing clinopyroxene compositions are not well constrained.

Table 9.1: Results of olivine-clinopyroxene geothermobarometry for the Doros gabbros

Sample	TOD21	TOD39	TOD40	TOD45	TOD47	TOD53
Unit	IOM	BOM	BOM	MOG	FOG	FMOG
Ol-cpx geothermometry from Loucks (1996)						
$K_{D\,Fe/Mg}^{Ol/Aug}$	2.17	2.15	1.90	3.46	3.60	2.33
T (°C)	1033	1035	1064	924	915	1016
Cpx geobarometry from CpxBar (Nimis & Ulmer, 1998)						
P(BH) (kbar)	2.28	2.03	1.92	7.93	7.43	0.69
P(MA) (kbar)	2.76	2.19	2.56	7.93	7.41	2.34

An alternative indication of the depth of emplacement may be gleaned from field evidence, from the presence of the zone of brecciated rock on the northern margin of Doros intrusion (described in Chapter 3). This feature is interpreted as a phreatomagmatic breccia pipe, formed when the intruding magma superheated the meteoric water in the sediments with which it came into contact, resulting in an explosive vent (Tămaș & Milési, 2002; Lorenz, 2003). The fragments of exploded rock from the layers above then collapsed back down into the vent (Lorenz, 2003). This interpretation is based on the steep sides of the pipe, the matrix-supported nature and sub-rounded clasts of the breccia, and the incorporation of sedimentary material (Tămaș & Milési, 2002).

In this case, it is likely that the Doros magma came into contact with fluid-rich Karoo metasedimentary rocks. Karoo sandstones form a significant proportion of the breccia matrix and clast material (Section 3.3.4). However, since there are fragments of Doros gabbro within the breccia, it was not the intrusion of the first gabbroic magmas that caused the phreatomagmatic explosion. The foliated gabbro, at least, was already present and fully-crystallised at this time. However there is a late phase of magmatism in the Doros intrusion, represented by the bostonite dykes. It is clear from their chilled margins that these formed quite some time after the main phase of gabbro emplacement. Indeed, one such dyke is documented cross-cutting the basal melagabbro not far from the location of the breccia pipe (Fig. A.1). It is therefore proposed that it was the late-stage intrusion of bostonitic magma, likely fluid-rich itself, that triggered the phreatomagmatic explosion.

Phreatomagmatic breccia pipes generally form at shallow levels, between 1 and 2.5 km depth (Tămaș & Milési, 2002), so this is evidence in itself. However, the clasts within the breccia provide further constraints on the minimum depth below surface of the intruding magma at this time. Two quartz latite fragments from the breccia have been analysed in this study (Table A.6) and have compositions similar to the Springbok or Goboboseb silicic magma types of the Etendeka succession (Fig. 9.1). These lavas have been shown to be derived from the Messum Complex (Milner & Ewart, 1989), approximately 70 km south of Doros, and currently the only other candidate for correlation between the Etendeka succession and Damaraland Complexes. This implies that these lavas existed at surface, above the Doros intrusion, at the time of the formation of the breccia pipe. Outcrop of the breccia pipe presently sits at an elevation of between 600 and 680 m. If the present stratigraphic levels of the quartz latites in the Huab region (Miller,

2008c) may be extrapolated, this implies that the intrusion that caused the breccia must have been a minimum of 260 m below surface, taking the Goboboseb unit (or 470 m for Springbok). The actual depth is likely to have been greater than this, since the initial level of intrusion of the bostonite magma may be below present exposure and there may have been overlying strata that have not been identified as fragments in the breccia. However, this is consistent with a shallow-level intrusion, potentially a subvolcanic chamber.

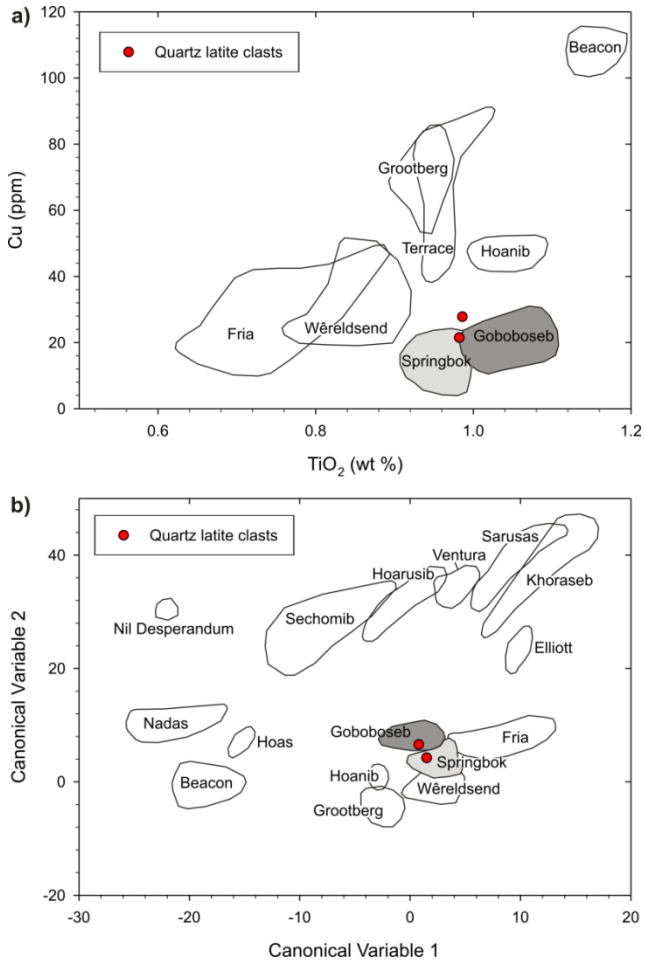


Figure 9.1: Compositions of quartz latite clasts in the Doros breccia pipe relative to the main silicic magma types of the Etendeka succession (Milner & Duncan, 1987; Marsh *et al.*, 2001; Ewart *et al.*, 1998b, 2004b). a) Cu against TiO_2. b) The canonical variables from the discriminant function analysis of Milner & Duncan (1987), a standard means of geochemical classification for the Etendeka quartz latites. CV 1 = $-27.952*TiO_2 + 0.41343*Al_2O_3 + 1.0670*Fe_2O_3 - 14.870*P_2O_5 + 0.00458*Ba + 0.05536*Zr - 0.08252*Cu + 3.3561$; CV 2 = $-2.3059*TiO_2 - 0.35222*Al_2O_3 + 3.1557*Fe_2O_3 - 46.007*P_2O_5 + 0.00435*Ba + 0.12755*Zr - 0.02577*Cu - 36.302$.

9.4 Origin of the Doros layering: Multiple mingling magma mushes

As discussed in Chapter 1, understanding the origin of the layering in a mafic intrusion is essential for deciphering the petrogenesis of the intrusion as a whole. I have previously outlined why this aspect of study is so controversial, and introduced the debates between single-pulse and multiple-pulse emplacement, and liquids versus crystal mushes. I now consider the Doros intrusion in this light.

Based on the combined field, petrographic, geochemical and geophysical characteristics documented in the previous chapters, I argue that the Doros intrusion, and the layering within it, is not consistent with the post-emplacement differentiation of a single batch of crystal-free melt. Instead, I propose that:

1) The Doros intrusion formed by multiple, successive, sill-like intrusions of magma over a short interval of time; and
2) The majority of these magmas were already carrying a crystal load at the time of emplacement, i.e. these were magma mushes in the general sense.

Evidence for this argument is presented as follows:

9.4.1 Intrusive internal layer contacts

Several units in the complex show intrusive contacts and are therefore indisputably new inputs of magma. The nature of some of these contacts further suggests that the intruding magmas were crystal-bearing. Specifically:

1) The IOM unit is clearly a later intrusion into the complex, shown by cross-cutting relations with the BOM and MOG, the sharply-defined interfingering upper contact and incorporated xenoliths of the pre-existing layers (Fig. 3.8b, d). The interfingering contact between the IOM and MOG units suggests that these magmas interacted in a plastic manner, but maintained their distinct characteristics, i.e. they were mingling but not mixing *per se*. It is proposed that at this time the intruding IOM magma was transporting a substantial crystal load, such that the cumulate framework of the mush remained intact and there was only minor mixing of interstitial liquids. A similar scenario is described by Gibb & Henderson (2006) in the Shiant Isles Main Sill, considered by many as a classic example of a mafic intrusion built from multiple magma mush emplacements.

2) The BOM-MOG interface is also marked by patchy intermingling (Fig. 3.7a), suggesting incomplete mixing of an incoming, more leucocratic magma with the pre-existing, semi-crystalline BOM. There are xenoliths of olivine-rich material within the basal MOG (Fig. 3.7b) that were entrained during emplacement, either from the BOM, or more likely given their fine grain-size and extremely olivine-rich nature, from the magma conduit or the margins of the cumulate pile in a lower chamber. The greater extent of mixing here, in contrast with at the margins of the IOM as described above, is suggested to be due to a much shorter time interval between emplacements and possibly a predominantly liquid MOG.

3) The MOG-FOG contact is a wide transition zone of interlayered units, suggesting mingling of contrasting magmas. There are also xenoliths of MOG within the FOG unit (Fig. 3.9.b), indicating that the FOG was a new, later input of magma, that entrained semi-solid fragments of the MOG.

In each case, the nature of the intermingling, the lack of any evidence for solid-state deformation and the absence of interlayer chill margins suggests that successive emplacement of magmas was within a short time period – each new magma was emplaced before the pre-existing magma had completely solidified.

The bostonite dykes are also intrusive into the BOM and MOG units and therefore represent a later influx of magma. However, their sharp contacts and fine-grained margins that include skeletal magnetite (Fig. 3.16b) indicate rapid cooling against a host rock which was almost, if not completely, solidified and therefore emplacement was after a much longer time interval. This apparent time gap between the emplacement of the main Doros gabbroic phase and the bostonite magma is not unusual. In fact, late alkaline magmatism is fairly common in the Damaraland Intrusive Complexes (Miller, 2008b). For example, nepheline syenites in the Messum Complex have been shown to have been emplaced as much as 5 m.y. after the earliest gabbroic phase (Milner *et al*., 1995; Renne *et al*., 1996).

9.4.2 Phenocrysts in the chill margin

The presence of plagioclase, clinopyroxene and olivine phenocrysts within the glass of the chill margin is indisputable evidence that the chilled gabbroic sill and basal olivine melagabbro magmas were carrying crystals on emplacement. These crystals are euhedral and not skeletal, and disparate in grain size to the glassy matrix. They clearly did not form as a result of the rapid cooling of the melt at the boundary, but rather as phenocrysts carried up by the melt from a lower, fractionating magma chamber and trapped in the margin on quenching. Similar evidence for mush intrusion has been documented for the Shiant Isles Main Sill (Gibb & Henderson, 1992).

The phenocryst content of the chill margin might be expected to quantitatively represent the average phenocryst assemblage of the magma on emplacement. However, it is noted that the chill margin to the BOM contains relatively few olivine phenocrysts, in contrast with the clearly olivine-dominated load of the body of the unit. It is suggested that this material represents relatively phenocryst-poor intercumulus liquid from the basal olivine melagabbro mush, accumulated at the boundary by marginal shear during emplacement, while phenocrysts were concentrated towards the centre of the mush layer (Ross, 1986; Gibb & Henderson, 2006). With a sufficient contrast in temperature between the magma and host rocks, quenching can take place at the margins before phenocrysts begin to settle (Gibb & Henderson, 1992). Alternatively, this distribution of phenocrysts may result from an increase in flow rate, and therefore carrying capacity, during emplacement, caused by a progressive widening of the feeder conduit (Gibb & Henderson, 2006). Hence the proportion of phenocrysts documented in the chill margin (~20% for both the BOM and gabbroic sill) is only a minimum estimate for the original crystal load of these magmas.

9.4.3 Crystal size distributions

Evidence for phenocrysts carried by the original magma is further given by the presence of two or more populations of crystals of the same mineral, but of different sizes, documented in some layers.

In the foliated magnetite gabbro there is a population of anomalously large, euhedral plagioclase crystals (Fig. 4.9d) as well as large coin-shaped magnetite crystals (Fig. 3.11b), while in the intrusive olivine melagabbro there is a population of large euhedral olivine crystals (Fig. 4.4). The relative proportions of these 'primocrysts' are difficult to quantify, due to the paucity of material and the gradational range in crystal sizes, but are estimated at between 5 and 30% in these units. This may be more accurately assessed with a quantitative textural analysis study (as in Marsh, 1998; Jerram *et al*., 2010). A similar occurrence of primocrysts has been recorded as evidence of mush intrusion in the Ferrar Dolerite Sills (Bédard *et al*., 2007). These authors discuss the difficulties of relating primocryst proportions to the original crystal load of the magma mush. The contrast in grain size between the primocrysts and the host rock suggests that these crystals were formed earlier, under different conditions, and became entrained in the rising magma.

9.4.4 Plagioclase schlieren

The schlieren and linear concentrations of plagioclase documented in the basal olivine melagabbro (Figs. 3.6a, 9.2 below) and intrusive olivine melagabbro (Fig. 3.8a) suggest that these were crystal-laden magmas at the time of emplacement.

The schlieren are interpreted to represent localised concentrations of fine-grained plagioclase crystals and plagioclase-enriched intercumulus melt, accumulated in low-pressure dilation zones within the olivine-dominated cumulate pile, formed by flow shear (Petford, 2009). A similar origin has been proposed for comparable anorthositic schlieren in the Ferrar Dolerites (Marsh, 2004, 2006; Bédard *et al.*, 2007). The plagioclase in these enclaves is of identical composition to that in the surrounding melagabbro (Section 4.2.2). The already-formed cumulus olivine was simply transported by the flow, and therefore is a consistent size throughout the unit. However, the intercumulus melt that was concentrated in the dilational pockets crystallised under lower pressure conditions, producing the large, euhedral pyroxene grains within the schlieren (Fig. 3.6b). Since major lateral flow of the magma mainly occurred during emplacement, olivine crystals were already present at this time. The proportion of phenocrysts must have been less than 55% for flow to have occured (Marsh, 2013). The abundance of schlieren in the centre of the layer is consistent with the strongest flow occurring in this zone.



Figure 9.2: Plagioclase schlieren in a boulder of basal olivine melagabbro, interpreted as an olivine mush.

9.4.5 Magmatic foliation of the upper units

The variable, but omnipresent, layer-parallel magmatic foliation (alignment of cumulus plagioclase, and/or olivine) described in the Upper Foliated Series was most likely produced during the emplacement and lateral spreading of an already crystal-bearing magma.

In general, this type of preferred orientation of elongate minerals may be produced by compaction, alignment during gravitational settling of phenocrysts or crystallising phases, or during flow of a phenocryst-bearing magma (Nicolas, 1992; Boudreau & McBirney, 1997; McBirney & Nicolas, 1997). Post-emplacement compaction was not a significant contributor here, as there is no evidence of compaction deformation in the minerals (as described by McBirney & Nicolas, 1997). Similarly, sub-solidus plastic deformation cannot apply (Nicolas, 1992). These processes would also have suppressed the localised distortions in the foliation documented near the lower contact of the FOG. A key piece of evidence is the stark contrast in texture between the MOG and overlying FOG-FG. These rock types have essentially identical bulk compositions and the same cumulus phases (plagioclase with minor olivine), yet the former is completely unfoliated. The processes of compaction and gravitational settling of the cumulus minerals crystallising post-emplacement should have affected these rock types in the same manner.

The proposed solution to the problem is that the MOG formed from a largely crystal-free magma, containing only a few rounded olivine phenocrysts. Cumulus plagioclase formed from *in situ* fractional crystallisation and the resulting rock is thus relatively homogeneous. The foliated gabbros, on the other hand, originated from a new injection of magma that contained significant platy plagioclase phenocrysts and minor elongate olivine phenocrysts on emplacement. These were aligned by flow in the laterally-spreading magma, as well as by subsequent settling. The relatively dense olivine crystals tended to

accumulate near the bottom of the layer, forming the FOG, while the plagioclase crystals, having less of a density contrast with the magma, adopted their most natural, bottom-parallel positions, while remaining relatively evenly dispersed in suspension. Crystallisation of the intercumulus melt preserved these orientations.

The presence of irregular, more linear alignments of plagioclase and olivine at the bottom contact of the FOG is further testament to the phenocryst-bearing nature of this magma. These features suggest shearing and eddied magmatic flow within the crystal mush against a more solid floor and around entrained solid fragments, during the lateral emplacement of the sill. Similar features have been documented in the Ferrar Dolerites, and this process has also been numerically modelled (Petford & Marsh, 2008). For the cumulus minerals to have been affected by these flow patterns, they must have been already present in the magma on emplacement. This pattern of dominantly 'non-dynamic' planar foliation in the interior of the body and 'dynamic' flow-related linear foliation near the margins has also been observed in the Skaergaard Intrusion (McBirney & Nicolas, 1997).

A comparable foliation is not seen in the basal olivine melagabbro unit, although it is interpreted to have formed in a similar manner of flow and crystal settling of olivine phenocrysts (Section 9.4.4). This is because all the olivine below the FOG is characteristically equant and not prismatic (Chapter 4). This change in habit of olivine crystals through the intrusion is further evidence of input of a new phenocryst population at the level of the FOG.

Although compaction was not the primary cause of the planar foliation in the gabbros, it likely contributed to some extent, along with slumping and disturbances caused by new magma influxes, to the mobilisation of plagioclase-rich intercumulus melt and relatively buoyant small-volume plagioclase mushes (Philpotts & Carroll, 1996; Bédard *et al*., 2007). These were liberated from the cumulate mush pile and rose upwards in channels to form the foliated leucogabbro and plagioclase enclaves in the core of the complex (e.g. Figs. 3.12b, d). Localised distorted foliations associated with leucocratic veins, as in Figure 3.12d, are evidence of their passage. Alignment of the plagioclase within the enclaves indicates that at least a portion of this material was crystalline at the time of flow. A similar process has been documented in the Ferrar Dolerite Sills (Bédard *et al*., 2007).

Pockets of volatile-rich intercumulus melt that were not liberated, but that remained trapped in the mush pile, likely formed the gabbro pegmatite enclaves and lenses (Fig. 3.14). Pegmatitic bodies are a common feature of mafic intrusions, and a similar origin has been ascribed to these elsewhere (e.g. Skaergaard Intrusion, Larsen & Brooks, 1994; Graveyard Point Intrusion, White, 2007; Smartville Intrusive Complex, Beard & Day, 1986; Ferrar Sills, Wilhelm & Wörner, 1996; Karoo dolerites, Mitchell *et al*., 1997). The mineral compositions in the Doros pegmatites are similar to those in the host foliated gabbro (Chapter 4). The mineral textures and absence of a foliation in the pegmatite bodies are consistent with *in situ* inward crystallisation of a phenocryst-free melt. By this process, progressive crystallisation from the margins of a magma body inwards forms an increasingly thick, solid outer layer and leads to slower

cooling rates, excluding a last phase of hot, trace element-enriched liquid in the centre that takes a long time to crystallise (Marsh, 2006). The presence of fluids causes localised increased diffusion rates (Puffer & Horter, 1993). Mafic pegmatites elsewhere have also been reported to grade to cores of more felsic material (Larsen & Brooks, 1994), like the Doros pegmatites. The bostonitic enclaves documented here (e.g. Fig. 3.15) are interpreted as the products of extreme fractionation of the trapped volatile-rich intercumulus melt – essentially mesostasis – as the fractionation modelling suggests (Fig. 5.16). The hydrous alteration assemblage (Section 4.5) supports the presence of a fluid phase.

9.4.6 Cumulus crystal enclaves

The magnetite, olivine and clinopyroxene cumulate enclaves described in the intrusion clearly represent small-volume magma mushes. Such enclaves commonly form in the infilling zone, where incoming magma mushes drop their phenocryst load due to the sudden decrease in velocity when the magma starts to spread laterally (Marsh, 2006). The enclaves all occur within the core of the Doros intrusion, thus were likely located over the inferred axial feeder zone. This shows, firstly, that new material was being injected into the pre-existing upper foliated gabbro sequence and secondly, that these injections were laden with crystals. The proportion of crystals in these mushes cannot be assessed, since the original volume of each magma influx is unknown.

9.4.7 Modal and grain-size layering

The small-scale modal and grain-size layering documented within the Upper Foliated Series (Figs. 3.9c, 3.12c, 9.3 below) is evidence of the continuous influx and mingling of magma mushes in this disturbed central zone. Such alternating successions of finer-grained and coarser-grained (and typically foliated) gabbro, or different types of gabbro, cannot have been produced by progressive crystallisation of a single liquid (Zieg & Marsh, 2012). Each new magma was emplaced while the host was still only partially crystallised. Figure 9.3 shows that some crystal settling occurred post-emplacement, during solidification, but the layering itself cannot have formed entirely as a result of crystal settling, since it truncates existing rock textures.



Figure 9.3: Modal layering with a gradational upward decrease in olivine content in a boulder in the core of the head of the complex.

9.4.8 Internal chill margins

While the major units in the Doros intrusion do not show chilled internal contacts, due to closely-spaced successive emplacements, some of the small-volume enclaves in the core of the complex do show glassy material at their margins (e.g. Fig. 9.4). This likely formed when a new influx of magma chilled against the pre-existing, already cooled host. Chill margins to the bostonite dykes, indicating later emplacement, have also been described (Section 3.3.4). This is further evidence for multiple pulses of magma.

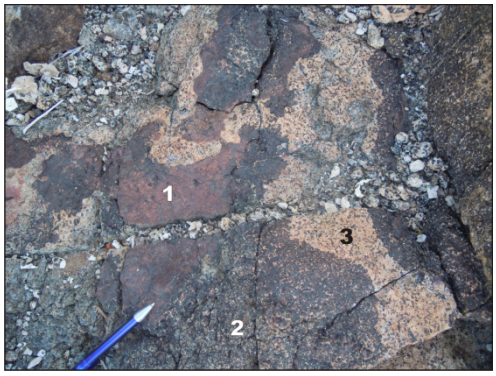


Figure 9.4: Fine-grained, red, chilled material (1) marginal to a pyroxene-rich coarse-grained gabbro (2), mingling with leucocratic gabbro (3) in the core of the head of the complex.

9.4.9 Resorbed phenocrysts

Olivine crystals in the MOG unit show resorption textures (Fig. 4.6a), which are indicative of disequilibrium conditions. These are interpreted as sparse olivine phenocrysts carried in a more evolved, leucocratic magma, with which they partially reacted. Variable modal abundances indicate that some redistribution of the olivine has occurred due to settling, but the original proportions of olivine phenocrysts were likely between 5 and 10%.

9.4.10 Crystal accumulation at contacts

Some of the small gabbro layers in the MOG-FOG transition zone show concentrations of cumulus crystals at their basal and lateral contacts (Fig. 9.5). There is no plausible reason documented in the literature for these crystals to preferentially nucleate in an undulose, centimetre-scale zone at the margins of a progressively crystallising liquid magma. Alternatively, it is proposed that these layers formed from new injections of crystal-bearing magma, and the phenocrysts were either trapped by faster cooling at the layer margins, or deposited from suspension during lateral flow.



Figure 9.5: An intruding coarse-grained gabbro layer showing accumulations of cumulus clinopyroxene crystals against the basal contact with homogeneous massive olivine gabbro.

9.4.11 Sharp compositional contacts and reversals in chemical trends

I have described several abrupt changes in mineralogy and whole-rock major and trace element compositions through the stratigraphy, which do not correspond with a simple one-stage liquid line of descent (see Sections 4.4 and 5.6). This is contrary to what was predicted by Latypov (2009) for the progressive crystallisation of a single magma batch. Rather than a gradual, progressive change in these parameters from base to top of the intrusion, the chemical compositions reveal a series of punctuated trends of fractional crystallisation. These are summarised in stratigraphic (not necessarily chronological) order as follows (also see Fig. 9.6):

1) Relatively evolved compositions in the chilled sill;
2) A return to primitive compositions and a trend of olivine accumulation and progressive upward differentiation within the BOM unit;
3) A continuation of the BOM trend, accompanied by plagioclase accumulation, within the MOG (as preserved in xenoliths within the IOM);
4) A return to primitive compositions and an almost identical trend of differentiation to (2) within the IOM unit;
5) An abrupt return to more primitive compositions in the FOG, followed by a trend of progressive upward differentiation and plagioclase accumulation through the FG and locally in the FL;
6) A return to more primitive compositions and a reversed trend towards more magnesian compositions in the FMG and FMOG;
7) A continuation of (1), trending towards evolved compositions in the bostonite.

The reversals in the differentiation trend at the level of the BOM, IOM, FOG and FMOG can only have been achieved by a new injection of more primitive magma at each of these points. The intrusion is therefore built from a minimum of five discrete pulses of magma. However, there may be more injections that do not have sufficient compositional contrast with the pre-existing magma to be identified chemically.

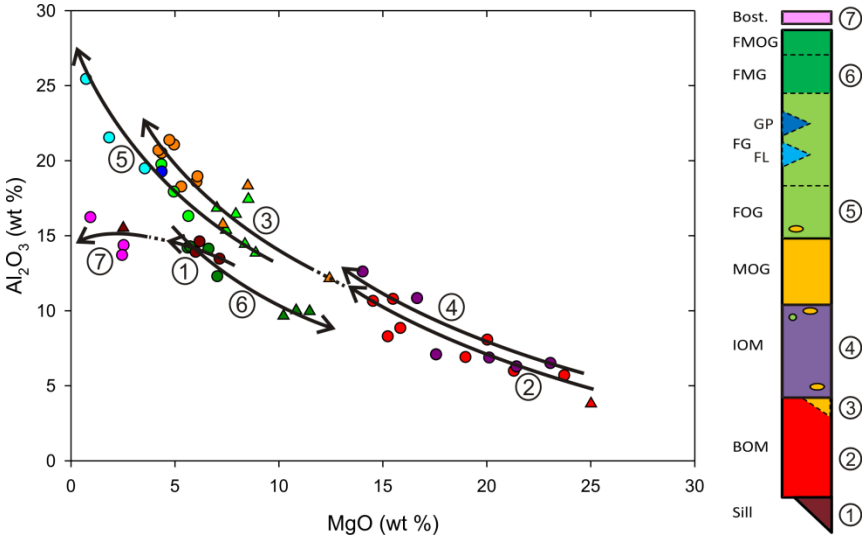


Figure 9.6: Whole-rock Al_2O_3 vs. MgO compositions for the Doros suite (this study; Hodgson & Botha, 1974; Marsh & Duncan, 2008) with numbered arrows showing the major trends in fractionation in stratigraphic order (see text for explanation).

While the abrupt change in whole-rock compositions at the level of the FMG (e.g. Figs. 4.18, 5.5), associated with the first appearance of cumulus magnetite, may be consistent with the expected liquid line of descent, the reappearance of cumulus magnesian olivine in the FMOG can only be explained by a new input of more primitive magma. However, although not well-exposed, the contacts between these units appear to be gradational (Section 3.3.3), and the chemical trends are a progression (Figs. 4.18, 5.5). Therefore, it is proposed that there was an intrusion of a magnetite- and olivine-bearing mush into the semi-crystallised foliated gabbro, followed by density settling and segregation into a magnetite-dominated basal section and a more olivine-rich layer above. It is possible that the descending magnetite phenocrysts penetrated the underlying semi-crystalline FG (no contact is observed). The largest magnetite grains settled to the deepest levels, producing the lowermost gabbro pockmarked with coin-shaped porphyritic magnetite (Fig. 3.11b). Thus mixing has obscured the precise level of emplacement of this new magma mush.

9.4.12 Reversals in mineral chemical trends

There is not a sufficient density of mineral compositional data for the Doros intrusion to comprehensively test for the second criteria for single-pulse liquid magma emplacement of Latypov (2009), i.e. progressive trends in solid solution minerals from high- to low-temperature compositions without reversals or breaks. However, where there are multiple analyses for a layer, i.e. in the BOM and IOM, the olivine compositions appear to show a reversed trend towards more magnesian compositions (Fig. 4.19b) – the opposite of what would be expected with progressive fractionation.

The reversal in Fe-Ti oxide trace element chemistry (Ni, V; Fig. 4.23d) documented at the level of the FOG is strong evidence for a new input of more primitive magma at this point. However, while increased ilmenite Mg contents (Fig. 4.24), plagioclase Fe-contents (Fig. 4.20) and the characteristically V-rich

nature (Fig. 4.23) of titanomagnetites in the FMG and FMOG may similarly be consistent with whole-rock and mineralogical evidence for input of a compositionally different magma at this level, this may also be a consequence of the shift from intercumulus to cumulus magnetite in the system.

9.4.13 Overlapping incompatible trace element compositions

The incompatible trace element (ITE) compositions of all the major units in the main body of the intrusion (apart from the MOG) are very similar (Figs. 5.10, 9.7), i.e. there is no trend of progressive incompatible element enrichment with stratigraphic height, as would be expected with a single fractionating body of liquid magma (Latypov, 2009). I argue that this is because each unit is a mush of cumulus crystals and trapped intercumulus melt. The large An range in normally-zoned intercumulus feldspar documented in the melagabbros and magnetite gabbros, down to An <30, supports this interpretation. The MOG shows similar REE patterns, but slightly more variation in the levels of enrichment, consistent with its inferred origins from a relatively crystal-poor melt.

The relative proportions of crystals and melt are difficult to assess from the ITE chemistry since the majority of the Doros mushes have olivine as a significant phenocryst phase, and the low partition coefficients of the these elements in olivine make the contribution of this mineral to whole-rock compositions difficult to recognise.

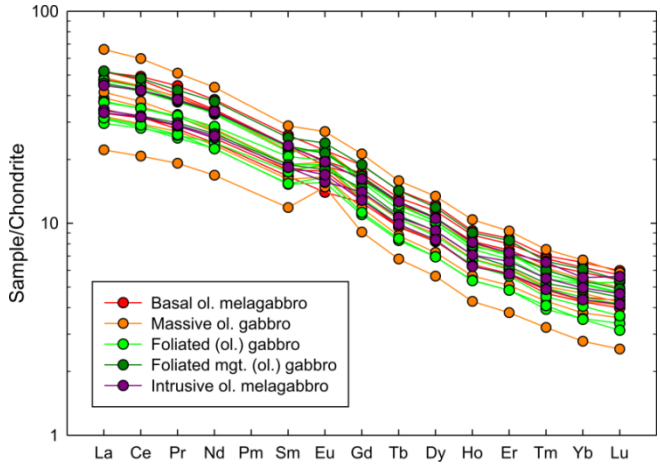


Figure 9.7: REE abundances for the major units of the Doros intrusion, normalised to CI chondrite of Anders & Grevesse (1989). These units are interpreted as separate inputs of magma mush.

9.4.14 Magnetic reversals

The magnetic forward modelling in Chapter 8 shows that there are three different polarities of remanent magnetisation in the Doros stratigraphic section, corresponding to the chilled gabbroic sill, the succession from the BOM to FOG, and the succession from the FG to FMOG (Fig. 9.8). This indicates that a geomagnetic reversal occurred in the interval between successive emplacements of magma. This implies that there was a minimum of two discrete influxes of magma in the complex, if the gabbroic sill and upper foliated succession are considered to have been magmas emplaced at different stratigraphic levels

at the same time, but potentially three influxes, if these units are distinct in time. Furthermore, the variable inclinations and declinations of the remanence within these stratigraphic sections, shown by the modelling, suggest additional episodes of magma emplacement that record the changing properties of the geomagnetic field without reversals, and that as such are more difficult to distinguish.

While there is mineralogical and compositional evidence for a new influx of magma at the level of the FMG/FMOG (Section 9.4.11), evidence for a new input of magma at the level of the FG, as the magnetic stratigraphy suggests, has not been described prior to this. This may indicate that there are influxes of material that may not be detected by chemical means. Alternatively, it may be a consequence of the mixing between mushes described in Section 9.4.11. Since the remanence in these rocks is hosted predominantly in the Fe-Ti oxide minerals (see discussion in Chapter 8), redistribution of these phenocrysts may have resulted in a mixing of the magnetic signal downwards. The forward modelling cannot assess changing magnetic properties within the modelled FG unit.

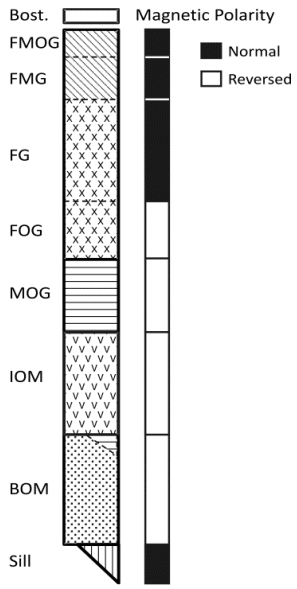


Figure 9.8: Magnetic stratigraphy of the Doros intrusion inferred from the quantitative modelling of aeromagnetic data in Chapter 8.

9.4.15 Melt inclusion compositions

The melt inclusions hosted in olivines from the Basal Zone melagabbros show compositions that clearly reflect interactions with a bostonitic melt phase (Chapter 7). The whole-rock and mineral compositions of the bostonite show that it is a late-stage extreme fractionation product of the Doros liquid (Chapters 4 and 5) that cannot have co-existed with a primitive BOM or IOM magma in a closed system scenario. Furthermore, cross-cutting relations indicate that the bostonite dykes formed later than the melagabbro units in the Doros Complex. These olivine phenocrysts must have interacted with pre-existing bostonitic material during their formation in a lower, staging chamber, before being transported to their present location in the form of a magma mush. This supports the notion of a complex, open system of magma

reservoirs and conduits actively fractionating and feeding magma – the magma mush column of Marsh (2004).

To summarise, the combined field, petrographic, geochemical and geophysical evidence suggests the Doros intrusion consists of at least seven distinct major magma injections (see Fig. 9.9), at the level of the:

1) Chilled gabbroic sill (the lowermost unit in the intrusion);
2) BOM (from field evidence of physical separation from the sill, reversals in mineralogy and whole-rock and mineral chemistry, and a reversal in remanence polarity);
3) MOG (from field evidence of magma mingling);
4) IOM (from intrusive layer contacts and reversals in mineralogy and whole-rock and mineral chemistry);
5) FOG (from field evidence of interlayering and foliation textures, and reversals in mineralogy and whole-rock and mineral chemistry);
6) FMOG/FMG (from reversals in mineralogy and whole-rock and mineral chemistry); and
7) Bostonite (from field evidence of intrusion in dyke form).

A further minor injection potentially exists at the level of the FG, indicated by the reversal in remanence polarity. There were also several small-volume injections that produced the clinopyroxene, olivine and magnetite cumulate enclaves and small-scale layering in the foliated sequence. This is a refinement of the previous emplacement model of Hodgson & Botha (1974).

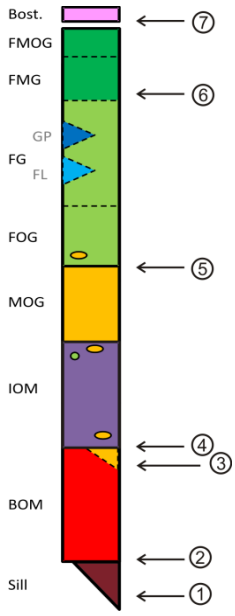


Figure 9.9: Schematic stratigraphic column for the Doros intrusion indicating the levels of intrusion inferred for each magma influx. See text for explanation.

Furthermore, the majority of these magma injections were transporting a crystal load. Specifically, the BOM and IOM contained significant olivine phenocrysts, with minor plagioclase and clinopyroxene (at least 20%, less than 55%) on emplacement (from evidence of phenocrysts in the chilled margin, the plastic nature of intermingling, flow-induced schlieren and crystal size distributions). The MOG was predominantly liquid, but contained sparse olivine phenocrysts (5 - 10%; from evidence of resorption textures). The magma that formed the FOG to FG sequence was carrying significant plagioclase and lesser olivine phenocrysts (from foliation textures). The FMG-FMOG contained magnetite, olivine and lesser plagioclase crystals (from foliation textures and crystal size distributions). The chilled gabbroic sill was emplaced with a load of at least 20% crystals, predominantly of plagioclase, with lesser clinopyroxene and olivine (from evidence of phenocrysts in the chill margin). In addition, cumulus crystal accumulations against layer margins and in small enclaves represent deposited phenocryst loads of varying mineralogy that cannot be correlated with specific major units in the intrusion.

Due to factors such as flow and gravitational settling that affect the distribution of phenocrysts in the gabbros, and the difficulties in identifying *in situ*-grown versus initially-present crystals, due to overgrowth and chemical re-equilibration, the original phenocryst content of the Doros mushes cannot easily be quantified.

9.5 Petrogenesis of each rock type

From the combined field, petrographic, geochemical and geophysical evidence, and the discussion above, the origin of each rock unit in the Doros intrusion may be inferred as follows:

9.5.1 Chilled gabbroic sill

The chilled sill is the lowermost unit identified in the Doros intrusion. It is only documented on surface as a few metres of partial outcrop at one site on the south-eastern side of the complex. However, aeromagnetic imaging has shown that it occurs as extensive subcrop in the southern portion of the complex and may be in the region of 200 m thick. In the absence of observable contact relations with the BOM, the relative chronology of emplacement cannot be inferred. However, the mineralogy and chemistry of the sill indicate that this was a relatively evolved magma that was carrying plagioclase, clinopyroxene and sparse olivine phenocrysts and quenched before significant further fractionation. On emplacement, it underwent alteration by fluids driven off the rapidly-heated host rocks (Damaran schists).

9.5.2 Basal olivine melagabbro

The basal olivine melagabbro is the lowermost major unit mapped on surface, with an exposed thickness of at least 100 m. It has the most primitive chemical composition of all the Doros gabbros. These primitive characteristics and the presence of a basal chill margin suggest that this was the earliest-formed unit in the main body of the Doros intrusion. As has been described, the texture, mineralogy and composition of the basal olivine melagabbro suggest that this layer most likely represents an olivine

cumulate mush, derived from the early stages of fractionation in a lower magma chamber. Flow during emplacement concentrated intercumulus liquid in pockets in the mush pile and at the margins, producing the plagioclase-rich schlieren and relatively phenocryst-poor chill margin described. The outer portion of the BOM quenched against the host rock and this margin was hydrothermally altered and partially brecciated during contact metamorphism.

It is clear that this chill margin does not by any means represent the bulk composition of the original Doros magma, only the leading edge of the first mush emplacement.

9.5.3 Massive olivine melagabbro

The MOG is inferred to have been emplaced in predominantly liquid form, containing only minor olivine phenocrysts, within a very short time of the BOM, such that there was mixing of interstitial liquids across the interface. Subsequent to emplacement, the olivine phenocrysts settled and significant crystallisation of cumulus plagioclase occurred.

9.5.4 Intrusive olivine melagabbro

The IOM was emplaced as an olivine mush, almost identical in composition to the BOM. It intruded largely into the MOG unit, but also transgressed the upper reaches of the BOM and lower foliated gabbros. At the time, these units were mostly crystallised, so interfingered with, rather than mixed with, the incoming magma. Much of the lower part of the MOG was enveloped, leaving only remnants of (possibly more solid) material as xenoliths, rounded by thermal erosion. The plagioclase schlieren in the IOM layer likely formed from flow channelisation, as in the BOM, as well as from more complete thermal digestion of the leucocratic MOG xenoliths.

9.5.5 Foliated (olivine) gabbro

The foliated olivine gabbro to foliated gabbro sequence represents a mush of predominantly plagioclase and minor elongate olivine phenocrysts. The intruding magma interlayered with, and entrained relatively more solid fragments of, the pre-existing MOG. During emplacement and lateral spreading, and subsequent settling, the phenocrysts became aligned. The relatively denser olivine crystals accumulated near the bottom of the layer, forming the FOG, and leaving the upper reaches comparatively olivine-free, forming the FG.

9.5.6 Foliated magnetite (olivine) gabbro

The foliated magnetite gabbro to foliated magnetite olivine gabbro sequence represents a magnetite-olivine-plagioclase mush, emplaced within a short space of time into the semi-crystalline foliated gabbro, resulting in partial mixing. The elongate olivine and plagioclase crystals adopted a planar orientation during flow and settling. Density settling segregated the magma into a magnetite-dominated basal section,

followed by more olivine-rich cumulates. This is the uppermost unit preserved in the main body of the complex.

9.5.7 Foliated leucogabbro

Textural and field evidence shows that the foliated leucogabbro veins and enclaves in the core of the complex formed from slurries of evolved intercumulus melt and plagioclase crystals that were mobilised by compaction, slumping, new magma influxes, or other disruptions to the mush pile. This relatively buoyant material accumulated and rose upward into the semi-crystalline layers above, where it collected and interlayered with existing mushes.

9.5.8 Cumulus crystal enclaves

The small-volume clinopyroxene, olivine and magnetite cumulate enclaves formed when new influxes of magma deposited their phenocryst load near the infilling zone, due to the associated change in flow velocity.

9.5.9 Gabbro pegmatite

The pegmatite dykes and enclaves formed from pockets of trapped, fluid-rich residual liquid within the mostly-crystallised upper foliated gabbros. Whole-rock and mineral compositions are evidence of the evolved nature and late formation of this material. The absence of a foliation, the coarse grain-size, and the mineral textures and compositions indicate localised slow cooling and *in situ* inward crystallisation of a phenocryst-free melt. On crystallisation of the pegmatites, fluids were released and circulated into the surrounding rock, causing hydrothermal alteration and minor copper mineralisation in the pegmatites and lesser effects in the foliated gabbros.

9.5.10 Bostonite

The evolved whole-rock and mineral chemistry of this rock type and the fractionation modelling indicate that the bostonitic material formed from the last, most extreme fractionation phase of the Doros melt. This takes two forms. The first is as enclaves of melt trapped in the mush pile, associated with the pegmatites. The second is as dykes that cross-cut the intrusion. Cross-cutting relations and fine-grained margins indicate an origin of the latter from an equivalent evolved, late-stage melt fraction derived from a lower chamber, some time after emplacement of the main body of the Doros intrusion.

9.6 Chronology of emplacement

It is evident from cross-cutting relations that the stratigraphic succession does not necessarily reflect the chronology of emplacement. In the absence of precise age dating or a detailed palaeomagnetic study, the precise chronology cannot be constrained, and there remains some ambiguity for the chilled gabbroic sill

and intrusive olivine melagabbro units. However, based on the available evidence, I propose the following emplacement history for the Doros intrusion (illustrated in Fig. 9.10):

Stage 1: Formation of the BOM

An olivine-rich magma mush intruded along the sub-vertical contact between Damaran metasediments and granite, or along a structural plane in the deformed Damaran metasediments. On encountering the sub-horizontal basal Karoo strata, lateral spreading was initiated. The olivine crystals became concentrated in the centre of the layer during flow. The margins of the magma chilled immediately on contact with the cold wall-rock. Fluids released from the wall-rock due to contact metamorphism triggered the brecciation of the marginal gabbro. Thereafter, the magma solidified progressively inwards by crystallisation of the intercumulus liquid.

Stage 2: Formation of the MOG

A relatively crystal-poor magma, bearing entrained solid fragments of olivine cumulate from the feeder chamber or conduit, was emplaced into the centre of the BOM layer, before the latter had completely cooled and solidified. Incomplete mixing of the two magmas took place. Subsequently, the minor olivine phenocrysts carried in the magma began to settle and there was extensive crystallisation of plagioclase, as the cumulus phase, followed by clinopyroxene and Fe-Ti oxides.

Stage 3: Formation of the FOG, FG and pegmatite

A magma mush dominated by plagioclase phenocrysts, with minor olivine, intruded into the still plastic MOG layer. In the process, the two magmas intermingled and interlayered. The elongate plagioclase and olivine crystals became aligned by flow of the mush during emplacement. Olivine phenocrysts concentrated near the base by settling. Subsequently, there was progressive crystallisation of the intercumulus liquid, predominantly as clinopyroxene and magnetite. Fluids excluded by crystallisation collected in dilational pockets within the mush pile, assisting crystals here to attain pegmatitic grain sizes. On completion of solidification, some of these fluids were released into the surrounding rock, causing alteration and minor copper mineralisation.

Stage 4: Formation of the FMG, FMOG and FL

A magnetite-olivine-plagioclase magma mush intruded into the still semi-liquid FG layer. Moderate mixing of these magmas took place, followed by the settling and density segregation of the phenocrysts. Some of the magnetite phenocrysts sank into the underlying foliated gabbro to become the foliated magnetite gabbro.

Destabilisation of the underlying FG by the incoming magma, and compaction due to loading, forced some of the plagioclase-rich intercumulus liquid remaining in the mush pile to be displaced upward as feldspathic dykelets and enclaves.

Stage 5: Formation of the IOM

An olivine mush, identical in composition to the BOM, intruded into the MOG unit, such that it also transgressed the upper parts of the BOM and lower parts of the FOG and FG. The new magma reheated and mingled with these pre-existing layers and also entrained semi-solid fragments of this material. Subsequently, the magma progressively solidified by crystallisation of the intercumulus liquid.

Stage 6: Formation of the chilled gabbroic sill

A plagioclase-, clinopyroxene- and olivine-bearing magma mush intruded below the now mostly solid BOM. Rapid cooling and crystallisation occurred on contact with the cold host rocks. Fluids released by metamorphism of the host rocks caused hydrothermal alteration.

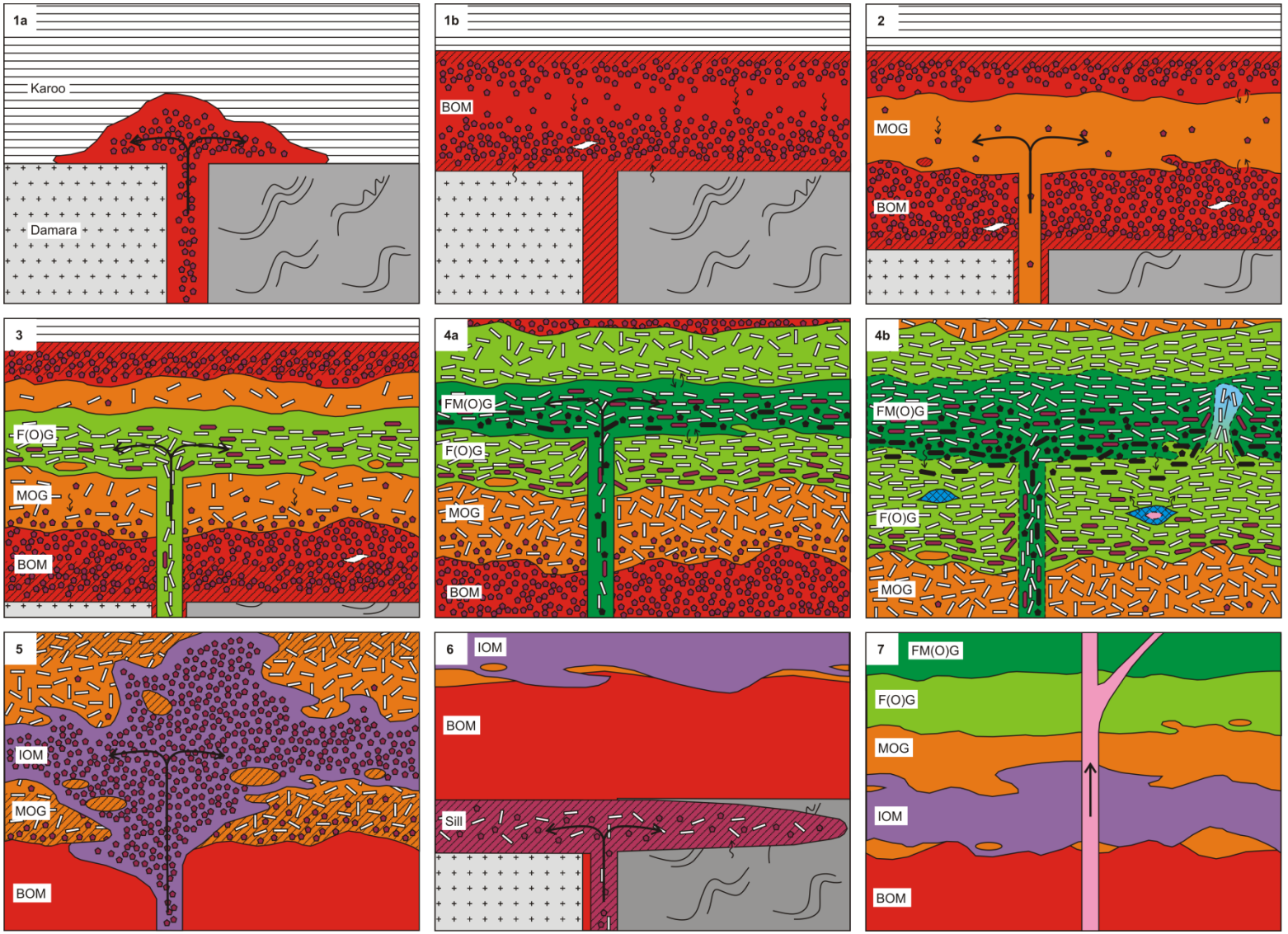
Stage 7: Formation of the bostonite dykes and breccia pipe

An evolved, fluid-rich melt from the final phases of crystallisation of a lower magma chamber intruded the now solid gabbro package, in the form of narrow dykes. The margins of the magma quenched on contact. This was followed by fluid-enhanced crystallisation of the now insulated central zone of the dykes.

As the bostonite magma came into contact with Karoo metasediments outside the complex, it triggered a phreatomagmatic eruption, forming a pipe of brecciated host rock.

While the relative chronology of Stages 4, 5 and 6 may not be confirmed, this sequence is inferred for the following reasons: The magnetite gabbros of Stage 4 must have formed within a relatively short time of the underlying foliated gabbros, due to the absence of a clear contact. The IOM of Stage 5 is suggested to have been emplaced subsequent to this since the presence of entrained xenoliths of pegmatite in this unit indicates that crystallisation of the upper units had already progressed to a mature stage at this time. It is unclear what arrested the IOM at this low level, rather than continuing to ascend to a more liquid upper layer. The chilled gabbroic sill of Stage 6 was likely emplaced along the basal BOM contact. As discussed in Section 1.2.4.3, under-accretion occurs when the previous intrusions are already solid. In addition, the extent of quenching in the sill suggests that all of the surrounding rock was cold, and therefore that the BOM was by this time completely solid. The emplacement of late bostonitic material to a higher level, cross-cutting the intrusion, was likely driven by its volatile content, but may also have been facilitated by fractures in the now solid host.

Figure 9.10 (overleaf): A schematic representation of the proposed emplacement model for the Doros intrusion. Numbers correspond to the stages described in the text. Hatching indicates quenched or progressively crystallising material; uniform fills (no crystals) indicate completely solid layers. Colours correspond to the stratigraphic column (e.g. Fig. 9.9). Olivine crystals are shown in dark red, plagioclase in white and magnetite in black.


1a
Karoo
Damara
1b
BOM
2
MOG
BOM
3
F(O)G
MOG
BOM
4a
FM(O)G
F(O)G
MOG
BOM
4b
FM(O)G
F(O)G
MOG
5
IOM
MOG
BOM
6
IOM
BOM
Sill
7
FM(O)G
F(O)G
MOG
IOM
BOM

9.7 Implications for Doros and other layered mafic intrusions

This interpretation of the formation of the Doros layered mafic intrusion from multiple influxes of crystal-bearing magma has several important implications.

Firstly, it predicts the existence of one or more staging chambers below the Doros intrusion, to supply these episodic influxes of material over a short space of time. The changing composition of the magmas fed upward may be due to a combination of factors. The staging chamber (or chambers) was itself undergoing fractional crystallisation and therefore producing cumulates and increasingly evolved melts. Furthermore, periodic replenishment from below, as well as removal of material to feed the chamber above, may have caused a return to more primitive compositions (Shervais *et al*., 2006). In addition, different parts of this chamber may have been tapped, thereby sourcing different material. A reflection seismic study may provide insight into the presence and nature of these staging chambers, as has been the case for the Messum and Cape Cross Complexes (Bauer *et al*., 2003).

Secondly, as discussed in Chapter 1, a multiple intrusion of this nature requires intra-accretion of a high flux of magma pulses. If each successive magma in the Doros intrusion was emplaced into the liquid-rich central zone of the pre-existing sill, this implies that the upper half of the intrusion, predicted to show a reflected sequence of rock units (as in the Shiant Isles Main Sill; Gibb & Henderson, 2006), is absent. This means that the original thickness of the intra-accreted package may have been approximately twice what it is presently. This is a very rough estimate, since the upper part of the intrusion is unlikely to have been as thick as the lower part, but, on the other hand, there may be more layers from the central zone that are not represented. Nevertheless, this approach provides a working figure to gauge the magma flux. Assuming the minimum present-day depth extent determined from the magnetic forward modelling (Chapter 8), this gives an original thickness for the complete package of ~1 km. If the BOM was indeed the first magma emplaced, and had an original thickness of approximately 200 m (twice its present extent), the calculations of Cawthorn (2012) indicate that it would take approximately 150 years to cool to the point when intra-accretion would be precluded. Considering that this magma has been shown to have been carrying a significant crystal load (Section 9.4), the time before emplacement of the MOG magma must have been considerably less than this. This may be regarded as an upper limit for the time frame of successive emplacements, at least initially.

Thirdly, the Doros intrusion provides yet another example of a layered mafic intrusion with characteristics that support the multiple intrusion and magma mush hypotheses. This strongly suggests that the processes described here are likely to have operated in other, larger layered mafic intrusions, although the evidence may be less apparent. Clearly, phenocryst-bearing magmas have an important role to play and models of emplacement, flow and differentiation must be considered in this light. It further implies that, even the largest of these intrusions, such as the Bushveld Complex of South Africa, are likely to have lower-level staging chambers in the deep crust or upper mantle and therefore cannot be considered as closed systems. A corollary to this is that the bulk compositions of layered mafic intrusions

do not necessarily represent original liquids, as workers are so often wont to assume, and thus their crystallisation and evolution cannot adequately be modelled by simple, single-batch, monobaric fractional crystallisation or assimilation-fractional crystallisation processes.

9.8 Summary of findings

The Doros Complex is a shallow-level lopolith, emplaced within a few kilometres of the surface into the metasedimentary rocks of the Damara Belt. The field, petrographic, geochemical and geophysical evidence compiled in this study all point to the formation of the layering of the Doros Complex by multiple closely-spaced influxes of crystal-bearing magmas (magma mushes), rather than from the post-emplacement differentiation of a single batch of liquid magma. Seven distinct major injections of magma are envisaged, as well as several smaller pulses. These findings are in line with the ‘magmatic mush column’ hypothesis proposed by Marsh (2004).

Chapter 10: Nature of the Doros Mantle Source

10.1 Introduction

The chemical composition of the Doros gabbroic suite, discussed in the preceding chapters, not only provides insight into the dynamics of magma emplacement within the intrusion (Chapter 9), but also holds important information on the source of the magmas themselves. Specifically, this includes the site of melting, the degree of melting, the material involved, the factors responsible for this melting episode and when this occurred relative to other magmatic activity at this time. This has implications for our understanding of the regional tectonomagmatic events of the Paraná-Etendeka Large Igneous Province and the role of the Tristan mantle plume.

10.2 Are all the Doros units derived from a common source?

In Chapter 9 it was shown that the Doros Complex was built from multiple pulses of magma of varying compositions. Thus this raises the possibility that all the Doros magmas may not have originally been derived from the same mantle source or melting episode.

Radiogenic isotope compositions are an essential parameter in detecting the original site and components of melting, since they retain the signature of their source through subsequent evolution of the magma, unless they are contaminated. As discussed in Chapter 6, apart from the three high-I_{Sr} samples that are interpreted as altered, the Doros samples form a tight cluster in both Sr- and Nd-, and Pb-isotopic space (Figs. 6.3, 6.6). This is a strong indication that all the units recognised in the complex were derived from the same original magma source, before being modified by subsequent processes of fractional crystallisation and crystal accumulation. This is consistent with the short time period between successive magma mush emplacements inferred in Chapter 9.

This cluster of isotopic compositions includes a sample of one of the bostonite dykes that cross-cut the intrusion. As discussed in Chapter 3, field evidence indicates that the dykes were emplaced later than the Doros gabbros, yet affinities with the clearly comagmatic bostonitic enclaves within the main body of the intrusion suggest a petrogenetic connection. The similar isotopic composition of the bostonite to the rest of the Doros suite supports the previous interpretation, based on whole-rock and mineral geochemistry, that the bostonite is a late-stage enriched product of the same basaltic parental Doros magma. However, it is noted that the bostonite compositions are consistently at the most enriched extreme of the Doros cluster (Figs. 6.1, 6.4).

The dolerite dykes that intrude the Doros gabbros, however, have been shown to have dissimilar isotopic compositions to the Doros suite, indicating a dissimilar, more enriched mantle source and/or significant

crustal contamination (Section 6.6). This corroborates petrographic evidence for distinct mineralogical and textural characteristics for the dykes (Chapter 4) and cross-cutting relations and thick chill margins that indicate a younger age (Chapter 3).

In fact, the dolerite sampled in this study has strong geochemical affinities with the Horingbaai dyke suite of the Etendeka Province (Figs. 6.6, 10.1, 10.4, 10.7, 10.10), particularly the subset of these interpreted by Thompson *et al.* (2001), from their major and trace element compositions and isotopic ratios (especially high I_{Sr}; see Fig. 6.3), to be significantly contaminated by Damaran crust. Some representatives of the Horingbaai suite crop out to the north and north-west of the complex (the closest are shown as yellow stars in Fig. A.1; Thompson *et al*., 2001). The ages of these dykes are constrained by field relations at between 132 and 131 Ma (Thompson *et al*., 2001). The Horingbaai magmas show a dominant E-MORB-like depleted mantle component and are interpreted to have originated from late-stage decompression melts during lithospheric thinning prior to continental break-up (Thompson *et al*., 2001). These distinct source characteristics may be seen particularly well in a plot of 1/Pb versus initial $^{206}Pb/^{204}Pb$ (Fig. 10.1), where the Horingbaai samples show a strong trend from MORB-like compositions towards a crustal end member. The Doros dolerite lies within the most contaminated portion of this spectrum. From this combined evidence, it may be concluded that the dolerite is not a part of the Doros intrusion and is in fact a member of the Horingbaai suite.

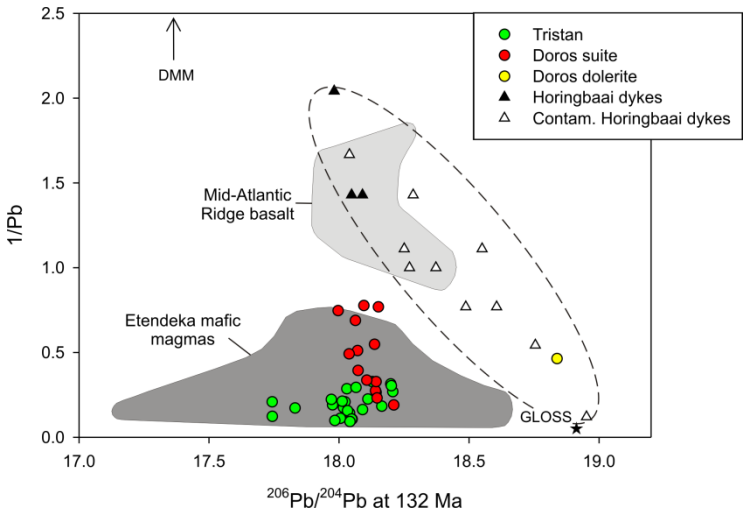


Figure 10.1: Initial $^{206}Pb/^{204}Pb$ against elemental Pb concentrations for the Doros units, compared with the Horingbaai dolerite dyke suite (Thompson *et al*., 2001), fields for the other Etendeka mafic magma types (Tafelberg, Tafelkop, Khumib, Esmeralda; Peate & Hawkesworth, 1996; Ewart *et al*., 1998a; Peate *et al*., 1999; Gibson *et al*., 2000; Thompson *et al*., 2001; Ewart *et al*., 2004a), Mid-Atlantic Ridge basalts (Taylor *et al*., 1997; PetDB[1]), representing local MORB, and Tristan group lavas (Cohen & O'Nions, 1982; Newsom *et al*., 1986; Le Roex *et al*., 1990; Cliff *et al*., 1991; Ewart *et al*., 2004a). Average Depleted MORB Mantle (DMM; 1/Pb ~56 ppm) is from Workman & Hart (2005); global subducting sediment (GLOSS) is from Plank & Langmuir (1998). The dashed ellipse highlights the array of Horingbaai samples between MORB-like compositions and an enriched contaminant with similar Pb isotopic characteristics to GLOSS. The Doros dolerite lies within this array.

[1] Derived from the following sources, hosted by the Petrological Database PetDb: O'Nions *et al*., 1977; Sun *et al*., 1979; Ito *et al*., 1980, 1987; Humphris & Thompson, 1985; Hanan *et al*., 1986; Le Roex *et al*., 1987; Fontignie & Schilling, 1996; Douglass *et al*., 1999; Le Roux, 2000; Jenner & O'Neill, 2012.

The trace element characteristics of the Doros suite also suggest a common mantle source. Under normal circumstances, the compositional characteristics inherited from the source are obscured in the trace element chemistry by the later effects of fractional crystallisation and accumulation. However, in Chapter 9 it was shown that the major units in the Doros intrusion have very similar REE patterns (Fig. 9.7) and this was proposed to reflect their origin as discrete magma mushes without significant loss of interstitial liquid, such that the effects of fractionation have been reduced. Therefore, these apparent shared characteristics in the Doros mushes originate from their common magma source. Although significant fractionation for the bostonite dykes has led to substantially higher levels of enrichment in the REE (Fig. 5.5), the slope of enrichment is similar to the main suite, indicating that they are comagmatic. As an example, a simple fractionation model in Figure 10.2 (one of many iterations of possible parent and daughter compositions, fractionating mineral assemblages and partition coefficients) confirms that derivation of the most REE-enriched bostonite compositions by fractional crystallisation from a Doros gabbro is plausible. This is in agreement with the isotopic evidence.

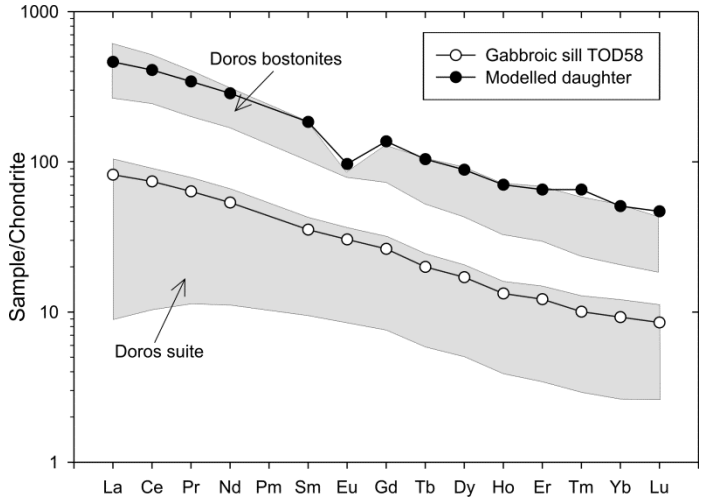


Figure 10.2: Simple fractionation model in terms of the REE indicating that a liquid of bostinitic composition may plausibly be derived by 86% fractional crystallisation (specifically 41% plagioclase, 32% clinopyroxene, 11% olivine and 11% magnetite) from a Doros gabbro (in this case the chilled gabbroic sill). The sill is selected as a parent because of its approximately cotectic mineral proportions (Figs. 5.2, 5.13) and its similarity in terms of REE concentrations to the calculated original Doros liquids of Fig. 5.15. Partition coefficients used for this modelling are in Table E.6.

Once again, in terms of trace element compositions, the Doros dolerite is shown to have distinct characteristics to the Doros suite. While in the same range of enrichment as the Doros gabbros, the dolerite displays an almost flat REE pattern, indicating comparatively more relative enrichment in the HREE, and this fits well with the Horingbaai suite (Fig. 10.3).

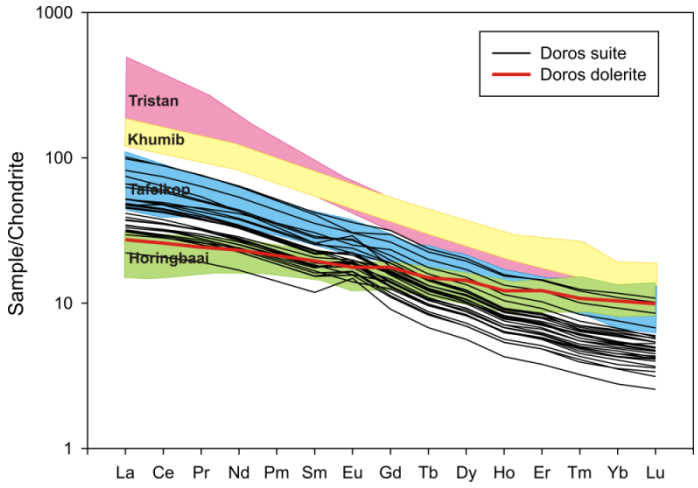


Figure 10.3: Rare earth element concentrations for the major units of the Doros suite, in relation to fields for the Tafelkop (Ewart *et al*., 1998; Gibson *et al*., 2000; Thompson *et al*., 2001), Khumib (Ewart *et al*., 2004) and Horingbaai (Thompson *et al*., 2001) magma groups of the Etendeka, as well as modern-day Tristan group lavas (Cliff *et al*., 1991; Ewart *et al*., 2004; Willbold *et al*., 2006). Normalised to CI chondrite of Anders & Grevesse (1989). Note the similarity in the patterns of the Doros dolerite dyke (in red) and the Horingbaai dyke suite.

10.3 Nature of the Doros mantle source

As indicated in Chapter 6, the Sr-, Nd- and Pb-isotopic compositions of the Doros suite suggest a depleted mantle source, with components of both lower and upper mantle material. Specifically, the suite consistently plots between Tristan plume compositions and MORB-like mantle compositions. This is corroborated in the combined isotopes of Figure 10.4, and a plot of elemental versus isotopic Sr (Fig. 10.5), where the Doros suite clearly lies between the southern Mid-Atlantic Ridge (MAR) basalt field, representing local asthenosphere, and the present-day Tristan group, representing plume compositions. The presence of a significant plume component in the Doros magmas is particularly evident in Figure 10.5. There is no obvious displacement towards an enriched mantle or crustal component in these cases.

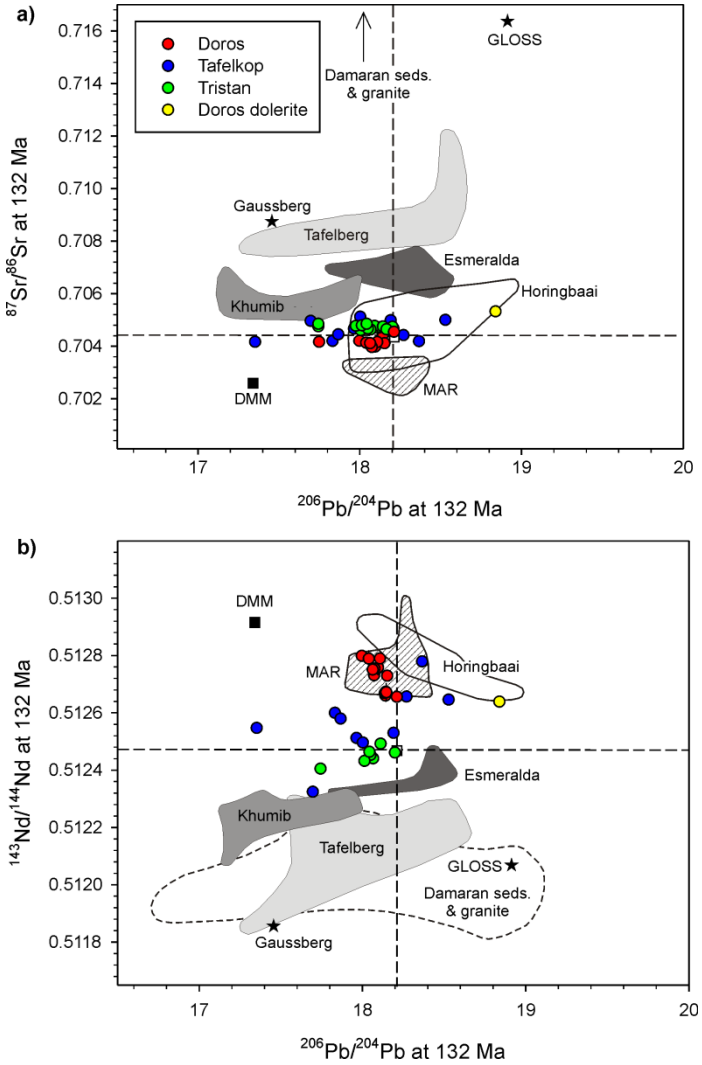


Figure 10.4: Initial a) Sr- and b) Nd-isotopic compositions against initial ^{206}Pb for the Doros suite, Etendeka mafic magma groups and southern Mid-Atlantic Ridge (MAR) basalts (Taylor *et al*., 1997; PetDB[1]). Compositions for Damaran metasediments and granitoid rocks are from McDermott & Hawkesworth (1990), McDermott *et al*. (1996) and Jung *et al.* (1998). All other sources are as in Figs. 6.3 and 6.6.

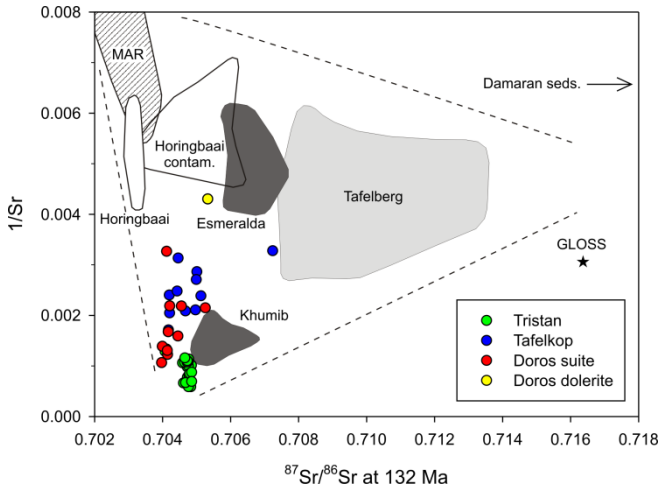


Figure 10.5: Initial Sr versus 1/Sr for the Doros suite, Etendeka mafic magma groups, Tristan group lavas and southern Mid-Atlantic Ridge (MAR) basalts, as well as global subducting sediment (GLOSS) and Damaran metasedimentary rocks (all sources as in Fig. 10.3). The Paraná-Etendeka mafic magmas essentially define a 3-component system, between Tristan plume compositions, depleted mantle and an enriched crustal component, as indicated by the dashed lines.

The Doros source components can be quantified to some extent by simple isotopic mixing calculations. The model parameters and end member compositions are compiled in Table E.5 and two examples of viable models are presented in Figure 10.6. The southern Mid-Atlantic Ridge basalts reflect local depleted mantle variably mixed with plume material (Fontignie & Schilling, 1996). The most depleted end member of this range is therefore taken as representative of the plume-free (N-MORB) local mantle asthenosphere that may have contributed to the Doros source. Simple mixing modelling with an average Tristan basalt composition (Trumbull *et al*., 2003) suggests that there is approximately 20 - 40% enriched plume material to 60 - 80% depleted mantle material in the Doros source (Fig. 10.6). However, there appears to be a small displacement towards more enriched initial Sr ratios in the Doros suite. This variation could partially be a result of variation in the plume component (the calculated range is given by the box in Fig. 10.5; Trumbull *et al*., 2003), or caused by minor hydrothermal alteration of these samples, which was shown to affect I_{Sr} ratios in Chapter 6. However, it must also be considered that this potentially reflects a very minor enriched component in the source, either from the crust or mantle.

Possible crustal contaminants were listed in Section 6.2, and it is clear that these may plausibly be restricted to two end members: the Damaran upper crust, or the pre-Damara Archaean basement. It is immediately obvious in Figure 10.6a that the average Archaean basement is too enriched in ε_{Nd} to produce the required displacement in the Doros gabbros. However, the Damaran crust presents a viable contaminant. The Sr- and Nd-isotopic compositions of the average Damaran granitoid and sedimentary components are similar (Table E.5) and therefore either end member may be used to the same effect. The results of the mixing modelling with average Damaran metasediments in Figure 10.6a indicate that the observed Doros compositions may be explained by a maximum of 3% of assimilated Damaran crust. The absence of orthopyroxene in the Doros gabbros confirms that crustal contamination of these magmas cannot have been significant.

Alternatively, the enriched component may reside in the mantle. The so-called 'enriched mantle' (EM) identified in ocean island basalts has a wide variety of compositions and has been attributed to many different sources, including recycled continental crustal material in various forms, recycled oceanic material and metasomatised lithospheric mantle (Stracke, 2012, and references therein). The purported end members of this spectrum, EMI and EMII of Zindler & Hart (1986), are not sufficiently well-constrained for modelling of age-corrected data, therefore proxies for the sources of these compositions are considered instead. The inferred composition of the local SCLM (identified in Paraná-Etendeka mafic potassic magmas by Gibson *et al*., 1995) and ancient subducted sediments interpreted by Ewart *et al.* (2004a) as a significant source component in the Etendeka system (represented by typical Gaussberg lamproite of Murphy *et al*., 2002), are clealy not plausible candidates (Fig. 6.3). However, the average composition of subducted marine sediments (GLOSS; Plank & Langmuir, 1998), representing recycled upper crustal material, attributed by many as the source of EMII-like compositions (e.g. Weaver, 1991; Workman, et al., 2004; Jackson e*t al*., 2007), offers appropriately high I_{Sr} and low ε_{Nd} (Fig. 6.3). The results of the mixing modelling (Fig. 10.6b) show that the Doros compositions may be plausibly explained by incorporation of up to 5% subducted sediments in the mantle source.

Either way, the enriched component in the Doros source revealed by the modelling is relatively minor, not enough to cause any significant displacement in isotopic compositions in Figures 10.1, 10.4 and 10.5.

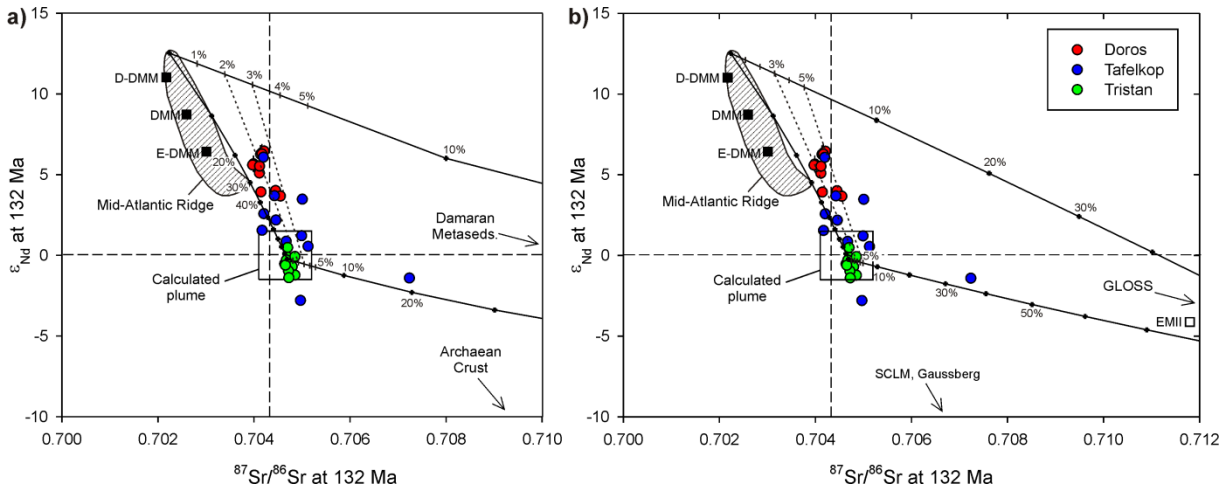


Figure 10.6: Modelled Sr-Nd mixing curves between plume-free southern Mid-Atlantic Ridge (MAR) basalt (O'Nions *et al*., 1977), representing a depleted mantle component, and average Tristan basalt (Trumbull *et al*., 2003), representing a plume component, with an additional enriched a) crustal component, represented by average Damaran metasediments (McDermott & Hawkesworth, 1990), or b) mantle component, represented by global subducting sediment (GLOSS; Plank & Langmuir, 1998). Also shown are the average Archaean basement in this region (Mingram *et al*., 2000), local SCLM (Gibson *et al*., 1995), Gaussberg lamproite (Murphy *et al*., 2002) and the calculated EMII composition of Workman *et al*. (2004). Tristan group samples, the calculated plume composition, Tafelkop basalt samples and Depleted MORB Mantle end members are as in Figure 6.3. The field of MAR basalts is from Taylor *et al.* (1997) and PetDB[1].

Immobile incompatible trace element ratios may also be used to shed light on the mantle source of magmas, and detect any crustal component involved, as long as consideration is taken in the choice of elements so as to remove the effects of fractionation and accumulation.

The Th-Nb system may be considered a good proxy for crustal input, since crustal material shows a distinctive relative enrichment in Th (Pearce, 2008). Figure 10.7 shows Th/Yb and Nb/Yb ratios for the Doros gabbros. Again, the Doros suite lies in the mantle array, between Tristan group compositions and MORB. Displacement in the direction of crustal end members is negligible for most of the suite, indicating that these magmas are relatively uncontaminated.

The sample of chill margin (for which there is no isotopic analysis) is an exception in this regard, showing a displacement in Th/Yb towards Damaran crust (Fig. 10.7). There is clear evidence for entrained fragments of Damaran metasedimentary material in the Doros marginal rocks in the field (e.g. Fig. 3.3c). Elevated concentrations of Na_2O, U (1.4 ppm), Th (4.7 ppm) and Pb (7.7 ppm) were also noted for the chill margin sample (see Chapter 5), which strongly suggest local assimilation of country rock. Concentrations of U, Th and Pb in the Nama, Khuiseb, Khan and Etusis Formations of the Damara have ranges of 1 - 22 ppm, 0.5 - 10 ppm and 5 - 49 ppm, respectively (McDermott & Hawkesworth, 1990). The Doros granite pluton has 3 - 9 ppm U, 20 - 63 ppm Th, and 20 - 35 ppm Pb (Schmitt *et al*., 2000). While compositional data for the Karoo metasedimentary rocks in this area are not available, it is noted that these are currently under investigation as a viable uranium prospect. Thus, any small amount of assimilation of this material would be sufficient to produce the elevated concentrations in the chill margin. The chilled sill does not show as marked an enrichment in these elements, despite field evidence of entrainment. It is suggested that sedimentary xenoliths were completely digested in the chilled margins of the complex, but remained intact in the interior of the sill. The chill margin is thus considered the only material in the Doros intrusion to be significantly contaminated and this likely took place by assimilation of the host rock during shallow-level emplacement.

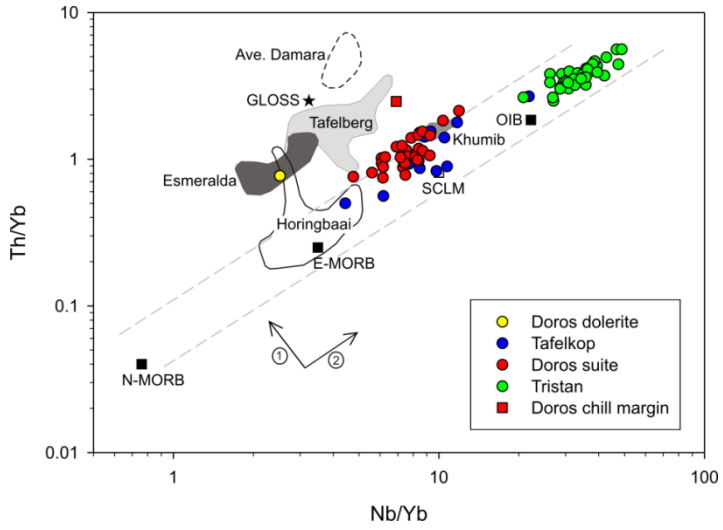


Figure 10.7: Th/Yb vs. Nb/Yb for the Doros suite, in relation to Tristan group compositions (Cliff *et al*., 1991; Ewart *et al*., 2004a; Willbold & Stracke, 2006), the Etendeka mafic magma groups (Erlank *et al*., 1984; Peate & Hawkesworth, 1996; Ewart *et al*., 1998a; Gibson *et al*., 2000; Thompson *et al*., 2001; Ewart *et al*., 2004a) and average Damara metasediments (McDermott & Hawkesworth, 1990). MORB and ocean island basalt (OIB) from Sun & McDonough (1989); typical sub-continental lithospheric mantle (SCLM) from McDonough (1990); global subducting sediment (GLOSS) from Plank & Langmuir (1998). Vectors 1 and 2 represent approximate directions of crustal contamination and fractional crystallisation, respectively.

In a similar vein, a plot of Th/Ta against Th/Tb (Fig. 10.8) can distinguish between contrasting mantle source compositions. Correlation lines correspond to different mantle sources, while displacement to higher relative Th suggests crustal contamination. While fractionation in the Doros suite has led to some scatter, it is still evident that the Doros chill margin lies on the same trend as the rest of the Doros suite, but with distinctly higher Th/Ta and Th/Tb, confirming a crustal influence. As discussed in Chapter 6, the extremely low concentrations of trace elements in the olivine-rich xenolith (< 0.2 ppm for the elements concerned) means greater sensitivity to errors in measurement and may be the cause of the apparent displacement of this sample from the main suite.

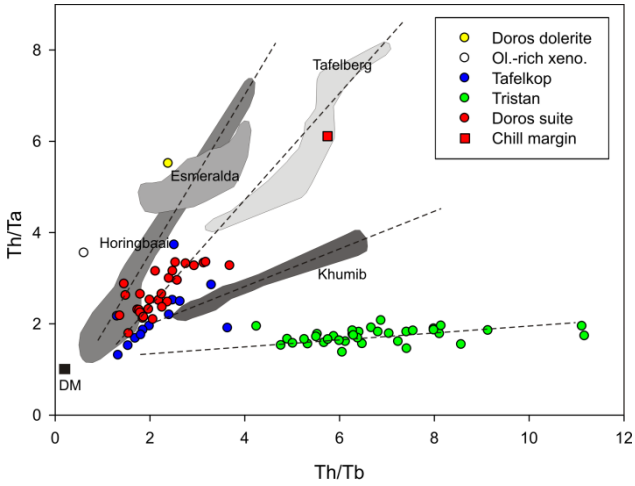


Figure 10.8: Th/Ta against Th/Tb for the Doros suite, compared with compositions for modern-day Tristan lavas (Ewart *et al*., 2004; Willbold *et al*., 2006) and the mafic magma groups of the Paraná-Etendeka Province (Peate & Hawkesworth, 1996; Peate *et al*., 1999; Thompson *et al*., 2001). Dashed lines highlight the trends of the Horingbaai, Tafelberg, Khumib and Tristan groups. Depleted Mantle (DM) is from Workman & Hart (2005). The different trends suggest different source components (discussed in Section 10.5), while displacement along the trend suggests crustal contamination.

The major and trace element compositions of the early Doros liquid, preserved as olivine-hosted melt inclusions in the Lower Zone melagabbros, are also not consistent with significant crustal contamination (e.g. Fig. 7.9).

Thus, based on several lines of isotopic and trace element evidence, it is proposed that the Doros magmas in general were sourced from relatively minor, enriched, plume-derived asthenospheric material and more substantial, depleted upper mantle material, with a negligible contribution from either local crust or recycled sediments in the mantle source.

10.4 Doros in the context of the Damaraland Intrusive Suite

As discussed in Chapter 1, Doros is a member of the Damaraland Intrusive Suite, which includes a wide range of mafic, felsic, alkaline and carbonatitic lithologies, and which is valued for the insights it provides into the mantle source of the Paraná-Etendeka magmatism. All the Damaraland intrusions show a detectable isotopic signature of the Tristan mantle plume, although in the felsic lithologies this is largely obscured by crustal contamination (Trumbull *et al*., 2000). Doros is similar in Sr- and Nd-isotopic composition to the uncontaminated mafic and alkaline units of the Damaraland Suite, but extends to more depleted, MORB-like compositions (Fig. 10.9). The source is therefore similar, but reflects a greater proportion of depleted mantle material.

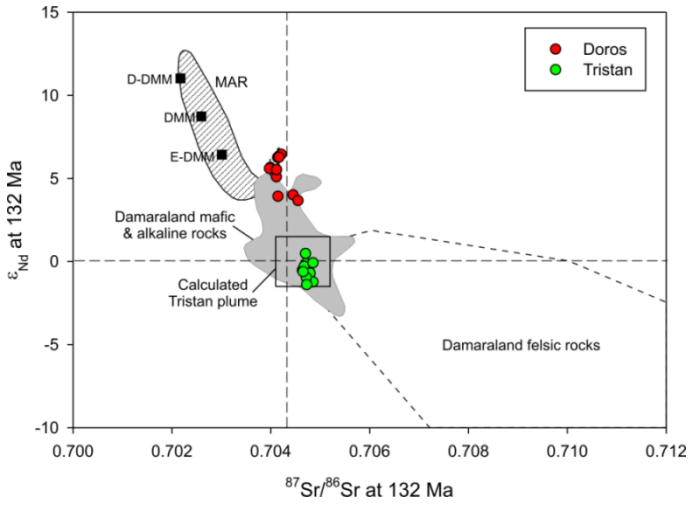


Figure 10.9: Initial Sr- and Nd-isotopic compositions for the Doros intrusion in relation to the Damaraland Suite, specifically the Okenyenya, Messum, Erongo, Etaneno, Kalkfeld, Brandberg, Paresis, Ondurakorume, Okorusu and Osongombo Complexes (Milner & Le Roex, 1996; Le Roex & Lanyon, 1998; Harris *et al*., 1999; Mingram *et al*., 2000; Trumbull *et al*., 2000, 2003). The mafic and alkaline lithologies (gabbro, basalt, syenite, basanite, phonolite, nephelinite, tephrite, carbonatite, lamprophyre) are distinguished from the felsic lithologies (granite, granodiorite, monzodiorite, monzonite, quartz syenite, trachydacite, rhyolite) in this plot. Sources for Mid-Atlantic Ridge, Depleted Mantle, modern Tristan basalts and calculated ancient plume material are as in Figs. 6.3 and 10.4.

A comparison of the incompatible trace element compositions of the mafic rock types of the Damaraland intrusions reveals a further distinction (Fig. 10.10). Whereas the Doros gabbros have Zr/Yb and Nb/Yb compositions within the mantle array, gabbroic rocks from the other Damaraland intrusions have distinctly lower Zr/Yb. This apparent displacement may reflect an enriched SCLM component in the source, as has been suggested for some of the mafic components of the Paraná-Etendeka volcanic succession (e.g. Peate & Hawkesworth, 1996; Gibson *et al*., 1999; Marques *et al*., 1999).

These distinctions in composition between Doros and the mafic units from the other Damaraland intrusions, i.e. a greater proportion of depleted mantle material and absence of a lithospheric mantle component, suggest that the Doros magmatism occurred at an earlier stage in the development of the LIP, in the first phase of decompression melting of plume and entrained ambient mantle material and before plume impingement caused significant melting of the sub-continental lithosphere. This is in agreement with geophysical evidence for contrasting directions of remanent magnetisation in the Doros intrusion compared to the Messum, Brandberg and Cape Cross Complexes (Chapter 8).This is despite some of these intrusions being located to the east of Doros (earlier in the plume trajectory; Fig. 1.2), implying that the distribution of the Damaraland complexes reflects structural controls in addition to plume-generated compositional variations in the mantle.

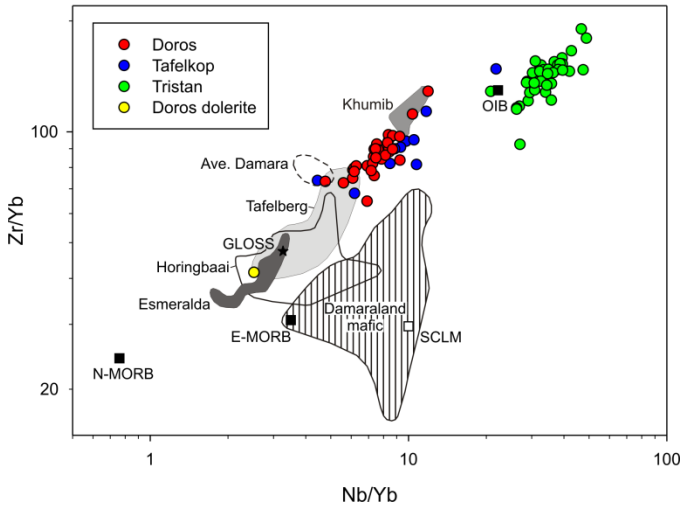


Figure 10.10: Zr/Yb versus Nb/Yb for the Doros suite, Tristan group lavas, Etendeka mafic magma groups and the field of mafic rock types in the Damaraland intrusive suite (gabbros and basalts from the Okenyenya, Paresis and Messum Complexes; Le Roex *et al*., 1996; Duncan *et al*., 1998; Trumbull *et al*., 2000). Data sources are as in Figure 10.7.

10.5 Doros in the context of the Etendeka LIP, with particular reference to the Tafelkop group

The Etendeka mafic magmas essentially reflect a 3-component mixing system, between Tristan plume-derived asthenospheric melts, depleted MORB-like mantle (DMM) and an enriched component (subducted material, lithospheric mantle, lower or upper crust, or some combination of these; see discussion in Chapter 1; Miller, 2008c). This is evident in terms of isotopes and trace element ratios (Figs. 7.3, 7.6, 10.4, 10.7) but is perhaps displayed best in Figure 10.5. In essence, the Tafelkop basalts are considered to be largely-uncontaminated plume melts, with a significant component of MORB (Ewart *et al*., 2004a; Miller, 2008c). The Khumib basalts have a similarly large plume component, but also significant subducted sedimentary material (Ewart *et al*., 2004a; Miller, 2008c). The Horingbaai dyke suite shows a dominant depleted mantle component, with minor crustal contamination (Thompson *et al*., 2001; Ewart *et al*., 2004a; Miller, 2008c). The Tafelberg and Esmeralda lavas have the greatest crustal component, and minimal plume involvement, with a larger MORB-mantle contribution in the latter (Ewart *et al*., 2004a; Miller, 2008c). The proportions of each of these components, as modelled by Ewart *et al*. (2004a), are summarised in Table 10.1 below.

Table 10.1: Modelled mantle source compositions of the Etendeka mafic magma types from Ewart *et al*. (2004a)

Magma type	Tristan plume mantle	MORB mantle	Subducted sediment +/- crust
Khumib	45 - 75%	5 - 10%	20 - 40%
Tafelberg	2 - 25%	5 - 55%	2 - 20%
Esmeralda	< 10%	60 - 90%	10 - 30%
Horingbaai	5 - 15%	85 - 95%	< 2%
Tafelkop	25 - 75%	10 - 50%	3 - 15%

As discussed in Chapter 1, it has previously been proposed that there are geochemical affinities between Doros and the Tafelkop group. However, until now this argument has been weakened by the absence of published isotopic analyses for the Doros rocks and a reliance on comparisons in major and trace element compositions between Doros cumulate rocks and Tafelkop lavas. It has been shown in Chapter 5 that the identification of a so-called "orthocumulate group" in the Doros suite by Marsh *et al*. (2001) and Marsh & Duncan (2008) is not justified texturally or geochemically, nor can these rocks be considered to represent liquid compositions. The trace element ratios Ti/Y, Ti/Zr and Zr/Y used as an additional means of identification for the Tafelkop group in previous studies, in the absence of isotope data, are not appropriate for comparison, since these are strongly affected by fractional crystallisation.

The new data from this study allow a direct comparison of the inherited source characteristics of these two magma types. The isotopic compositions offer the most robust means for evaluation. However, it is apparent from the preceding sections that there are also trace element characteristics that allow us to see through the effects of fractional crystallisation and accumulation.

It is evident from the material presented here that the Doros intrusive suite shows some similarities with the Horingbaai-type magmas, due to their common dominant depleted mantle component, and with the Khumib basalt group, due to their common plume signature, but it is clear, particularly in Figure 10.5, that these groups have divergent properties. However, the Doros suite shows consistent, strong similarities in source composition with the Tafelkop magma group. There is overlap in isotopic compositions, although the Tafelkop group shows greater variability (Figs. 6.3, 6.6, 10.5), and in trace element compositions (Figs. 10.7, 10.8, 10.10). The greater spread of data in the Tafelkop group is ascribed to additional variable contamination of these rocks. The trends in Pb-isotopic space for the two suites are essentially identical (Fig. 6.5), indicating the same reservoir separation age, and therefore equivalent origins in the same melting event.

There are also strong similarities in the slope and level of enrichment in the REEs between the Doros mushes and the Tafelkop group (Fig. 10.3). However, this is still a comparison of cumulate and volcanic rocks. Alternatively, the comparison can be made between the Tafelkop lavas and the approximate compositions of the original liquids of the Doros mushes, which were back-calculated from the whole-rock and cumulus mineral compositions in Chapter 5 (Section 5.6). Figure 10.11 shows that there is a

remarkably good correlation in REE abundances between the calculated Doros liquids and the Tafelkop suite. This is additional strong evidence in favour of a common magma source.

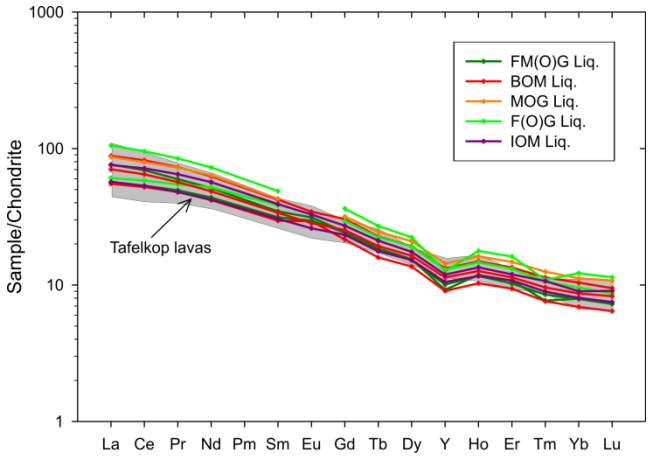


Figure 10.11: REE and Y compositions of calculated original liquids for the Doros mushes (see Section 5.6 for explanation) with the field of Tafelkop group lavas from the Etendeka succession (Ewart *et al*., 1998a; Gibson *et al*., 2000; Thompson *et al*., 2001).

Thus, based on the spatial proximity of Doros to the present outcrop of the Tafelkop lavas, the apparent thickening of these lavas towards Doros (Marsh *et al*., 2001) and the strong geochemical affinities between the Doros and Tafelkop magmas shown here, the Doros Complex is confirmed as the eruptive source for the Tafelkop lavas. This has several important implications.

Firstly, it implies that the Tafelkop volcanic rocks originally covered a greater area than their present outcrop, around the Doros eruptive centre. This was envisaged by Miller *et al*. (2008c), as approximated in Figure 10.12. This also allows the source of the Tafelkop lavas to be pinpointed geographically.

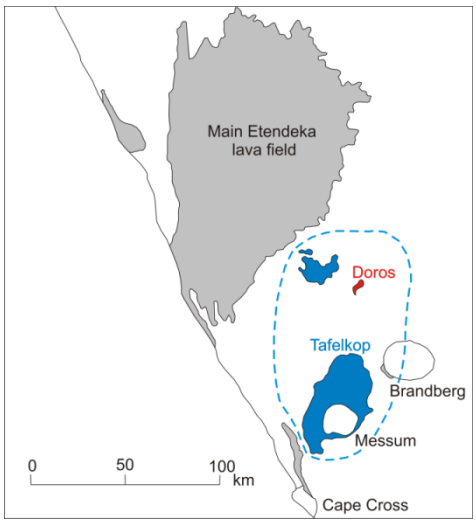


Figure 10.12: The possible original extent of the Tafelkop basalts (after Miller *et al*., 2008c).

Furthermore, it is the second case, after the Messum Complex and its products, where a link between Damaraland intrusive units and Etendeka volcanic units has been firmly established. Thus it provides an additional piece of evidence that many of the Damaraland Complexes are the roots of the volcanoes that fed the Etendeka lavas.

Thirdly, this provides us with a more complete magma system to investigate, from plutonic cumulates through to their volcanic products – a section of the magma mush column of Marsh (2004). In terms of major elements, the Tafelkop lavas fall in the intermediate range of the Doros compositional spectrum, between the basal melagabbros and the massive olivine and foliated gabbros (Figs. 5.3, 5.4), i.e. without the effects of significant accumulation of olivine or plagioclase, or the fractionation evident in the most evolved units in the suite. In many respects they are compositionally similar to the lower levels of the massive olivine gabbro unit, now mostly engulfed by the intrusive olivine melagabbro – the same component of the suite considered best representative of early Doros liquid compositions in Chapter 5. It is suggested that the lava erupted was similar in composition and phenocryst proportions to the original liquid of the MOG layer. The MOG unit has been interpreted from its texture and composition as being predominantly liquid on emplacement, with sparse olivine phenocrysts, unlike the other major units in the Doros intrusion, which likely had significant crystal loads (see discussion in Chapter 9). The Tafelkop basalts are typically olivine-phyric (0 - 25%), but are also observed to have phenocrysts of clinopyroxene and plagioclase (Miller, 2008c). It is suggested that the relatively higher liquid proportion of this magma, and therefore lower density, resulted in a greater propensity for eruption from the Doros chamber. The observed variability in isotopic compositions of the Tafelkop lavas may be a consequence of minor crustal contamination during the ascent of these magmas from the Doros chamber to the surface.

Finally, this connection to the Tafelkop lavas links the Doros magmatism to the earliest eruptive phase in the Paraná-Etendeka event. This is in agreement with its inferred origins in the early stage of the LIP, from chemical comparisons with the other Damaraland intrusions (Section 10.4). This magmatism is therefore proposed to be associated with early decompression melting in the upwelling Tristan plume head, involving enriched, plume-derived asthenosphere and entrained, depleted mantle material, in line with what has been proposed for the Tafelkop group (Ewart *et al*., 1998a, 2004a). The lack of significant crustal contamination is suggested to be a result of this relatively early stage in the history of plume-lithosphere interactions. There is no evidence of significant lithospheric thinning at this time (Gibson *et al*., 2000). Later stages are likely to have seen more extensive melting of plume material, as the plume head impinged on the lithosphere and this and subsequent rifting and lithospheric thinning produced sufficient conductive heating to cause significant contamination of melts as they ascended. Only on emplacement into the upper levels of the crust did minor assimilation of wall-rock occur to affect the chilled margins of the Doros intrusion.

As discussed in the introduction, it has been proposed that the Tafelkop lavas represent a phase of "ferropicrite" magmatism within the Paraná-Etendeka Large Igneous Province (Gibson *et al*., 2000; Thompson *et al*., 2001). A volumetrically-minor, high-MgO (> 12 wt. %) and high-FeO_{Total} (> 13.5 wt.

%; Tuff *et al*., 2005) phase has been recognised as the earliest phase of magmatism in several continental flood basalt provinces around the world (e.g. Deccan, Pechenga, Ethiopia, Siberia; Gibson *et al*., 2000, Tuff *et al*., 2005). Such compositions are suggested to correspond to high-temperature melts at the axes of mantle plume starting heads (Gibson, 2002; Tuff *et al*., 2005). These ferropicrite magmas show distinctive chemical characteristics, in particular high Ni contents, high Fe/Mn and low Ca, in the whole rocks and in early-formed olivine (Herzberg, 2011). There is much debate over the origin of this unusual chemistry. A hypothesis that has gained recent favour is that it is a result of deep partial melting of a mantle source containing a component of olivine-free garnet pyroxenite, i.e. eclogite, as opposed to normal mantle peridotite alone (Tuff *et al*., 2005). This pyroxenitic material is proposed to have been derived from remnants of recycled oceanic crust in the mantle (Gibson *et al*., 2000; Tuff *et al*., 2005). In a rising plume that contains both peridotite and very minor pyroxenitic material, the pyroxenite will begin to melt first, since it has a lower solidus temperature, and therefore it contributes greater volumes of melt than the peridotite, giving these early melts a strong pyroxenite signature (Tuff *et al*., 2005). With increased lithospheric thinning, the associated rapid upwelling and shallower melting produces large volumes of peridotitic melts that dilute the pyroxenitic signature, even as this component is quickly exhausted (Gibson, 2002; Tuff *et al*., 2005).

While the Doros rocks are cumulate rocks, and therefore these ferropicritic chemical characteristics are less easy to detect, the Doros olivines are clearly enriched in Ni relative to those in the Etendeka succession with equivalent Fo content, and there is a good correlation with whole-rock Fe/Mn, in agreement with a ferropicritic history (Chapters 4 and 5). Experimental modelling on a representative Tafelkop basalt by Tuff *et al*. (2005) has suggested initiation of melting at ≥ 5 GPa (~165 km depth), in a garnet-bearing pyroxenite source, and thus the same could be expected for the parental Doros melts. While the original composition of the early, primitive Doros liquid preserved in olivine-hosted melt inclusions has been largely obscured by entrapment of solid phases and extensive mixing with a bostonitic component (Chapter 7), a prominent characteristic that can be detected is the unusually low Ca/Al_2O_3 ratios, coupled with relatively steeply-dipping REE patterns. As discussed in Chapter 7, this may be consistent with a garnet- and clinopyroxene-bearing source.

The small component of recycled oceanic crust inferred in the ferropicrite source could be the origin of the minor enriched mantle material revealed by modelling of the Sr-isotopic compositions of the Doros suite (Section 10.3).

10.6 A petrogenetic model for Doros-Tafelkop magmatism

On this basis, a petrogenetic model is envisaged as follows (Fig. 10.13):

1) The proto-Tristan plume ascended through the mantle, and in the process, entrained ambient mantle material, including minor garnet pyroxenite (recycled oceanic crust);

2) As it ascended, at depths of > 165 km, adiabatic decompression led to partial melting in the plume head. The pyroxene-rich components began to melt first, followed by peridotite;
3) These early melts rose up through the crust, fractionating in the processes, via a series of interconnected conduits and chambers, including the shallow-level Doros intrusion. Ultimately a component of this melt was erupted on surface as the Tafelkop lava sequence;
4) Impingement of the plume on the base of the lithosphere and increased lithospheric thinning led to rapid upwelling of the mantle and greater volumes of melting, producing the main episode of flood volcanism (and associated intrusive magmatism) in the Paraná-Etendeka event.

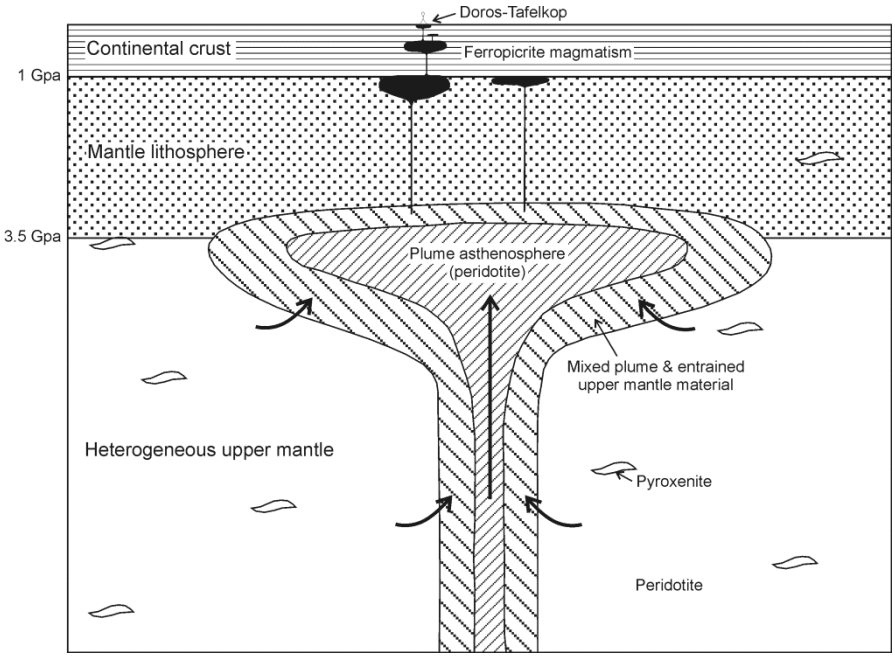


Figure 10.13: Schematic illustration (after Gibson, 2002; Tuff *et al*., 2005) of the petrogenetic model envisaged for the Doros-Tafelkop magmatism (see text for explanation). Early melts of peridotitic and pyroxenitic material in the rising Tristan plume head (initially separated at ≥ 5 GPa) produced ferropicritic melts with a negligible crustal or lithospheric mantle component.

10.7 Summary of findings

The Doros magmas all originated from the same mantle source and melting episode. This source comprised enriched, plume-derived asthenospheric material and entrained, depleted mantle material, with a negligible contribution from an enriched component, likely relict subducted material in the source. The chill margin is the only material in the complex to show evidence of crustal contamination, in the form of wall-rock assimilation during emplacement. The Doros magmas likely originated from relatively deep, early decompression melting of pyroxenitic material in the heterogeneous Tristan plume starting head. A component of this magma erupted on surface to form the Tafelkop group lavas basal to the Etendeka succession. The dolerite dykes that cross-cut the Doros intrusion are part of the late-stage Horingbaai suite of the Etendeka LIP.

Chapter 11: Conclusions

11.1 Introduction

This thesis has presented extensive new petrographic, geochemical and geophysical data for the Doros Gabbroic Complex, a layered intrusion within the early Cretaceous Paraná-Etendeka Large Igneous Province (LIP) in Namibia. These include whole-rock rare earth element and radiogenic isotope analyses, melt inclusion analyses, as well as aeromagnetic and physical property data, none of which have previously been obtained for this intrusion. This arguably constitutes the most comprehensive and wide-ranging study of any of the Damaraland Complexes to date.

The results of the study make important contributions in three main fields of research. Firstly, they have led to improved characterisation and knowledge of the geology and geometry of the Doros intrusion, both on the surface and at depth. Secondly, they have provided insight into the emplacement dynamics and crystallisation history of the intrusion, which has implications, by example, for other layered mafic intrusions. Finally, these results have shed light on the mantle source of the magmatism and its relation to regional tectonomagmatic events in the context of the Paraná-Etendeka LIP.

11.2 Geology and geometry of the Doros intrusion

Layered mafic intrusions (LMI) have been the focus of many decades of research, since they preserve a unique record of the spectrum of melting and differentiation processes operating in magma systems and provide a vital link between melt generation at depth and eruption on surface. Despite the attention they have received and the progress that has been made, there are still many fundamental questions concerning the origin of such intrusions that remain unanswered, or at least, lack consensus. Specifically these pertain to the nature of the input material, the style and mechanism of emplacement, the conditions and processes of differentiation, the formation of igneous layering and the connection between magma chambers and the greater magmatic system. The first step in our quest for a better understanding of these enigmatic features is the characterisation of individual LMIs, in terms of their geometries, the nature of the layering and their compositions both on a small and large scale. A better characterisation of the geology and geometry of the Doros intrusion is a primary contribution of this Ph.D. thesis.

Previous research on the Doros Complex (Reuning & Martin, 1957; Hodgson & Botha, 1974; Marsh & Duncan, 2008) largely entailed mapping and limited chemistry, for the purposes of characterisation, and a rudimentary interpretation of the crystallisation history. In this study, detailed mapping, sampling and field observations, combined with aeromagnetic image interpretation and forward modelling, have provided better constraints on the surface extents and contact relations of the constituent lithologies, as

well as the 3D geometry of the Doros intrusion. The intrusion was determined to be a shallow-level lopolith, at least 500 m thick (an improvement on previous estimates derived solely from surface data), emplaced into the metasedimentary rocks of the Damara Orogenic Belt and the overlying Karoo strata. As a suggestion for future research, the addition of a gravity (and/or seismic) study, in combination with the existing aeromagnetic data, could contribute to better constraining the geometry of the host lithologies at depth, and potentially to elucidating the sub-surface Doros feeder system.

The main body of the Doros intrusion has been shown to consist of a sequence of roughly-concordant, sill-like gabbro layers, dipping in towards the centre. The stratigraphy broadly comprises a partially-exposed, fine-grained gabbroic sill, overlain by a sequence of massive, olivine-cumulate melagabbros, followed by a massive, plagioclase-cumulate gabbro layer, and topped by a series of variable, strongly foliated, plagioclase-, olivine- or magnetite-cumulate gabbro layers. A syenitic (bostonite) phase occurs as cross-cutting dykes or enclaves within the gabbros. The fundamental mineralogy is essentially the same throughout the main package (plagioclase + calcic clinopyroxene + oxy-exsolved Fe-Ti oxides ± olivine), and hence the layering is defined by variations in the modal proportions of these minerals, and in the mineral and rock textures.

A detailed petrographic study and an extensive set of whole-rock and mineral major and trace element analyses, combined with major element modelling, have shown that the stratigraphic order of appearance of cumulus minerals and overall trends in rock compositions are consistent with the fractional crystallisation of olivine, clinopyroxene, plagioclase, magnetite, K-feldspar and apatite, accompanied by variable degrees of accumulation, from a basaltic parental magma. Melt inclusion chemical analyses and trace element inverse modelling has allowed further constraints to be placed on the composition of the parental liquid.

11.3 Emplacement dynamics and the magmatic mush column hypothesis

Most previous interpretations and modelling of the origins of the layering in mafic intrusions have been largely predicated on the assumption of formation by emplacement as a single batch of crystal-free melt, and hence have centred on the processes resulting from convection, crystallisation and compaction within the magma chamber. However, a growing body of literature suggests that this initial assumption is not, in fact, the norm and that the injection process itself has a far greater role to play than previously supposed. There is increasing consensus that large magma bodies grow from multiple incremental, small-volume, sill-like emplacements of magma, and not from a single instantaneous, large-volume emplacement. Marsh (2004) has pioneered the idea that there is a complex magmatic system of staging chambers and conduits from source to surface, all actively processing and crystallising magma, at overlapping times – the magmatic mush column. The resulting material erupted on surface, or observed in a high-level intrusion, therefore is argued to have had a complex, multi-stage, multi-depth history of differentiation. The Doros Complex has provided a unique opportunity to evaluate this hypothesis, the second major thrust of the thesis.

Based on the combined field, petrographic, geochemical and geophysical evidence from this research, a compelling argument has been put forward in favour of an origin for the Doros Complex by multiple, closely-spaced influxes of crystal-bearing magmas (magma mushes), rather than from the post-emplacement differentiation of a single batch of liquid magma. This evidence includes intrusive layer relations, textural evidence for primocrysts, disequilibrium features, and stratigraphic reversals in mineral and whole-rock chemistry and magnetic properties. At least seven distinct major injections of magma have been identified in the stratigraphy, as well as several smaller pulses. Based on this interpretation, a comprehensive emplacement history for the Doros intrusion has been compiled. It is suggested that precise dating of the Doros gabbros and bostonite dykes in future may further constrain the relative chronology of emplacement.

These findings represent a departure from the traditional single-pulse liquid magma model for the formation of such intrusions and provide strong support for the magmatic mush column hypothesis. This further implies the existence of one or more staging chambers below the Doros Complex and a high magma flux. These results may also be applied in part to other, larger LMIs, where the emplacement history is more obscure. There is clearly considerable complexity that exists at every scale. Most importantly, these findings emphasise the role of phenocryst-bearing magmas in the construction of LMIs, and the significance of open system processes.

11.4 Nature of the Doros source and implications for the LIP

The Paraná-Etendeka Large Igneous Province is one of the largest known LIPs and has been attributed to the impact of the Tristan mantle plume on the lithosphere and the associated opening of the South Atlantic Ocean, during the early Cretaceous breakup of West Gondwana. While the geochemistry of the Paraná and Etendeka bimodal volcanic rocks has been extensively studied, there is still little agreement on the exact role of the mantle plume in the production of the magma types observed. This is largely because the majority of the lavas do not show a recognisable plume signature, since their primary compositions have been obscured by crustal contamination. Furthermore, while it has long been speculated that the Damaraland Intrusive Suite contributed material to the volcanic succession, this has relied largely on evidence of proximity and contemporaneity. The final major contribution of this thesis is the insight it provides into the mantle source of the Doros magmas and its relation to regional tectonomagmatic events in the LIP.

A comprehensive trace element and Sr-, Nd- and Pb- isotopic analysis of the Doros rock types in this study has shown that all the Doros magmas originated from the same mantle source and melting episode. In addition, a significant Tristan plume component was identified in this source, confirming the integral role of the plume in Paraná-Etendeka magmatism. Quantitative isotopic modelling of mixing processes has constrained the source of the magmas to comprise a dominant depleted MORB-like mantle

component (60 - 80%), with a lesser enriched, plume-derived, asthenospheric component (20 - 40%) and a minor contribution likely from recycled oceanic crust (< 5%). The chilled margin to the complex is the only rock type that shows significant evidence of crustal contamination, due to local assimilation of the Damaran host rock on emplacement.

Furthermore, this research has provided crucial evidence in support of Doros as the eruptive site for the Tafelkop "ferropicrite" lavas of the Etendeka Province, corroborating the proposed genetic relationship between the Damaraland intrusions and the flood volcanic succession, and thereby linking the Doros magmatism to the earliest eruptive phase in the Paraná-Etendeka event. The distinctive chemistry of this magma group has been attributed to the early, relatively deep, decompression melting of pyroxenitic material in the heterogeneous Tristan plume starting head, corresponding with the initial impact of the plume on the base of the lithosphere. These early LIP magmas are interpreted to form prior to significant thinning and conductive heating of the lithosphere and therefore do not show a lithospheric mantle and/or crustal component, as is ubiquitous in the remainder of the Paraná-Etendeka intrusive and extrusive suite. Precise geochronology and/or a detailed palaeomagnetic study correlated with existing magnetostratigraphy for the Etendeka succession may contribute to constraining the timing of Doros magmatism within the Paraná-Etendeka event and corroborate these findings.

In summary, this research has made a valuable contribution to our understanding of the petrogenesis and mode of emplacement of the Doros layered intrusion and its relation to the greater Paraná-Etendeka magmatic system in the early Cretaceous.

References

Albarède, F. (1996). *Introduction to Geochemical Modelling.* Cambridge: Cambridge University Press, 543 pp.

Allègre, C. J., Lewin, E., & Dupré, B. (1988). A coherent crust-mantle model for the uranium-thorium-lead isotopic system. *Chemical Geology*, *70*, 211-234.

Anders, E., & Grevesse, N. (1989). Abundances of the elements: Meteoritic and solar. *Geochimica et Cosmochimica Acta, 53*, 197-214.

Andersen, D. J., & Lindsley, D. H. (1985). New (and final!) models for the Ti-magnetite/ilmenite geothermometer and oxygen barometer. *Abstract AGU 1985 Spring Meeting, Eos Transactions. 66*, p. 416. American Geophysical Union.

Anderson, D. L. (2005). Large Igneous Provinces, Delamination, and Fertile Mantle. *Elements, 1*, 271-275.

Annen, C. (2011). Implications of incremental emplacement of magma bodies for magma differentiation, thermal aureole dimensions and plutonism-volcanism relationships. *Tectonophysics, 500*, 3-10.

Ariskin, A. A., & Yaroshevsky, A. A. (2006). Crystallization Differentiation of Intrusive Magmatic Melt: Development of a Convection-Accumulation Model. *Geochemistry International, 44*(1), 72-93.

Ashwal, L. D., Webb, S. J., & Knoper, M. W. (2005). Magmatic stratigraphy in the Bushveld Northern Lobe: continuous geophysical and mineralogical data from the 2950 m Bellevue drillcore. *South African Journal of Geology, 108*, 199-232.

Asimow, P. D., & Ghiorso, M. S. (1998). Algorithmic Modifications Extending MELTS to Calculate Subsolidus Phase Relations. *American Mineralogist, 83*, 1127-1131.

Bachmann, O., & Bergantz, G. (2008). The Magma Reservoirs That Feed Supereruptions. *Elements, 4*, 17-21.

Barbey, P. (2009). Layering and schlieren in granitoids: A record of interactions between magma emplacement, crystallization and deformation in growing plutons. *Geologica Belgica, 12*(3/4), 109-133.

Bauer, K., Trumbull, R. B., & Vietor, T. (2003). Geophysical images and a crustal model of intrusive structures beneath the Messum ring complex, Namibia. *Earth and Planetary Science Letters, 216*, 65-80.

Beard, J. S., & Day, H. W. (1986). Origin of gabbro pegmatite in the Smartville intrusive complex, northern Sierra Nevada, California. *American Mineralogist, 71*, 1085-1099.

Bédard, J. H. (2005). Partitioning coefficients between olivine and silicate melts. *Lithos, 83*, 394-419.

Bédard, J. H. (2006a). Trace element partitioning in plagioclase feldspar. *Geochimica et Cosmochimica Acta, 70*, 3717-3742.

Bédard, J. H. (2006b). A catalytic delamination-driven model for coupled genesis of Archaean crust and sub-continental lithospheric mantle. *Geochimica et Cosmochimica Acta, 70*, 1188-1214.

Bédard, J. H. (2009). Parental magmas of Grenville Province massif-type anorthosites, and conjectures about why massif anorthosites are restricted to the Proterozoic. *Earth and Environmental Science Transactions of the Royal Society of Edinburgh, 100*, 1-27.

Bédard, J. H., Marsh, B. D., Hersum, T. G., Naslund, H. R., & Mukasa, S. B. (2007). Large-scale Mechanical Redistribution of Orthopyroxene and Plagioclase in the Basement Sill, Ferrar Dolerites, McMurdo

DryValleys, Antarctica: Petrological, Mineral-chemical and Field Evidence for Channelized Movement of Crystals and Melt. *Journal of Petrology, 48*(12), 2289-2326.

Berg, J. H., & Docka, J. A. (1983). Geothermometry in the Kiglapait contact aureole, Labrador. *American Journal of Science, 283*, 414-434.

Blatt, H., & Tracy, R. J. (1996). *Petrology: Igneous, Sedimentary, and Metamorphic* (2nd ed.). New York: W. H. Freeman, 529 pp.

Boudreau, A. E., & McBirney, A. R. (1997). The Skaergaard Layered Series. Part III. Non-dynamic Layering. *Journal of Petrology, 38*(8), 1003-1020.

British Geological Survey. (2013). *International Geomagnetic Reference Field (IGRF) Synthesis Form*. Retrieved December 6, 2013, from http://www.geomag.bgs.ac.uk/data_service/models_compass/igrf.html.

Bryan, S. E., & Ernst, R. E. (2008). Revised definition of Large Igneous Provinces (LIPs). *Earth-Science Reviews, 86*, 175-202.

Buddington, A. F., & Lindsley, D. H. (1964). Iron-titanium oxide minerals and synthetic equivalents. *Journal of Petrology, 5*, 310-357.

Campbell, I. H. (2005). Large Igneous Provinces and the mantle plume hypothesis. *Elements, 1*, 265-269.

Cawthorn, R. G. (2012). Multiple sills or a layered intrusion? Time to decide. *South African Journal of Geology, 115*(3), 283-290.

Cawthorn, R. G., & Walraven, F. (1998). Emplacement and Crystallization Time for the Bushveld Complex. *Journal of Petrology, 39*(9), 1669-1687.

Cawthorn, R. G., Eales, H. V., Walraven, F., Uken, R., & Watkeys, M. K. (2006). The Bushveld Complex. In M. R. Johnson, C. R. Anhaeusser, & R. J. Thomas, *The Geology of South Africa*. Johannesburg/ Pretoria: Geological Society of South Africa/ Council for Geoscience, pp. 261-281.

Charlier, B., Namur, O., Toplis, M. J., Schiano, P., Cluzel, N., Higgins, M. D., & Vander Auwera, J.(2011). Large-scale silicate liquid immiscibility during differentiation of tholeiitic basalt to granite and the origin of the Daly gap. *Geology, 39*, 907-910.

Chesley, J. T., & Ruiz, J. (1998). Crust–mantle interaction in large igneous provinces: Implications from the Re-Os isotope systematics of the Columbia River flood basalts. *Earth and Planetary Science Letters, 154*, 1-11.

Clark, D. A. (1997). Magnetic petrophysics and magnetic petrology: aids to geological interpretation of magnetic surveys. *Journal of Australian Geology & Geophysics, 17*(2), 83-103.

Clark, D. A. (1999). Magnetic petrology of igneous intrusions: implications for exploration and magnetic interpretation. *Exploration Geophysics, 30*, 5-26.

Cliff, R. A., Baker, P. E., & Mateer, N. J. (1991). Geochemistry of Inaccessible Island volcanics. *Chemical Geology, 92*, 251-260.

Coffin, M. F., & Edholm, O. (1992). Volcanism and continental break-up: a global compilation of large igneous provinces. In B. C. Storey, T. Alabaster, & R. J. Pankhurst (Eds.), *Magmatism and the Causes of Continental Break-up* (No. 68). Geological Society, London, Special Publications, pp. 17-30.

Cohen, R. S., & O'Nions, R. K. (1982). Identification of recycled continental material in the mantle from Sr, Nd and Pb isotope investigations. *Earth and Planetary Science Letters, 61*, 73-84.

Coleman, D. S., Gray, W., & Glazner, A. F. (2004). Rethinking the emplacement and evolution of zoned plutons: Geochronologic evidence for incremental assembly of the Tuolumne Intrusive Suite, California. *Geology, 32*, 433-436.

Cooper, G. R. (2004). Mag2dc Version 2.11 for Microsoft Windows. School of Geosciences, University of the Witwatersrand, Johannesburg, South Africa, from http://www.wits.ac.za/academic/science/geosciences/research/geophysics/gordoncooper/6511.

Courtillot, V., & Renne, P. R. (2003). On the ages of flood basalt events. *Comptes Rendus Geoscience, 335*, 113-140.

Danyushevsky, L. V., Della-Pasqua, F. N., & Sokolov, S. (2000). Re-equilibration of melt inclusions trapped by magnesian olivine phenocrysts from subduction-related magmas: petrological implications. *Contributions to Mineralogy and Petrology, 138*, 68-83.

Danyushevsky, L. V., Leslie, R. A., Crawford, A. J., & Durance, P. (2004). Melt Inclusions in Primitive Olivine Phenocrysts: the Role of Localized Reaction Processes in the Origin of Anomalous Compositions. *Journal of Petrology, 45*(12), 2531-2553.

de Saint-Blanquat, M., Horsman, E., Habert, G., Morgan, S., Vanderhaeghe, O., Law, R., & Tikoff, B. (2011). Multiscale magmatic cyclicity, duration of pluton construction, and the paradoxical relationship between tectonism and plutonism in continental arcs. *Tectonophysics, 500*, 20-33.

Deer, W. A., Howie, R. A., & Zussman, J. (1992). *An Introduction to the Rock-Forming Minerals* (2nd ed.). London: Longman, pp. 696.

Defant, M. J., & Drummond, M. S. (1990). Derivation of some modern arc magmas by melting of young subducted lithosphere. *Nature, 347*(6294), 662-665.

Douglass, J., Schilling, J. G., & Fontignie, D. (1999). Plume-ridge interactions of the Discovery and Shona mantle plumes with the southern Mid-Atlantic Ridge (40°-55°S). *Journal of Geophysical Research, 104*(B2), 2941-2962.

Duncan, A. R., Milner, S. C., & Jerram, D. A. (1998). Southern Etendeka Volcanism, northwestern Namibia. *'Magmatic diversity: Volcanoes and their roots', Excursion Guide, Field Excursion C4, IAVCEI International Volcanology Congress*.

Elburg, M., Kamenetsky, V. S., Nikogosian, I., Foden, J., & Sobolev, A. V. (2006). Coexisting High- and Low-Calcium Melts Identified by Mineral and Melt Inclusion Studies of a Subduction-Influenced Syncollisional Magma from South Sulawesi, Indonesia. *Journal of Petrology, 47*(12), 2433-2462.

Erlank, A. J., Marsh, J. S., Duncan, A. R., Miller, R. M., Hawkesworth, C. J., Betton, P. J., & Rex, D. C.. (1984). Geochemistry and petrogenesis of the Etendeka volcanic rocks from SWA/Namibia. In A. J. Erlank, *Petrogenesis of the Volcanic Rocks of the Karoo Province, Special Publication of the Geological Society of South Africa* (Vol. 13). Johannesburg: Geological Society of South Africa, pp. 195-245.

Ernesto, M., Marques, L. S., Piccirillo, E. M., Molina, E. C., Ussami, N., Comin-Chiaramonti, P., & Bellieni, G. (2002). Paraná Magmatic Province-Tristan da Cunha plume system:fixed versus mobile plume, petrogenetic considerations and alternative heat sources. *Journal of Volcanology and Geothermal Research, 118*, 15-36.

Ernst, R. E., & Buchan, K. L. (2003). Recognising mantle plumes in the geological record. *Annual Reviews of Earth and Planetary Sciences, 31*, 469-523.

Ernst, R. E., Buchan, K. E., & Campbell, I. H. (2005). Frontiers in Large Igneous Province research. *Lithos, 79*, 271-297.

Ewart, A., Marsh, J. S., Milner, S. C., Duncan, A. R., Kamber, B. S., & Armstrong, R. A. (2004a). Petrology and Geochemistry of Early Cretaceous Bimodal Continental Flood Volcanism of the NW Etendeka, Namibia. Part 1: Introduction, Mafic Lavas and Re-evaluation of Mantle Source Components. *Journal of Petrology, 45*(1), 59-105.

Ewart, A., Marsh, J. S., Milner, S. C., Duncan, A. R., Kamber, B. S., & Armstrong, R. A. (2004b). Petrology and Geochemistry of Early Cretaceous Bimodal Continental Flood Volcanism of the NW Etendeka, Namibia. Part 2: Characteristics and Petrogenesis of the High-Ti Latite and High-Ti and Low-Ti Voluminous Quartz Latite Eruptives. *Journal of Petrology, 45*(1), 107-138.

Ewart, A., Milner, S. C., Armstrong, R. A., & Duncan, A. R. (1998a). Etendeka Volcanism of the Goboboseb Mountains and Messum Igneous Complex, Namibia. Part I: Geochemical Evidence of Early Cretaceous Tristan Plume Melts and the Role of Crustal Contamination in the Paraná–Etendeka CFB. *Journal of Petrology, 39*(2), 191-225.

Ewart, A., Milner, S. C., Armstrong, R. A., & Duncan, R. A. (1998b). Etendeka Volcanism of the Goboboseb Mountains and Messum Igneous Complex, Namibia. Part II: Voluminous Quartz Latite Volcanism of the Awahab Magma System. *Journal of Petrology, 39*(2), 227-253.

Faure, G., & Mensing, T. M. (2005). *Isotopes: Principles and Applications* (3rd ed.). New Jersey: John Wiley, pp. 897.

Fedo, C. M., Nesbitt, H. W., & Young, G. M. (1995). Unraveling the effects of potassium metasomatism in sedimentary rocks and paleosols, with implications for paleoweathering conditions and provenance. *Geology, 23*, 921-924.

Ferris, J., Johnson, A., & Storey, B. (1998). Form and extent of the Dufek intrusion, Antarctica, from newly compiled aeromagnetic data. *Earth and Planetary Science Letters, 154*, 185-202.

Fontignie, D., & Schilling, J.-G. (1996). Mantle heterogeneities beneath the South Atlantic: a Nd-Sr-Pb isotope study along the Mid-Atlantic Ridge (3°S-46°S). *Earth and Planetary Science Letters, 142*, 209-221.

Foss, C. (2006). Evaluation of strategies to manage remanent magnetization effects in magnetic field inversion. *76th SEG Annual Meeting.* New Orleans: Society of Exploration Geophysicists, doi:10.1190/1.2370410.

Foulger, G. R. (2002). Plumes, or plate tectonic processes? *Astronomy and Geophysics, 43*, 6.19-6.23.

Frost, B. R. (1991). Introduction to oxygen fugacity and its petrologic importance. (D. H. Lindsley, Ed.) *Oxide Minerals: Petrologic and Magnetic Significance, Reviews in Mineralogy, 25*, pp. 1-9.

Frost, B. R., & Lindsley, D. H. (1991). Occurrence of iron-titanium oxides in igneous rocks. (D. H. Lindsley, Ed.) *Oxide Minerals: Petrologic and Magnetic Significance, Reviews in Mineralogy, 25*, pp. 433-468.

Gaetani, G., Cherniak, D., & Watson, B. (2002). Diffusive Reequilibration of CaO in Olivine-Hosted Melt Inclusions. *Geochimica et Cosmochimica Acta, 66 Supplement 1*, 254.

Gallagher, K., & Hawkesworth, C. J. (1994). Mantle plumes, continental magmatism and asymmetry in the South Atlantic. *Earth and Planetary Science Letters, 123*, 105-117.

Galland, O., Planke, S., Neumann, E., & Malthe-Sørenssen, A. (2009). Experimental modelling of shallow magma emplacement: Application to saucer-shaped intrusions. *Earth and Planetary Science Letters, 277*, 373-383.

Ghiorso, M. S., & Sack, R. O. (1995). Chemical Mass Transfer in Magmatic Processes. IV. A Revised and Internally Consistent Thermodynamic Model for the Interpolation and Extrapolation of Liquid-Solid Equilibria in Magmatic Systems at Elevated Temperatures and Pressures. *Contributions to Mineralogy and Petrology, 119*, 197-212.

Gibb, F. G., & Henderson, C. M. (1992). Convection and crystal settling in sills. *Contributions to Mineralogy and Petrology, 109*, 538-545.

Gibb, F. G., & Henderson, C. M. (2006). Chemistry of the Shiant Isles Main Sill, NW Scotland, and Wider Implications for the Petrogenesis of Mafic Sills. *Journal of Petrology, 47*(1), 191-230.

Gibson, S. A. (2002). Major element heterogeneity in Archean to Recent mantle plume starting-heads. *Earth and Planetary Science Letters, 195*, 59-74.

Gibson, S. A., Thompson, R. A., & Dickin, A. P. (2000). Ferropicrites: geochemical evidence for Fe-rich streaks in upwelling mantle plumes. *Earth and Planetary Science Letters, 174*, 355-374.

Gibson, S. A., Thompson, R. N., & Day, J. A. (2006). Timescales and mechanisms of plume-lithosphere interactions: $^{40}Ar/^{39}Ar$ geochronology and geochemistry of alkaline igneous rocks from the Paraná-Etendeka large igneous province. *Earth and Planetary Science Letters, 251*, 1-17.

Gibson, S. A., Thompson, R. N., Dickin, A. P., & Leonardos, O. H. (1995). High-Ti and low-Ti mafic potassic magmas: Key to plume-lithosphere interactions and continental flood-basalt genesis. *Earth and Planetary Science Letters, 136*, 149-165.

Gibson, S. A., Thompson, R. N., Leonardos, O. H., Dickin, A. P., & Mitchell, J. G. (1999). The limited extent of plume-lithosphere interactions during continental flood-basalt genesis: geochemical evidence from Cretaceous magmatism in southern Brazil. *Contributions to Mineralogy and Petrology, 137*, 147-169.

Glazner, A. F., Bartley, J. M., Coleman, D. S., Gray, W., & Taylor, R. Z. (2004). Are plutons assembled over millions of years by amalgamation from small magma chambers? *GSA Today, 14*(4/5), 4-11.

Godel, B., Barnes, S. J., & Maier, W. D. (2011). Parental magma composition inferred from trace element in cumulus and intercumulus silicate minerals: An example from the Lower and Lower Critical Zones of the Bushveld Complex, South-Africa. *Lithos, 125*, 537–552.

Goldstein, S. L., O'Nions, R. K., & Hamilton, P. J. (1984). A Sm-Nd isotopic study of atmospheric dusts and particulates from major river systems. *Earth and Planetary Science Letters, 70*, 221-236.

Google Earth Pro 7.0.2. (2010). Doros Crater, 20°45'14.31"S 14°17'19.36"E, eye alt. 11.33 m. GeoEye 2013.

Gorring, M. L., & Naslund, H. R. (1995). Geochemical reversals within the lower 100 m of the Palisades sill, New Jersey. *Contributions to Mineralogy and Petrology, 119*, 263-276.

Goudie, A. S., & Eckardt, F. (1999). The evolution of the morphological framework of the Central Namib Desert, Namibia, since the early Cretaceous. *Geografiska Annaler, 81A*(3), 443-458.

Green, D. H., & Ringwood, A. E. (1967). The genesis of basaltic magmas. *Contributions to Mineralogy and Petrology, 15*(2), 103-190.

Grove, T. L., Kinzler, R. J., & Bryan, W. B. (1992). Fractionation of mid-ocean ridge basalt (MORB). (J. P. Morgan, D. K. Blackman, & J. M. Sinton, Eds.) *Mantle Flow and Melt Generation at Mid-Ocean Ridges*, American Geophysical Union, Geophysical Monograph, 92, pp. 281-310.

Gudmundsson, A. (2011). Deflection of dykes into sills at discontinuities and magma-chamber formation. *Tectonophysics, 500*, 50-64.

Habert, G., & de Saint-Blanquat, M. (2004). Rate of construction of the Black Mesa bysmalith, Henry Mountains, Utah. *Geological Society, London, Special Publications, 234*, 163-173.

Haggerty, S. E. (1991). Oxide Textures - A Mini-Atlas. (D. H. Lindsley, Ed.) *Oxide Minerals: Petrologic and Magnetic Significance, Reviews in Mineralogy, 25*, pp. 129-219.

Haggerty, S. E., & Baker, I. (1967). The Alteration of Olivine in Basaltic and Associated Lavas Part I: High Temperature Alteration. *Contributions to Mineralogy and Petrology, 16*, 233-257.

Hanan, B. B., Kingsley, R. H., & Schilling, J. G. (1986). Pb isotope evidence in the South Atlantic for migrating ridge-hot spot interactions. *Nature, 322*, 137-144.

Harris, C., Marsh, J. S., & Milner, S. C. (1999). Petrology of the Alkaline Core of the Messum Igneous Complex, Namibia: Evidence for the Progressively Decreasing Effect of Crustal Contamination. *Journal of Petrology, 40*(9), 1377-1397.

Hart, S. R. (1984). A large-scale isotopic anomaly in the southern hemisphere mantle. *Nature, 309*, 753-757.

Hart, S. R. (1988). Heterogeneous mantle domains: signatures, genesis and mixing chronologies. *Earth and Planetary Science Letters, 90*, 273-296.

Hawkesworth, C. J., Gallagher, K., Kelley, S., Mantovani, M., Peate, D. W., Regelous, M., & Rogers, N. W. (1992). Paraná magmatism and the opening of the South Atlantic. In B. C. Storey, T. Alabaster, & R. J. Pankhurst (Eds.), *Magmatism and the Causes of Continental Break-up* (Vol. 68). Geological Society, London, Special Publications, pp. 221-240.

Hawkesworth, C., & Scherstén, A. (2007). Mantle plumes and geochemistry. *Chemical Geology, 241*, 319-331.

Henderson, C. M., Gibb, F. G., & Foland, K. A. (2000). Mineral fractionation and pre- and post-emplacement processes in the uppermost part of the Shiant Isles Main Sill. *Mineralogical Magazine, 64*(5), 779-790.

Herzberg, C. (1995). Generation of plume magmas through time: an experimental perspective. *Chemical Geology, 126*, 1-16.

Herzberg, C. (2011). Identification of Source Lithology in the Hawaiian and Canary Islands: Implications for Origins. *Journalof Petrology, 52*(1), 113-146.

Himmelberg, G. R., & Ford, A. B. (1977). Iron-titaniumo xideso f the Dufek intrusion, Antarctica. *American Mineralogist, 62*, 623-633.

Hirschmann, M. M., Ghiorso, M. S., & Stolper, E. M. (1999). Calculation of Peridotite Partial Melting from Thermodynamic Models of Minerals and Melts. II. Isobaric Variations in Melts near the Solidus and owing to Variable Source Composition. *Journal of Petrology, 40*(2), 297-313.

Hodgson, F. D., & Botha, B. J. (1974). The Doros Complex, South West Africa. *Neues Jahrbuch für Mineralogie - Monatshefte, 9*, 398-418.

Holness, M. B. (2005). Spatial Constraints on Magma Chamber Replenishment Events from Textural Observations of Cumulates: the Rum Layered Intrusion, Scotland. *Journal of Petrology, 46*(8), 1585-1601.

Holness, M. B., & Isherwood, C. E. (2003). The aureole of the Rum Tertiary Igneous Complex, Scotland. *Journal of the Geological Society, London, 160*, 15-27.

Holness, M. B., Stripp, G., Humphreys, M. C., Veksler, I. V., Nielsen, T. F., & Tegner, C. (2011). Silicate Liquid Immiscibility within the Crystal Mush: Late-stage Magmatic Microstructures in the Skaergaard Intrusion, East Greenland. *Journal of Petrology, 52*(1), 175-222.

Horstman, E. L. (1957). The distribution of lithium, rubidium and caesium in igneous and sedimentary rocks. *Geochimica et Cosmochimica Acta, 12*, 1-28.

Hort, M., Marsh, B. D., & Spohn, T. (1993). Igneous layering through oscillatory nucleation and crystal settling in well-mixed magmas. *Contributions to Mineralogy and Petrology, 114*, 425-440.

Humphris, S. E., & Thompson, G. (1985). Petrological and geochemical variations along the Mid-Atlantic Ridge between 46°S and 32°S: Influence of the Tristan da Cunha mantle plume. *Geochimica et Cosmochimica Acta, 49*, 1445-1464.

Huppert, H. E., & Sparks, R. S. (1984). Double-diffusive convection due to crystallization in magmas. *Annual Reviews in Earth and Planetary Sciences, 12*, 11-37.

Husch, J. M. (1990). Palisades Sill: Origin of the olivine zone by separate magmatic injection rather than gravity settling. *Geology, 18*, 699-702.

Ila, P., & Frey, F. A. (2000). Trace element analysis of USGS standards AGV2, BCR2, BHVO2, DTS2 and GSP2 by INAA. *Journal of Radioanalytical and Nuclear Chemistry, 244*(3), 599-602.

Irving, A. J., & Frey, F. A. (1984). Trace-Element Abundances in Megacrysts and Their Host Basalts - Constraints on Partition-Coefficients and Megacryst Genesis. *Geochimica et Cosmochimica Acta, 48*(6), 1201-1221.

Ito, E., White, W. M., & Göpel, C. (1987). The O, Sr, Nd and Pb isotope geochemistry of MORB. *Chemical Geology, 62*, 157-176.

Ito, E., White, W. M., von Drach, V., Hofmann, A. W., & James, D. E. (1980). Isotopic studies of ocean ridge basalts. *Carnegie Institute of Washington Yearbook, 80*, 465-471.

Jackson, M. G., & Dasgupta, R. (2008). Compositions of HIMU, EM1, and EM2 from global trends between radiogenic isotopes and major elements in ocean island basalts. *Earth and Planetary Science Letters, 276*, 175-186.

Jakobsen, J. K., Tegner, C., Brooks, C. K., Kent, A. J., Lesher, C. E., Nielsen, T. F., & Wiedenbeck, M. (2010). Parental magma of the Skaergaard intrusion: constraints from melt inclusions in primitive troctolite blocks and FG-1 dykes. *Contributions to Mineralogy and Petrology, 159*, 61-79.

Jakobsen, J. K., Tegner, C., Veksler, I. V., & Brooks, C. K. (2005). Immiscible Iron- and Silica-rich Melts in the Skaergaard Intrusion: Implications for Igneous Differentiation and Mineralization. *Geology, 33*, 885-888.

Jenner, F. E., & O'Neill, H. S. (2012). Analysis of 60 elements in 616 ocean floor basaltic glasses. *Geochemistry Geophysics Geosystems, 13*, Q02005.

Jerram, D. A., Davis, G. R., Mock, A., Charrier, A., & Marsh, B. D. (2010). Quantifying 3D crystal populations, packing and layering in shallow intrusions: A case study from the Basement Sill, Dry Valleys, Antarctica. *Geosphere, 6*(5), 537-548.

Jerram, D., Mountney, N., Holzförster, F., & Stollhofen, H. (1999). Internal stratigraphic relationships in the Etendeka Group in the Huab Basin, NW Namibia: understanding the onset of flood volcanism. *Journal of Geodynamics, 28*, 393-418.

Jones, A. P., Price, G. D., Price, N. J., DeCarli, P. S., & Clegg, R. A. (2002). Impact induced melting and the development of large igneous provinces. *Earth and Planetary Science Letters, 202*, 551-561.

Jung, S., Mezger, K., & Hoernes, S. (1998). Petrology and geochemistry of syn- to post-collisional metaluminous A-type granites – a major and trace element and Nd–Sr–Pb–O-isotope study from the Proterozoic Damara Belt, Namibia. *Lithos, 45*, 147-175.

Kamber, B. S., & Collerson, K. D. (1999). Origin of ocean island basalts: A new model based on lead and helium isotope systematics. *Journal of Geophysical Research, 104*, 25479-25491.

Kamenetsky, V. S., & Gurenko, A. A. (2007). Cryptic crustal contamination of MORB primitive melts recorded in olivine-hosted glass and mineral inclusions. *Contributions to Mineralogy and Petrology, 153*, 465-481.

Kamenetsky, V. S., Sobolev, A. V., Eggins, S. M., Crawford, A. J., & Arculus, R. J. (2002). Olivine-enriched melt inclusions in chromites from low-Ca boninites, Cape Vogel, Papua New Guinea: evidence for ultramafic primary magma, refractory mantle source and enriched components. *Chemical Geology, 183*, 287-303.

Keiding, J. K., Trumbull, R. B., Veksler, I. V., & Jerram, D. A. (2011). On the significance of ultra-magnesian olivines in basaltic rocks. *Geology, 39*(12), 1095-1098.

Keiding, J. K., Trumbull, R. B., Veksler, I. V., & Jerram, D. A. (2011). On the significance of ultra-magnesian olivines in basaltic rocks. *Geology, 39*(12), 1095-1098.

Kelsey, C. H. (1965). Calculation of the C.I.P.W. norm. *Mineralogical Magazine, 34*, 276-282.

Kent, A. J. (2008). Melt inclusions in basaltic and related volcanic rocks. In K. D. Putirka, & F. J. Tepley (Eds.), *Reviews in Mineralogy and Geochemistry: Minerals, Inclusions and Vocanic Processes* (Vol. 69). Geochemical Society/Mineralogical Society of America, pp. 273-331.

Kent, A. J., Baker, J. A., & Wiedenbeck, M. (2002). Contamination and melt aggregation processes in continental flood basalts: constraints from melt inclusions in Oligocene basalts from Yemen. *Earth and Planetary Science Letters, 202*, 577-594.

Kent, A. J., Jacobsen, B., Peate, D. W., Waight, T. E., & Baker, J. A. (2004). Isotope Dilution MC-ICP-MS Rare Earth Element Analysis of Geochemical Reference Materials NIST SRM 6 10, NIST SRM 6 12, NIS T SRM 6 14, BHVO-2G, BHVO-2, BCR-2G, JB-2, WS-E, W-2, AGV-1 and AGV-2. *Geostandards and Geoanalytical Research, 28*(3), 417-429.

Kirstein, L. A., Kelley, S., Hawkesworth, C., Turner, S., Mantovani, M., & Wijbrans, J. (2001). Protracted felsic magmatic activity associated with opening of the South Atlantic. *Journal of the Geological Society, London, 158*, 583-592.

Kossert, K. (2003). Half-life measurements of ^{87}Rb by liquid scintillation counting. *Applied Radiation and Isotopes, 59*, 377-382.

Kramers, J. D., & Tolstikhin, I. N. (1997). Two terrestrial lead isotope paradoxes, forward transport modelling, core formation and the history of the continental crust. *Chemical Geology, 139*, 75-110.

Kruger, F. J. (2005). Filling the Bushveld Complex magma chamber: lateral expansion, roof and floor interaction, magmatic unconformities, and the formation of giant chromitite, PGE and Ti-V-magnetitite deposits. *Mineralium Deposita, 40*, 451-472.

Larsen, R. B., & Brooks, C. K. (1994). Origin and Evolution of Gabbroic Pegmatites in the Skaergaard Intrusion, East Greenland. *Journal of Petrology, 35*(6), 1651-1679.

Latypov, R. (2009). Testing theValidity of the Petrological Hypothesis 'No Phenocrysts, No Post-emplacement Differentiation'. *Journal of Petrology, 50*(6), 1047-1069.

Le Maitre, R. W. (1989). *A Classification Of Igneous Rocks And Glossary Of Terms. Recommendations of the IUGS Commission on the Systematics of Igneous Rocks.* Oxford: Blackwell, pp. 193.

Le Roex, A. P., & Lanyon, R. (1998). Isotope and Trace Element Geochemistry of Cretaceous Damaraland Lamprophyres and Carbonatites, Northwestern Namibia: Evidence for Plume-Lithosphere Interactions. *Journal of Petrology, 39*(6), 1117-1146.

Le Roex, A. P., Cliff, R. A., & Adair, B. J. (1990). Tristan da Cunha, South Atlantic: Geochemistry and Petrogenesis of a Basanite-Phonolite Lava Series. *Journal of Petrology, 31*(4), 779-812.

Le Roex, A. P., Dick, H. J., Gulen, L., Reid, A. M., & Erlank, A. J. (1987). Local and regional heterogeneity in MORB from the Mid-Atlantic Ridge between 54.5°S and 51°S: Evidence for geochemical enrichment. *Geochimica et Cosmochimica Acta, 51*, 541-555.

Le Roex, A. P., Watkins, R. T., & Reid, A. M. (1996). Geochemical evolution of the Okenyenya sub-volcanic ring complex, northwestern Namibia. *Geological Magazine, 133*(6), 645-670.

Le Roux, P. J. (2000). *The geochemistry of selected mid-ocean ridge basalts from the southern Mid-Atlantic Ridge (40-55°S).* Ph.D. Thesis, University of Cape Town.

Lemarchand, F., Benoit, V., & Calais, G. (1987). Trace element distribution coefficients in alkaline series. *Geochimica et Cosmochimica Acta, 51*, 1071-1081.

Lepage, L. D. (2003). ILMAT: an Excel worksheet for ilmenite-magnetite geothermometry and geobarometry. *Computers & Geosciences, 29*, 673-678.

Letts, S., Torsvik, T. H., Webb, S., & Ashwal, L. D. (2009). Palaeomagnetism of the 2054 Ga Bushveld Complex (South Africa): Implications for Emplacement and Cooling. *Geophysical Journal International, 179*(2), 850-872.

Li, C., Ripley, E. M., Sarkar, A., Shin, D., & Maier, W. D. (2005). Origin of phlogopite-orthopyroxene inclusions in chromites from the Merensky Reef of the Bushveld Complex, South Africa. *Contributions to Mineralogy and Petrology, 150*, 119-130.

Liou, J. G. (1971). Synthesis and stability relations of prehnite, Ca2Al2Si3O10(OH)2. *The American Mineralogist, 56*, 507-531.

Lister, G. F. (1966). The Composition and Origin of Selected Iron-Titanium Deposits. *Economic Geology, 61*, 275-310.

Loncarevic, B. D., Feininger, T., & Lefebvre, D. (1990). The Sept-Iles layered mafic intrusion: geophysical expression. *Canadian Journal of Earth Sciences, 27*, 501-512.

Lorenz, V. (2003). Maar-Diatreme Volcanoes, their Formation, and their Setting in Hard-rock or Soft-rock Environments. *GeoLines, 15*, 72-83.

Loucks, R. R. (1996). A precise olivine-augite Mg-Fe exchange geothermometer. *Contributions to Mineralogy and Petrology, 125*, 140-150.

Lowenstern, J. B. (2003). Melt Inclusions Come of Age: Volatiles, Volcanoes, and Sorby's Legacy. *Developments in Volcanology, 5*, 1-21.

Lugmair, G. W. (1978). Lunar initial $^{143}Nd/^{144}Nd$: Differential evolution of the lunar crust and mantle. *Earth and Planetary Science Letters, 39*, 349-357.

Malthe-Sørenssen, A., Planke, S., Svensen, H., & Jamtveit, B. (2004). Formation of saucer-shaped sills. *Geological Society, London, Special Publications, 234*, 215-227.

Mangan, M. T., & Marsh, B. D. (1992). Solidification Front Fractionation in Phenocryst-Free Sheet-Like Magma Bodies. *Journal of Geology, 100*(5), 605-620.

Marques, L. S., Dupré, B., & Piccirillo, E. M. (1999). Mantle source compositions of the Paraná Magmatic Province (southern Brazil): evidence from trace element and Sr-Nd-Pb isotope geochemistry. *Journal of Geodynamics, 28*, 439-458.

Marsh, B. (2004). A Magmatic Mush Column Rosetta Stone:The McMurdo Dry Valleys of Antarctica. *EOS, Transactions, American Geophysical Union, 85*(47), 497-508.

Marsh, B. (2006). Dynamics of Magmatic Systems. *Elements, 2*, 287-292.

Marsh, B. D. (1989). On Convective Style and Vigor in Sheet-like Magma Chambers. *Jounal of Petrology, 30*(3), 479-530.

Marsh, B. D. (1998). On the Interpretation of Crystal Size Distributions in Magmatic Systems. *Journal of Petrology, 39*(4), 553-599.

Marsh, B. D. (2013). On some fundamentals of igneous petrology. *Contributions to Mineralogy and Petrology, 166*, 665-690.

Marsh, J. S., & Duncan, A. R. (2008). Doros Gabbroic Complex. In R. M. Miller, *The Geology of Namibia* (Vol. 3). Windhoek: Geological Survey of Namibia, pp. 18-75 - 18-78.

Marsh, J. S., Ewart, A., Milner, S. C., Duncan, A. R., & Miller, R. M. (2001). The Etendeka Igneous Province: magma types and their stratigraphic distribution with implications for the evolution of the Paraná-Etendeka flood basalt province. *Bulletin of Volcanology, 62*, 464-486.

McBirney, A. R. (1989). The Skaergaard Layered Series: I. Structure and Average Compositions. *Journal of Petrology, 30*(2), 363-397.

McBirney, A. R., & Nakamura, Y. (1974). Immiscibility in late-stage magmas of the Skaergaard intrusion. *Carnegie Institution of Washington Yearbook, 73*, 348-352.

McBirney, A. R., & Nicolas, A. (1997). The Skaergaard Layered Series. Part II. Magmatic flow and Dynamic Layering. *Journal of Petrology, 38*(5), 569-580.

McCallum, I. S., Raedeke, I. D., & Mathez, E. A. (1980). Investigations of the Stillwater Complex: Part I. Stratigraphy and structure of the banded zone. *American Journal of Science, 280A*, 59-87.

McDermott, F., & Hawkesworth, C. J. (1990). Intracrustal recycling and upper-crustal evolution: A case study from the Pan-African Damara mobile belt, central Namibia. *Chemical Geology, 83*, 263-280.

McDermott, F., Harris, N. B., & Hawkesworth, C. J. (1996). Geochemical constraints on crustal anatexis: a case study from the Pan-African Damara granitoids of Namibia. *Contributions to Mineralogy and Petrology, 123*, 406-423.

McDonough, W. F. (1990). Constraints on the composition of the continental lithospheric mantle. *Earth and Planetary Science Letters, 101*, 1-18.

McDonough, W. F., & Sun, S.-s. (1995). The composition of the Earth. *Chemical Geology, 120*, 223-253.

McEnroe, S. A., Brown, L. L., & Robinson, P. (2009). Remanent and induced magnetic anomalies over a layered intrusion: Effects from crystal fractionation and magma recharge. *Tectonophysics, 478*, 119-134.

McKenzie, D., & O'Nions, R. K. (1991). Partial Melt Distributions from Inversion of Rare Earth Element Concentrations. *Journal of Petrology, 32*(5), 1021-1091.

Menand, T. (2011). Physical controls and depth of emplacement of igneous bodies: A review. *Tectonophysics, 500*, 11-19.

Meurer, W. P., & Boudreau, A. E. (1996). Compaction of Density-Stratified Cumulates: Effect on Trapped-Liquid Distribution. *The Journal of Geology, 104*(1), 115-120.

Michaut, C., & Jaupart, C. (2011). Two models for the formation of magma reservoirs by small increments. *Tectonophysics, 500*, 34-49.

Michel, J., Baumgartner, L., Putlitz, B., Schaltegger, U., & Ovtcharova, M. (2008). Incremental growth of the Patagonian Torres del Paine laccolith over 90 k.y. *Geology, 36*, 459-462.

Middlemost, E. A. (1994). Naming materials in the magma/igneous rock system. *Earth-Science Reviews, 37*, 215-224.

Míková, J., & Denková, P. (2007). Modified chromatographic separation scheme for Sr and Nd isotope analysis in geological silicate samples. *Journal of Geosciences, 52*, 221-226.

Miller, C. F., Furbish, D. J., Walker, B. A., Claiborne, L. L., Koteas, G. C., Bleick, H. A., & Miller, J. S.. (2011). Growth of plutons by incremental emplacement of sheets in crystal-rich host: Evidence from Miocene intrusions of the Colorado River region, Nevada, USA. *Tectonophysics, 500*, 65-77.

Miller, J. S. (2008a). Assembling a pluton... one increment at a time. *Geology, 36*, 511-512.

Miller, R. M. (2008b). Early Cretaceous Anorogenic Ring Complexes and Plutons of the Damaraland Suite. In R. M. Miller, *The Geology of Namibia* (Vol. 3). Windhoek: Geological Survey of Namibia, pp. 18-1 - 18-138.

Miller, R. M. (2008c). Early Cretaceous Etendeka Group. In R. M. Miller, *The Geology of Namibia* (Vol. 3). Windhoek: Geological Survey of Namibia, pp. 17-1 - 17-57.

Miller, R. M. (2008d). Karoo Supergroup. In R. M. Miller, *The Geology of Namibia* (Vol. 3). Windhoek: Geological Survey of Namibia, pp. 16-1 - 16-115.

Miller, R. M. (2008d). Neoproterozoic and Early Palaeozoic Rocks of the Damara Orogen. In R. M. Miller, *The Geology of Namibia* (Vol. 2). Windhoek: Geological Survey of Namibia, pp. 13-1 - 13-410.

Milligan, P. R., & Gunn, P. J. (1997). Enhancement and presentation of airborne geophysical data. *Journal of Australian Geology & Geophysics, 17*(2), 63-75.

Milner, S. C., & Duncan, A. R. (1987). Geochemical characterisation of quartz latite units in the Etendeka Formation. *Communications of the Geological Survey of South West Africa/Namibia, 3*, 83-90.

Milner, S. C., & Ewart, A. (1989). The geology of the Goboboseb Mountain volcanics and their relationship to the Messum Complex, Namibia. *Communications of the Geological Survey of Namibia, 5*, 31-40.

Milner, S. C., & Le Roex, A. P. (1996). Isotope characteristics of the Okenyenya igneous complex, northwestern Namibia: constraints on the composition of the early Tristan plume and the origin of the EM 1 mantle component. *Earth and Planetary Science Letters, 141*, 277-291.

Milner, S. C., Duncan, A. R., & Ewart, A. (1992). Quartz latite rheoignimbrite flows of the Etendeka Formation, north-western Namibia. *Bulletin of Volcanology, 54*, 200-219.

Milner, S. C., Duncan, A. R., Wittingham, A. M., & Ewart, A. (1995). Trans-Atlantic correlation of eruptive sequences and individual silicic volcanic units within the Paraná-Etendeka igneous province. *Journal of Volcanology and Geothermal Research, 69*, 137-157.

Mingram, B., Trumbull, R. B., Littman, S., & Gerstenberger, H. (2000). A petrogenetic study of anorogenic felsic magmatism in the Cretaceous Paresis ring complex, Namibia: evidence for mixing of crust and mantle-derived components. *Lithos, 54*, 1-22.

Mitchell, A. A., Naicker, S. B., Marsh, J. S., & Dunlevey, J. N. (1997). The petrology and significance of a stratiform mafic segregation pegmatite in a Karoo-aged dolerite sheet. *South African Journal of Geology, 100*(3), 251-260.

Molyneux, T. C. (1972). X-ray data and chemical analyses of some titanomagnetite and ilmenite samples from the Bushveld Complex, South Africa. *Mineralogical Magazine, 38*, 863-871.

Morse, S. A. (1979a). Kiglapait Geochemistry I: Systematics, Sampling, and Density. *Journal of Petrology, 20*(3), 555-590.

Morse, S. A. (1979b). Kiglapait Geochemistry II: Petrography. *Journal of Petrology, 20*(3), 591-624.

Morse, S. A. (1980). Kiglapait Mineralogy II: Fe-Ti Oxide Minerals and the Activities of Oxygen and Silica. *Journal of Petrology, 21*(4), 685-719.

Morse, S. A. (2008). The Internal Magma Reservoir of Large Intrusions Revealed by Multiphase Rayleigh Fractionation. *Journal of Petrology, 49*(11), 2081-2098.

Morse, S. A., Brady, J. B., & Sporleder, B. A. (2004). Experimental Petrology of the Kiglapait Intrusion: Cotectic Trace for the Lower Zone at 5 kbar in Graphite. *Journal of Petrology, 45*(11), 2225-2259.

Moskowitz, B. M. (1981). Methods for estimating Curie temperatures of titanomaghemites from Experimental J_S-T data. *Earth and Planetary Science Letters, 53*, 84-88.

Moune, S., Sigmarsson, O., Schiano, P., Thordarson, T., & Keiding, J. K. (2012). Melt inclusion constraints on the magma source of Eyjafjallajökull 2010 flank eruption. *Journal of Geophysical Research, 117*, B00C07.

Murphy, D. T., Collerson, K. D., & Kamber, B. S. (2002). Lamproites from Gaussberg, Antarctica: Possible Transition Zone Melts of Archaean Subducted Sediments. *Journal of Petrology, 43*(6), 981-1001.

Namur, O., Charlier, B., Toplis, M. J., Higgins, M. D., Hounsell, V., Liégeois, J.-P., & Vander Auwera, J. (2011). Differentiation of Tholeiitic Basalt to A-Type Granite in the Sept Iles Layered Intrusion, Canada. *Journal of Petrology, 52*(3), 487-539.

Namur, O., Charlier, B., Toplis, M. J., Higgins, M. D., Liégeois, J.-P., & Vander Auwera, J. (2010). Crystallization Sequence and Magma Chamber Processes in the Ferrobasaltic Sept Iles Layered Intrusion, Canada. *Journal of Petrology, 51*(6), 1203-1236.

Naslund, H. R., & McBirney, A. R. (1996). Mechanisms of formation of igneous layering. In R. G. Cawthorn, *Layered Intrusions*. Amsterdam: Elsevier, pp. 1-43.

Nesbitt, H. W., & Young, G. M. (1982). Early Proterozoic climates and plate motions inferred from major element chemistry of lutites. *Nature, 299*, 715-717.

Newsom, H. E., White, W. M., Jochum, K. P., & Hofmann, A. W. (1986). Siderophile and chalcophile element abundances in oceanic basalts, Pb isotope evolution and growth of the Earth's core. *Earth and Planetary Science Letters, 80*, 299-313.

Nicolas, A. (1992). Kinematics in Magmatic Rocks with Special Reference to Gabbros. *Journal of Petrology, 33*(4), 891-915.

Nimis, P., & Ulmer, P. (1998). Clinopyroxene geobarometry of magmatic rocks Part 1: An expanded structural geobarometer for anhydrous and hydrous, basic and ultrabasic systems. *Contributions to Mineralogy and Petrology, 133*, 122-135.

Norrish, K., & Hutton, J. T. (1969). An accurate X-ray spectrographic method for the analysis of a wide range of geological samples. *Geochimica et Cosmochimica Acta, 33*(4), 431-453.

O'Connor, J. M., & Duncan, R. A. (1990). Evolution of the Walvis Ridge-Rio Grande Rise Hot Spot System Implicationsf or African and South American Plate Motions Over Plumes. *Journal of Geophysical Research, 95*(B11), 17475-17502.

O'Nions, R. K., Hamilton, P. J., & Evensen, N. M. (1977). Variations in $^{143}Nd/^{144}Nd$ and $^{87}Sr/^{86}Sr$ ratios in oceanic basalts. *Earth and Planetary Science Letters, 34*, 13-22.

Osborn, E. F., & Tait, D. B. (1952). The system diopside-forsterite-anorthite. *American Journal of Science Bowen Vol.*, 413-433.

Pang, K.-N., Zhou, M.-F., Lindsley, D., Zhao, D., & Malpas, J. (2008). Origin of Fe-Ti Oxide Ores in Mafic Intrusions: Evidence from the Panzhihua Intrusion, SW China. *Journal of Petrology, 49*(2), 295-313.

Passchier, C. W., Trouw, R. A., Goscombe, B., Gray, D., & Kröner, A. (2007). Intrusion mechanisms in a turbidite sequence: the Voetspoor and Doros plutons in NW Namibia. *Journal of Structural Geology, 29*, 481-496.

Pearce, J. A. (2008). Geochemical fingerprinting of oceanic basalts with applications to ophiolite classification and the search for Archean oceanic crust. *Lithos, 100*, 14-48.

Peate, D. W., & Hawkesworth, C. J. (1996). Lithospheric to asthenospheric transition in Low-Ti flood basalts from southern Paraná, Brazil. *Chemical Geology, 127*, 1-24.

Peate, D. W., Hawkesworth, C. J., & Mantovani, M. S. (1992). Chemical stratigraphy of the Parana lavas (South America): classification of magma types and their spatial distribution. *Bulletin of Volcanology, 55*, 119-139.

Peate, D. W., Hawkesworth, C. J., Mantovani, M. M., Rogers, N. W., & Turner, S. P. (1999). Petrogenesis and Stratigraphy of the High-Ti/Y Urubici Magma Type in the Paraná Flood Basalt Province and Implications for the Nature of 'Dupal'-Type Mantle in the South Atlantic Region. *Journal of Petrology, 40*(3), 451-473.

Peate, D. W., Hawkesworth, C. J., Mantovani, M. S., & Shukowsky, W. (1990). Mantle plumes and flood-basalt stratigraphy in the Paraná, South America. *Geology, 18*, 1223-1226.

Petford, N. (2009). Which effective viscosity? *Mineralogical Magazine, 73*(2), 167-191.

Petford, N., & Marsh, B. D. (2008). Image-based modelling of lateral magma flow: the Basement Sill, Antarctica. *LASI III*, Elba Island, pp. 65-66.

Petraske, A. K., Hodge, D. S., & Shaw, R. (1978). Mechanisms of emplacement of basic intrusions. *Tectonophysics*(46), 41-63.

Petry, C., Chakraborty, S., & Palme, H. (2004). Experimental determination of Ni diffusion coefficients in olivine and their dependence on temperature, composition, oxygen fugacity, and crystallographic orientation. *Geochimica et Cosmochimica Acta, 68*(20), 4179-4188.

Peucat, J. J., Visal, P., Bernard-Griffiths, J., & Condie, K. C. (1989). Sr, Nd, and Pb isotopic systematics in the Archean low- to high-grade transition zone of southern India: Syn-accretion vs. post-accretion granulites. *The Journal of Geology, 97*(5), 537-549.

Philpotts, A. R., & Ague, J. J. (2009). *Principles of Igneous and Metamorphic Petrology* (2nd ed.). Cambridge: Cambridge University Press, pp. 667.

Philpotts, A. R., & Carroll, M. (1996). Physical properties of partly melted tholeiitic basalt. *Geology, 24*, 1029-1032.

Philpotts, A. R., Carroll, M., & Hill, J. M. (1996). Crystal-Mush Compaction and the Origin of Pegmatitic Segregation Sheets in a Thick Flood-Basalt Flow in the Mesozoic Hartford Basin, Connecticut. *Journal of Petrology, 37*(4), 811-836.

Plank, T., & Langmuir, C. H. (1998). The chemical composition of subducting sediment and its consequences for the crust and mantle. *Chemical Geology, 145*, 325-394.

Puffer, J. H., & Horter, D. L. (1993). Origin of pegmatitic segregation veins within flood basalts. *Geological Society of America Bulletin, 105*(6), 738-748.

Putirka, K. D. (2008). Thermometers and barometers for volcanic systems. In K. D. Putirka, & F. J. Tepley (Eds.), *Minerals, Inclusions and Volcanic Processes, Reviews in Mineralogy and Geochemistry* (Vol. 69). Geochemical Society/Mineralogical Society of America, pp. 61-120.

Raczek, I., Stoll, B., Hofmann, A. W., & Jochum, K. P. (2001). High-Precision Trace Element Data for the USGS Reference Materials BCR-1, BCR-2, BHVO-1, BHVO-2, AGV-1, AGV-2, DTS-1, DTS-2, GSP-1 and GSP-2 by ID-TIMS and MIC-SSMS. *Geostandards Newsletter, 25*, 77-86.

Raedeke, L. D., & McCallum, I. S. (1984). Investigations in the Stillwater Complex: Part II. Petrology and Petrogenesis of the Ultramafic Series. *Journal of Petrology, 25*(2), 395-420.

Rehkämper, M., & Hofmann, A. W. (1997). Recycled ocean crust and sediment in Indian Ocean MORB. *Earth and Planetary Science Letters, 147*, 93-106.

Renne, P. R., Ernesto, M., Pacca, I. G., Coe, R. S., Glen, J. M., Prévot, M., & Perrin, M. (1992). The age of Paraná flood volcanism, rifting of Gondwanaland, and the Jurassic-Cretaceous boundary. *Science, 258*, 975-979.

Renne, P. R., Glen, J. M., Milner, S. C., & Duncan, A. R. (1996). Age of Etendeka flood volcanism and associated intrusions in southwestern Africa. *Geology, 24*, 659-662.

Reuning, E., & Martin, H. (1957). Die Prä-Karroo-Landschaft, die Karroo-Sedimente and Karroo-Eruptivgesteine des südlichen Kaokofeldes in Südwestafrika. *Neues Jahrbuch für Mineralogie Abhandlungen, 91*, 193-212.

Roedder, E. (1979). Origin and significance of magmatic inclusions. *Bulletin de Minéralogie, 102*, 487-510.

Roelofse, F., & Ashwal, L. D. (2012). The LowerMain Zone in the Northern Limb of the Bushveld Complex - a >1.3 km Thick Sequence of Intruded and Variably Contaminated Crystal Mushes. *Journal of Petrology, 53*(7), 1449-1476.

Ross, M. E. (1986). Flow differentiation, phenocryst alignment, and compositional trends within a dolerite dike at Rockport, Massachusetts. *Geological Society of America Bulletin, 97*, 232-240.

Rowe, M. C., Nielsen, R. L., & Kent, J. R. (2006). Anomalously high Fe contents in rehomogenized olivine-hosted melt inclusions from oxidized magmas. *American Mineralogist, 91*, 82-91.

Ryan, J. G., & Langmuir, C. H. (1987). The systematics of lithium abundances in young volcanic rocks. *Geochimica et Cosmochimica Acta, 51*, 1727-1741.

Salters, V. J., & White, W. M. (1998). Hf isotope constraints on mantle evolution. *Chemical Geology, 145*, 447-460.

Salvioli-Mariani, E., Toscani, L., & Bersani, D. (2004). Magmatic evolution of the Gaussberg lamproite (Antarctica): volatile content and glass composition. *Mineralogical Magazine, 68*(1), 83-100.

Saunders, A. D., Jones, S. M., Morgan, L. A., Pierce, K. L., Widdowson, M., & Xu, Y. G. (2007). Regional uplift associated with continental large igneous provinces: The roles of mantle plumes and the lithosphere. *Chemical Geology, 241*, 282-318.

Sawkins, F. J. (1976). Metal Deposits Related to Intracontinental Hotspot and Rifting Environments. *The Journal of Geology, 84*(6), 653-671.

Schiano, P. (2003). Primitive mantle magmas recorded as silicate melt inclusions in igneous minerals. *Earth-Science Reviews, 63*, 121-144.

Schiano, P., Eiler, J. M., Hutcheon, I. D., & Stolper, E. M. (2000). Primitive CaO-rich, silica-undersaturated melts in island arcs: evidence for the involvement of clinopyroxene-rich lithologies in the petrogenesis of arc magmas. *Geochemistry, Geophysics, Geosystems, 1*(32), 1999GC000032.

Schmitt, A. K., Emmermann, R., Trumbull, R., Bühn, B., & Henjes-Kunst, F. (2000). Petrogenesis and $^{40}Ar/^{39}Ar$ geochronology of the Brandberg Complex, Namibia: evidence for a major mantle contribution in metaluminous and peralkaline granites. *Journal of Petrology, 41*, 1207-1239.

Schmitt, R. S., Trouw, R. A., Passchier, C. W., Medeiros, S. R., & Armstrong, R. (2012). 530 Ma syntectonic syenites and granites in NW Namibia – Their relation with collision along the junction of the Damara and Kaoko belts. *Gondwana Research, 21*, 362–377.

Shervais, J. W., Vetter, S. K., & Hanan, B. B. (2006). Layered mafic sill complex beneath the eastern Snake River Plain: Evidence from cyclic geochemical variations in basalt. *Geology, 34*, 365-368.

Sheth, H. C. (1999). Flood basalts and large igneous provinces from deep mantle plumes: Fact, fiction, and fallacy. *Tectonophysics, 311*, 1-29.

Siedner, G., & Mitchell, J. G. (1976). Episodic mesozoic volcanism in Namibia and Brazil: A K-Ar Isochron study bearing on the opening of the south atlantic. *Earth and Planetary Science Letters, 30*(2), 292-302.

Sobolev, A. V. (1996). Melt Inclusions in Minerals as a Source of Principle Petrological Information. *Petrology, 4*(3), 228-239.

Sobolev, A. V., & Shimizu, N. (1993). Ultra-depleted primary melt included in an olivine from the Mid-Atlantic Ridge. *Nature, 363*, 151-154.

Spandler, C. J., Arculus, R. J., Eggins, S. M., Mavrogenes, J. A., Price, R. C., & Reay, A. J. (2003). Petrogenesis of the Greenhills Complex, Southland, New Zealand: magmatic differentiation and cumulate formation at the roots of a Permian island-arc volcano. *Contributions to Mineralogy and Petrology, 144*, 703-721.

Stacey, J. S., & Kramers, J. D. (1975). Approximation of terrestrial lead isotope evolution by a two-stage model. *Earth and Planetary Science Letters, 26*, 207-221.

Steiger, R. H., & Jäger, E. (1977). Subcommission on geochronology: Convention on the use of decay constants in geo- and cosmochronology. *Earth and Planetary Science Letters, 36*, 359-362.

Stewart, K., Turner, S., Kelley, S., Hawkesworth, C., Kirstein, L., & Mantovani, M. (1996). 3-D, ^{40}Ar-^{39}Ar geochronology in the Paraná continental flood basalt province. *Earth and Planetary Science Letters, 143*, 95-109.

Stormer, J. C. (1983). The effects of recalculation on estimates of temperature and oxygen fugacity from analyses of multicomponent iron-titanium oxides. *American Mineralogist, 68*, 586-594.

Stracke, A. (2012). Earth's heterogeneous mantle: A product of convection-driven interaction between crust and mantle. *Chemical Geology, 330-331*, 274-299.

Streckeisen, A. (1976). To each plutonic rock its proper name. *Earth-Science Reviews, 12*, 1-33.

Sun, S., Nesbitt, R. W., & Sharaskin, A. Y. (1979). Geochemical characteristics of mid-ocean ridge basalts. *Earth and Planetary Science Letters, 44*, 119-138.

Sun, S., & McDonough, W. F. (1989). Chemical and isotopic systematics of oceanic basalts: implications for mantle composition and processes. In S. D. Saunders, & M. J. Norry, *Magmatism in the Ocean Basins* (Vol. 42). Geological Society Special Publication, pp. 313-345.

Tait, S. R., & Jaupart, C. (1996). The production of chemically stratified and adcumulate plutonic igneous rocks. *Mineralogical Magazine, 60*, 99-114.

Tămaș, C., & Milési, J.-P. (2002). Hydrovolcanic breccia pipe structures – general features and genetic criteria – I. Phreatomagmatic breccias. *Geologia, 47*(1), 127-147.

Taylor, R. N., Thirlwall, M. F., Murton, B. J., Hilton, D. R., & Gee, M. A. (1997). Isotopic constraints on the influence of the Icelandic plume. *Earth and Planetary Science Letters, 148*, E1-E8.

Taylor, S. R., & McLennan, S. M. (1995). The geochemical evolution of the continental crust. *Reviews of Geophysics, 33*(2), 241-265.

Tegner, C., Wilson, J. R., & Brooks, C. K. (1993). Intraplutonic Quench Zones in the Kap Edvard Holm Layered Gabbro Complex, East Greenland. *Journal of Petrology, 34*(4), 681-710.

Telford, W. M., Geldart, L. P., & Sheriff, R. E. (1990). *Applied Geophysics* (2nd ed.). Cambridge: Cambridge University Press, pp. 770.

Thompson, R. N., & Gibson, S. A. (2000). Transient high temperatures in mantle plume heads inferred from magnesian olivines in Phanerozoic picrites. *Nature, 407*, 502-506.

Thompson, R. N., Gibson, S. A., Dickin, A. P., & Smith, P. M. (2001). Early Cretaceous Basalt and Picrite Dykes of the Southern Etendeka Region, NW Namibia: Windows into the Role of the Tristan Mantle Plume in Paraná-Etendeka Magmatism. *Journal of Petrology, 42*(11), 2049-2081.

Thompson, R. N., Ottley, C. J., Smith, P. M., Pearson, D. G., Dickin, A. P., Morrison, M. A., Leat, P. T., & Gibson, S. A. (2005). Source of the Quaternary Alkalic Basalts, Picrites and Basanites of the Potrillo Volcanic Field, New Mexico, USA: Lithosphere or Convecting Mantle? *Journal of Petrology, 46*(8), 1603-1643.

Thompson, R. N., Riches, A. J., Antoshechkina, P. M., Pearson, D. G., Nowell, G. M., Ottley, C. J., Dickin, A. P., Hards, V. L., Nguno, A.-K., & Niku-Paavola, V. (2007). Origin of CFBMagmatism: Multi-tiered Intracrustal Picrite-Rhyolite Magmatic Plumbing at Spitzkoppe, Western Namibia, during Early Cretaceous Etendeka Magmatism. *Journal of Petrology, 48*(6), 1119-1154.

Toplis, M. J. (2005). The thermodynamics of iron and magnesium partitioning between olivine and liquid: criteria for assessing and predicting equilibrium in natural and experimental systems. *Contributions to Mineralogy and Petrology, 149*, 22-39.

Torsvik, T. H., Rousse, S., Labails, C., & Smethurst, M. A. (2009). A new scheme for the opening of the South Atlantic Ocean and the dissection of an Aptian salt basin. *Geophysical Journal International, 177*, 1315-1333.

Trompetter, W. J., Reyes, A. G., Vickridge, I. C., & Markwitz, A. (1999). Lithium and boron distributions in geological samples. *Nuclear Instruments and Methods in Physics Research B, 158*, 568-574.

Trumbull, R. B., Buhn, B., Romer, R. L., & Volker, F. (2003). The Petrology of Basanite-Tephrite Intrusions in the Erongo Complex and Implications for a Plume Origin of Cretaceous Alkaline Complexes in Namibia. *Journal of Petrology, 44*(1), 93-111.

Trumbull, R. B., Emmermann, R., Bühn, B., Gerstenberger, H., Mingram, B., Schmitt, A., & Volker, F. (2000). Insights on the genesis of the Cretaceous Damaraland igneous complexes in Namibia from a Nd- and Sr-isotopic perspective. *Communications of the Geological Survey of Namibia, 12*, 313-325.

Trumbull, R., Vietor, T., Hahne, K., Wackerle, R., & Ledru, P. (2004). Aeromagnetic mapping and reconnaissance geochemistry of the Early Cretaceous Henties Bay-Outjo dike swarm, Etendeka Igneous Province, Namibia. *Journal of African Earth Sciences, 40*, 17-29.

Tuff, J., Takahashi, E., & Gibson, S. A. (2005). Experimental Constraints on the Role of Garnet Pyroxenite in the Genesis of High-Fe Mantle Plume Derived Melts. *Journal of Petrology, 46*(10), 2023-2058.

Veksler, I. V., Dorfman, A. M., Borisov, A. A., Wirth, R., & Dingwell, D. B. (2007). Liquid Immiscibility and the Evolution of Basaltic Magma. *Journal of Petrology, 48*(11), 2187-2210.

Vietor, T., Trumbull, R. B., Novaczyk, N. R., Hutchins, D. G., & Emmermann, R. (2001). Insights on the deep roots of Mesozoic ring complexes in Namibia from aeromagnetic and gravity modelling of the Messum and Brandberg complexes. *Zeitschrift der Deutschen Geologischen Gesellschaft, 152*(2-4), 157-174.

Watts, A. B. (2007). An Overview, Vol. 6: Crust and lithosphere dynamics. In G. Schubert (Ed.), *Treatise of Geophysics*. Amsterdam: Elsevier, pp. 1-48.

Weaver, B. L. (1991). The origin of ocean island basalt end-member compositions: trace element and isotopic constraints. *Earth and Planetary Science Letters, 104*, 381-397.

White, C. M. (2007). The Graveyard Point Intrusion: an Example of Extreme Differentiation of Snake River Plain Basalt in a Shallow Crustal Pluton. *Journal of Petrology, 48*(2), 303-325.

Wigand, M. O. (2005). *Geochemie und Geochronologie des Erongo-Komplexes, Namibia.* PhD Thesis. GeoForschungsZentrum Potsdam.

Wilhelm, S., & Wörner, G. (1996). Crystal size distribution in Jurassic Ferrar flows and sills (Victoria Land, Antarctica): evidence for processes of cooling, nucleation, and crystallisation. *Contributions to Mineralogy and Petrology, 125*, 1-15.

Willbold, M., & Stracke, A. (2006). Trace element composition of mantle end-members: Implications for recycling of oceanic and upper and lower continental crust. *Geochemistry, Geophysics, Geosystems, 7*(4), 1-30.

Wilson, A. H. (2012). A Chill Sequence to the Bushveld Complex: Insight into the First Stage of Emplacement and Implications for the Parental Magmas. *Journal of Petrology, 53*(6), 1123-1168.

Wilson, S. A. (1997). *Data compilation for USGS reference material BHVO-2, Hawaiian Basalt.* U.S. Geological Survey Open-File Report.

Workman, R. K., & Hart, S. R. (2005). Major and trace element composition of the depleted MORB mantle (DMM). *Earth and Planetary Science Letters, 231*, 53-72.

Workman, R. K., Hart, S. R., Jackson, M., Regelous, M., Farley, K. A., Blusztajn, J., Kurz, M., & Staudigel, H. (2004). Recycled metasomatized lithosphere as the origin of the Enriched Mantle II (EM2) end-member: Evidence from the Samoan Volcanic Chain. *Geochemistry Geophysics Geosystems, 5*(4), Q04008.

Zartman, R. E., & Haines, S. M. (1988). The plumbotectonic model for Pb isotopic systematics among major terrestrial reservoirs – A case for bi-directional transport. *Geochimica et Cosmochimica Acta, 52*, 1327-1339.

Zieg, M. J., & Marsh, B. D. (2012). Multiple Reinjections and Crystal-mush Compaction in the Beacon Sill, McMurdo DryValleys, Antarctica. *Journal of Petrology, 53*(12), 2567-2591.

Zindler, A., & Hart, S. (1986). Chemical Geodynamics. *Annual Reviews of Earth and Planetary Science, 14*, 493-571.

Appendix A: Mapping

Table A.1: Locations of all sampled material (waypoints correspond to map in Figure A.1)

Sample	Waypt.	Location		Description
		Longitude (S)	Latitude (E)	
TOD2	8	20°44''7.4'	14°29''56.5'	Damaran turbiditic schists east of Doros
TOD3	29	20°45''39.6'	14°17''38.4'	Basal chill margin contact with Damaran metasediments
TOD4	29	20°45''39.6'	14°17''38.4'	Damaran metamorphic aureole
TOD5A-B	31	20°45''39.3'	14°17''38.2'	Basal ol. melagabbro
TOD6A-C	32	20°45''35.8'	14°17''35'	Basal ol. melagabbro + feldsp. enclaves
TOD7	28	20°45''30.7'	14°17''32.8'	Intrusive ol. melagabbro
TOD8	33	20°45''23'	14°17''30.7'	Intrusive ol. melagabbro
TOD9	35	20°45''12.4'	14°17''20.5'	Coarse-grained massive ol. gabbro
TOD10	36	20°45''12.2'	14°17''20.8'	Porphyritic dolerite dyke
TOD11	36	20°45''12.2'	14°17''20.8'	Intrusive ol. melagabbro
TOD12A-B	36	20°45''12.2'	14°17''20.8'	Massive ol. gabbro
TOD13A	42	20°44''54.8'	14°17''48.3'	Foliated mgt. ol. gabbro
TOD13B	42	20°44''54.8'	14°17''48.3'	Foliated mgt. gabbro
TOD13C	42	20°44''54.8'	14°17''48.3'	Foliated mgt. gabbro
TOD14	44	20°45''1.1'	14°17''47.1'	Foliated mgt. gabbro
TOD15	45	20°45''8'	14°17''50.3'	Foliated gabbro
TOD16	45	20°45''8'	14°17''50.3'	Foliated gabbro
TOD17	47	20°45''11.7'	14°17''51'	Poikilitic foliated ol. gabbro
TOD18	48	20°45''16.4'	14°17''50.2'	Banded transitional ol. gabbro
TOD19	52	20°44''58.4'	14°17''17.1'	Intrusive ol. melagabbro
TOD20	55	20°44''56.9'	14°17''11.6'	Massive ol. gabbro
TOD21	54.5	20°44''57.5'	14°17''7.6'	Intrusive ol. melagabbro + massive ol. gabbro xenolith
TOD22	58	20°44''45.5'	14°17''39.9'	Foliated ol. gabbro
TOD23	59	20°44''44.8'	14°17''47.9'	Foliated mgt. gabbro
TOD24	61	20°44''45.9'	14°18''0.6'	Foliated mgt. gabbro
TOD25	62	20°44''42'	14°18''6.7'	Foliated gabbro
TOD26	64	20°44''51.7'	14°18''22.1'	Foliated gabbro
TOD27	64	20°44''51.7'	14°18''22.1'	Massive ol. gabbro xenolith in foliated ol. gabbro
TOD28	65	20°44''53.6'	14°18''30.1'	Banded transitional ol. gabbro
TOD29	65	-	-	Foliated leucogabbro boulder
TOD30	66	20°44''54.7'	14°18''32.5'	Banded transitional ol. gabbro
TOD31	73	20°45''10.2'	14°17''8.8'	Contact between intrusive ol. melagabbro & massive ol. gabbro
TOD32	74	20°45''11.4'	14°17''5.8'	Intrusive ol. melagabbro
TOD33	75	20°45''11.3'	14°16''56.2'	Massive ol. gabbro
TOD34	78	20°45''18.2'	14°17''1.2'	Foliated leucogabbro
TOD35A	81	20°45''31.1'	14°16''54.9'	Coarse-grained gabbro xenolith in intrusive ol. melagabbro
TOD35B	81	20°45''31.1'	14°16''54.9'	Intrusive ol. melagabbro + ol.-rich xenolith
TOD36	-	-	-	Boulder of massive ol. gabbro + feldsp. vein
TOD37	86	20°45''54.7'	14°16''14.7'	Massive ol. gabbro (host to 38)
TOD38	86	20°45''54.7'	14°16''14.7'	Ol.-rich xenolith in massive ol. gabbro
TOD39	87.5	20°46''14'	14°16''3.8'	Basal ol. melagabbro + feldsp. enclaves

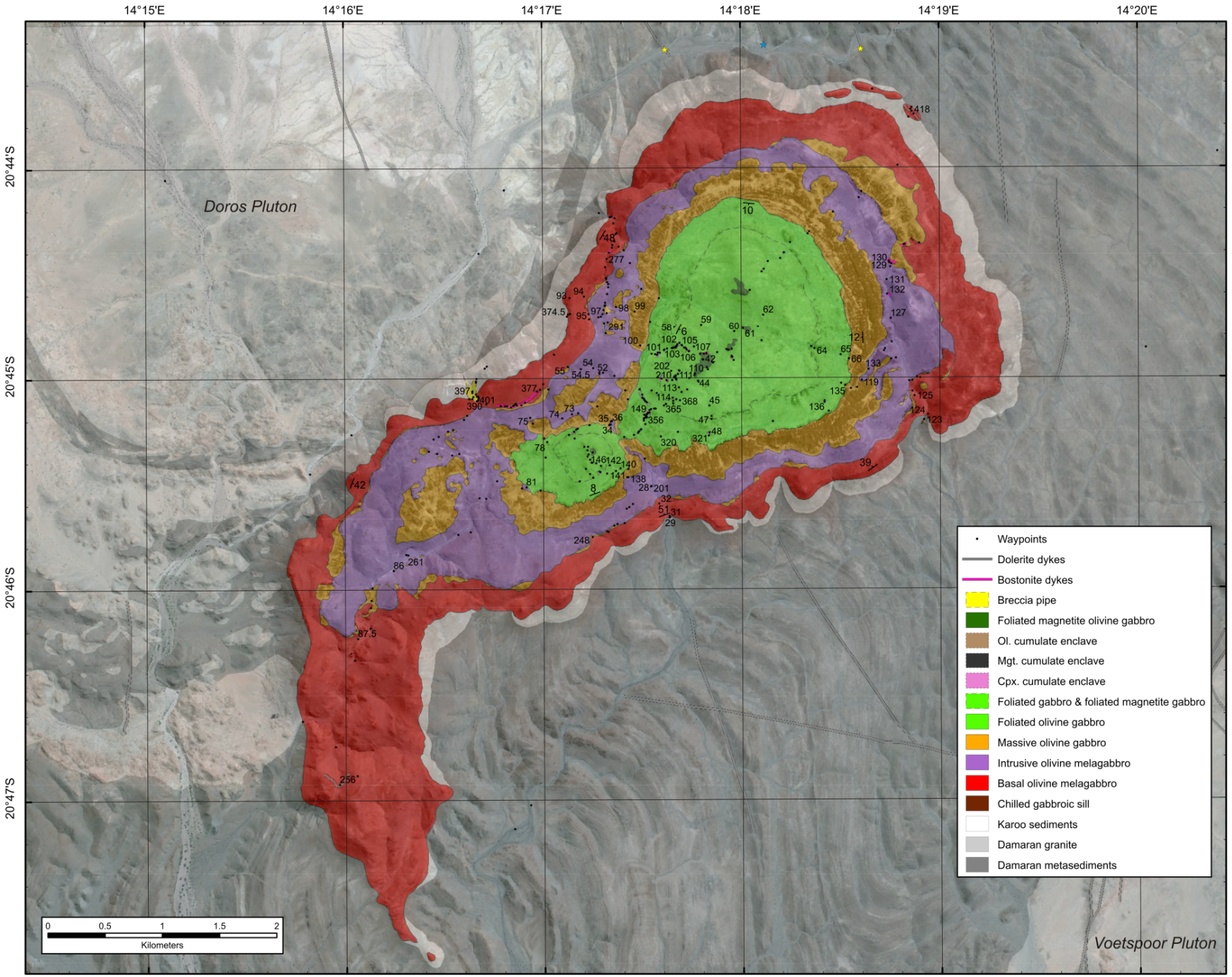
Table A.1 cont.

Sample	Waypt.	Location		Description
		Eastings	Northings	
TOD40	93	20°44''37'	14°17''8.2'	Basal ol .melagabbro
TOD41	94	20°44''36.7'	14°17''12.6'	Basal ol. melagabbro
TOD42	95	20°44''41.7'	14°17''14'	Basal ol. melagabbro
TOD43	97	20°44''41.7'	14°17''18.2'	Massive ol. gabbro
TOD44	98	20°44''39.7'	14°17''22.2'	Massive ol. gabbro
TOD45	99	20°44''40.9'	14°17''27.9'	Massive ol. gabbro
TOD46	100	20°44''50.8'	14°17''29.5'	Weakly foliated ol. gabbro
TOD47	101	20°44''52'	14°17''36.9'	Foliated ol. gabbro
TOD48	102	20°44''51.1'	14°17''40.4'	Banded transitional ol. gabbro
TOD49	103	20°44''51.4'	14°17''40.2'	Gabbro pegmatite
TOD50	105	20°44''50.8'	14°17''42.2'	Foliated leucogabbro
TOD51	107	20°44''53.3'	14°17''47.6'	Foliated mgt. gabbro
TOD52	110	20°44''57.1'	14°17''49.6'	Foliated mgt. ol. gabbro
TOD53	111	20°44''58.8'	14°17''46'	Foliated mgt. ol. gabbro
TOD54	113	20°45''2.7'	14°17''41.2'	Foliated gabbro
TOD55	114	20°45''5.7'	14°17''39.3'	Gabbro pegmatite
TOD56	119	20°45''0.7'	14°18''36.5'	Intrusive ol. melagabbro
TOD57	123	20°45''12'	14°18''55.2'	Chilled gabbroic sill
TOD58	123	20°45''12'	14°18''55.2'	Chilled gabbroic sill
TOD59	123	20°45''12'	14°18''55.2'	Chill margin to sill in contact with Damaran metasediments
TOD60	123	20°45''12'	14°18''55.2'	Chill margin to sill in contact with Damaran metasediments
TOD61	123	20°45''12'	14°18''55.2'	Damaran metasediments outside metamorphic aureole
TOD62	124	20°45''10.6'	14°18''56.4'	Basal ol. melagabbro
TOD63	125	20°45''5.2'	14°18''52.4'	Basal ol. melagabbro
TOD64	129	20°44''27.2'	14°18''44.8'	Centre of bostonite dyke
TOD65	129	20°44''27.2'	14°18''44.8'	Margin of bostonite dyke
TOD66	130	20°44''26.7'	14°18''44.7'	Centre of bostonite dyke
TOD67	129	20°44''27.2'	14°18''44.8'	Massive ol. gabbro
TOD68A	131	20°44''32'	14°18''44.1'	Massive ol. gabbro xenolith in intrusive ol. melagabbro
TOD68B	131	20°44''32'	14°18''44.1'	Intrusive ol melagabbro (host to 68A)
TOD69	132	20°44''36.1'	14°18''44.2'	Margin of bostonite dyke
TOD70	133	20°44''57.7'	14°18''38.5'	Intrusive ol. melagabbro
TOD71	135	20°45''2.2'	14°18''31.5'	Massive ol. gabbro
TOD72	136	20°45''6.6'	14°18''25.2'	Banded transitional ol. gabbro
TOD73	140	20°45''25.7'	14°17''23.4'	Banded transitional ol. gabbro
TOD74	142	20°45''24.8'	14°17''20.1'	Banded transitional ol. gabbro
TOD75	141	20°45''26.5'	14°17''22'	Foliated leucogabbro
TOD76	146	20°45''21.8'	14°17''13.7'	Foliated ol. gabbro
TOD77	149	20°45''9.9'	14°17''31.7'	Cpx. cumulate enclave
TOD79	202	20°44''58'	14°17''38.8'	Magnetite cumulate enclave
TOD80	256	20°46''55.5'	14°15''58.2'	Porphyritic dolerite dyke

Table A.1 cont.

Sample	Waypt.	Location		Description
		Eastings	Northings	
TOD81	277	20°44''24.3'	14°17''20.1'	Bostonite dyke
TOD82	291	20°44''44.1'	14°17''19.7'	Porphyritic dolerite dyke
TOD83	365	20°45''7.4'	14°17''37.3'	Olivine cumulate enclave
TOD84	377	20°45''6.6'	14°17''39.4'	Bostonite dyke
TOD85	390	20°45''3.8'	14°16''58.2'	Qtz. latite fragment in breccia
TOD86	390	20°45''6.5'	14°16''40.1'	Qtz. latite fragment (flow bottom) in breccia
TOD87	390	20°45''6.5'	14°16''40.1'	Qtz latite fragment (flow top) in breccia
TOD88	390	20°45''6.5'	14°16''40.1'	Foliated ol. gabbro fragment in breccia
TOD89	418	20°43''44.2'	14°18''51.8'	Porphyritic dolerite dyke

Figure A.1 (overleaf): Geological map of the Doros Intrusion showing the major lithological units and selected minor units and dykes defined in this study. Waypoints specifically referred to in the text are numbered. Structural data are from Hodgson & Botha (1974). Yellow stars indicate Horingbaai-type dolerite dykes and blue stars indicate Tafelkop-type dykes analysed by Thompson *et al.* (2001).


14°15'E
14°16'E
14°17'E
14°18'E
14°19'E
14°20'E
20°44'S
20°45'S
20°46'S
20°47'S
Doros Pluton
Voetspoor Pluton
Waypoints
Dolerite dykes
Bostonite dykes
Breccia pipe
Foliated magnetite olivine gabbro
Ol. cumulate enclave
Mgt. cumulate enclave
Cpx. cumulate enclave
Foliated gabbro & foliated magnetite gabbro
Foliated olivine gabbro
Massive olivine gabbro
Intrusive olivine melagabbro
Basal olivine melagabbro
Chilled gabbroic sill
Karoo sediments
Damaran granite
Damaran metasediments
0
0.5
1
1.5
2
Kilometers

Appendix B: Petrography

Table B.1: Details of sample material available for petrographic analysis

Type of material	**Samples available**
Damaran aureole	TOD4; TOD59*; TOD60; TOD61
Chill margin	TOD3*; TOD59*; TOD60
Chilled gabbroic sill	TOD57*; TOD58*
Basal olivine melagabbro	TOD5A-B; TOD6A-C; TOD39*; TOD40*; TOD41*; TOD42*; TOD62*; TOD63*
Intrusive olivine melagabbro	TOD7; TOD8; TOD11; TOD19; TOD21*; TOD31; TOD32; TOD35B*; TOD56; TOD68B; TOD70*
Olivine-rich xenolith	TOD35B*; TOD38X
Feldspathic enclave in basal olivine melagabbro	TOD6A-C; TOD39*
Massive olivine gabbro	TOD9; TOD12A-B; TOD20; TOD30*; TOD31; TOD33; TOD36*; TOD37*; TOD43*; TOD44*; TOD45*; TOD46*; TOD67; TOD71*; TOD72
Massive olivine gabbro xenolith	TOD21X*; TOD27X*; TOD68A*
Feldspathic enclave in massive olivine gabbro	TOD36*
Banded transitional olivine gabbros	TOD18; TOD28*; TOD35A; TOD48*; TOD73; TOD74
Foliated gabbro	TOD14; TOD15*; TOD16; TOD17; TOD23*; TOD25; TOD26*; TOD54
Foliated olivine gabbro	TOD22*; TOD47*; TOD76*; TOD88
Foliated magnetite gabbro	TOD13B*; TOD13C*; TOD24; TOD51
Foliated magnetite olivine gabbro	TOD13A; TOD52; TOD53*
Foliated leucogabbro	TOD29*; TOD34*; TOD50; TOD75*
Gabbro pegmatite	TOD49; TOD55*
Pyroxene cumulate enclave	TOD77*
Magnetite cumulate enclave	TOD79
Olivine cumulate enclave	TOD83*
Porphyritic dolerite	TOD10*; TOD80*; TOD82; TOD89
Bostonite	TOD64*; TOD66*; TOD84*
Marginal bostonite	TOD65; TOD69

**Thin sections available*

Appendix C: Whole-rock chemistry

Table C.1: Whole-rock major (wt. %) and trace element (ppm) compositions of the Doros suite

Sample	TOD58	TOD60	TOD38	TOD39	TOD40	TOD42	TOD62	TOD63	TOD21	TOD35B	TOD70	TOD37	TOD43	TOD44	TOD45	TOD71	TOD68
Unit	Sill	Ch. M.	BOMx	BOM	BOM	BOM	BOM	BOM	IOM	IOM	IOM	MOG	MOG	MOG	MOG	MOG	MOGx
SiO_2	47.62	55.27	43.37	45.66	44.15	45.99	45.01	43.46	43.13	45.77	45.37	48.19	49.36	48.68	49.36	49.49	50.58
TiO_2	2.61	2.04	0.70	1.39	1.46	1.69	1.59	1.15	1.47	1.08	1.19	0.79	1.64	1.23	1.31	1.21	1.40
Al_2O_3	13.60	15.12	3.81	10.69	6.86	8.24	8.81	5.99	6.87	12.52	7.07	18.21	18.10	18.45	20.37	20.52	15.62
Fe_2O_{3T}	13.4	11.2	17.4	13.1	17.3	14.9	16.5	18.4	16.6	10.9	16.0	6.98	8.34	7.37	7.15	6.77	7.27
MnO	0.21	0.10	0.23	0.17	0.22	0.20	0.21	0.23	0.20	0.14	0.22	0.11	0.12	0.11	0.11	0.10	0.11
MgO	5.85	2.45	25.04	15.34	18.82	15.12	15.76	21.26	20.07	13.92	17.49	8.45	5.25	5.98	4.32	4.17	7.24
CaO	9.61	3.29	8.58	10.63	7.71	10.43	8.08	7.19	8.67	11.96	9.97	14.22	12.71	14.09	13.48	13.28	12.80
Na_2O	3.20	6.69	0.31	1.26	1.02	1.21	1.42	0.88	1.52	1.85	0.86	1.60	2.23	1.83	2.24	2.42	2.47
K_2O	0.57	0.29	0.07	0.32	0.39	0.45	0.53	0.35	0.33	0.29	0.28	0.26	0.54	0.38	0.44	0.45	0.69
P_2O_5	0.28	0.24	0.03	0.10	0.14	0.12	0.43	0.12	0.11	0.08	0.09	0.05	0.15	0.09	0.11	0.11	0.18
SO_3	0.03	0.19	0.03	0.03	0.06	0.02	0.02	0.02	0.01	0.00	0.02	0.04	0.02	0.02	0.04	0.05	0.02
Cr_2O_3	0.10	0.08	0.29	0.26	0.30	0.17	0.19	0.30	0.24	0.17	0.20	0.16	0.08	0.12	0.07	0.07	0.15
NiO	0.02	0.02	0.15	0.10	0.13	0.09	0.11	0.16	0.11	0.07	0.11	0.04	0.02	0.03	0.02	0.02	0.03
H_2O-	0.28	0.44	0.09	0.22	0.13	0.15	0.19	0.17	0.04	0.07	0.09	0.11	0.19	0.10	0.09	0.06	0.10
LOI	2.07	1.88	-0.23	0.69	0.61	0.58	0.30	-0.01	0.15	0.71	0.27	0.49	0.80	0.69	0.61	0.72	0.75
Total	99.44	99.26	99.88	99.94	99.27	99.31	99.16	99.70	99.49	99.54	99.24	99.71	99.54	99.17	99.72	99.45	99.43
Mg #	46	30	74	70	68	67	65	70	71	72	68	71	55	62	55	55	66
Li	17.3	4.12	3.74	3.63	5.83	4.82	7.23	5.21	4.59	4.04	5.38	2.00	3.66	2.20	3.52	4.00	3.46
Sc	18.3	18.9	29.1	24.4	21.8	29.0	19.1	21.1	26.9	29.2	31.7	22.8	18.5	19.6	16.0	17.0	26.9
V	387	365	222	327	326	388	317	275	393	288	315	207	293	234	232	256	274
Cr	483	446	1928	1705	1923	1093	1186	2073	1624	1133	1429	1078	385	577	358	357	998
Co	37.0	28.6	132	82.1	109	87.0	91.8	126	99.9	60.9	103	41.2	28.8	26.9	23.9	25.0	34.7
Ni	133	149	1124	697	1004	689	851	1267	879	521	874	282	140	165	110	116	248
Cu	126	60.7	28.3	51.5	98.7	84.2	106	69.4	60.1	58.5	67.9	23.4	90.5	51.1	66.5	71.2	254
Zn	102	101	97.6	82.4	116	97.6	117	120	145	90.8	104	41.0	59.1	43.8	49.4	54.9	51.7
Rb	9.09	4.15	0.775	4.65	7.87	7.57	10.8	6.39	6.45	4.40	5.48	3.09	7.86	4.85	4.98	7.24	10.8
Sr	716	223	117	457	443	367	362	216	280	454	252	755	715	773	830	807	623
Y	18.4	22.0	5.18	8.57	11.3	12.6	12.4	8.90	11.2	8.84	9.99	5.80	10.9	7.70	8.80	9.64	14.5
Zr	133	123	21.7	59.2	85.7	96.1	84.8	59.0	72.7	54.8	60.4	35.9	84.3	55.6	64.6	62.4	107
Nb	12.7	13.1	1.07	5.06	7.03	8.32	7.91	5.04	5.63	4.33	4.90	2.77	7.42	4.59	5.26	5.52	9.11
Ba	267	169	23.3	112	138	148	158	106	122	103	99.1	117	159	109	137	154	230
La	19.3	23.8	2.09	7.76	11.2	12.1	12.2	8.09	10.5	7.73	8.02	5.21	11.4	7.49	9.16	9.75	15.5

Sample	TOD58	TOD60	TOD38	TOD39	TOD40	TOD42	TOD62	TOD63	TOD21	TOD35B	TOD70	TOD37	TOD43	TOD44	TOD45	TOD71	TOD68
Unit	Sill	Ch. M.	BOMx	BOM	BOM	BOM	BOM	BOM	IOM	IOM	IOM	MOG	MOG	MOG	MOG	MOG	MOGx
Ce	44.6	53.1	6.23	18.9	26.7	29.7	28.6	19.1	25.5	19.0	19.3	12.5	26.9	17.8	21.4	22.6	36.1
Pr	5.66	6.78	1.01	2.57	3.51	3.96	3.61	2.48	3.41	2.57	2.56	1.71	3.50	2.41	2.83	2.90	4.55
Nd	24.2	28.6	5.00	11.4	15.3	17.3	15.6	10.8	15.2	11.6	11.4	7.62	15.1	10.6	12.2	12.6	19.8
Sm	5.20	5.98	1.38	2.62	3.36	3.83	3.41	2.45	3.41	2.68	2.69	1.75	3.24	2.37	2.63	2.79	4.24
Eu	1.70	1.71	0.472	0.988	1.05	1.24	1.10	0.784	1.09	0.941	0.878	0.830	1.25	0.927	1.04	1.09	1.52
Gd	5.17	5.85	1.49	2.55	3.26	3.69	3.37	2.46	3.18	2.51	2.76	1.79	3.22	2.32	2.54	2.72	4.17
Tb	0.725	0.816	0.211	0.349	0.449	0.519	0.478	0.348	0.458	0.356	0.387	0.246	0.440	0.317	0.357	0.378	0.576
Dy	4.14	4.72	1.22	2.01	2.57	2.96	2.77	1.99	2.55	2.01	2.24	1.37	2.48	1.77	2.01	2.17	3.26
Ho	0.738	0.855	0.214	0.348	0.457	0.512	0.489	0.355	0.451	0.345	0.394	0.238	0.448	0.314	0.353	0.378	0.578
Er	1.93	2.30	0.542	0.911	1.19	1.35	1.27	0.919	1.15	0.910	1.05	0.602	1.14	0.809	0.912	0.974	1.46
Tm	0.243	0.301	0.070	0.113	0.154	0.170	0.165	0.119	0.158	0.117	0.133	0.078	0.149	0.104	0.117	0.122	0.182
Yb	1.503	1.902	0.424	0.692	0.955	1.06	1.01	0.729	0.899	0.703	0.807	0.451	0.885	0.614	0.698	0.760	1.09
Lu	0.207	0.263	0.063	0.097	0.131	0.145	0.139	0.105	0.136	0.100	0.113	0.062	0.121	0.087	0.100	0.103	0.142
Hf	3.51	3.40	0.802	1.75	2.31	2.77	2.25	1.60	2.08	1.60	1.75	1.10	2.26	1.58	1.76	1.72	2.86
Ta	0.684	0.771	0.036	0.264	0.361	0.453	0.430	0.265	0.267	0.176	0.261	0.155	0.422	0.263	0.304	0.298	0.480
Pb	3.65	7.66	0.405	1.34	1.96	2.18	2.31	1.54	1.74	1.32	1.43	1.17	2.12	1.44	1.76	1.83	3.04
Th	2.277	4.70	0.127	0.608	1.08	1.14	1.41	0.885	0.928	0.621	0.821	0.337	1.04	0.585	0.804	0.939	1.59
U	0.580	1.42	0.043	0.179	0.296	0.316	0.297	0.195	0.240	0.161	0.176	0.082	0.237	0.144	0.181	0.202	0.347
Ti	n. a.	n. a.	n. a.	n. a.	n. a.	n. a.	n. a.	n. a.	7846	6434	n. a.	n. a.	n. a.	n. a.	n. a.	n. a.	n. a.
Ga	n. a.	n. a.	n. a.	n. a.	n. a.	n. a.	n. a.	n. a.	17.0	19.2	n. a.	n. a.	n. a.	n. a.	n. a.	n. a.	n. a.
Cs	n. a.	n. a.	n. a.	n. a.	n. a.	n. a.	n. a.	n. a.	0.140	0.138	n. a.	n. a.	n. a.	n. a.	n. a.	n. a.	n. a.
W	n. a.	n. a.	n. a.	n. a.	n. a.	n. a.	n. a.	n. a.	0.352	0.071	n. a.	n. a.	n. a.	n. a.	n. a.	n. a.	n. a.

Table C.1 cont.

Sample	TOD28	TOD48	TOD22	TOD47	TOD47R	TOD76	TOD15	TOD26	TOD13B	TOD13C	TOD53	TOD29	TOD75	TOD55	TOD55R	TOD77	TOD66	TOD84
Unit	FOG*	FOG*	FOG	FOG	FOG	FOG	FG	FG	FMG	FMG	FMOG	FL	FL	Peg.	Peg.	Cpx. Cum.	Bost.	Bost.
SiO_2	47.89	49.38	48.06	48.25	47.28	48.44	49.48	49.75	45.52	45.94	41.66	50.91	48.35	51.55	50.30	49.72	51.98	57.14
TiO_2	1.61	1.27	1.33	1.49	1.43	1.65	1.53	1.79	2.93	2.96	3.33	0.89	2.02	1.00	0.94	1.99	2.71	1.17
Al_2O_3	13.74	15.25	16.31	14.33	14.62	16.68	17.75	16.19	14.00	14.19	9.62	24.88	19.05	19.04	19.38	7.31	14.09	13.53
Fe_2O_{3T}	9.90	8.66	9.42	10.82	10.73	10.16	7.33	7.69	14.15	14.15	22.51	3.11	8.08	4.92	4.83	9.91	11.83	9.50
MnO	0.14	0.13	0.14	0.15	0.14	0.14	0.10	0.11	0.14	0.14	0.23	0.07	0.11	0.08	0.07	0.16	0.16	0.14
MgO	8.81	7.40	7.86	8.30	9.43	6.95	4.89	5.60	5.52	5.68	10.19	0.71	3.46	4.30	4.74	10.18	2.48	2.42
CaO	14.45	14.12	12.69	12.89	12.41	11.73	14.24	15.12	12.47	13.44	9.84	11.28	11.97	14.26	13.67	17.45	7.16	3.62
Na_2O	1.40	1.86	1.95	1.68	2.49	2.03	2.28	2.16	2.58	2.06	1.42	3.36	2.48	2.37	3.24	1.15	4.54	5.12
K_2O	0.34	0.35	0.37	0.42	0.40	0.52	0.60	0.41	0.80	0.50	0.29	1.55	1.45	1.06	0.99	0.45	1.81	5.49
P_2O_5	0.10	0.09	0.10	0.11	0.11	0.12	0.12	0.11	0.14	0.13	0.09	0.21	0.17	0.09	0.10	0.13	0.87	0.14
SO_3	0.02	0.04	0.03	0.02	0.00	0.04	0.02	0.02	0.02	0.01	0.02	0.11	0.02	0.03	0.01	0.03	0.12	0.00
Cr_2O_3	0.14	0.06	0.05	0.06	0.04	0.05	0.02	0.02	0.02	0.02	0.02	0.01	0.03	0.04	0.03	0.17	0.01	0.01
NiO	0.04	0.03	0.04	0.04	0.04	0.04	0.01	0.02	0.02	0.01	0.03	0.01	0.01	0.01	0.01	0.03	0.00	0.01
H_2O-	0.13	0.17	0.17	0.17	0.12	0.13	0.12	0.10	0.16	0.12	0.11	0.13	0.08	0.09	0.07	0.07	0.22	0.10
LOI	0.65	0.66	0.60	0.56	0.63	0.83	0.88	0.67	1.25	0.59	0.16	1.99	2.13	1.09	1.15	0.99	1.61	1.24
Total	99.38	99.47	99.11	99.31	99.87	99.51	99.38	99.75	99.72	99.94	99.54	99.19	99.43	99.95	99.51	99.73	99.60	99.63
Mg #	64	63	62	60	63	58	57	59	44	44	47	31	46	63	66	67	29	34
Li	4.20	1.85	2.92	3.85	3.92	3.73	3.26	1.37	21.0	3.72	3.86	1.18	3.19	20.7	2.17	2.10	1.50	9.36
Sc	35.1	17.6	18.3	23.1	26.4	19.9	30.2	28.5	34.3	32.1	28.1	1.23	18.3	21.9	25.5	63.9	8.15	n. a.
V	430	185	241	291	355	346	360	397	1144	1157	2263	59.9	405	475	242	590	142	63.1
Cr	935	133	150	231	266	203	5.65	22.9	3.41	2.38	4.25	1.66	102	589	172	1120	1.26	60.4
Co	48.9	13.2	36.1	42.8	44.3	46.6	24.9	23.0	50.1	46.2	115	5.62	25.6	44.5	10.2	40.3	20.3	10.2
Ni	280	57.1	214	251	273	267	79.8	88.1	71.6	66.1	167	6.65	54.1	160	50.4	220	4.68	52.6
Cu	52.2	4.46	57.9	71.8	99.4	86.7	59.1	49.2	48.8	47.2	58.9	155	166	180	20.3	28.9	557	46.8
Zn	69.3	26.6	52.5	66.8	99.3	76.2	56.0	43.6	87.2	81.4	146	31.3	70.2	120	59.5	62.9	130	154
Rb	5.59	8.81	4.61	5.29	5.57	8.38	9.32	4.38	15.0	6.85	4.50	23.6	16.3	10.4	13.3	6.39	14.6	65.5
Sr	529	977	720	637	619	758	757	750	597	597	430	1150	917	714	974	306	448	277
Y	10.6	7.17	7.35	9.06	10.5	10.6	10.8	8.74	12.5	11.2	9.55	12.1	13.2	21.8	9.30	16.0	45.2	99.0
Zr	67.1	43.5	51.6	65.3	78.4	81.5	76.2	47.9	85.4	81.3	67.0	108	101	159	57.4	89.9	273	1066
Nb	5.18	4.21	4.40	5.42	6.58	7.25	7.10	3.69	8.04	7.21	5.88	10.0	9.56	15.4	5.24	5.83	30.1	98.4
Ba	134	190	109	150	175	229	182	165	191	160	113	367	258	316	242	135	516	862
La	8.72	7.36	7.29	8.81	10.3	11.1	10.6	6.94	12.3	10.7	8.00	17.5	14.7	23.1	9.74	11.1	60.5	141

Sample	TOD28	TOD48	TOD22	TOD47	TOD47R	TOD76	TOD15	TOD26	TOD13B	TOD13C	TOD53	TOD29	TOD75	TOD55	TOD55R	TOD77	TOD66	TOD84
Unit	FOG*	FOG*	FOG	FOG	FOG	FOG	FG	FG	FMG	FMG	FMOG	FL	FL	Peg.	Peg.	Cpx. Cum.	Bost.	Bost.
Ce	21.0	17.5	17.2	21.0	25.1	26.5	25.3	16.9	29.0	25.7	19.4	38.5	34.9	53.4	23.0	28.7	141	306
Pr	2.86	2.34	2.25	2.82	3.31	3.41	3.33	2.32	3.78	3.35	2.65	4.80	4.46	6.74	3.02	4.02	17.3	35.6
Nd	12.9	10.2	10.2	12.4	14.8	14.8	15.0	10.9	17.0	15.1	11.9	19.3	19.4	28.9	13.3	18.7	73.5	138
Sm	3.04	2.26	2.25	2.78	3.30	3.20	3.35	2.57	3.73	3.40	2.78	3.81	4.13	6.18	2.93	4.49	14.6	26.9
Eu	1.11	0.921	0.872	1.06	1.18	1.24	1.20	1.07	1.34	1.20	1.00	1.63	1.54	2.01	1.12	1.40	4.64	4.32
Gd	3.13	2.21	2.16	2.78	3.12	3.07	3.18	2.58	3.71	3.28	2.88	3.50	3.88	6.22	2.74	4.59	13.7	24.8
Tb	0.443	0.307	0.301	0.381	0.423	0.420	0.446	0.358	0.517	0.459	0.395	0.480	0.531	0.861	0.380	0.637	1.83	3.71
Dy	2.47	1.69	1.69	2.11	2.41	2.41	2.49	2.02	2.88	2.59	2.23	2.73	2.99	4.93	2.12	3.66	10.2	21.8
Ho	0.439	0.298	0.299	0.376	0.410	0.419	0.431	0.352	0.502	0.450	0.394	0.479	0.512	0.872	0.362	0.635	1.77	3.90
Er	1.12	0.768	0.768	0.959	1.08	1.08	1.15	0.895	1.32	1.16	0.994	1.25	1.33	2.28	0.935	1.62	4.51	10.7
Tm	0.147	0.099	0.095	0.120	0.137	0.133	0.139	0.109	0.160	0.145	0.126	0.157	0.169	0.293	0.118	0.202	0.552	1.38
Yb	0.851	0.572	0.577	0.727	0.830	0.835	0.846	0.660	0.988	0.870	0.788	0.967	1.04	1.78	0.732	1.23	3.25	8.27
Lu	0.128	0.076	0.082	0.101	0.113	0.114	0.115	0.089	0.131	0.119	0.109	0.131	0.138	0.246	0.099	0.164	0.434	1.02
Hf	2.00	1.33	1.48	1.85	2.13	2.20	2.16	1.49	2.48	2.34	1.97	2.63	2.69	4.23	1.62	2.77	6.95	25.4
Ta	0.302	0.238	0.239	0.306	0.305	0.403	0.391	0.204	0.442	0.401	0.344	0.541	0.525	0.819	0.230	0.324	1.60	5.26
Pb	1.62	1.14	1.29	1.56	1.78	2.03	1.78	1.30	2.97	1.77	1.64	3.91	2.54	4.31	1.44	1.45	5.26	20.8
Th	0.798	0.546	0.602	0.685	0.862	0.950	0.827	0.534	1.02	0.859	0.614	1.77	1.10	2.74	0.753	0.930	4.72	17.7
U	0.195	0.128	0.145	0.168	0.223	0.219	0.195	0.121	0.236	0.206	0.144	0.392	0.240	0.686	0.182	0.202	1.03	2.85
Ti	n. a.	n. a.	n. a.	n. a.	8318	n. a.	n. a.	n. a.	n. a.	n. a.	n. a.	n. a.	n. a.	n. a.	5712	n. a.	n. a.	6654
Ga	n. a.	n. a.	n. a.	n. a.	25.2	n. a.	n. a.	n. a.	n. a.	n. a.	n. a.	n. a.	n. a.	n. a.	31.0	n. a.	n. a.	65.4
Cs	n. a.	n. a.	n. a.	n. a.	0.123	n. a.	n. a.	n. a.	n. a.	n. a.	n. a.	n. a.	n. a.	n. a.	0.038	n. a.	n. a.	0.265
W	n. a.	n. a.	n. a.	n. a.	0.095	n. a.	n. a.	n. a.	n. a.	n. a.	n. a.	n. a.	n. a.	n. a.	0.067	n. a.	n. a.	1.18

Rock unit abbreviations as follows: Ch. M. = chill margin; BOM = basal olivine melagabbro; IOM = intrusive olivine melagabbro; MOG = massive olivine gabbro; FOG = foliated olivine gabbro; FOG* = banded transitional olivine gabbro; FG = foliated gabbro; FMG = foliated magnetite gabbro; FMOG = foliated magnetite olivine gabbro; FL = foliated leucogabbro; Peg. = gabbro pegmatite; Cpx. Cum. = clinopyroxene cumulate enclave; Bost. = bostonite. Xenoliths denoted with 'x'; repeat analyses with 'R'. n. a. = not analysed. Total Fe as Fe_2O_3. Mg # calculated with all Fe as FeO. All analyses shown in figures have been renormalised volatile-free. Details of analytical procedures may be found in Section 2.1.

Table C.2: Additional whole-rock major and trace element analyses from this study

Sample	TOD10	TOD85	TOD86
Unit	Dolerite	Q. latite	Q. latite
SiO_2	49.01	67.81	67.68
TiO_2	1.25	0.97	0.97
Al_2O_3	14.38	12.09	11.90
Fe_2O_{3T}	12.09	6.55	7.38
MnO	0.20	0.06	0.10
MgO	7.66	1.29	0.91
CaO	12.13	2.17	1.93
Na_2O	1.56	2.99	3.74
K_2O	0.35	4.08	3.25
P_2O_5	0.11	0.22	0.22
SO_3	0.02	0.01	0.00
Cr_2O_3	0.08	0.00	0.00
NiO	0.02	0.00	0.00
H_2O-	0.45	0.07	0.40
LOI	0.62	1.32	0.96
Total	99.94	99.65	99.47
Mg #	56	28	20
Li	3.94	10.5	15.5
Sc	32.8	13.8	14.1
V	331	47.5	47.0
Cr	339	3.00	3.02
Co	44.0	12.8	10.7
Ni	138	5.28	0.388
Cu	133	21.2	27.4
Zn	77.6	89.8	106
Rb	4.59	148	126
Sr	232	194	173
Y	17.2	39.0	39.1
Zr	69.9	264	266
Nb	4.24	18.9	18.9
Ba	68.6	797	607
La	6.42	42.2	43.8
Ce	15.6	90.6	92.0
Pr	2.16	10.5	10.6
Nd	10.5	41.3	41.7
Sm	2.87	8.45	8.47
Eu	0.988	1.69	1.70
Gd	3.46	8.24	8.23
Tb	0.542	1.23	1.24
Dy	3.48	7.58	7.58
Ho	0.676	1.43	1.42
Er	1.94	4.23	4.25
Tm	0.261	0.592	0.584
Yb	1.68	3.90	3.87
Lu	0.241	0.564	0.558
Hf	1.98	6.87	6.84

Sample	TOD10	TOD85	TOD86
Unit	Dolerite	Q. latite	Q. latite
Pb	2.15	20.7	21.6
Th	1.30	13.1	13.0
U	0.354	3.23	3.19
Ti	n. a.	5832	5971
Ga	n. a.	39.7	33.1
Cs	n. a.	3.26	3.28
W	n. a.	0.933	0.933

Q. latite = quartz latite. n. a. = not analysed. Total Fe as Fe_2O_3.

Table C.3: CIPW normative mineral abundances for all analyses

Sample	TOD58	TOD60	TOD38	TOD39	TOD40	TOD42	TOD62	TOD63	TOD21	TOD35B	TOD70	TOD37	TOD43	TOD44	TOD45	TOD71
Unit	Sill	Ch. M.	BOMx	BOM	BOM	BOM	BOM	BOM	IOM	IOM	IOM	MOG	MOG	MOG	MOG	MOG
Normative mineral abundance (wt. %)																
Quartz		1.13											1.18	0.37	1.10	0.80
Orthoclase	3.39	1.69	0.39	1.87	2.33	2.66	3.13	2.09	1.94	1.72	1.67	1.56	3.21	2.26	2.61	2.69
Albite	27.11	56.58	2.64	10.69	8.64	10.21	11.98	7.48	10.32	13.35	7.32	13.53	18.89	15.48	18.93	20.49
Anorthite	21.02	10.40	8.80	22.57	12.97	15.72	16.11	11.33	10.95	25.00	14.56	41.74	37.75	40.99	44.23	43.79
Nepheline									1.37	1.24						
Diopside	20.52	3.70	26.99	23.78	19.66	28.47	17.16	19.02	25.24	27.18	27.72	22.91	19.85	22.96	17.93	17.47
Hypersthene	8.64	15.34	10.83	10.70	16.55	14.40	17.66	12.79			16.24	9.08	11.60	11.40	9.21	8.71
Olivine	6.61		43.29	22.26	29.59	18.89	23.32	38.34	41.09	24.52	23.76	6.36				
Magnetite	2.91	2.43	3.79	2.85	3.76	3.23	3.59	4.00	3.60	2.37	3.48	1.52	1.81	1.60	1.55	1.47
Ilmenite	4.96	3.88	1.33	2.64	2.78	3.20	3.02	2.19	2.79	2.06	2.27	1.50	3.11	2.33	2.49	2.30
Apatite	0.64	0.55	0.06	0.22	0.32	0.29	0.99	0.28	0.26	0.19	0.21	0.11	0.34	0.22	0.26	0.26

Sample	TOD68	TOD28	TOD48	TOD22	TOD47	TOD47R	TOD76	TOD15	TOD26	TOD13B	TOD13C	TOD53	TOD29	TOD75	TOD55	TOD55R
Unit	MOGx	FOG*	FOG*	FOG	FOG	FOG	FOG	FG	FG	FMG	FMG	FMOG	FL	FL	Peg.	Peg.
Normative mineral abundance (wt. %)																
Quartz			0.02					0.43	0.81				0.97		1.70	
Orthoclase	4.08	2.04	2.04	2.20	2.46	2.37	3.06	3.56	2.43	4.71	2.98	1.74	9.14	8.56	6.27	5.83
Albite	20.90	11.84	15.78	16.50	14.23	18.66	17.17	19.32	18.29	17.24	17.42	12.03	28.45	20.99	20.04	21.95
Anorthite	29.50	30.20	32.22	34.66	30.34	27.54	34.88	36.41	33.25	24.25	27.97	19.01	48.24	36.56	38.19	35.45
Nepheline						1.30				2.50						2.94
Diopside	26.42	33.03	30.20	22.45	26.76	27.03	18.36	27.25	33.26	30.35	31.31	24.12	5.34	17.87	25.85	25.55
Hypersthene	11.35	11.79	13.05	11.65	15.63		17.30	6.00	4.93		1.42	6.02	1.71	4.96	3.07	
Olivine	0.86	3.26		5.22	2.71	15.97	1.19			9.04	7.91	22.94		1.53		3.08
Magnetite	1.58	2.15	1.88	2.05	2.35	2.33	2.21	1.59	1.67	3.08	3.08	4.90	0.68	1.76	1.07	1.05
Ilmenite	2.66	3.06	2.42	2.52	2.84	2.71	3.14	2.90	3.41	5.56	5.62	6.32	1.70	3.85	1.89	1.79
Apatite	0.43	0.24	0.21	0.22	0.26	0.24	0.28	0.27	0.26	0.33	0.31	0.22	0.48	0.40	0.21	0.23

Table C.3 cont.

Sample	TOD77	TOD66	TOD84	TOD10	ET1	TOD85	TOD86
Unit	Cpx. Cum.	Bost.	Bost.	Dolerite	Basalt	Q. latite	Q. latite
Normative mineral abundance (wt. %)							
Quartz	0.29	0.75		1.30	6.14	26.10	25.39
Orthoclase	2.64	10.68	32.46	2.09	6.78	24.14	19.20
Albite	9.77	38.43	33.27	13.24	22.55	25.27	31.67
Anorthite	13.45	12.72		31.18	20.90	7.52	6.08
Nepheline			3.10				
Diopside	58.18	14.45	14.39	23.18	16.54	1.53	1.78
Hypersthene	7.12	9.85		21.51	16.52	9.35	9.39
Olivine			7.73				
Magnetite	2.15	2.57	0.16	2.63	2.60	1.43	1.61
Ilmenite	3.78	5.15	2.22	2.37	3.78	1.84	1.85
Apatite	0.30	2.02	0.34	0.26	0.46	0.52	0.51
Acmite			3.81				

Calculated from the scheme of Kelsey (1965) assuming FeO = $0.85Fe_2O_{3T}$. Rock unit abbreviations as in Table C.1.

Table C.4: Whole-rock Sr-, Nd- and Pb-isotopic analyses for the Doros suite and an associated dolerite dyke

Sample	Unit	Rb (ppm)	Sr (ppm)	$^{87}Rb/^{86}Sr$	$^{87}Sr/^{86}Sr$	$(^{87}Sr/^{86}Sr)_{132}$	Sm (ppm)	Nd (ppm)	$^{147}Sm/^{144}Nd$	$^{143}Nd/^{144}Nd$	$(^{143}Nd/^{144}Nd)_{132}$	$\varepsilon_{Nd\ 132}$
Doros intrusive suite												
TOD38	BOMx	0.775	117	0.01916	0.704201 ± 20	0.704166 ± 21	1.38	5.00	0.1673	0.512938 ± 19	0.512793 ± 27	6.3 ± 0.5
TOD39	BOM	4.65	457	0.02943	0.704262 ± 18	0.704209 ± 20	2.62	11.4	0.1390	0.512919 ± 15	0.512799 ± 18	6.5 ± 0.3
TOD40	BOM	7.87	443	0.05135	0.706937 ± 24	0.706843 ± 27	3.36	15.3	0.1326	0.512846 ± 18	0.512731 ± 22	5.1 ± 0.4
TOD58	Sill	9.09	733	0.03588	0.709591 ± 24	0.709525 ±25	5.20	24.2	0.1298	0.512773 ± 12	0.512660 ± 14	3.8 ± 0.3
TOD71	MOG	7.24	814	0.02574	0.704192 ± 38	0.704144 ± 40	2.79	12.6	0.1336	0.512785 ± 11	0.512669 ± 15	3.9 ± 0.3
TOD68	MOGx	10.8	628	0.04976	0.704540 ± 41	0.704449 ± 45	4.24	19.8	0.1293	0.512785 ± 11	0.512674 ± 14	4.0 ± 0.3
TOD26	FG	4.38	750	0.01689	0.704144 ± 14	0.704113 ± 15	2.57	10.9	0.1432	0.512853 ± 14	0.512729 ± 18	5.1 ± 0.3
TOD22	FOG	4.61	720	0.01851	0.704023 ± 15	0.703989 ± 17	2.25	10.2	0.1332	0.512873 ± 21	0.512758 ± 26	5.7 ± 0.5
TOD76	FOG	8.38	766	0.03167	0.704194 ± 23	0.704136 ± 26	3.20	14.8	0.1307	0.512902 ± 14	0.512789 ± 28	6.3 ± 0.5
TOD13B	FMG	15.0	597	0.07272	0.704298 ± 16	0.704164 ± 20	3.73	17.0	0.1327	0.512904 ± 14	0.512790 ± 16	6.3 ± 0.3
TOD75	FL	16.3	938	0.05032	0.704062 ± 14	0.703970 ± 14	4.13	19.4	0.1291	0.512866 ± 13	0.512755 ± 17	5.6 ± 0.3
TOD55	Peg.	10.4	714	0.04197	0.709517 ± 17	0.709440 ± 21	6.18	28.9	0.1291	0.512783 ± 13	0.512672 ± 32	4.0 ± 0.6
TOD77	Cpx. Cum.	6.39	306	0.06037	0.704227 ± 17	0.704115 ± 28	4.49	18.7	0.1452	0.512877 ± 13	0.512751 ± 18	5.5 ± 0.4
TOD66	Bost.	14.6	457	0.09227	0.704720 ± 32	0.704550 ± 39	14.6	73.5	0.1202	0.512760 ± 7	0.512656 ± 8	3.7 ± 0.2
Additional samples												
TOD10	Dolerite	4.59	232	0.05712	0.705432 ± 16	0.705326 ± 19	2.87	10.5	0.1655	0.512782 ± 18	0.512639 ± 21	3.3 ± 0.4

Sample	Unit	U (ppm)	Th (ppm)	Pb (ppm)	$^{238}U/^{204}Pb$	$^{235}U/^{204}Pb$	$^{232}Th/^{204}Pb$	$^{206}Pb/^{204}Pb$	$(^{206}Pb/^{204}Pb)_{132}$	$^{207}Pb/^{204}Pb$	$(^{207}Pb/^{204}Pb)_{132}$	$^{208}Pb/^{204}Pb$	$(^{208}Pb/^{204}Pb)_{132}$
Doros intrusive suite													
TOD38	BOMx	0.0430	0.127	0.405	6.60	0.0480	20.2	17.8837 ± 34	17.7472 ± 211	15.5775 ± 29	15.5708 ± 38	37.6632 ± 80	37.5309 ± 223
TOD39	BOM	0.179	0.608	1.34	8.37	0.0609	29.5	18.1693 ± 22	17.9961 ± 123	15.5633 ± 18	15.5548 ± 23	37.9429 ± 51	37.7499 ± 180
TOD40	BOM	0.296	1.08	1.96	9.51	0.0692	36.0	18.2679 ± 16	18.0711 ± 222	15.5743 ± 16	15.5647 ± 25	38.0910 ± 42	37.8554 ± 283
TOD58	Sill	0.580	2.28	3.65	10.0	0.0730	40.8	18.3479 ± 13	18.1402 ± 122	15.5819 ± 14	15.5718 ± 19	38.2906 ± 45	38.0230 ± 203
TOD71	MOG	0.202	0.939	1.83	6.97	0.0507	33.6	18.2804 ± 10	18.1363 ± 159	15.5816 ± 10	15.5746 ± 17	38.1800 ± 36	37.9601 ± 112
TOD68	MOGx	0.347	1.59	3.04	7.18	0.0522	34.1	18.2910 ± 8	18.1425 ± 56	15.5805 ± 8	15.5733 ± 11	38.2019 ± 25	37.9785 ± 69
TOD26	FG	0.121	0.534	1.30	5.85	0.0425	26.7	18.2722 ± 18	18.1512 ± 141	15.5746 ± 17	15.5687 ± 23	38.0982 ± 55	37.9230 ± 147
TOD22	FOG	0.145	0.602	1.29	7.07	0.0514	30.4	18.2416 ± 14	18.0953 ± 138	15.5619 ± 13	15.5547 ± 19	38.0174 ± 42	37.8181 ± 153
TOD76	FOG	0.219	0.950	2.03	6.77	0.0491	30.3	18.1786 ± 8	18.0386 ± 173	15.5551 ± 9	15.5483 ± 17	37.9300 ± 27	37.7312 ± 280
TOD13B	FMG	0.236	1.02	2.97	5.00	0.0362	22.4	18.2101 ± 14	18.1067 ± 47	15.5680 ± 13	15.5630 ± 15	38.0035 ± 39	37.8570 ± 102
TOD75	FL	0.240	1.10	2.54	5.94	0.0431	28.1	18.1960 ± 9	18.0731 ± 131	15.5542 ± 10	15.5482 ± 16	37.9723 ± 31	37.7883 ± 105
TOD55	Peg.	0.686	2.74	4.31	10.1	0.0731	41.6	18.3545 ± 15	18.1460 ± 331	15.5860 ± 16	15.5759 ± 31	38.3023 ± 34	38.0297 ± 450
TOD77	Cpx. Cum.	0.202	0.930	1.45	8.76	0.0636	41.7	18.2440 ± 11	18.0627 ± 114	15.5684 ± 12	15.5596 ± 17	38.0682 ± 39	37.7950 ± 140
TOD66	Bost.	1.03	4.72	5.26	12.4	0.0898	58.8	18.4666 ± 8	18.2104 ± 137	15.5902 ± 9	15.5777 ± 15	38.4210 ± 30	38.0356 ± 131
Additional samples													
TOD10	Dolerite	0.354	1.30	2.15	10.6	0.0766	39.9	19.0567 ± 10	18.8383 ± 151	15.6775 ± 10	15.6669 ± 17	38.6154 ± 32	38.3538 ± 122

Rock unit abbreviations are as in Table C.1. Isotopic and elemental concentrations analysed by MC-ICPMS. See Section 2.2 for details of analytical procedures and age corrections. Uncertainties reported on measured and initial ratios are 2 standard errors of the mean (2σ).

Appendix D: Mineral chemistry

Table D.1: Microprobe analyses of olivines in rocks of the Doros suite

Sample	TOD59 Chill		TOD39 BOM					TOD40 BOM					TOD21 IOM				
Point	1/22	7/26	2/14	3/15 C	3/16 R	7/23	11/28	1/1	4/5	7/7	8/8	19/25	2/3	2/4	12/16 C	12/17 R	13/19
Comment				Core	Rim										Core	Rim	
SiO_2	30.14	31.10	38.09	37.97	37.88	37.39	38.15	38.06	38.16	38.22	38.27	37.97	37.65	37.83	38.13	38.04	38.05
TiO_2	34.42	30.64	0.03	0.07	0.03	0.05	0.05	0.04	0.06	0.05	0.05	0.03	0.05	0.05	0.06	0.04	0.04
Al_2O_3	1.16	2.56	0.01	0.01	0.02	0.01	0.02	0.04	0.01	0.01	0.03	0.02	0.02	0.01	0.01	0.01	0.03
FeO_T	3.32	2.45	23.20	23.96	23.92	23.31	22.74	24.85	24.94	24.14	24.30	24.76	25.27	25.48	25.52	25.49	25.06
MnO	0.03	0.02	0.33	0.36	0.37	0.33	0.36	0.34	0.36	0.35	0.36	0.34	0.35	0.34	0.34	0.34	0.37
MgO	0.37	0.05	37.30	36.80	37.09	37.48	37.79	36.47	36.36	37.05	37.00	36.26	35.88	35.91	35.83	35.98	36.36
CaO	27.48	27.67	0.25	0.33	0.24	0.21	0.21	0.24	0.15	0.15	0.19	0.20	0.18	0.25	0.20	0.17	0.20
Na_2O	0.07	0.08	0.02	0.01	0.02	0.02	0.02	0.01	0.01	0.01	0.02	0.01	0.02	0.01	0.02	0.01	0.02
K_2O	0.02	0.05	0.00	0.00	0.01	0.00	0.00	0.00	0.00	0.00	0.00	0.00	0.00	0.00	0.00	0.00	0.00
Cr_2O_3	0.09	0.04	0.01	0.02	0.00	0.00	0.03	0.02	0.01	0.00	0.00	0.00	0.00	0.00	0.00	0.00	0.00
NiO	0.00	0.02	0.23	0.21	0.23	0.24	0.26	0.24	0.23	0.27	0.26	0.26	0.27	0.24	0.24	0.23	0.25
BaO	0.05	0.03	0.00	0.00	0.00	0.00	0.01	0.00	0.00	0.00	0.00	0.00	0.00	0.01	0.00	0.00	0.00
Total	97.14	94.70	99.47	99.75	99.81	99.05	99.64	100.32	100.28	100.26	100.49	99.86	99.69	100.13	100.35	100.31	100.38
Structural formula per 4 O																	
Si	0.82	0.86	1.00	1.00	1.00	0.99	1.00	1.00	1.00	1.00	1.00	1.00	1.00	1.00	1.00	1.00	1.00
Al	0.04	0.08	0.00	0.00	0.00	0.00	0.00	0.00	0.00	0.00	0.00	0.00	0.00	0.00	0.00	0.00	0.00
Ti	0.70	0.64	0.00	0.00	0.00	0.00	0.00	0.00	0.00	0.00	0.00	0.00	0.00	0.00	0.00	0.00	0.00
Fe^{2+}_T	0.08	0.06	0.51	0.53	0.53	0.52	0.50	0.55	0.55	0.53	0.53	0.55	0.56	0.56	0.56	0.56	0.55
Mn	0.00	0.00	0.01	0.01	0.01	0.01	0.01	0.01	0.01	0.01	0.01	0.01	0.01	0.01	0.01	0.01	0.01
Mg	0.01	0.00	1.46	1.45	1.46	1.48	1.48	1.43	1.42	1.45	1.44	1.43	1.42	1.41	1.41	1.41	1.43
Ca	0.80	0.82	0.01	0.01	0.01	0.01	0.01	0.01	0.00	0.00	0.01	0.01	0.01	0.01	0.01	0.00	0.01
Na	0.00	0.00	0.00	0.00	0.00	0.00	0.00	0.00	0.00	0.00	0.00	0.00	0.00	0.00	0.00	0.00	0.00
K	0.00	0.00	0.00	0.00	0.00	0.00	0.00	0.00	0.00	0.00	0.00	0.00	0.00	0.00	0.00	0.00	0.00
Cr	0.00	0.00	0.00	0.00	0.00	0.00	0.00	0.00	0.00	0.00	0.00	0.00	0.00	0.00	0.00	0.00	0.00
Ni	0.00	0.00	0.00	0.00	0.00	0.01	0.01	0.01	0.00	0.01	0.01	0.01	0.01	0.01	0.01	0.00	0.01
Ba	0.00	0.00	0.00	0.00	0.00	0.00	0.00	0.00	0.00	0.00	0.00	0.00	0.00	0.00	0.00	0.00	0.00
Total	2.46	2.47	3.00	3.00	3.00	3.01	3.00	3.00	3.00	3.00	3.00	3.00	3.00	3.00	2.99	3.00	3.00
Mg #	17	4	74	73	73	74	75	72	72	73	73	72	72	72	71	72	72
Fo	16.45	3.48	73.85	72.95	73.13	73.86	74.46	72.07	71.92	72.94	72.78	72.02	71.39	71.25	71.17	71.28	71.81
Fa	82.80	95.73	25.77	26.65	26.46	25.77	25.14	27.55	27.68	26.67	26.82	27.59	28.21	28.37	28.44	28.33	27.77
Te	0.76	0.79	0.37	0.41	0.41	0.37	0.40	0.38	0.40	0.39	0.40	0.38	0.40	0.38	0.38	0.38	0.42
Name	Altered	Altered	Chrys.	Chrys.	Chrys.	Chrys.	Chrys.	Chrys.	Chrys.	Chrys.	Chrys.	Chrys.	Chrys.	Chrys.	Chrys.	Chrys.	Chrys.

Sample	TOD45 MOG			TOD47 FOG					TOD53 FMOG			
Point	6/12	11/21 C	11/22 R	2/8	7/12	14/20 C	14/21 R	15/22	4/3	5/4	12/10	7/17 C
Comment		Core	Rim			Core	Rim					Core
SiO_2	36.38	36.13	36.18	32.70	36.43	33.26	35.88	35.60	36.61	36.25	36.97	37.17
TiO_2	0.05	0.05	0.05	0.05	0.04	0.04	0.06	0.05	0.06	0.04	0.05	0.05
Al_2O_3	0.01	0.01	0.01	0.01	0.02	0.01	0.00	0.00	0.02	0.03	0.02	0.02
FeO_T	33.85	33.32	33.24	33.11	32.95	33.33	33.41	33.31	33.65	33.40	33.83	33.69
MnO	0.53	0.52	0.51	0.49	0.50	0.53	0.51	0.51	0.50	0.52	0.52	0.54
MgO	29.29	29.34	29.66	29.54	29.95	29.48	29.89	29.54	30.16	29.81	30.32	30.16
CaO	0.33	0.29	0.22	0.23	0.23	0.25	0.19	0.32	0.30	0.32	0.27	0.29
Na_2O	0.02	0.04	0.03	0.00	0.03	0.02	0.02	0.03	0.02	0.03	0.04	0.03
K_2O	0.00	0.00	0.00	0.00	0.00	0.00	0.01	0.01	0.01	0.01	0.01	0.01
Cr_2O_3	0.01	0.00	0.00	0.00	0.00	0.00	0.00	0.01	0.00	0.00	0.00	0.00
NiO	0.14	0.15	0.13	0.15	0.17	0.17	0.17	0.15	0.06	0.05	0.06	0.04
BaO	0.00	0.00	0.01	0.00	0.00	0.00	0.00	0.00	0.00	0.00	0.00	0.00
Total	100.62	99.85	100.04	96.27	100.33	97.08	100.15	99.52	101.40	100.46	102.08	101.99
Structural formula per 4 O												
Si	1.00	1.00	1.00	0.95	1.00	0.96	0.99	0.99	0.99	0.99	1.00	1.00
Al	0.00	0.00	0.00	0.00	0.00	0.00	0.00	0.00	0.00	0.00	0.00	0.00
Ti	0.00	0.00	0.00	0.00	0.00	0.00	0.00	0.00	0.00	0.00	0.00	0.00
Fe^{2+}_T	0.78	0.77	0.77	0.80	0.76	0.80	0.77	0.77	0.76	0.77	0.76	0.76
Mn	0.01	0.01	0.01	0.01	0.01	0.01	0.01	0.01	0.01	0.01	0.01	0.01
Mg	1.20	1.21	1.22	1.28	1.22	1.26	1.23	1.22	1.22	1.22	1.22	1.21
Ca	0.01	0.01	0.01	0.01	0.01	0.01	0.01	0.01	0.01	0.01	0.01	0.01
Na	0.00	0.00	0.00	0.00	0.00	0.00	0.00	0.00	0.00	0.00	0.00	0.00
K	0.00	0.00	0.00	0.00	0.00	0.00	0.00	0.00	0.00	0.00	0.00	0.00
Cr	0.00	0.00	0.00	0.00	0.00	0.00	0.00	0.00	0.00	0.00	0.00	0.00
Ni	0.00	0.00	0.00	0.00	0.00	0.00	0.00	0.00	0.00	0.00	0.00	0.00
Ba	0.00	0.00	0.00	0.00	0.00	0.00	0.00	0.00	0.00	0.00	0.00	0.00
Total	3.00	3.00	3.00	3.05	3.00	3.04	3.01	3.01	3.00	3.01	3.00	3.00
Mg #	61	61	61	61	62	61	61	61	62	61	61	61
Fo	60.29	60.71	61.03	61.04	61.47	60.81	61.09	60.88	61.15	61.03	61.13	61.09
Fa	39.09	38.68	38.37	38.39	37.95	38.57	38.31	38.52	38.28	38.37	38.27	38.29
Te	0.62	0.61	0.60	0.58	0.58	0.62	0.59	0.60	0.58	0.60	0.60	0.62
Name	Hyal.	Hyal.	Hyal.	Hyal.	Hyal.	Hyal.	Hyal.	Hyal.	Hyal.	Hyal.	Hyal.	Hyal.

Rock unit abbreviations are as in Table C.1. C = core; R = rim; Chrys. = chysolite; Hyal. = hyalosiderite. Mg # = 100x [Mg/(Mg+Fe)]. Additional olivine Mg # for sample TOD70 are presented in Table F.3.

Table D.2: Microprobe analyses of feldspars in rocks of the Doros suite

Sample	TOD59 Chill			TOD39 BOM													
Point	3/18 C	3/19 R	2/24	4/17 C	4/18 R	8/25 C	8/24 R1	8/26 R2	8/27 R3	13/29 C	13/30 R1	13/31 R2	13/32 R3	14/25 C	14/26 R	19/30	19/31
SiO_2	73.01	73.35	71.43	50.21	51.66	46.96	52.25	54.51	56.06	51.61	48.68	51.88	54.94	54.06	55.57	47.05	54.56
TiO_2	0.00	0.00	0.03	0.10	0.11	0.09	0.19	0.16	0.15	0.09	0.09	0.17	0.18	0.19	0.18	0.12	0.17
Al_2O_3	20.56	20.90	21.36	28.34	28.95	27.63	25.17	23.58	23.01	28.28	30.31	28.04	26.36	28.47	27.90	28.46	24.66
FeO_T	0.06	0.05	0.30	0.44	0.46	0.40	0.39	0.53	0.36	0.35	0.37	0.38	0.50	0.42	0.44	0.39	0.51
MnO	0.00	0.00	0.00	0.00	0.00	0.01	0.00	0.00	0.00	0.00	0.00	0.01	0.02	0.00	0.00	0.00	0.00
MgO	0.01	0.01	0.04	0.01	0.01	0.01	0.01	0.02	0.02	0.01	0.01	0.01	0.02	0.03	0.01	0.01	0.03
CaO	0.24	0.44	0.61	13.33	13.36	14.41	10.50	8.67	7.49	12.90	15.28	12.61	10.19	11.51	10.66	13.85	8.83
Na_2O	11.99	11.88	11.31	4.01	3.85	3.45	5.55	6.09	6.79	4.18	3.09	4.42	5.63	4.98	5.40	3.74	6.09
K_2O	0.06	0.07	0.27	0.30	0.30	0.19	0.43	0.74	0.97	0.30	0.17	0.33	0.50	0.48	0.57	0.21	0.85
Cr_2O_3	0.00	0.01	0.00	0.00	0.00	0.00	0.00	0.00	0.00	0.00	0.00	0.00	0.01	0.00	0.00	0.01	0.00
NiO	0.00	0.00	0.00	0.02	0.01	0.01	0.01	0.00	0.01	0.02	0.00	0.01	0.02	0.00	0.00	0.00	0.00
BaO	0.00	0.02	0.00	0.00	0.02	0.00	0.03	0.06	0.09	0.01	0.00	0.02	0.05	0.03	0.03	0.03	0.07
Total	105.93	106.73	105.35	96.76	98.71	93.17	94.52	94.34	94.94	97.75	97.99	97.87	98.42	100.16	100.76	93.88	95.76
Structural formula per 8 O																	
Si	3.01	3.00	2.96	2.37	2.38	2.32	2.51	2.61	2.66	2.40	2.28	2.41	2.53	2.45	2.50	2.30	2.58
Al	1.00	1.01	1.04	1.58	1.57	1.61	1.42	1.33	1.29	1.55	1.67	1.54	1.43	1.52	1.48	1.64	1.37
Ti	0.00	0.00	0.00	0.00	0.00	0.00	0.01	0.01	0.01	0.00	0.00	0.01	0.01	0.01	0.01	0.00	0.01
$Fe^{2+}{}_T$	0.00	0.00	0.01	0.02	0.02	0.02	0.02	0.02	0.01	0.01	0.01	0.01	0.02	0.02	0.02	0.02	0.02
Mn	0.00	0.00	0.00	0.00	0.00	0.00	0.00	0.00	0.00	0.00	0.00	0.00	0.00	0.00	0.00	0.00	0.00
Mg	0.00	0.00	0.00	0.00	0.00	0.00	0.00	0.00	0.00	0.00	0.00	0.00	0.00	0.00	0.00	0.00	0.00
Ca	0.01	0.02	0.03	0.67	0.66	0.76	0.54	0.44	0.38	0.64	0.77	0.63	0.50	0.56	0.51	0.73	0.45
Na	0.96	0.94	0.91	0.37	0.34	0.33	0.52	0.57	0.62	0.38	0.28	0.40	0.50	0.44	0.47	0.35	0.56
K	0.00	0.00	0.01	0.02	0.02	0.01	0.03	0.05	0.06	0.02	0.01	0.02	0.03	0.03	0.03	0.01	0.05
Cr	0.00	0.00	0.00	0.00	0.00	0.00	0.00	0.00	0.00	0.00	0.00	0.00	0.00	0.00	0.00	0.00	0.00
Ni	0.00	0.00	0.00	0.00	0.00	0.00	0.00	0.00	0.00	0.00	0.00	0.00	0.00	0.00	0.00	0.00	0.00
Ba	0.00	0.00	0.00	0.00	0.00	0.00	0.00	0.00	0.00	0.00	0.00	0.00	0.00	0.00	0.00	0.00	0.00
Total	4.98	4.97	4.97	5.03	5.01	5.05	5.04	5.02	5.03	5.01	5.03	5.02	5.02	5.02	5.01	5.06	5.04
An #	1	2	3	65	66	70	51	44	38	63	73	61	50	56	52	67	44
An	1.09	2.00	2.85	63.65	64.59	69.02	49.87	42.15	35.78	61.96	72.51	60.04	48.59	54.57	50.50	66.37	42.32
Ab	98.58	97.62	95.65	34.65	33.68	29.90	47.70	53.57	58.70	36.33	26.53	38.09	48.58	42.72	46.29	32.43	52.82
Or	0.32	0.38	1.50	1.71	1.73	1.08	2.43	4.28	5.52	1.72	0.96	1.87	2.84	2.71	3.21	1.20	4.85
Name	Alb.	Alb.	Alb.	Lab.	Lab.	Lab.	Lab.	And.	And.	Lab.	Byt.	Lab.	Lab.	Lab.	Lab.	Lab.	And.

Sample	TOD40 BOM									TOD21 IOM								
Point	2/2	10/12 C	10/13 R1	10/14 R2	10/15 R3	13/16	13/17	16/19	18/24	4/6	5/7 C	5/8 R	6/9 R2	6/10 R1	6/11 C	11/18	22/24 C	22/25 R
SiO_2	54.10	50.31	61.63	67.34	50.23	54.80	65.95	56.12	53.80	57.33	52.63	62.65	63.22	55.62	49.38	56.39	49.35	56.28
TiO_2	0.14	0.09	0.19	0.19	0.09	0.15	0.16	0.16	0.15	0.17	0.11	0.16	0.18	0.18	0.10	0.17	0.09	0.17
Al_2O_3	29.21	31.30	25.59	22.83	30.61	28.66	23.11	26.86	28.10	24.42	28.10	22.19	22.23	25.87	29.70	24.99	30.11	25.37
FeO_T	0.33	0.29	0.31	0.64	0.40	0.38	0.50	0.62	0.71	0.37	0.31	0.38	0.39	0.33	0.29	0.36	0.33	0.32
MnO	0.00	0.00	0.00	0.01	0.02	0.00	0.00	0.01	0.00	0.00	0.00	0.00	0.00	0.00	0.00	0.00	0.00	0.00
MgO	0.02	0.02	0.02	0.38	0.02	0.02	0.01	0.03	0.04	0.02	0.01	0.02	0.01	0.02	0.01	0.01	0.01	0.01
CaO	12.22	15.07	7.44	3.57	14.80	11.53	4.24	9.89	11.95	8.14	12.19	4.79	4.51	9.68	14.68	8.85	15.01	9.14
Na_2O	4.43	3.03	6.09	5.89	3.36	4.86	6.61	5.68	4.64	6.78	4.71	8.19	8.20	6.11	3.34	6.55	3.14	6.36
K_2O	0.31	0.16	0.98	3.51	0.15	0.35	2.34	0.48	0.34	0.52	0.28	1.44	1.64	0.46	0.16	0.43	0.15	0.51
Cr_2O_3	0.00	0.00	0.00	0.00	0.01	0.01	0.00	0.00	0.00	0.00	0.00	0.00	0.01	0.00	0.01	0.01	0.00	0.00
NiO	0.00	0.00	0.00	0.01	0.01	0.01	0.01	0.00	0.03	0.00	0.00	0.00	0.00	0.00	0.02	0.00	0.00	0.00
BaO	0.02	0.01	0.09	0.17	0.02	0.03	0.16	0.03	0.02	0.08	0.01	0.16	0.17	0.05	0.00	0.04	0.01	0.08
Total	100.78	100.27	102.35	104.54	99.72	100.82	103.08	99.88	99.78	97.83	98.34	99.98	100.58	98.33	97.69	97.80	98.17	98.24
Structural formula per 8 O																		
Si	2.43	2.29	2.69	2.86	2.31	2.46	2.84	2.54	2.45	2.63	2.43	2.80	2.81	2.55	2.31	2.60	2.30	2.58
Al	1.55	1.68	1.31	1.14	1.66	1.52	1.17	1.43	1.51	1.32	1.53	1.17	1.16	1.40	1.64	1.36	1.65	1.37
Ti	0.00	0.00	0.01	0.01	0.00	0.01	0.01	0.01	0.01	0.01	0.00	0.01	0.01	0.01	0.00	0.01	0.00	0.01
Fe^{2+}_T	0.01	0.01	0.01	0.02	0.02	0.01	0.02	0.02	0.03	0.01	0.01	0.01	0.01	0.01	0.01	0.01	0.01	0.01
Mn	0.00	0.00	0.00	0.00	0.00	0.00	0.00	0.00	0.00	0.00	0.00	0.00	0.00	0.00	0.00	0.00	0.00	0.00
Mg	0.00	0.00	0.00	0.02	0.00	0.00	0.00	0.00	0.00	0.00	0.00	0.00	0.00	0.00	0.00	0.00	0.00	0.00
Ca	0.59	0.74	0.35	0.16	0.73	0.55	0.20	0.48	0.58	0.40	0.60	0.23	0.21	0.48	0.74	0.44	0.75	0.45
Na	0.39	0.27	0.51	0.49	0.30	0.42	0.55	0.50	0.41	0.60	0.42	0.71	0.71	0.54	0.30	0.59	0.28	0.57
K	0.02	0.01	0.05	0.19	0.01	0.02	0.13	0.03	0.02	0.03	0.02	0.08	0.09	0.03	0.01	0.03	0.01	0.03
Cr	0.00	0.00	0.00	0.00	0.00	0.00	0.00	0.00	0.00	0.00	0.00	0.00	0.00	0.00	0.00	0.00	0.00	0.00
Ni	0.00	0.00	0.00	0.00	0.00	0.00	0.00	0.00	0.00	0.00	0.00	0.00	0.00	0.00	0.00	0.00	0.00	0.00
Ba	0.00	0.00	0.00	0.00	0.00	0.00	0.00	0.00	0.00	0.00	0.00	0.00	0.00	0.00	0.00	0.00	0.00	0.00
Total	4.99	5.00	4.94	4.90	5.02	5.00	4.91	5.00	5.01	5.02	5.02	5.01	5.01	5.02	5.02	5.02	5.02	5.02
An #	60	73	40	25	71	57	26	49	59	40	59	24	23	47	71	43	73	44
An	59.30	72.65	37.91	19.39	70.28	55.59	22.33	47.69	57.59	38.71	57.92	22.46	21.17	45.48	70.19	41.72	71.92	43.00
Ab	38.90	26.43	56.15	57.90	28.87	42.40	63.00	49.56	40.46	58.35	40.50	69.50	69.66	51.95	28.90	55.87	27.23	54.14
Or	1.79	0.92	5.94	22.70	0.85	2.01	14.67	2.76	1.95	2.94	1.58	8.04	9.17	2.57	0.91	2.41	0.86	2.86
Name	Lab.	Byt.	And.	Olig.	Byt.	Lab.	Olig.	And.	Lab.	And.	Lab.	Olig.	Olig.	And.	Byt.	And.	Byt.	And.

Sample	TOD45 MOG						TOD47 FOG								TOD26 FG		
Point	2/4	3/5 C	3/6 R1	3/7 R2	9/15 C	9/16 R	5/2 C	5/3 R	3/10 C	3/9 R1	3/11 R2	8/13	8/14	17/24	1/10 C	1/11 R	4/13
SiO_2	52.26	53.30	52.46	51.65	49.76	50.19	49.16	53.13	44.48	48.23	45.72	48.62	56.47	50.18	51.54	58.37	52.33
TiO_2	0.11	0.11	0.11	0.08	0.09	0.11	0.08	0.21	0.10	0.14	0.14	0.09	0.13	0.13	0.11	0.14	0.11
Al_2O_3	29.31	29.24	29.94	30.32	31.61	31.46	29.57	27.11	26.51	24.37	25.34	28.67	24.70	29.64	30.07	26.73	29.98
FeO_T	0.39	0.41	0.47	0.44	0.44	0.46	0.41	0.42	0.35	0.36	0.43	0.35	0.37	0.43	0.24	0.25	0.23
MnO	0.00	0.01	0.01	0.00	0.02	0.00	0.01	0.01	0.01	0.00	0.00	0.00	0.00	0.00	0.02	0.00	0.00
MgO	0.05	0.05	0.04	0.04	0.06	0.05	0.03	0.04	0.02	0.03	0.03	0.02	0.01	0.02	0.01	0.01	0.01
CaO	12.94	12.55	13.30	13.85	15.23	15.01	14.83	11.45	14.01	10.96	12.76	14.21	8.57	14.34	13.48	8.90	12.69
Na_2O	4.18	4.33	4.02	3.73	2.93	3.09	3.16	4.80	3.40	5.01	4.12	3.44	5.74	3.49	3.81	5.65	4.11
K_2O	0.44	0.48	0.41	0.37	0.23	0.24	0.23	0.54	0.27	0.55	0.28	0.26	0.93	0.28	0.31	0.82	0.37
Cr_2O_3	0.01	0.00	0.01	0.00	0.00	0.00	0.00	0.01	0.01	0.00	0.02	0.01	0.00	0.00	0.00	0.01	0.00
NiO	0.00	0.00	0.00	0.00	0.01	0.00	0.00	0.01	0.00	0.01	0.01	0.00	0.00	0.00	0.00	0.00	0.00
BaO	0.02	0.02	0.00	0.00	0.00	0.00	0.02	0.01	0.00	0.03	0.02	0.03	0.04	0.02	0.01	0.07	0.00
Total	99.70	100.50	100.77	100.48	100.37	100.60	97.51	97.74	89.16	89.68	88.87	95.69	96.97	98.53	99.62	100.94	99.84
Structural formula per 8 O																	
Si	2.39	2.41	2.37	2.35	2.27	2.28	2.31	2.47	2.30	2.46	2.36	2.33	2.62	2.33	2.36	2.59	2.38
Al	1.58	1.56	1.60	1.62	1.70	1.69	1.64	1.48	1.61	1.46	1.54	1.62	1.35	1.62	1.62	1.40	1.61
Ti	0.00	0.00	0.00	0.00	0.00	0.00	0.00	0.01	0.00	0.01	0.01	0.00	0.00	0.00	0.00	0.00	0.00
Fe^{2+}_T	0.01	0.02	0.02	0.02	0.02	0.02	0.02	0.02	0.02	0.02	0.02	0.01	0.01	0.02	0.01	0.01	0.01
Mn	0.00	0.00	0.00	0.00	0.00	0.00	0.00	0.00	0.00	0.00	0.00	0.00	0.00	0.00	0.00	0.00	0.00
Mg	0.00	0.00	0.00	0.00	0.00	0.00	0.00	0.00	0.00	0.00	0.00	0.00	0.00	0.00	0.00	0.00	0.00
Ca	0.63	0.61	0.64	0.67	0.74	0.73	0.75	0.57	0.78	0.60	0.71	0.73	0.43	0.71	0.66	0.42	0.62
Na	0.37	0.38	0.35	0.33	0.26	0.27	0.29	0.43	0.34	0.49	0.41	0.32	0.52	0.31	0.34	0.49	0.36
K	0.03	0.03	0.02	0.02	0.01	0.01	0.01	0.03	0.02	0.04	0.02	0.02	0.06	0.02	0.02	0.05	0.02
Cr	0.00	0.00	0.00	0.00	0.00	0.00	0.00	0.00	0.00	0.00	0.00	0.00	0.00	0.00	0.00	0.00	0.00
Ni	0.00	0.00	0.00	0.00	0.00	0.00	0.00	0.00	0.00	0.00	0.00	0.00	0.00	0.00	0.00	0.00	0.00
Ba	0.00	0.00	0.00	0.00	0.00	0.00	0.00	0.00	0.00	0.00	0.00	0.00	0.00	0.00	0.00	0.00	0.00
Total	5.02	5.01	5.01	5.01	5.01	5.01	5.02	5.01	5.07	5.07	5.07	5.03	4.99	5.02	5.01	4.97	5.00
An #	63	62	65	67	74	73	72	57	69	55	63	70	45	69	66	47	63
An	61.54	59.88	63.14	65.83	73.20	71.86	71.22	55.10	68.39	53.00	62.10	68.50	42.71	68.32	64.98	44.28	61.70
Ab	35.97	37.39	34.54	32.08	25.48	26.77	27.46	41.80	30.04	43.84	36.28	30.01	51.77	30.09	33.24	50.87	36.16
Or	2.49	2.73	2.32	2.09	1.32	1.37	1.32	3.09	1.57	3.17	1.62	1.49	5.52	1.59	1.78	4.86	2.14
Name	Lab.	Lab.	Lab.	Lab.	Byt.	Byt.	Byt.	Lab.	Lab.	Lab.	Lab.	Lab.	And.	Lab.	Lab.	And.	Lab.

Sample	TOD26 FG cont.					TOD13C FMG										
Point	7/16 C	7/17 R	10/19	12/20 C	12/21 R	2/1 R	2/3 C	4/5 I	4/23 Rep. of 5	4/6 R1	4/7 R2	4/8 R3	4/9 C	10/7 C	10/8 R1	10/9 R2
SiO_2	48.60	54.60	51.73	52.41	56.55	51.81	52.85	68.08	69.02	62.61	53.00	61.19	51.06	52.73	58.96	59.79
TiO_2	0.11	0.16	0.09	0.12	0.13	0.12	0.13	0.24	0.21	0.09	0.12	0.11	0.12	0.11	0.17	0.13
Al_2O_3	27.62	25.31	30.57	30.01	28.42	28.95	28.49	19.47	20.26	23.21	27.70	23.39	27.91	29.67	27.61	27.42
FeO_T	0.23	0.24	0.27	0.23	0.20	0.31	0.35	0.25	0.22	0.40	0.31	0.34	0.32	0.31	0.35	0.32
MnO	0.01	0.00	0.01	0.00	0.00	0.02	0.00	0.01	0.00	0.00	0.00	0.00	0.01	0.01	0.00	0.00
MgO	0.01	0.01	0.03	0.02	0.01	0.01	0.02	0.00	0.00	0.02	0.01	0.02	0.01	0.02	0.01	0.02
CaO	13.10	9.31	13.59	13.17	10.75	12.82	12.66	0.85	0.86	5.61	12.24	6.26	12.66	12.50	9.40	8.94
Na_2O	4.17	5.38	3.71	3.75	4.70	4.34	4.25	1.46	1.43	6.37	4.58	6.27	4.28	4.27	5.17	5.43
K_2O	0.34	0.82	0.30	0.36	0.55	0.30	0.36	11.67	11.58	1.60	0.32	1.21	0.28	0.26	0.59	0.65
Cr_2O_3	0.00	0.00	0.00	0.01	0.00	0.00	0.00	0.01	0.00	0.00	0.00	0.00	0.00	0.00	0.00	0.01
NiO	0.00	0.00	0.01	0.00	0.00	0.00	0.00	0.00	0.00	0.00	0.00	0.01	0.01	0.01	0.00	0.00
BaO	0.01	0.03	0.01	0.00	0.03	0.01	0.02	0.29	0.29	0.15	0.02	0.09	0.01	0.01	0.02	0.04
Total	94.20	95.86	100.32	100.09	101.35	98.70	99.12	102.35	103.89	100.07	98.29	98.88	96.66	99.91	102.28	102.76
Structural formula per 8 O																
Si	2.36	2.57	2.35	2.38	2.51	2.39	2.42	3.01	3.00	2.78	2.45	2.75	2.41	2.58	2.40	2.60
Al	1.58	1.40	1.64	1.61	1.49	1.57	1.54	1.01	1.04	1.22	1.51	1.24	1.55	1.42	1.59	1.41
Ti	0.00	0.01	0.00	0.00	0.00	0.00	0.00	0.01	0.01	0.00	0.00	0.00	0.00	0.01	0.00	0.00
Fe^{2+}_T	0.01	0.01	0.01	0.01	0.01	0.01	0.01	0.01	0.01	0.01	0.01	0.01	0.01	0.01	0.01	0.01
Mn	0.00	0.00	0.00	0.00	0.00	0.00	0.00	0.00	0.00	0.00	0.00	0.00	0.00	0.00	0.00	0.00
Mg	0.00	0.00	0.00	0.00	0.00	0.00	0.00	0.00	0.00	0.00	0.00	0.00	0.00	0.00	0.00	0.00
Ca	0.68	0.47	0.66	0.64	0.51	0.63	0.62	0.04	0.04	0.27	0.61	0.30	0.64	0.44	0.61	0.42
Na	0.39	0.49	0.33	0.33	0.40	0.39	0.38	0.13	0.12	0.55	0.41	0.55	0.39	0.44	0.38	0.46
K	0.02	0.05	0.02	0.02	0.03	0.02	0.02	0.66	0.64	0.09	0.02	0.07	0.02	0.03	0.02	0.04
Cr	0.00	0.00	0.00	0.00	0.00	0.00	0.00	0.00	0.00	0.00	0.00	0.00	0.00	0.00	0.00	0.00
Ni	0.00	0.00	0.00	0.00	0.00	0.00	0.00	0.00	0.00	0.00	0.00	0.00	0.00	0.00	0.00	0.00
Ba	0.00	0.00	0.00	0.00	0.00	0.00	0.00	0.01	0.00	0.00	0.00	0.00	0.00	0.00	0.00	0.00
Total	5.05	5.00	5.00	4.99	4.96	5.02	5.00	4.87	4.86	4.93	5.01	4.93	5.02	4.94	5.00	4.94
An #	63	49	67	66	56	62	62	24	25	33	60	36	62	62	50	48
An	62.23	46.50	65.78	64.61	53.99	60.96	60.93	4.89	4.99	29.46	58.54	32.87	61.05	60.87	48.31	45.75
Ab	35.85	48.63	32.49	33.29	42.72	37.34	37.01	15.20	15.01	60.54	39.64	59.57	37.35	37.63	48.08	50.29
Or	1.92	4.88	1.73	2.10	3.29	1.70	2.06	79.92	80.00	10.00	1.82	7.56	1.61	1.51	3.61	3.96
Name	Lab.	And.	Lab.	Lab.	Lab.	Lab.	Lab.	Orth.	Orth.	And.	Lab.	And.	Lab.	Lab.	Lab.	And.

Sample	TOD53 FMOG						TOD75 FL			TOD55 Peg.				TOD84 Bost.					
Point	9/5 R2	9/6 R1	9/7 C	1/13 R1	1/14 R2	1/15 R3	1/25	1/26	6/30	2/3 R2	2/4 R1	2/5 C	4/7	1/26	1/27	1/28	4/32	9/39	10/40
SiO_2	57.46	57.63	50.47	60.15	52.54	55.12	55.59	57.18	56.04	51.87	51.74	51.80	52.80	68.27	75.71	75.89	75.56	76.03	76.24
TiO_2	0.11	0.11	0.13	0.10	0.13	0.12	0.13	0.10	0.13	0.10	0.09	0.09	0.11	0.02	0.03	0.01	0.08	0.04	0.05
Al_2O_3	25.56	26.00	27.71	25.18	29.16	27.76	26.29	25.49	26.52	29.32	29.04	29.31	29.50	18.86	21.23	20.93	21.56	21.10	21.19
FeO_T	0.53	0.45	0.39	0.32	0.31	0.38	0.41	0.43	0.38	0.49	0.52	0.63	0.58	0.05	0.13	0.03	0.25	0.20	0.31
MnO	0.00	0.00	0.00	0.01	0.00	0.00	0.00	0.01	0.00	0.00	0.00	0.00	0.00	0.00	0.01	0.00	0.01	0.00	0.00
MgO	0.04	0.03	0.02	0.02	0.35	0.02	0.04	0.03	0.02	0.08	0.06	0.08	0.07	0.01	0.01	0.01	0.00	0.00	0.00
CaO	8.52	8.79	12.52	7.35	12.50	10.88	10.00	8.93	10.20	13.15	13.24	13.37	13.36	0.09	0.24	0.25	0.48	0.17	0.17
Na_2O	6.49	6.45	4.41	7.03	4.43	5.39	5.58	5.91	5.35	4.17	4.21	3.99	4.01	0.82	8.97	9.24	9.10	9.13	8.38
K_2O	0.75	0.70	0.32	1.06	0.30	0.44	0.64	0.81	0.65	0.22	0.23	0.22	0.24	14.91	0.16	0.08	0.18	0.16	0.36
Cr_2O_3	0.01	0.00	0.02	0.01	0.00	0.00	0.01	0.00	0.00	0.01	0.01	0.00	0.00	0.00	0.01	0.00	0.00	0.00	0.01
NiO	0.00	0.00	0.00	0.00	0.00	0.01	0.00	0.01	0.00	0.00	0.00	0.00	0.00	0.00	0.01	0.00	0.00	0.00	0.00
BaO	0.05	0.06	0.03	0.04	0.00	0.04	0.05	0.07	0.06	0.02	0.01	0.00	0.00	0.34	0.02	0.00	0.03	0.01	0.06
Total	99.51	100.22	96.01	101.28	99.71	100.16	98.73	98.96	99.37	99.44	99.14	99.51	100.66	103.37	106.51	106.43	107.25	106.85	106.77
Structural formula per 8 O																			
Si	2.60	2.59	2.40	2.66	2.40	2.49	2.54	2.60	2.55	2.38	2.38	2.37	2.39	3.03	3.06	3.06	3.04	3.06	3.07
Al	1.36	1.38	1.55	1.31	1.57	1.48	1.42	1.37	1.42	1.58	1.57	1.58	1.57	0.99	1.01	1.00	1.02	1.00	1.00
Ti	0.00	0.00	0.00	0.00	0.00	0.00	0.00	0.00	0.00	0.00	0.00	0.00	0.00	0.00	0.00	0.00	0.00	0.00	0.00
Fe^{2+}_T	0.02	0.02	0.02	0.01	0.01	0.01	0.02	0.02	0.01	0.02	0.02	0.02	0.02	0.00	0.00	0.00	0.01	0.01	0.01
Mn	0.00	0.00	0.00	0.00	0.00	0.00	0.00	0.00	0.00	0.00	0.00	0.00	0.00	0.00	0.00	0.00	0.00	0.00	0.00
Mg	0.00	0.00	0.00	0.00	0.02	0.00	0.00	0.00	0.00	0.01	0.00	0.01	0.00	0.00	0.00	0.00	0.00	0.00	0.00
Ca	0.41	0.42	0.64	0.35	0.61	0.53	0.49	0.44	0.50	0.65	0.65	0.66	0.65	0.00	0.01	0.01	0.02	0.01	0.01
Na	0.57	0.56	0.41	0.60	0.39	0.47	0.50	0.52	0.47	0.37	0.38	0.35	0.35	0.07	0.70	0.72	0.71	0.71	0.65
K	0.04	0.04	0.02	0.06	0.02	0.03	0.04	0.05	0.04	0.01	0.01	0.01	0.01	0.84	0.01	0.00	0.01	0.01	0.02
Cr	0.00	0.00	0.00	0.00	0.00	0.00	0.00	0.00	0.00	0.00	0.00	0.00	0.00	0.00	0.00	0.00	0.00	0.00	0.00
Ni	0.00	0.00	0.00	0.00	0.00	0.00	0.00	0.00	0.00	0.00	0.00	0.00	0.00	0.00	0.00	0.00	0.00	0.00	0.00
Ba	0.00	0.00	0.00	0.00	0.00	0.00	0.00	0.00	0.00	0.00	0.00	0.00	0.00	0.01	0.00	0.00	0.00	0.00	0.00
Total	5.02	5.02	5.03	5.01	5.02	5.01	5.01	5.00	4.99	5.02	5.02	5.01	5.00	4.94	4.79	4.80	4.81	4.80	4.76
An #	42	43	61	37	61	53	50	46	51	64	63	65	65	6	1	1	3	1	1
An	40.27	41.28	59.96	34.45	59.88	51.42	47.94	43.37	49.38	62.74	62.65	64.12	63.92	0.47	1.44	1.46	2.80	1.01	1.08
Ab	55.51	54.81	38.22	59.63	38.41	46.10	48.41	51.94	46.87	36.01	36.05	34.63	34.72	7.68	97.42	97.98	95.95	97.86	96.20
Or	4.22	3.91	1.82	5.92	1.71	2.48	3.65	4.68	3.75	1.25	1.30	1.26	1.37	91.86	1.14	0.56	1.25	1.13	2.72
Name	And.	And.	Lab.	And.	Lab.	Lab.	And.	And.	Lab.	Lab.	Lab.	Lab.	Lab.	Orth.	Alb.	Alb.	Alb.	Alb.	Alb.

Rock unit abbreviations are as in Table C.1. C = core; R = rim; I. = interstice; Rep. = repeat analysis; Alb. = albite; Lab. = labradorite; And. = andesine; Byt. Bytownite; Olig. = oligoclase; Orth. = orthoclase. An # = 100xCa/(Ca+Na).

Table D.3: Microprobe analyses of pyroxenes in rocks of the Doros suite

Sample	TOD59 Chill	TOD39 BOM										TOD40 BOM					
Point	1b/23	1/11 C	1/12 R1	1/13 R2	5/19 C	5/20 R1	5/21 R2	5/22 R3	16/27 C	16/28 R1	16/29 R2	3/3	3/4	5/6	9/10 C	9/11 R	14/18
SiO_2	50.99	50.94	50.61	49.45	49.49	48.93	49.62	49.73	49.30	49.04	48.53	50.85	50.45	50.25	50.31	50.32	50.30
TiO_2	1.06	1.08	1.04	1.32	1.37	1.98	1.35	1.32	1.35	1.31	1.94	1.12	1.98	1.46	1.63	1.18	1.27
Al_2O_3	2.67	2.43	2.31	3.27	3.37	3.18	3.10	3.06	3.39	3.43	3.40	3.31	2.78	3.13	3.14	3.25	3.19
Fe_2O_3*	1.94	2.06	2.67	2.89	2.90	3.33	3.31	3.75	3.58	3.78	4.25	1.59	2.19	2.39	2.40	2.43	2.10
FeO*	5.74	5.07	4.62	4.10	4.37	3.99	4.34	3.32	3.54	3.43	3.04	5.16	5.39	4.95	5.14	4.51	4.88
MnO	0.13	0.15	0.15	0.14	0.14	0.14	0.14	0.14	0.13	0.14	0.14	0.11	0.14	0.14	0.14	0.14	0.13
MgO	15.14	15.18	15.16	14.64	14.54	14.53	15.02	14.85	14.84	14.87	14.56	15.02	14.74	14.81	14.82	14.91	14.86
CaO	21.24	21.76	21.79	21.88	21.85	21.86	21.35	21.80	21.72	21.86	21.83	21.86	21.70	21.84	21.71	21.99	21.81
Na_2O	0.39	0.36	0.36	0.40	0.42	0.47	0.40	0.59	0.47	0.37	0.56	0.37	0.53	0.41	0.44	0.38	0.38
K_2O	0.00	0.01	0.01	0.01	0.00	0.01	0.01	0.01	0.00	0.00	0.01	0.00	0.00	0.00	0.00	0.00	0.01
Cr_2O_3	0.51	0.32	0.34	0.74	0.62	0.40	0.30	0.33	0.76	0.68	0.48	0.90	0.31	0.62	0.53	0.83	0.69
NiO	0.05	0.02	0.04	0.06	0.04	0.04	0.06	0.02	0.03	0.02	0.04	0.05	0.04	0.03	0.07	0.07	0.05
BaO	0.00	0.01	0.01	0.00	0.00	0.00	0.00	0.01	0.00	0.00	0.00	0.00	0.01	0.00	0.00	0.00	0.00
Total	99.85	99.39	99.11	98.90	99.11	98.86	98.99	98.93	99.12	98.93	98.79	100.34	100.26	100.03	100.33	100.01	99.67
Structural formula per 4 cations																	
Si	1.89	1.90	1.89	1.85	1.85	1.84	1.86	1.86	1.84	1.84	1.82	1.88	1.87	1.86	1.86	1.86	1.87
Al	0.12	0.11	0.10	0.14	0.15	0.14	0.14	0.13	0.15	0.15	0.15	0.14	0.12	0.14	0.14	0.14	0.14
Ti	0.03	0.03	0.03	0.04	0.04	0.06	0.04	0.04	0.04	0.04	0.05	0.03	0.06	0.04	0.05	0.03	0.04
Fe^{2+}	0.18	0.16	0.14	0.13	0.14	0.13	0.14	0.10	0.11	0.11	0.10	0.16	0.17	0.15	0.16	0.14	0.15
Fe^{3+}	0.05	0.06	0.08	0.08	0.08	0.09	0.09	0.11	0.10	0.11	0.12	0.04	0.06	0.07	0.07	0.07	0.06
Mn	0.00	0.00	0.00	0.00	0.00	0.00	0.00	0.00	0.00	0.00	0.00	0.00	0.00	0.00	0.00	0.00	0.00
Mg	0.84	0.84	0.84	0.82	0.81	0.81	0.84	0.83	0.83	0.83	0.82	0.83	0.81	0.82	0.82	0.82	0.82
Ca	0.84	0.87	0.87	0.88	0.88	0.88	0.86	0.87	0.87	0.88	0.88	0.86	0.86	0.87	0.86	0.87	0.87
Na	0.03	0.03	0.03	0.03	0.03	0.03	0.03	0.04	0.03	0.03	0.04	0.03	0.04	0.03	0.03	0.03	0.03
K	0.00	0.00	0.00	0.00	0.00	0.00	0.00	0.00	0.00	0.00	0.00	0.00	0.00	0.00	0.00	0.00	0.00
Cr	0.01	0.01	0.01	0.02	0.02	0.01	0.01	0.01	0.02	0.02	0.01	0.03	0.01	0.02	0.02	0.02	0.02
Ni	0.00	0.00	0.00	0.00	0.00	0.00	0.00	0.00	0.00	0.00	0.00	0.00	0.00	0.00	0.00	0.00	0.00
Ba	0.00	0.00	0.00	0.00	0.00	0.00	0.00	0.00	0.00	0.00	0.00	0.00	0.00	0.00	0.00	0.00	0.00
Total	4.00	4.00	4.00	4.00	4.00	4.00	4.00	4.00	4.00	4.00	4.00	4.00	4.00	4.00	4.00	4.00	4.00
Mg #	78	80	79	80	79	79	79	80	80	80	79	80	78	79	78	80	80
Wo	44.12	45.07	45.06	46.08	45.97	45.99	44.52	45.72	45.58	45.65	46.01	45.63	45.25	45.51	45.20	45.85	45.66
En	43.76	43.75	43.62	42.90	42.57	42.53	43.58	43.33	43.33	43.21	42.69	43.63	42.77	42.94	42.93	43.25	43.28
Fs	12.13	11.19	11.33	11.01	11.46	11.48	11.90	10.95	11.09	11.13	11.30	10.74	11.98	11.55	11.86	10.90	11.06
Name	Aug.	Di.	Di.	Di.	Di.	Di.	Aug.	Di.	Di.	Di.	Di.	Di.	Di.	Di.	Di.	Di.	Di.

Sample	TOD40 BOM cont.				TOD21 IOM											TOD45 MOG	
Point	15/20 C	15/21 R1	15/22 R2	15/23 R3	1/1 R	1/2 C	3/5	9/12	10/13 R1	10/14 R2	10/15 C	21/20 C	21/21 R1	21/22 R2	21/23 R3	1/1 C	1/2 R1
SiO_2	50.72	50.78	51.06	50.50	50.47	51.47	48.77	50.55	52.07	51.20	50.24	51.01	50.00	50.31	50.12	50.40	51.03
TiO_2	1.68	1.10	1.04	1.53	1.40	1.07	1.85	1.45	1.28	1.63	1.33	1.13	1.33	1.21	1.74	1.34	1.18
Al_2O_3	2.61	3.27	2.92	3.08	3.11	2.26	4.30	3.09	1.65	2.43	3.42	2.62	3.14	3.14	2.72	2.93	2.50
Fe_2O_3*	2.31	1.71	1.81	1.89	1.87	1.55	2.53	2.30	1.69	1.62	1.91	1.86	2.02	2.22	2.42	2.62	2.78
FeO*	5.10	5.12	5.02	5.36	5.53	5.90	5.54	5.75	5.68	6.12	5.59	5.44	5.45	4.71	5.36	5.14	5.04
MnO	0.15	0.13	0.14	0.13	0.14	0.14	0.13	0.14	0.17	0.14	0.11	0.13	0.11	0.12	0.13	0.13	0.15
MgO	15.06	15.01	14.92	14.79	14.70	15.27	14.10	14.72	15.05	14.91	14.43	15.05	14.59	14.82	14.43	14.80	15.03
CaO	21.52	21.75	22.11	21.74	21.57	21.40	21.13	21.74	21.60	21.39	21.83	21.79	21.61	21.99	21.50	21.84	21.83
Na_2O	0.52	0.38	0.39	0.43	0.44	0.38	0.44	0.37	0.65	0.52	0.39	0.35	0.36	0.38	0.58	0.38	0.45
K_2O	0.01	0.01	0.01	0.00	0.00	0.01	0.01	0.00	0.01	0.00	0.01	0.01	0.01	0.00	0.00	0.01	0.00
Cr_2O_3	0.39	0.65	0.66	0.54	0.55	0.26	0.42	0.06	0.20	0.21	0.49	0.39	0.45	0.44	0.27	0.35	0.29
NiO	0.05	0.05	0.06	0.06	0.06	0.04	0.03	0.05	0.02	0.03	0.04	0.04	0.03	0.06	0.04	0.04	0.04
BaO	0.00	0.00	0.01	0.01	0.00	0.00	0.00	0.00	0.00	0.01	0.00	0.01	0.00	0.00	0.01	0.01	0.01
Total	100.12	99.95	100.15	100.06	99.84	99.74	99.25	100.22	100.07	100.21	99.79	99.83	99.10	99.40	99.32	99.99	100.33
Structural formula per 4 cations																	
Si	1.88	1.88	1.89	1.87	1.87	1.91	1.83	1.87	1.93	1.89	1.87	1.89	1.87	1.87	1.87	1.87	1.89
Al	0.11	0.14	0.13	0.13	0.14	0.10	0.19	0.13	0.07	0.11	0.15	0.11	0.14	0.14	0.12	0.13	0.11
Ti	0.05	0.03	0.03	0.04	0.04	0.03	0.05	0.04	0.04	0.05	0.04	0.03	0.04	0.03	0.05	0.04	0.03
Fe^{2+}	0.16	0.16	0.16	0.17	0.17	0.18	0.17	0.18	0.18	0.19	0.17	0.17	0.17	0.15	0.17	0.16	0.16
Fe^{3+}	0.06	0.05	0.05	0.05	0.05	0.04	0.07	0.06	0.05	0.05	0.05	0.05	0.06	0.06	0.07	0.07	0.08
Mn	0.00	0.00	0.00	0.00	0.00	0.00	0.00	0.00	0.01	0.00	0.00	0.00	0.00	0.00	0.00	0.00	0.00
Mg	0.83	0.83	0.82	0.82	0.81	0.84	0.79	0.81	0.83	0.82	0.80	0.83	0.81	0.82	0.80	0.82	0.83
Ca	0.85	0.86	0.88	0.86	0.86	0.85	0.85	0.86	0.86	0.85	0.87	0.87	0.87	0.88	0.86	0.87	0.86
Na	0.04	0.03	0.03	0.03	0.03	0.03	0.03	0.03	0.05	0.04	0.03	0.03	0.03	0.03	0.04	0.03	0.03
K	0.00	0.00	0.00	0.00	0.00	0.00	0.00	0.00	0.00	0.00	0.00	0.00	0.00	0.00	0.00	0.00	0.00
Cr	0.01	0.02	0.02	0.02	0.02	0.01	0.01	0.00	0.01	0.01	0.01	0.01	0.01	0.01	0.01	0.01	0.01
Ni	0.00	0.00	0.00	0.00	0.00	0.00	0.00	0.00	0.00	0.00	0.00	0.00	0.00	0.00	0.00	0.00	0.00
Ba	0.00	0.00	0.00	0.00	0.00	0.00	0.00	0.00	0.00	0.00	0.00	0.00	0.00	0.00	0.00	0.00	0.00
Total	4.00	4.00	4.00	4.00	4.00	4.00	4.00	4.00	4.00	4.00	4.00	4.00	4.00	4.00	4.00	4.00	4.00
Mg #	79	80	80	79	78	79	76	77	79	78	78	79	78	80	77	78	78
Wo	44.76	45.48	46.00	45.45	45.27	44.27	45.10	44.99	44.85	44.51	45.85	45.13	45.41	45.96	45.30	45.2	44.9
En	43.58	43.67	43.20	43.03	42.92	43.96	41.87	42.38	43.48	43.17	42.17	43.37	42.66	43.10	42.30	42.6	43.0
Fs	11.66	10.85	10.80	11.52	11.81	11.77	13.03	12.63	11.67	12.31	11.98	11.49	11.93	10.95	12.40	12.1	12.1
Name	Aug.	Di.	Di.	Di.	Di.	Aug.	Di.	Aug.	Aug.	Aug.	Di.	Di.	Di.	Di.	Di.	Di.	Aug.

Sample	TOD45 MOG cont.										TOD47 FOG						
Point	1/3 R2	4/8 C	4/9 R1	4/10 R2	10/17 C	10/18 R1	10/19 R2	10/20 R3	12/23 C	12/24 R	4/1	1/4 R3	1/5 R2	1/6 R1	1/7 C	10/15	11/16 C
SiO_2	50.30	50.68	50.01	50.15	49.62	50.69	50.44	50.18	49.83	49.13	50.45	46.96	47.25	46.52	46.33	47.73	50.01
TiO_2	1.22	1.18	1.59	1.68	1.54	1.17	1.31	1.23	1.36	1.73	1.39	1.68	1.23	1.49	1.19	1.26	1.39
Al_2O_3	3.28	3.12	3.09	2.56	3.64	2.48	2.89	3.27	3.46	3.72	2.88	2.62	2.75	2.93	2.72	2.72	2.97
Fe_2O_3*	2.71	2.64	2.59	2.57	2.94	2.41	2.81	2.71	2.91	3.49	2.55	6.04	6.47	6.66	6.79	5.55	2.85
FeO*	4.93	4.81	6.18	7.07	4.74	5.57	4.97	4.97	4.40	4.55	5.58	3.41	1.22	1.36	0.79	2.25	4.94
MnO	0.13	0.13	0.14	0.19	0.13	0.16	0.15	0.14	0.12	0.14	0.14	0.16	0.14	0.14	0.11	0.15	0.12
MgO	14.68	15.04	14.21	13.92	14.49	14.89	14.83	14.72	14.61	14.35	14.69	13.94	14.81	14.52	14.56	14.68	14.65
CaO	21.97	21.94	21.56	21.48	21.91	21.64	21.87	21.79	21.94	21.93	21.68	21.28	21.96	21.76	21.87	21.83	21.97
Na_2O	0.39	0.38	0.41	0.40	0.41	0.35	0.40	0.39	0.45	0.41	0.40	0.42	0.36	0.36	0.34	0.35	0.36
K_2O	0.01	0.00	0.00	0.00	0.00	0.00	0.00	0.00	0.00	0.00	0.00	0.00	0.00	0.00	0.00	0.01	0.01
Cr_2O_3	0.62	0.45	0.06	0.00	0.44	0.29	0.34	0.60	0.62	0.47	0.06	0.02	0.13	0.11	0.19	0.14	0.06
NiO	0.03	0.04	0.06	0.03	0.05	0.04	0.06	0.03	0.05	0.04	0.04	0.03	0.04	0.04	0.02	0.02	0.03
BaO	0.00	0.00	0.00	0.00	0.00	0.00	0.00	0.00	0.00	0.00	0.00	0.00	0.00	0.00	0.00	0.00	0.00
Total	100.27	100.41	99.90	100.05	99.90	99.69	100.07	100.03	99.75	99.96	99.86	96.57	96.36	95.89	94.91	96.69	99.36
Structural formula per 4 cations																	
Si	1.86	1.87	1.87	1.87	1.84	1.89	1.87	1.86	1.85	1.83	1.88	1.82	1.82	1.80	1.81	1.83	1.87
Al	0.14	0.14	0.14	0.11	0.16	0.11	0.13	0.14	0.15	0.16	0.13	0.12	0.12	0.13	0.13	0.12	0.13
Ti	0.03	0.03	0.04	0.05	0.04	0.03	0.04	0.03	0.04	0.05	0.04	0.05	0.04	0.04	0.04	0.04	0.04
Fe^{2+}	0.15	0.15	0.19	0.22	0.15	0.17	0.15	0.15	0.14	0.14	0.17	0.11	0.04	0.04	0.03	0.07	0.15
Fe^{3+}	0.08	0.07	0.07	0.07	0.08	0.07	0.08	0.08	0.08	0.10	0.07	0.18	0.19	0.19	0.20	0.16	0.08
Mn	0.00	0.00	0.00	0.01	0.00	0.01	0.00	0.00	0.00	0.00	0.00	0.01	0.00	0.00	0.00	0.00	0.00
Mg	0.81	0.83	0.79	0.78	0.80	0.83	0.82	0.81	0.81	0.80	0.81	0.80	0.85	0.84	0.85	0.84	0.82
Ca	0.87	0.87	0.86	0.86	0.87	0.86	0.87	0.87	0.87	0.87	0.86	0.88	0.91	0.90	0.92	0.90	0.88
Na	0.03	0.03	0.03	0.03	0.03	0.03	0.03	0.03	0.03	0.03	0.03	0.03	0.03	0.03	0.03	0.03	0.03
K	0.00	0.00	0.00	0.00	0.00	0.00	0.00	0.00	0.00	0.00	0.00	0.00	0.00	0.00	0.00	0.00	0.00
Cr	0.02	0.01	0.00	0.00	0.01	0.01	0.01	0.02	0.02	0.01	0.00	0.00	0.00	0.00	0.01	0.00	0.00
Ni	0.00	0.00	0.00	0.00	0.00	0.00	0.00	0.00	0.00	0.00	0.00	0.00	0.00	0.00	0.00	0.00	0.00
Ba	0.00	0.00	0.00	0.00	0.00	0.00	0.00	0.00	0.00	0.00	0.00	0.00	0.00	0.00	0.00	0.00	0.00
Total	4.00	4.00	4.00	4.00	4.00	4.00	4.00	4.00	4.00	4.00	4.00	4.00	4.00	4.00	4.00	4.00	4.00
Mg #	78	79	75	73	78	77	78	78	79	77	77	74	79	78	79	78	78
Wo	45.6	45.3	44.9	44.6	45.8	44.7	45.2	45.3	45.9	45.8	44.92	44.72	45.69	45.62	46.03	45.57	45.57
En	42.4	43.2	41.2	40.2	42.2	42.8	42.7	42.6	42.6	41.7	42.35	40.76	42.88	42.35	42.64	42.64	42.28
Fs	11.9	11.6	13.8	15.2	12.0	12.5	12.1	12.0	11.5	12.5	12.73	14.52	11.43	12.03	11.33	11.80	12.14
Name	Di.	Di.	Aug.	Aug.	Di.	Aug.	Di.	Di.	Di.	Di.	Aug.	Aug.	Di.	Di.	Di.	Di.	Di.

Sample	TOD47 FOG cont.				TOD26 FG					TOD13C FMG					TOD53 FMOG		
Point	11/17 R1	11/18 R2	12/19	16/23	2/12	5/14	6/15	8/18	13/22	x/1	3/4	5/1	6/2	9/6	3/1 C	3/2 R	11/8 C
SiO_2	50.30	50.43	49.71	49.38	50.07	49.96	49.68	45.40	49.12	49.62	48.92	50.16	49.46	49.93	50.02	50.80	51.80
TiO_2	1.19	1.22	1.70	1.25	1.41	1.33	1.42	1.77	1.65	1.51	1.76	1.58	1.77	1.68	1.73	1.37	1.08
Al_2O_3	2.98	1.84	2.73	2.91	3.14	3.14	3.12	3.14	3.53	3.10	3.18	2.68	3.05	3.07	3.27	2.36	1.81
Fe_2O_3*	3.00	3.35	3.16	3.70	2.85	3.34	3.25	7.57	3.34	3.28	3.46	2.45	2.78	2.69	2.51	2.55	2.44
FeO*	4.53	6.20	6.06	3.70	5.21	4.83	4.62	1.46	5.64	5.94	5.62	6.65	6.80	6.32	6.55	7.13	6.95
MnO	0.14	0.21	0.16	0.13	0.14	0.15	0.13	0.15	0.15	0.15	0.16	0.18	0.18	0.14	0.15	0.20	0.20
MgO	14.91	14.07	14.18	14.80	14.51	14.58	14.51	13.62	13.81	13.85	13.75	14.01	13.61	13.98	13.91	13.96	14.10
CaO	22.04	21.55	21.39	22.02	21.95	21.89	22.02	21.79	21.70	21.54	21.68	21.50	21.44	21.70	21.68	21.30	21.63
Na_2O	0.36	0.48	0.44	0.36	0.38	0.40	0.40	0.44	0.43	0.49	0.43	0.44	0.43	0.43	0.44	0.52	0.62
K_2O	0.01	0.01	0.00	0.01	0.01	0.01	0.00	0.00	0.00	0.01	0.00	0.00	0.00	0.00	0.01	0.01	0.01
Cr_2O_3	0.25	0.01	0.01	0.23	0.03	0.03	0.03	0.01	0.00	0.00	0.00	0.01	0.01	0.00	0.00	0.00	0.01
NiO	0.03	0.04	0.02	0.04	0.01	0.04	0.00	0.03	0.02	0.01	0.02	0.01	0.02	0.03	0.02	0.03	0.01
BaO	0.00	0.01	0.01	0.01	0.00	0.00	0.00	0.01	0.00	0.00	0.00	0.00	0.01	0.01	0.01	0.00	0.00
Total	99.74	99.42	99.58	98.54	99.71	99.69	99.18	95.39	99.38	99.50	98.98	99.67	99.57	99.98	100.30	100.22	100.65
Structural formula per 4 cations																	
Si	1.87	1.90	1.86	1.86	1.87	1.86	1.86	1.78	1.84	1.86	1.85	1.88	1.86	1.86	1.86	1.89	1.92
Al	0.13	0.08	0.12	0.13	0.14	0.14	0.14	0.15	0.16	0.14	0.14	0.12	0.14	0.14	0.14	0.10	0.08
Ti	0.03	0.03	0.05	0.04	0.04	0.04	0.04	0.05	0.05	0.04	0.05	0.04	0.05	0.05	0.05	0.04	0.03
Fe^{2+}	0.14	0.19	0.19	0.12	0.16	0.15	0.14	0.05	0.18	0.19	0.18	0.21	0.21	0.20	0.20	0.22	0.22
Fe^{3+}	0.08	0.09	0.09	0.10	0.08	0.09	0.09	0.22	0.09	0.09	0.10	0.07	0.08	0.08	0.07	0.07	0.07
Mn	0.00	0.01	0.01	0.00	0.00	0.00	0.00	0.00	0.00	0.00	0.01	0.01	0.01	0.00	0.00	0.01	0.01
Mg	0.83	0.79	0.79	0.83	0.81	0.81	0.81	0.80	0.77	0.77	0.77	0.78	0.76	0.78	0.77	0.78	0.78
Ca	0.88	0.87	0.86	0.89	0.88	0.87	0.88	0.92	0.87	0.87	0.88	0.86	0.86	0.87	0.86	0.85	0.86
Na	0.03	0.03	0.03	0.03	0.03	0.03	0.03	0.03	0.03	0.04	0.03	0.03	0.03	0.03	0.03	0.04	0.04
K	0.00	0.00	0.00	0.00	0.00	0.00	0.00	0.00	0.00	0.00	0.00	0.00	0.00	0.00	0.00	0.00	0.00
Cr	0.01	0.00	0.00	0.01	0.00	0.00	0.00	0.00	0.00	0.00	0.00	0.00	0.00	0.00	0.00	0.00	0.00
Ni	0.00	0.00	0.00	0.00	0.00	0.00	0.00	0.00	0.00	0.00	0.00	0.00	0.00	0.00	0.00	0.00	0.00
Ba	0.00	0.00	0.00	0.00	0.00	0.00	0.00	0.00	0.00	0.00	0.00	0.00	0.00	0.00	0.00	0.00	0.00
Total	4.00	4.00	4.00	4.00	4.00	4.00	4.00	4.00	4.00	4.00	4.00	4.00	4.00	4.00	4.00	4.00	4.00
Mg #	79	73	74	79	77	77	77	75	74	77	77	77	75	77	74	73	73
Wo	45.51	44.60	44.49	45.78	45.54	45.33	45.78	46.17	45.53	45.11	45.52	44.88	45.00	45.23	45.25	44.30	44.71
En	42.84	40.52	41.04	42.81	41.88	42.01	41.98	40.15	40.32	40.36	40.17	40.70	39.75	40.55	40.40	40.40	40.55
Fs	11.65	14.88	14.47	11.41	12.58	12.66	12.24	13.68	14.15	14.53	14.31	14.42	15.25	14.22	14.35	15.29	14.75
Name	Di.	Aug.	Aug.	Di.	Di.	Di.	Di.	Di.	Di.	Di.	Di.	Aug.	Di.	Di.	Di.	Aug.	Aug.

Sample	TOD53 FMOG cont.				TOD75 FL			TOD55 Peg.				TOD84 Bost.					
Point	11/9 R	13/11 C	13/12 R	6/16 C	2/27	4/28	5/29	1/1 R	1/2 C	6/9	6/10 Rep. of 9	3/29 R2	3/30 R1	3/33 C	7/36 R	7/37 C	8/38
SiO_2	51.08	49.63	50.11	50.38	49.88	48.50	50.14	49.90	49.64	50.43	49.68	51.43	51.91	51.97	50.86	51.67	52.28
TiO_2	1.43	1.80	1.35	1.76	1.67	1.71	1.32	1.51	1.45	1.35	1.62	0.58	0.62	0.85	0.58	0.94	1.24
Al_2O_3	2.60	3.37	2.61	3.05	2.42	2.32	1.77	3.45	3.47	2.92	3.22	0.55	0.56	0.81	0.35	0.88	0.25
Fe_2O_3*	2.52	2.83	3.22	2.53	3.26	4.25	3.13	2.54	3.17	2.64	3.10	2.54	1.84	1.99	5.42	2.18	26.78
FeO*	6.99	6.46	6.32	6.68	6.34	6.87	7.92	5.21	4.75	5.30	5.13	13.58	13.98	10.03	15.48	10.04	2.81
MnO	0.19	0.15	0.19	0.15	0.19	0.25	0.25	0.13	0.13	0.15	0.15	0.39	0.37	0.30	0.42	0.32	0.22
MgO	13.91	13.68	13.78	14.03	14.02	13.13	13.32	14.49	14.52	14.70	14.39	9.58	9.75	12.53	6.06	12.78	0.65
CaO	21.49	21.65	21.50	21.68	21.49	21.15	21.31	21.93	21.83	21.88	21.88	20.68	20.75	20.86	19.54	20.35	2.70
Na_2O	0.61	0.47	0.54	0.47	0.44	0.41	0.40	0.37	0.41	0.38	0.39	0.96	0.92	0.75	2.06	0.72	12.07
K_2O	0.01	0.01	0.00	0.01	0.01	0.00	0.02	0.01	0.00	0.01	0.01	0.00	0.01	0.00	0.00	0.00	0.00
Cr_2O_3	0.00	0.00	0.01	0.00	0.00	0.00	0.01	0.13	0.14	0.06	0.05	0.01	0.06	0.18	0.07	0.18	0.00
NiO	0.00	0.02	0.01	0.00	0.02	0.01	0.01	0.01	0.03	0.04	0.06	0.02	0.01	0.04	0.05	0.07	0.01
BaO	0.00	0.01	0.00	0.00	0.00	0.00	0.00	0.01	0.00	0.00	0.00	0.00	0.00	0.00	0.00	0.01	0.00
Total	100.82	100.07	99.64	100.73	99.74	98.60	99.59	99.68	99.54	99.85	99.68	100.32	100.78	100.31	100.88	100.14	99.01
Structural formula per 4 cations																	
Si	1.89	1.85	1.88	1.87	1.87	1.85	1.89	1.86	1.85	1.87	1.85	1.97	1.98	1.95	1.97	1.95	2.02
Al	0.11	0.15	0.12	0.13	0.11	0.10	0.08	0.15	0.15	0.13	0.14	0.02	0.03	0.04	0.02	0.04	0.01
Ti	0.04	0.05	0.04	0.05	0.05	0.05	0.04	0.04	0.04	0.04	0.05	0.02	0.02	0.02	0.02	0.03	0.04
Fe^{2+}	0.22	0.20	0.20	0.21	0.20	0.22	0.25	0.16	0.15	0.16	0.16	0.44	0.45	0.32	0.50	0.32	0.09
Fe^{3+}	0.07	0.08	0.09	0.07	0.09	0.12	0.09	0.07	0.09	0.07	0.09	0.07	0.05	0.06	0.16	0.06	0.78
Mn	0.01	0.00	0.01	0.00	0.01	0.01	0.01	0.00	0.00	0.00	0.00	0.01	0.01	0.01	0.01	0.01	0.01
Mg	0.77	0.76	0.77	0.77	0.78	0.75	0.75	0.80	0.81	0.81	0.80	0.55	0.55	0.70	0.35	0.72	0.04
Ca	0.85	0.87	0.86	0.86	0.86	0.87	0.86	0.87	0.87	0.87	0.87	0.85	0.85	0.84	0.81	0.82	0.11
Na	0.04	0.03	0.04	0.03	0.03	0.03	0.03	0.03	0.03	0.03	0.03	0.07	0.07	0.05	0.15	0.05	0.90
K	0.00	0.00	0.00	0.00	0.00	0.00	0.00	0.00	0.00	0.00	0.00	0.00	0.00	0.00	0.00	0.00	0.00
Cr	0.00	0.00	0.00	0.00	0.00	0.00	0.00	0.00	0.00	0.00	0.00	0.00	0.00	0.01	0.00	0.01	0.00
Ni	0.00	0.00	0.00	0.00	0.00	0.00	0.00	0.00	0.00	0.00	0.00	0.00	0.00	0.00	0.00	0.00	0.00
Ba	0.00	0.00	0.00	0.00	0.00	0.00	0.00	0.00	0.00	0.00	0.00	0.00	0.00	0.00	0.00	0.00	0.00
Total	4.00	4.00	4.00	4.00	4.00	4.00	4.00	4.00	4.00	4.00	4.00	4.00	4.00	4.00	4.00	4.00	4.00
Mg #	73	73	73	74	73	69	69	78	77	77	76	52	53	65	35	65	4
Wo	44.71	45.38	44.91	44.99	44.55	44.28	44.19	45.75	45.51	45.28	45.50	44.57	44.60	43.90	44.55	42.84	10.97
En	40.27	39.90	40.05	40.51	40.44	38.25	38.44	42.06	42.12	42.33	41.64	28.73	29.16	36.69	19.23	37.44	3.68
Fs	15.02	14.72	15.03	14.50	15.00	17.47	17.37	12.20	12.37	12.39	12.86	26.70	26.24	19.41	36.22	19.72	85.35
Name	Aug.	Di.	Aug.	Aug.	Aug.	Aug.	Aug.	Di.	Di.	Di.	Di.	Aug.	Aug.	Aug.	Aug.	Aug.	Aeg.

Sample	TOD84 Bost. Cont.				
Point	18/44 C	18/45 R	19/46 C	19/47 R1	19/48 R2
SiO_2	51.83	51.53	50.82	52.46	52.74
TiO_2	0.73	0.55	0.82	2.88	2.02
Al_2O_3	0.64	0.47	0.33	0.31	0.12
Fe_2O_3*	2.35	2.48	12.32	25.67	24.02
FeO*	9.93	13.58	12.51	3.83	3.22
MnO	0.31	0.39	0.39	0.18	0.47
MgO	12.59	9.69	3.08	0.43	0.16
CaO	20.74	20.81	13.87	2.22	1.03
Na_2O	0.72	0.89	5.46	12.44	12.85
K_2O	0.00	0.02	0.00	0.00	0.00
Cr_2O_3	0.10	0.01	0.02	0.00	0.00
NiO	0.03	0.02	0.02	0.01	0.00
BaO	0.01	0.00	0.00	0.00	0.00
Total	99.99	100.44	99.64	100.43	96.63
Structural formula per 4 cations					
Si	1.96	1.97	1.99	2.00	2.07
Al	0.03	0.02	0.02	0.01	0.01
Ti	0.02	0.02	0.02	0.08	0.06
Fe^{2+}	0.31	0.43	0.41	0.12	0.11
Fe^{3+}	0.07	0.07	0.36	0.74	0.71
Mn	0.01	0.01	0.01	0.01	0.02
Mg	0.71	0.55	0.18	0.02	0.01
Ca	0.84	0.85	0.58	0.09	0.04
Na	0.05	0.07	0.42	0.92	0.98
K	0.00	0.00	0.00	0.00	0.00
Cr	0.00	0.00	0.00	0.00	0.00
Ni	0.00	0.00	0.00	0.00	0.00
Ba	0.00	0.00	0.00	0.00	0.00
Total	4.00	4.00	4.00	4.00	4.00
Mg #	65	52	19	3	1
Wo	43.51	44.62	37.92	9.31	4.99
En	36.75	28.91	11.72	2.51	1.08
Fs	19.73	26.46	50.36	88.18	93.93
Name	Aug.	Aug.	Aeg.-aug.	Aeg.	Aeg.

Fe^{2+} and Fe^{3+} calculated from perfect stoichiometry. Rock unit abbreviations are as in Table C.1. C = core; R = rim; Rep. = repeat analysis; Aug. = augite; Di. = diopside; Aeg. = aegerine.

Table D.4: Microprobe analyses of Fe-Ti oxides in rocks of the Doros suite

Sample	TOD39 BOM			TOD40 BOM						TOD45 MOG				
Point	6/8 H	10/10 H	12/11 H	6/1	6/2	11/4	11/5	12/6	12/7	7/1 A	7/2 A	7/3 A	8/5 L	8/6 H
SiO_2	0.01	0.02	0.01	0.02	0.03	0.02	0.05	0.01	0.04	7.08	7.50	6.72	0.02	0.06
TiO_2	50.42	50.61	50.18	50.38	9.03	52.36	10.80	51.03	8.47	0.17	0.11	0.14	53.29	4.35
Al_2O_3	0.08	0.08	0.07	0.10	4.03	0.04	2.59	0.10	3.95	0.75	0.48	0.42	0.04	1.35
Fe_2O_3*	8.75	8.21	8.77	7.61	37.62	5.50	38.64	6.94	39.37	81.11	78.75	80.73	0.00	56.93
FeO*	32.07	32.59	32.45	34.03	36.33	33.54	35.98	35.10	36.27	4.80	6.52	6.09	41.17	33.96
MnO	0.50	0.51	0.55	0.45	0.22	0.46	0.28	0.43	0.31	0.07	0.25	0.22	0.83	0.18
MgO	7.09	6.87	6.73	6.00	1.60	7.30	3.06	5.73	1.30	1.55	0.31	0.15	1.85	0.33
CaO	0.00	0.01	0.01	0.02	0.00	0.01	0.03	0.01	0.03	0.75	1.32	1.21	0.00	0.04
Cr_2O_3	0.52	0.41	0.42	0.41	7.07	0.24	5.98	0.39	6.50	0.01	0.00	0.00	0.00	0.03
NiO	0.10	0.11	0.10	0.10	0.43	0.06	0.28	0.11	0.40	0.03	0.03	0.01	0.02	0.16
ZnO	0.01	0.03	0.00	0.00	0.33	0.00	0.08	0.00	0.23	0.00	0.02	0.01	0.02	0.04
V_2O_5	0.21	0.00	0.18	0.29	2.27	0.00	1.61	0.24	2.08	0.04	0.02	0.01	0.18	1.33
CoO	0.03	0.04	0.03	0.03	0.05	0.02	0.01	0.03	0.05	0.00	0.00	0.01	0.02	0.01
Total	99.80	99.49	99.50	99.43	99.01	99.55	99.39	100.13	99.00	96.35	95.32	95.73	97.44	98.78
Structural formula per 3 cations for spinel group or 2 cations for haematite group														
Si	0.00	0.00	0.00	0.00	0.00	0.00	0.00	0.00	0.00	0.19	0.20	0.18	0.00	0.00
Al	0.00	0.00	0.00	0.00	0.18	0.00	0.11	0.00	0.17	0.02	0.02	0.01	0.00	0.06
Ti	0.91	0.92	0.91	0.92	0.25	0.95	0.30	0.93	0.24	0.00	0.00	0.00	1.03	0.13
Fe^{2+}	0.65	0.66	0.66	0.69	1.14	0.67	1.11	0.71	1.14	0.11	0.15	0.14	0.88	1.10
Fe^{3+}	0.16	0.15	0.16	0.14	1.06	0.10	1.08	0.13	1.11	1.60	1.58	1.62	0.00	1.65
Mn	0.01	0.01	0.01	0.01	0.01	0.01	0.01	0.01	0.01	0.00	0.01	0.00	0.02	0.01
Mg	0.25	0.25	0.24	0.22	0.09	0.26	0.17	0.21	0.07	0.06	0.01	0.01	0.07	0.02
Ca	0.00	0.00	0.00	0.00	0.00	0.00	0.00	0.00	0.00	0.02	0.04	0.03	0.00	0.00
Cr	0.01	0.01	0.01	0.01	0.21	0.00	0.17	0.01	0.19	0.00	0.00	0.00	0.00	0.00
Ni	0.00	0.00	0.00	0.00	0.01	0.00	0.01	0.00	0.01	0.00	0.00	0.00	0.00	0.00
Zn	0.00	0.00	0.00	0.00	0.01	0.00	0.00	0.00	0.01	0.00	0.00	0.00	0.00	0.00
V^{3+}	0.00	0.00	0.00	0.00	0.05	0.00	0.03	0.00	0.04	0.00	0.00	0.00	0.00	0.03
Co	0.00	0.00	0.00	0.00	0.00	0.00	0.00	0.00	0.00	0.00	0.00	0.00	0.00	0.00
Total	2.00	2.00	2.00	2.00	3.00	2.00	3.00	2.00	3.00	2.00	2.00	2.00	2.00	3.00
TiO_2	53.16	53.23	52.80	52.57	10.37	55.02	12.07	52.60	9.60	0.20	0.13	0.16	53.79	4.39
FeO	37.61	38.12	37.96	39.49	46.40	39.20	44.72	40.24	45.73	6.15	8.42	7.73	46.21	38.11
Fe_2O_3	9.23	8.65	9.24	7.94	43.23	5.78	43.21	7.16	44.67	93.65	91.45	92.11	0.00	57.50
Usp %					37.95		38.25		35.04					13.52
Ilm %	90.64	91.24	90.65	91.98		94.14		92.78		2.29	2.22	2.35	100.00	
Name	Ilm.	Ilm.	Ilm.	Ilm.	Mgt.	Ilm.	Mgt.	Ilm.	Mgt.	Haem.	Haem.	Haem.	Ilm.	Mgt.

Sample	TOD47 FOG					TOD26 FG						TOD13C FMG				
Point	6/1 L	6/2 H	13/3 L	13/4 H	13/5 H	3/1 H	3/2 L	9/3 L	11/4 H	14/5 H	14/6 L	x/1	x/2	1/3 L	1/4 H	1/5 H
SiO_2	0.01	0.14	0.00	0.13	0.04	0.05	0.03	0.01	0.05	0.06	0.04	0.04	0.55	0.08	0.05	0.04
TiO_2	49.91	1.20	51.28	1.34	0.82	5.46	53.24	54.27	4.78	5.59	50.40	9.36	6.47	49.75	6.96	6.21
Al_2O_3	0.08	1.16	0.08	1.03	0.93	3.98	0.05	0.05	3.98	2.83	0.04	3.58	2.63	0.25	4.03	2.93
Fe_2O_3*	6.79	63.02	5.37	63.45	65.00	51.38	0.00	0.00	51.39	50.11	6.48	45.03	47.56	1.29	48.94	49.45
FeO*	36.29	31.00	35.86	31.01	30.73	34.17	38.18	37.24	32.55	33.28	36.39	35.54	34.33	39.07	33.97	32.41
MnO	0.78	0.08	0.77	0.12	0.08	0.32	0.88	0.85	0.30	0.16	0.82	0.44	0.17	0.60	0.32	0.14
MgO	4.33	0.50	5.28	0.65	0.53	1.01	4.35	4.49	1.17	0.88	4.53	2.30	1.19	2.87	2.06	1.93
CaO	0.00	0.02	0.00	0.06	0.02	0.00	0.00	0.01	0.05	0.11	0.00	0.01	0.13	0.01	0.00	0.03
Cr_2O_3	0.00	0.07	0.00	0.09	0.04	0.05	0.00	0.00	0.04	0.02	0.00	0.01	0.00	0.00	0.01	0.00
NiO	0.06	0.23	0.03	0.20	0.20	0.16	0.03	0.01	0.21	0.17	0.04	0.07	0.06	0.01	0.07	0.08
ZnO	0.02	0.02	0.01	0.02	0.01	0.03	0.01	0.02	0.04	0.04	0.02	0.08	0.03	0.00	0.06	0.08
V_2O_5	0.05	1.70	0.00	1.71	1.60	1.96	0.48	0.29	1.84	1.96	0.33	1.76	2.12	0.10	1.99	1.91
CoO	0.02	0.02	0.03	0.02	0.03	0.05	0.02	0.04	0.02	0.03	0.02	0.05	0.02	0.02	0.07	0.02
Total	98.34	99.16	98.71	99.82	100.03	98.62	97.27	97.28	96.42	95.24	99.11	98.27	95.26	94.05	98.53	95.23
Structural formula per 3 cations for spinel group or 2 cations for haematite group																
Si	0.00	0.01	0.00	0.00	0.00	0.00	0.00	0.00	0.00	0.00	0.00	0.00	0.02	0.00	0.00	0.00
Al	0.00	0.05	0.00	0.05	0.04	0.18	0.00	0.00	0.18	0.13	0.00	0.16	0.12	0.01	0.18	0.14
Ti	0.93	0.03	0.95	0.04	0.02	0.16	1.01	1.02	0.14	0.17	0.94	0.26	0.19	0.98	0.20	0.18
Fe^{2+}	0.76	1.00	0.74	0.99	0.98	1.08	0.80	0.78	1.05	1.10	0.75	1.12	1.13	0.86	1.07	1.06
Fe^{3+}	0.13	1.83	0.10	1.83	1.87	1.47	0.00	0.00	1.50	1.49	0.12	1.27	1.41	0.03	1.38	1.46
Mn	0.02	0.00	0.02	0.00	0.00	0.01	0.02	0.02	0.01	0.01	0.02	0.01	0.01	0.01	0.01	0.00
Mg	0.16	0.03	0.19	0.04	0.03	0.06	0.16	0.17	0.07	0.05	0.17	0.13	0.07	0.11	0.12	0.11
Ca	0.00	0.00	0.00	0.00	0.00	0.00	0.00	0.00	0.00	0.00	0.00	0.00	0.01	0.00	0.00	0.00
Cr	0.00	0.00	0.00	0.00	0.00	0.00	0.00	0.00	0.00	0.00	0.00	0.00	0.00	0.00	0.00	0.00
Ni	0.00	0.01	0.00	0.01	0.01	0.00	0.00	0.00	0.01	0.01	0.00	0.00	0.00	0.00	0.00	0.00
Zn	0.00	0.00	0.00	0.00	0.00	0.00	0.00	0.00	0.00	0.00	0.00	0.00	0.00	0.00	0.00	0.00
V^{3+}	0.00	0.04	0.00	0.04	0.03	0.04	0.01	0.00	0.04	0.04	0.00	0.04	0.05	0.00	0.04	0.04
Co	0.00	0.00	0.00	0.00	0.00	0.00	0.00	0.00	0.00	0.00	0.00	0.00	0.00	0.00	0.00	0.00
Total	2.00	3.00	2.00	3.00	3.00	3.00	2.00	2.00	3.00	3.00	2.00	3.00	3.00	2.00	3.00	3.00
TiO_2	51.42	1.22	53.12	1.35	0.82	5.76	55.63	56.72	5.17	6.03	51.77	9.96	7.01	52.65	7.43	6.77
FeO	41.58	34.91	41.31	34.72	34.16	40.05	44.37	43.28	39.17	39.91	41.57	42.08	41.39	45.98	40.31	39.29
Fe_2O_3	7.00	63.87	5.57	63.93	65.02	54.19	0.00	0.00	55.65	54.06	6.66	47.96	51.60	1.37	52.26	53.94
Usp %		3.70		4.03	2.46	18.60			16.46	18.98		29.71	22.06		22.67	20.12
Ilm %	92.96		94.39				100.00	100.00			93.30			98.63		
Name	Ilm.	Mgt.	Ilm.	Mgt.	Mgt.	Mgt.	Ilm.	Ilm.	Mgt.	Mgt.	Ilm.	Mgt.	Mgt.	Ilm.	Mgt.	Mgt.

Sample	TOD53 FMOG						TOD75 FL				TOD55 Peg.			
Point	10/1 H	10/2 L	3/3 H	3/4 L	8/5 H	8/6 L	3/6 L	3/7 H	3/8 H	7/9	3/3 H	3/5 L	5/6 L	5/7 H
SiO_2	0.05	0.05	1.57	0.04	0.13	0.04	0.01	0.08	0.09	0.02	0.43	0.02	0.08	0.04
TiO_2	2.93	51.94	7.21	54.28	2.62	52.13	50.73	10.88	10.39	52.95	3.59	53.72	51.70	3.95
Al_2O_3	4.40	0.16	3.44	0.04	5.14	0.08	0.03	2.70	2.88	0.05	1.10	0.04	0.06	2.66
Fe_2O_3*	53.02	2.49	44.63	0.00	53.96	3.03	3.62	43.23	43.69	0.00	55.92	0.00	0.35	56.97
FeO*	30.90	38.85	36.18	37.97	31.15	37.07	42.38	39.83	39.95	41.43	33.24	39.43	41.16	33.44
MnO	0.13	0.40	0.16	0.70	0.17	0.72	1.35	0.50	0.08	0.62	0.04	1.42	1.25	0.36
MgO	1.22	4.18	1.83	3.14	1.44	5.09	1.02	0.40	0.30	0.45	0.12	2.88	2.21	0.53
CaO	0.03	0.00	0.16	0.00	0.04	0.00	0.01	0.06	0.07	0.01	0.05	0.00	0.11	0.02
Cr_2O_3	0.00	0.00	0.01	0.00	0.00	0.00	0.03	0.00	0.00	0.00	0.00	0.00	0.00	0.00
NiO	0.07	0.02	0.07	0.00	0.07	0.02	0.02	0.03	0.05	0.00	0.06	0.00	0.03	0.05
ZnO	0.08	0.00	0.03	0.00	0.07	0.00	0.01	0.19	0.14	0.02	0.02	0.02	0.03	0.10
V_2O_5	3.32	0.00	2.18	0.00	3.60	0.13	0.00	0.76	0.80	0.00	0.68	0.00	0.00	0.66
CoO	0.04	0.04	0.04	0.04	0.03	0.04	0.02	0.04	0.02	0.02	0.00	0.03	0.02	0.01
Total	96.19	98.13	97.51	96.21	98.42	98.35	99.23	98.70	98.46	95.57	95.25	97.56	97.01	98.80
Structural formula per 3 cations for spinel group or 2 cations for haematite group														
Si	0.00	0.00	0.06	0.00	0.00	0.00	0.00	0.00	0.00	0.00	0.02	0.00	0.00	0.00
Al	0.20	0.00	0.15	0.00	0.23	0.00	0.00	0.12	0.13	0.00	0.05	0.00	0.00	0.12
Ti	0.09	0.97	0.21	1.05	0.07	0.97	0.96	0.31	0.30	1.05	0.11	1.02	0.99	0.11
Fe^{2+}	1.01	0.81	1.15	0.81	0.99	0.77	0.90	1.27	1.27	0.91	1.11	0.84	0.88	1.07
Fe^{3+}	1.55	0.05	1.27	0.00	1.54	0.06	0.07	1.24	1.25	0.00	1.68	0.00	0.01	1.64
Mn	0.00	0.01	0.01	0.02	0.01	0.02	0.03	0.02	0.00	0.01	0.00	0.03	0.03	0.01
Mg	0.07	0.16	0.10	0.12	0.08	0.19	0.04	0.02	0.02	0.02	0.01	0.11	0.08	0.03
Ca	0.00	0.00	0.01	0.00	0.00	0.00	0.00	0.00	0.00	0.00	0.00	0.00	0.00	0.00
Cr	0.00	0.00	0.00	0.00	0.00	0.00	0.00	0.00	0.00	0.00	0.00	0.00	0.00	0.00
Ni	0.00	0.00	0.00	0.00	0.00	0.00	0.00	0.00	0.00	0.00	0.00	0.00	0.00	0.00
Zn	0.00	0.00	0.00	0.00	0.00	0.00	0.00	0.01	0.00	0.00	0.00	0.00	0.00	0.00
V^{3+}	0.07	0.00	0.05	0.00	0.07	0.00	0.00	0.02	0.02	0.00	0.01	0.00	0.00	0.01
Co	0.00	0.00	0.00	0.00	0.00	0.00	0.00	0.00	0.00	0.00	0.00	0.00	0.00	0.00
Total	3.00	2.00	3.00	2.00	3.00	2.00	2.00	3.00	3.00	2.00	3.00	2.00	2.00	3.00
TiO_2	3.24	53.20	7.83	56.25	2.87	54.09	49.99	11.05	10.54	53.47	3.72	55.06	52.85	4.02
FeO	38.04	44.25	43.68	43.75	37.96	42.77	46.44	45.00	45.09	46.53	38.31	44.94	46.79	37.89
Fe_2O_3	58.72	2.55	48.49	0.00	59.17	3.14	3.57	43.95	44.37	0.00	57.97	0.00	0.36	58.09
Usp %	10.72		25.27		9.60			34.98	34.17		11.65			12.55
Ilm %		97.44		100.00		96.84	96.43			100.00		100.00	99.64	
Name	Mgt.	Ilm.	Mgt.	Ilm.	Mgt.	Ilm.	Ilm.	Mgt.	Mgt.	Ilm.	Mgt.	Ilm.	Ilm.	Mgt.

Fe^{2+} and Fe^{3+} calculated from perfect stoichiometry. Rock unit abbreviations are as in Table C.1. H = host; L = lamella; A = alteration; Ilm. = ilmenite; Mgt. = magnetite; Haem. = haematite. Ulvöspinel and ilmenite mol % calculated from the procedure of Stormer (1983).

Table D.5: Microprobe analyses of amphiboles in the Doros bostonite

Sample	TOD84 Bostonite				
Point	6/34	6/35	12/41	12/42	16/43
SiO_2	53.37	50.06	50.40	53.49	50.19
TiO_2	1.54	2.02	1.92	2.35	1.90
Al_2O_3	0.63	2.87	2.42	0.36	2.55
FeO_T	24.72	16.69	17.27	23.90	17.37
MnO	0.59	0.28	0.29	0.77	0.29
MgO	6.70	11.86	11.30	6.27	11.85
CaO	1.11	8.16	7.55	0.41	7.72
Na_2O	6.78	5.00	5.38	7.07	5.45
K_2O	1.45	1.13	1.20	1.44	1.17
Cr_2O_3	0.01	0.00	0.01	0.00	0.00
NiO	0.02	0.02	0.00	0.00	0.03
BaO	0.00	0.00	0.00	0.00	0.02
Total	96.94	98.07	97.74	96.07	98.53
Structural formula per 23 O					
Si	8.18	7.46	7.55	8.24	7.47
Al	0.11	0.50	0.43	0.07	0.45
Ti	0.18	0.23	0.22	0.27	0.21
Fe^{2+}_T	3.17	2.08	2.16	3.08	2.16
Mn	0.08	0.04	0.04	0.10	0.04
Mg	1.53	2.63	2.52	1.44	2.63
Ca	0.18	1.30	1.21	0.07	1.23
Na	2.02	1.44	1.56	2.11	1.57
K	0.28	0.21	0.23	0.28	0.22
Cr	0.00	0.00	0.00	0.00	0.00
Ni	0.00	0.00	0.00	0.00	0.00
Ba	0.00	0.00	0.00	0.00	0.00
Total	15.73	15.90	15.92	15.65	15.99
Mg #	32.05	55.46	53.42	31.17	54.46
Wo	3.73	21.65	20.54	1.48	20.44
En	31.36	43.78	42.78	31.39	43.65
Fs	64.91	34.57	36.68	67.13	35.90
Name	Fe-glauc.	Mg-kat.	Richt.	Fe-glauc.	Mg-kat.

Fe-glauc. = ferro-glaucophane; Mg-kat. = magnesio-katophorite; Richt. = richterite.

Table D.6: Equilibrium conditions determined from co-existing Fe-Ti oxides using the program ILMAT (Lepage, 2003) and the geothermobarometric method of Andersen & Lindsley (1985).

Sample	**T (°C)**	**$\log_{10} fO_2$**
Basal olivine melagabbro TOD40	788.11	-14.70
	734.36	-16.54
	758.84	-15.50
Foliated olivine gabbro TOD47	617.04	-17.90
Foliated gabbro TOD26	698.49	-16.75
Foliated magnetite gabbro TOD13C	500.36	-27.81
	575.61	-22.11
Foliated leucogabbro TOD75	642.00	-20.11
Gabbro pegmatite TOD55	366.72	-39.60

Appendix E: Modelling

Table E.1: Results of MELTS fractional crystallisation modelling (pressure at 1 kbar; fO_2 at QFM)

Stage	0	1	2	3	4	5	6	7	8
Temperature (°C)	1272	1222	1172	1122	1072	1022	972	922	872
Liquid	Parent KDO16	Daughter 1	Daughter 2	Daughter 3	Daughter 4	Daughter 5	Daughter 6	Daughter 7	Daughter 8
SiO_2	47.70	47.98	47.29	46.77	55.18	59.76	63.41	66.03	68.23
TiO_2	1.20	1.40	2.07	2.92	1.30	0.74	0.47	0.31	0.21
Al_2O_3	11.98	13.81	15.22	14.15	14.57	13.43	12.51	10.44	8.39
Fe_2O_3	1.55	1.72	2.10	2.64	1.93	1.51	1.17	0.98	0.88
FeO	7.88	8.23	10.79	13.96	8.31	5.57	3.83	2.87	2.29
MnO	0.14	0.16	0.24	0.33	0.53	0.64	0.70	0.85	1.06
MgO	12.25	10.03	7.14	4.94	2.38	1.35	0.80	0.47	0.25
CaO	14.08	13.85	10.81	8.41	5.97	4.80	3.73	3.15	2.85
Na_2O	1.76	2.09	3.07	3.87	5.78	6.65	7.22	7.93	8.88
K_2O	0.37	0.44	0.77	1.21	2.33	3.18	3.88	3.78	3.04
P_2O_5	0.10	0.12	0.21	0.36	0.74	0.95	0.78	0.68	0.63
H_2O	0.13	0.16	0.28	0.46	0.97	1.41	1.86	2.49	3.29
Liquid remaining (%)	100.00	83.24	46.70	28.06	13.42	9.20	6.89	5.10	3.85
Phases crystallised (%)									
Olivine		4.14	3.20	2.67	0.86	0.34	0.18	0.06	0.02
Clinopyroxene		11.75	23.83	7.31	4.70	0.65	0.22	0.17	0.12
Plagioclase			9.52	8.65	5.64	2.50	1.59	0.75	0.15
Magnetite					3.52	0.69	0.27	0.12	0.06
Apatite						0.03	0.08	0.04	0.02
K-feldspar								0.64	0.88
Phase compositions									
Olivine		Fo86	Fo81	Fo72	Fo64	Fo56	Fo48	Fo38	Fo27
Clinopyroxene		Mg# 86	Mg# 80	Mg# 72	Mg# 69	Mg# 67	Mg# 65	Mg# 62	Mg# 55
Plagioclase			An76	An66	An53	An42	An31	An22	An17
Magnetite					Ulv50	Ulv43	Ulv38	Ulv35	Ulv35
K-feldspar								An10 Or47	An8 Or47

Table E.2: Modelled liquid REE compositions for selected Doros samples, calculated from whole-rock chemistry according to the method of Godel *et al*. (2011; see text for details).

Sample	TOD13C	TOD40	TOD45	TOD39	TOD26	TOD47	TOD53	TOD55	TOD75	TOD70	TOD63	TOD21
La	18.0	20.8	20.4	12.9	14.3	24.7	13.3	46.3	27.9	13.4	16.5	17.7
Ce	41.9	49.4	48.0	31.5	35.1	57.6	32.2	108	67.0	32.2	39.0	43.2
Pr	5.33	6.50	6.45	4.28	4.86	7.55	4.41	13.8	8.67	4.27	5.05	5.77
Nd	23.3	28.4	28.8	19.0	23.5	32.9	19.8	61.3	39.1	19.1	22.0	25.7
Sm	5.11	6.22	6.31	4.36	5.64	7.17	4.61	13.2	8.47	4.49	4.99	5.77
Eu	1.76	1.94		1.64			1.66			1.46	1.60	1.85
Gd	4.83	6.03	6.24	4.25	5.80	7.15	4.78	13.7	8.20	4.59	5.02	5.38
Tb	0.67	0.83	0.89	0.58	0.81	0.98	0.66	1.91	1.14	0.64	0.71	0.78
Dy	3.75	4.75	5.07	3.34	4.64	5.42	3.71	11.1	6.49	3.73	4.05	4.31
Y	14.4	20.8	22.4	14.2	20.2	19.7		49.3	29.0	16.5	18.0	18.8
Ho	0.66	0.85	0.90	0.58	0.81	0.99	0.65	1.97	1.13	0.66	0.72	0.76
Er	1.72	2.20	2.35	1.52	2.09	2.57	1.65	5.20	2.96	1.75	1.87	1.95
Tm	0.19	0.28	0.30	0.19	0.26	0.26	0.21	0.67	0.38	0.22	0.24	0.27
Yb	1.29	1.77	1.82	1.15	1.56	1.98	1.31	4.09	2.34	1.34	1.49	1.52
Lu	0.18	0.24	0.26	0.16	0.21	0.28	0.18	0.57	0.31	0.19	0.21	0.23

Table E.3: Partition coefficients for REE in plagioclase used in modelling of the Doros liquid, calculated from the An# using the Blundy-Wood parameters fitted by Bédard (2006a)

Sample	TOD13C	TOD40	TOD45	TOD39	TOD26	TOD47	TOD53	TOD55	TOD75	TOD70	TOD63	TOD21
An#	48	51	67	60	60	63	49	64	49	62	54	47
T (°C)	1163	1432	1237	1353	1188	1186	1238	1193	1125	1399	1489	1463
La	0.188	0.178	0.127	0.148	0.147	0.138	0.185	0.135	0.184	0.142	0.167	0.193
Ce	0.179	0.170	0.119	0.140	0.139	0.130	0.176	0.127	0.175	0.135	0.159	0.185
Pr	0.167	0.160	0.109	0.130	0.127	0.119	0.164	0.116	0.162	0.125	0.149	0.175
Nd	0.133	0.131	0.0836	0.103	0.0988	0.0913	0.133	0.0892	0.129	0.100	0.123	0.146
Sm	0.122	0.122	0.0755	0.0946	0.0895	0.0825	0.122	0.0805	0.118	0.0913	0.114	0.136
Eu												
Gd	0.0965	0.0991	0.0571	0.0743	0.0685	0.0625	0.0970	0.0609	0.0919	0.0719	0.0924	0.112
Tb	0.0843	0.0880	0.0487	0.0648	0.0588	0.0534	0.0852	0.0520	0.0798	0.0628	0.0821	0.100
Dy	0.0728	0.0775	0.0411	0.0560	0.0499	0.0451	0.0740	0.0439	0.0686	0.0543	0.0722	0.0889
Y	0.0662	0.0714	0.0368	0.0508	0.0449	0.0404	0.0676	0.0393	0.0622	0.0494	0.0665	0.0823
Ho	0.0631	0.0684	0.0348	0.0484	0.0425	0.0382	0.0645	0.0371	0.0591	0.0470	0.0637	0.0790
Er	0.0549	0.0606	0.0296	0.0421	0.0364	0.0325	0.0564	0.0316	0.0511	0.0409	0.0564	0.0705
Tm	0.0480	0.0539	0.0253	0.0368	0.0313	0.0279	0.0496	0.0270	0.0445	0.0358	0.0502	0.0633
Yb	0.0424	0.0484	0.0219	0.0325	0.0273	0.0241	0.0440	0.0234	0.0391	0.0316	0.0450	0.0571
Lu	0.0378	0.0438	0.0192	0.0290	0.0240	0.0212	0.0394	0.0205	0.0347	0.0282	0.0408	0.0520

Temperature estimates are derived from MELTS (Ghiorso & Sack, 1995) calculations of the magma liquidus; An # from microprobe analyses.

Table E.4: Partition coefficients for REE in olivine used in modelling of the Doros liquid, calculated from the melt MgO content using the Blundy-Wood parameters fitted by Bédard (2005)

Sample	TOD13C	TOD40	TOD45	TOD39	TOD26	TOD47	TOD53	TOD55	TOD75	TOD70	TOD63	TOD21
MgO (wt. %)	7.05	7.57	9.83	8.87	8.75	9.17	7.31	9.39	7.24	9.07	7.99	6.99
La	0.00006	0.00019	0.00004	0.00009	0.00004	0.00003	0.00008	0.00003	0.00004	0.00011	0.00022	0.00027
Ce	0.00014	0.00041	0.00010	0.00021	0.00010	0.00009	0.00019	0.00009	0.00011	0.00024	0.00045	0.00057
Pr	0.00032	0.00082	0.00023	0.00046	0.00023	0.00021	0.00042	0.00020	0.00025	0.00051	0.00091	0.00111
Nd	0.00154	0.00318	0.00114	0.00199	0.00118	0.00107	0.00189	0.00105	0.00128	0.00213	0.00339	0.00406
Sm	0.00238	0.00462	0.00177	0.00298	0.00184	0.00169	0.00286	0.00166	0.00201	0.00317	0.00488	0.00579
Eu	0.00387	0.00700	0.00291	0.00467	0.00304	0.00280	0.00457	0.00275	0.00332	0.00493	0.00734	0.00863
Gd	0.00612	0.0104	0.00465	0.00714	0.00486	0.00451	0.00708	0.00443	0.00533	0.00747	0.0108	0.0125
Tb	0.00941	0.0149	0.00720	0.0106	0.00755	0.00704	0.0107	0.00691	0.00829	0.0110	0.0154	0.0178
Dy	0.0140	0.0210	0.0108	0.0154	0.0114	0.0107	0.0157	0.0105	0.0125	0.0159	0.0215	0.0247
Y	0.0177	0.0257	0.0137	0.0191	0.0145	0.0136	0.0196	0.0134	0.0160	0.0196	0.0261	0.0299
Ho	0.0198	0.0282	0.0154	0.0212	0.0162	0.0153	0.0218	0.0150	0.0179	0.0217	0.0287	0.0328
Er	0.0267	0.0364	0.0208	0.0278	0.0220	0.0208	0.0290	0.0204	0.0243	0.0284	0.0368	0.0417
Tm	0.0344	0.0451	0.0269	0.0351	0.0285	0.0270	0.0369	0.0265	0.0316	0.0357	0.0454	0.0513
Yb	0.0426	0.0542	0.0335	0.0428	0.0355	0.0337	0.0453	0.0332	0.0394	0.0433	0.0543	0.0611
Lu	0.0510	0.0631	0.0403	0.0506	0.0427	0.0406	0.0538	0.0400	0.0474	0.0510	0.0631	0.0707

Melt MgO content is derived from the An # using the regression of Bédard (2009).

Table E.5: Parameters for end members used in isotopic mixing modelling of the Doros source

	Atlantic N-MORB[1]	Ave. Tristan[2]	Ave. Damaran granite[3]	Ave. Damaran metased.[4]	Pre-Damara basement[5]	GLOSS[6]
Sr (ppm)	133	672	205	118	200	327
Nd (ppm)	11.7	46	56	37	30	27
$^{87}Sr/^{86}Sr$	0.702300	0.705040	0.754420	0.777086		0.717300
$^{143}Nd/^{144}Nd$	0.513290	0.512550	0.511953	0.511927		0.512180
$(^{87}Sr/^{86}Sr)_{132}$	0.702241	0.704691	0.744625	0.766321	0.715000	0.716366
$\varepsilon_{Nd\ 132}$	12.52	-0.24	-11.35	-12.54	-22.01	-7.80

1: Sample AD-3 of O'Nions *et al*. (1977); 2: Calculated by Trumbull *et al*. (2003); 3: Calc. from McDermott *et al*. (1996) and Jung *et al*. (1998); 4: Calc. from McDermott & Hawkesworth (1990); 5: Calc. by Mingram *et al*. 2000; 6: Calc. by Plank & Langmuir (1998).

Table E.6: Partition coefficients for gabbroic sill TOD58 used in the modelling of bostonitic daughter compositions

	Plag[1]	Cpx[2]	Ol[3]	Mgt[4]
La	0.218	0.0540	0.000138	0.015
Ce	0.210	0.0980	0.000309	0.016
Pr	0.198	0.150	0.000657	0.018
Nd	0.164	0.210	0.00276	0.026
Sm	0.152	0.260	0.00409	0.024
Eu	0.730	0.310	0.00636	0.025
Gd	0.124	0.300	0.0096	0.018
Tb	0.111	0.310	0.0142	0.019
Dy	0.0980	0.330	0.0204	0.018
Ho	0.0867	0.310	0.0280	0.018
Er	0.0770	0.300	0.0366	0.018
Tm	0.0687		0.0460	0.018
Yb	0.0618	0.280	0.0558	0.018
Lu	0.0560	0.280	0.0657	0.018

1: Calculated from the Blundy-Wood Parameters fitted by Bédard (2006), from An # = 0.41 and T = 1274 °C, with the exception of Eu, which is the typical Earth value of McKenzie & O'Nions (1991), since the fO_2 for this rock is not known. 2: From the calculated values of McKenzie & O'Nions (1991). 3: Calculated from the Blundy-Wood Parameters fitted by Bédard (2005), based on the melt MgO content (derived from the An # using the regression of Bédard, 2009). 4: From the compilation of Bédard (2006b).

Appendix F: Melt inclusions

Table F.1: Major element compositions (wt. %) of daughter phases and glass in unhomogenised olivine-hosted melt inclusions

Sample	Label	SiO_2	TiO_2	Al_2O_3	FeO_T	MnO	MgO	CaO	Na_2O	K_2O	P_2O_5	Total	Phase
TOD70 (IOM)	R1-1	38.29	0.01	11.45	6.04	0.36	32.34	0.16	0.11	0.19	0.01	88.97	glass (verm. comp)
	R1-2	68.05	0.20	20.61	1.09	0.00	0.04	0.68	11.66	0.08	0.00	102.42	glass (fsp. comp)
	R1-3	55.85	0.36	14.16	6.52	0.23	11.90	1.45	5.38	2.45	0.01	98.30	?
	R1-4	0.68	0.01	0.05	0.91	0.00	0.06	56.65	0.00	0.10	40.32	98.79	apatite
	R2-MI1-1	45.69	0.00	0.30	12.91	0.36	29.80	0.42	0.04	0.18	0.01	89.72	?
	R2-MI2-1	63.86	0.24	20.63	0.83	0.03	0.75	1.36	5.44	3.40	0.05	96.59	glass (fsp. comp)
	R2-MI2-2	0.04	37.51	0.10	53.31	0.10	3.58	0.05	0.00	0.03	0.00	94.72	Ilmenite
	R2-MI2-3	45.56	4.89	10.39	8.96	0.13	15.29	11.15	3.65	0.39	0.00	100.41	kaersutite
	R2-MI2-4	35.99	0.12	13.67	11.61	0.55	25.61	0.60	0.06	0.13	0.04	88.39	glass (verm. comp)
	R2-MI2-5	52.96	0.47	2.10	6.96	0.20	15.49	21.89	1.07	0.04	0.00	101.18	augite
	R2-MI2-5	61.25	0.07	6.62	5.16	0.24	13.93	1.46	0.23	0.45	0.01	89.41	glass
	R2-MI3-1	52.50	0.24	9.68	8.93	0.44	16.07	1.51	0.25	0.53	0.00	90.15	? (crystalline phase)
	R3 MI1-1	42.16	7.31	10.99	10.06	0.06	13.46	11.66	3.78	0.30	0.03	99.81	kaersutite
	R3 MI1-2	57.33	0.07	17.72	3.44	0.07	5.02	5.66	1.10	2.43	0.00	92.84	?
	R3 MI1-3	0.15	71.16	0.06	23.25	0.00	0.03	0.08	0.00	0.03	0.00	94.76	oxide
	R3 MI1-4	66.15	0.27	19.77	1.09	0.01	0.11	1.32	3.47	2.23	0.09	94.50	glass
	R3 MI3-1	50.16	1.71	3.22	8.07	0.11	14.55	22.30	0.60	0.00	0.01	100.73	augite
	R3 MI3-2	0.02	2.16	0.71	84.48	0.00	0.58	0.12	0.00	0.02	0.00	88.09	magnetite
	R3 MI2-1	52.70	0.86	1.97	7.32	0.21	15.59	21.97	1.03	0.03	0.01	101.70	augite
	R3 MI2-2	52.22	0.92	1.97	7.73	0.16	15.57	21.78	0.91	0.02	0.02	101.30	augite
	R3 MI2-3	61.23	0.18	20.56	0.87	0.05	0.05	1.67	3.87	6.08	0.08	94.64	glass (fsp. comp)
	R3 MI2-4	38.86	0.09	11.91	11.04	0.34	26.09	0.26	0.15	0.34	0.01	89.09	glass (verm. comp)
	R3 MI2-5	61.90	0.18	20.84	0.94	0.14	0.05	1.75	4.43	4.87	0.06	95.15	glass (fsp. comp)
	R4 MI1-1	50.25	1.27	3.36	8.02	0.15	14.56	22.34	0.93	0.01	0.00	100.89	augite
	R4 MI1-2	39.07	0.02	5.97	13.37	0.16	30.46	0.13	0.12	0.31	0.02	89.62	glass (verm. comp)
	R4 MI1-3	42.40	0.07	0.77	13.93	0.23	30.08	0.23	0.00	0.12	0.00	87.83	glass (verm. comp)
	R5-MI1-1	63.05	0.12	21.35	0.61	0.00	0.12	1.65	6.09	3.12	0.10	96.21	glass (fsp. comp)
	R5-MI1-2	40.95	6.24	12.40	9.77	0.00	13.16	11.88	3.26	0.71	0.01	98.38	kaersutite
	R5-MI1-3	41.29	6.13	12.33	9.98	0.10	13.18	11.77	3.24	0.66	0.00	98.68	kaersutite
	R5-MI2-1	41.02	0.06	8.94	10.24	0.13	28.38	0.16	0.13	0.56	0.00	89.64	glass (verm. comp)

Sample	Label	SiO_2	TiO_2	Al_2O_3	FeO_T	MnO	MgO	CaO	Na_2O	K_2O	P_2O_5	Total	Phase
TOD70 (IOM) cont.	R5-MI2-2	65.13	0.18	20.83	0.65	0.00	0.02	1.08	6.27	3.23	0.08	97.47	glass (fsp. comp)
	R5-MI2-3	43.35	4.81	10.98	9.71	0.18	14.55	11.30	3.73	0.33	0.00	98.93	kaersutite
	R5-MI2-4	0.81	43.00	0.19	48.37	0.31	2.23	0.12	0.00	0.03	0.01	95.06	ilmenite
	R5-MI2-5	38.22	0.13	11.13	12.90	0.39	25.40	0.29	0.06	0.41	0.04	88.97	glass (verm. comp)
	R5-MI2-6	43.61	5.38	10.93	9.61	0.12	14.57	11.32	3.69	0.32	0.03	99.58	kaersutite
	R5-MI3-1	50.69	1.51	2.87	7.77	0.18	14.80	22.40	0.76	0.00	0.02	100.99	augite
	R5-MI3-2	54.43	0.01	0.43	18.63	0.42	26.87	0.53	0.10	0.01	0.02	101.44	opx
	R6-MI1-1	67.50	0.14	21.93	1.25	0.00	0.05	0.16	5.38	2.28	0.00	98.69	glass (fsp. comp)
	R6-MI2-1	54.35	0.44	1.08	7.33	0.19	14.69	21.89	1.69	0.01	0.00	101.67	augite
	R6-MI2-2	0.01	1.87	2.27	74.58	0.16	0.94	0.03	0.00	0.02	0.01	79.89	magnetite
	R7 MI1-1	50.33	1.26	3.43	7.64	0.07	14.76	22.33	0.59	0.00	0.00	100.41	augite
	R7 MI2-1	36.98	0.14	13.04	10.34	0.29	27.65	0.34	0.08	0.21	0.00	89.08	glass (verm. comp)
	R7 MI3-1	42.00	7.20	10.75	10.45	0.15	12.45	11.58	3.64	0.45	0.06	98.73	kaersutite
	R8-1	66.79	0.32	19.94	1.09	0.00	0.09	1.21	6.61	3.95	0.00	100.00	glass (fsp. comp)
	R8-MI2-1	50.00	1.46	3.67	7.83	0.19	14.93	22.14	0.49	0.01	0.00	100.71	augite
	R8-MI3-1	42.53	7.14	10.00	10.10	0.07	13.18	11.17	3.93	0.38	0.03	98.53	kaersutite
TOD63 (BOM)	R1 MI1-1	67.31	0.35	19.20	0.83	0.04	0.03	0.08	9.23	3.60	0.00	100.67	fsp-glass
	R2 MI-1-1	64.42	0.07	21.04	0.88	0.00	0.01	0.03	6.52	4.40	0.08	97.45	fsp-glass
	R3 MI-1-1	38.19	9.46	12.67	9.69	0.00	16.35	0.15	1.01	8.71	0.02	96.25	mixture?
	R3 MI-1-2	0.27	0.00	0.01	0.95	0.00	0.11	53.56	0.19	0.04	39.48	94.59	apatite
	R3 MI-1-3	51.62	1.37	2.53	7.44	0.08	15.39	21.86	0.96	0.03	0.01	101.28	augite
	R3 MI-2-1	44.23	6.65	8.35	9.12	0.08	14.19	10.76	4.18	0.78	0.05	98.40	kaersutite
	R4 MI-1-1	55.18	0.05	1.30	14.89	0.33	28.79	0.78	0.05	0.01	0.04	101.42	opx
	R4 MI-1-2	54.15	0.06	2.92	15.02	0.23	27.67	1.30	0.07	0.00	0.03	101.46	opx
	R4 MI-1-3	57.08	0.04	16.47	4.12	0.08	10.31	0.68	5.34	3.72	0.07	97.91	glass
	R5 MI-1-1	49.72	1.28	3.78	7.28	0.04	14.54	22.68	0.61	0.02	0.02	99.97	augite
	R5 MI-1-2	35.74	0.00	11.33	18.69	0.35	7.07	18.11	0.08	0.13	0.00	91.49	glass (verm. comp)
	R5 MI-1-3	33.92	0.03	11.61	12.91	0.23	27.61	0.62	0.14	0.09	0.01	87.17	glass (verm. comp)
	R8 MI-1-1	61.90	0.01	26.83	0.78	0.00	0.09	0.07	14.75	0.12	0.07	104.63	glass
	R6 MI-1-1	40.73	0.03	7.34	11.38	0.13	28.12	0.34	0.27	0.56	0.00	88.90	glass
	R6 MI-1-2	55.94	0.16	0.65	15.01	0.33	29.32	0.65	0.06	0.01	0.00	102.14	opx
	R6 MI-1-3	55.89	0.20	0.75	14.96	0.29	28.57	1.17	0.19	0.04	0.00	102.07	opx

Sample	Label	SiO_2	TiO_2	Al_2O_3	FeO_T	MnO	MgO	CaO	Na_2O	K_2O	P_2O_5	Total	Phase
TOD42 (BOM)	R1 MI-1-1	41.85	0.02	4.51	13.19	0.31	28.07	0.18	0.09	0.51	0.02	88.75	glass
	R1 MI-2-1	45.52	0.03	2.17	11.10	0.16	30.29	0.06	0.10	0.20	0.00	89.63	glass
	R2 MI-1-1	67.60	0.27	21.37	0.98	0.00	0.01	0.56	11.98	0.02	0.00	102.80	glass
	R2 MI-1-2	41.20	5.54	11.11	10.90	0.05	18.43	0.02	0.42	9.79	0.00	97.46	kaersutite
	R2 MI-1-3	61.45	0.20	17.32	2.47	0.13	3.07	0.07	0.13	13.25	0.00	98.10	glass
	R3 MI-1-1	0.11	0.03	0.04	0.78	0.00	0.09	42.54	0.08	0.01	0.00	43.68	?
	R4 MI-1-1	68.14	0.22	21.85	0.91	0.00	0.01	0.23	9.02	0.00	0.00	100.38	glass
	R6 MI-1-1	65.23	0.22	19.73	1.55	0.07	0.16	0.51	5.24	4.15	0.00	96.86	glass
	R8 MI-1-1	50.46	1.71	3.02	8.35	0.19	14.45	21.77	0.96	0.01	0.03	100.95	augite
	R8 MI-1-2	35.76	0.09	9.79	14.99	0.42	26.72	0.14	0.05	0.19	0.01	88.15	glass (verm. comp)
	R9 MI-1-1	68.51	0.19	20.06	1.37	0.09	0.12	0.34	11.32	0.64	0.00	102.63	glass
TOD39 (BOM)	R1 MI1	65.78	0.19	21.27	1.77	0.00	0.46	2.21	9.08	0.25	0.00	101.01	glass
	R1 MI1-1	49.86	1.40	3.79	6.99	0.05	14.18	22.06	0.96	0.01	0.02	99.32	augite
	R1 MI1-2	0.05	2.65	1.91	75.07	0.08	1.01	0.13	0.02	0.02	0.00	80.94	magnetite
	R1 MI1-3	43.95	0.03	4.41	6.79	0.02	31.06	0.28	0.10	0.51	0.03	87.17	mixture?
	R2 MI1	41.15	0.02	6.82	9.80	0.02	29.65	0.35	0.51	0.65	0.03	89.00	glass (verm. comp)
	R2 MI2-1	67.41	0.26	21.34	0.86	0.00	0.03	0.55	11.51	0.02	0.00	101.99	glass
	R2 MI2-2	53.37	0.18	0.90	7.96	0.11	14.19	21.62	1.83	0.15	0.05	100.36	augite
	R4 MI1	64.40	0.06	20.33	0.38	0.05	0.47	0.30	5.84	5.21	0.00	97.04	glass
	R4 MI2-1	0.09	0.50	5.31	70.08	0.28	2.85	0.17	0.03	0.01	0.00	79.32	magnetite
	R4 MI2-2	50.82	0.96	2.81	7.23	0.12	14.90	22.66	0.69	0.02	0.04	100.25	augite
	R4 MI2-3	36.96	10.35	13.62	13.60	0.09	12.63	0.16	0.33	9.07	0.00	96.80	amphibole?
	R4 MI2-4	43.97	0.01	2.26	5.79	0.24	35.10	0.24	0.02	0.18	0.00	87.81	glass (verm. comp)

For details of the analytical procedure see Section 2.4. Verm. = vermiculite; fsp. = feldspar; opx = orthopyroxene.

Table F.2: Uncorrected major element compositions (wt. %) of homogenised melt inclusions

Sample	Label	SiO_2	TiO_2	Al_2O_3	FeO_T	MnO	MgO	CaO	Na_2O	K_2O	P_2O_5	Total	K_D
TOD-70	g 2 mi1	49.94	2.89	10.89	21.41	0.29	6.57	2.92	3.11	0.90	0.36	99.27	0.24
	g 2 mi2	39.59	6.88	9.64	27.53	0.23	5.80	2.42	5.18	1.72	0.74	99.72	0.16
	g 3 mi1	48.92	6.07	12.57	19.68	0.22	4.16	1.83	3.96	1.76	0.75	99.92	0.16
	g 3 mi2	48.85	1.32	11.87	23.80	0.24	3.12	2.44	6.32	1.49	0.76	100.21	0.10
	g 3 mi3-3,2	50.53	1.50	14.08	18.04	0.16	4.50	2.33	4.04	2.69	1.06	98.94	0.20
	g 4 mi1	59.57	1.41	12.19	12.12	0.19	4.40	2.01	3.78	2.36	0.08	98.11	0.28
	g 5 mi1-1,2	48.39	1.20	12.56	21.18	0.21	5.16	4.19	3.59	1.61	0.78	98.85	0.19
	g 6 mi1-1,2	42.09	4.12	5.12	25.84	0.23	4.68	12.52	2.64	0.51	0.30	98.05	0.14
	g 6 mi2-2,2	51.76	3.42	11.80	18.24	0.22	5.76	2.27	3.22	1.00	0.66	98.34	0.25
	g 6 mi3	50.99	3.04	11.61	20.99	0.22	4.99	1.98	4.35	0.96	0.70	99.82	0.19
	g 6 mi4	46.43	7.15	10.96	22.17	0.26	4.10	2.44	4.33	1.00	0.72	99.56	0.15
	g 6 mi5	45.37	6.05	12.05	24.27	0.24	2.81	2.28	4.06	1.74	0.73	99.59	0.09
	g 6 mi6	48.22	1.38	8.71	25.11	0.31	2.72	6.33	4.74	1.20	0.31	99.03	0.09
	g 6 mi7	41.62	6.34	6.92	24.23	0.25	1.50	12.22	3.86	0.90	0.70	98.52	0.05
	g 8 mi1	45.81	1.32	3.38	22.64	0.24	5.14	18.55	1.56	0.24	0.09	98.97	0.18
	g 9 mi1	44.18	6.35	12.13	23.15	0.31	4.11	2.09	5.28	2.02	0.75	100.36	0.14
	g 9 mi2	47.64	4.29	12.41	20.24	0.23	4.22	2.14	4.97	2.33	1.12	99.58	0.17
	g 10 mi1-1,2	47.44	6.19	12.16	21.44	0.19	4.48	1.79	4.28	1.72	0.68	100.37	0.17
	g 10 mi2,1	46.12	5.86	13.97	19.27	0.32	5.96	4.92	1.73	0.92	0.25	99.30	0.24
	g 11 mi1,2	48.44	2.20	14.09	18.83	0.30	6.66	4.24	3.25	1.27	0.61	99.89	0.28
	g 12 mi1-1,2	41.73	3.12	9.70	27.48	0.30	6.19	8.94	1.41	0.40	0.27	99.54	0.17
	g 12 mi2	57.11	2.35	11.52	14.98	0.21	6.13	2.85	2.83	1.40	0.31	99.69	0.33
	g 12 mi3	48.22	2.17	11.23	23.89	0.28	4.27	2.89	3.70	0.95	0.58	98.19	0.14
	g 13 mi1-1,2	45.03	4.80	15.39	17.73	0.34	6.90	2.95	2.13	3.26	0.80	99.32	0.31
	g 14 mi1,2	46.84	4.82	11.04	22.65	0.32	5.37	2.66	4.29	1.77	0.57	100.34	0.18
	g 15 mi1-1,2	49.88	4.36	11.54	20.36	0.21	5.49	1.85	5.21	1.22	0.57	100.69	0.21
	g 16 mi1	47.91	3.89	12.17	20.51	0.19	5.59	2.17	5.26	1.67	0.64	99.98	0.21
	g 16 mi2-2,2	51.15	1.22	11.11	24.87	0.20	5.52	1.49	3.51	1.16	0.50	100.73	0.17
	g 17 mi1	49.10	5.79	11.31	19.00	0.25	5.49	5.58	2.41	0.98	0.21	100.12	0.22
	g 18 mi1	47.24	5.14	11.01	23.42	0.22	5.55	2.23	3.61	1.44	0.50	100.36	0.19
	g 19 mi1	50.79	6.26	12.29	16.34	0.22	6.92	2.22	2.84	1.62	0.21	99.70	0.34
	g 19 mi2	48.54	8.55	12.73	17.29	0.19	4.89	1.65	3.87	2.04	0.78	100.53	0.22
	g 20 mi1	46.93	4.18	11.68	21.84	0.24	4.60	2.10	4.94	2.03	0.86	99.39	0.16

Sample	Label	SiO_2	TiO_2	Al_2O_3	FeO_T	MnO	MgO	CaO	Na_2O	K_2O	P_2O_5	Total	K_D
TOD-70 cont.	g 21 mi1	47.17	1.08	11.53	20.02	0.22	7.11	7.91	2.26	1.01	0.26	98.56	0.29
	g 21 mi2	48.45	4.99	12.15	18.95	0.27	6.53	2.36	4.95	1.14	0.54	100.33	0.27
	R1_MI_1,1-1,2	51.57	2.30	12.98	15.98	0.17	5.87	1.69	5.80	1.48	0.55	98.39	0.29
	R1_MI_2,1	52.57	4.63	12.97	14.41	0.22	6.62	1.96	3.76	1.91	0.18	99.21	0.37
	R2_MI1,1	46.22	4.53	13.13	19.47	0.31	6.32	2.63	4.09	1.15	0.37	98.23	0.26
	R2_MI2,1	49.80	1.81	12.14	18.17	0.25	5.92	3.43	3.44	1.55	0.65	97.15	0.26
	R3_MI_1,1-1,2	48.28	4.61	9.03	17.74	0.28	7.72	6.20	1.95	1.14	0.34	97.29	0.34
	R4_MI1,1	48.28	3.34	11.04	22.81	0.17	5.00	1.80	6.02	1.20	0.65	100.31	0.17
	R4_MI_1,1-1,2	49.32	3.39	11.33	19.79	0.24	5.31	2.53	4.29	1.33	0.49	98.02	0.21
	R6_MI_1,1-1,2	49.81	5.65	12.00	17.62	0.15	6.11	1.81	3.23	2.24	0.22	98.84	0.28
	R7_MI_1,1-1,2	46.86	2.64	12.04	21.64	0.19	4.85	2.18	5.31	1.82	0.85	98.38	0.17
	R8_MI_1,1-1,2	50.03	3.36	12.33	15.59	0.16	6.91	2.05	5.34	1.33	0.59	97.70	0.35
DO-09-2	MI 1-1-2	49.32	4.53	13.18	13.34	0.13	9.23	2.40	5.87	1.36	0.44	99.79	0.51
	MI 2-1	51.29	2.57	11.30	15.22	0.21	9.09	3.83	3.41	2.10	0.27	99.30	0.44
	MI 3-1	45.25	1.57	16.10	18.17	0.16	10.32	4.99	2.36	0.66	0.25	99.84	0.41
	MI 3-2	52.68	0.79	14.97	13.46	0.11	6.50	1.98	4.74	1.41	0.61	97.25	0.35
	MI 4-1-2	50.58	2.99	12.84	15.98	0.16	9.32	2.20	3.58	1.49	0.22	99.34	0.43
	MI 5-1-2	49.87	3.10	12.28	16.86	0.19	9.70	2.42	3.03	1.28	0.47	99.18	1.14
	MI 6-1-2	53.44	2.74	13.58	11.47	0.14	8.45	1.79	5.38	2.14	0.48	99.57	0.53
	MI 7-1-2	51.85	0.45	16.45	12.82	0.18	5.44	1.97	4.84	1.79	0.68	96.45	0.31
	MI 8-1	52.50	0.25	16.25	14.39	0.25	5.06	2.20	5.12	1.49	0.73	98.24	0.26
	MI 9-1	46.40	2.12	12.97	17.85	0.18	9.08	6.95	2.70	0.80	0.45	99.50	0.37
	MI 10-1	47.18	0.73	10.61	14.88	0.23	9.44	12.57	1.68	0.43	1.54	99.30	0.46
	MI 11-1	52.53	2.84	13.97	15.02	0.23	7.47	1.93	3.33	1.92	0.10	99.34	0.37
	MI 12-1-2	44.43	3.25	13.48	21.68	0.33	10.10	3.21	1.92	0.63	0.11	99.12	0.34
	MI 13-1	51.42	1.39	11.04	20.27	0.26	7.31	2.91	2.90	1.17	0.09	98.77	0.28
	MI 13-2	50.36	3.73	12.13	18.37	0.18	6.88	3.68	2.63	1.18	0.11	99.25	0.29
	MI 15-1	55.90	2.62	12.45	12.78	0.12	7.42	2.01	3.48	1.31	0.62	98.71	0.44
DO-09-9	MI 1-1-3	51.93	4.92	13.86	12.23	0.16	7.48	3.01	4.85	1.52	0.35	100.32	0.48
	MI 1-4	48.52	6.78	12.27	16.86	0.15	8.04	2.48	3.93	1.43	0.47	100.93	0.37
	MI 3-1	52.74	4.05	12.95	15.00	0.16	5.73	3.26	2.83	1.76	0.28	98.76	0.30
	MI 4-1	50.78	1.83	12.73	22.46	0.24	3.93	2.14	4.52	1.23	0.47	100.33	0.14
	MI 5-1-2	48.59	4.97	11.70	20.17	0.18	5.20	2.44	4.41	1.38	0.46	99.49	0.20
	MI 6-1	45.55	4.22	12.72	21.65	0.28	4.88	2.34	5.71	1.87	0.82	100.04	0.18

Sample	Label	SiO_2	TiO_2	Al_2O_3	FeO_T	MnO	MgO	CaO	Na_2O	K_2O	P_2O_5	Total	K_D
DO-09-9 cont.	MI 7-1	44.54	0.91	11.73	28.85	0.23	2.91	3.77	5.10	1.22	0.76	100.02	0.08
	MI 8-1-2	36.49	4.15	14.79	30.17	0.26	3.88	8.12	1.43	0.30	0.35	99.92	0.10
	MI 9-1	54.09	5.22	10.63	14.30	0.28	7.13	2.85	3.35	1.69	0.27	99.81	0.38
	MI 9-2	56.33	2.22	12.83	13.76	0.23	6.09	2.75	2.91	1.95	0.27	99.34	0.34
	MI 10-1-2	52.78	2.75	12.86	14.71	0.19	7.13	1.73	5.65	1.31	0.61	99.68	0.38
	MI 11-1	51.12	2.65	14.39	15.56	0.20	6.99	2.25	3.90	1.59	0.66	99.31	0.35
	MI 12-1-2	47.45	6.46	13.47	16.31	0.14	6.56	2.34	5.05	1.41	0.63	99.81	0.31
	MI 13-1	55.20	2.27	13.81	13.02	0.12	6.71	2.18	3.88	1.81	0.56	99.56	0.40
	MI 14-1-3	53.60	2.39	14.37	12.56	0.16	6.72	2.67	4.41	1.83	0.20	98.90	0.42
	MI 15-1	46.80	1.16	14.51	22.13	0.32	5.68	3.10	2.77	1.70	0.78	98.94	0.20
	MI 16-1-2	48.00	1.44	17.32	14.09	0.11	8.57	6.12	3.24	1.13	0.14	100.15	0.48
	MI 17-1-2	54.77	1.08	17.24	8.96	0.16	5.48	3.36	3.83	4.03	0.61	99.50	0.47
	MI 18-1-2	53.73	3.95	12.74	14.56	0.16	6.72	2.22	3.76	2.04	0.21	100.08	0.36

Melt Mg # = 100MgO /(MgO+0.88FeO_T). Host olivine Fo content = 100Mg /(Mg+Fe). $K_D = (FeO/MgO)_{Ol}/(0.88FeO_T/MgO)_{Liq}$. See Section 2.4 for details of the analytical procedure.

Table F.3: Major element compositions (wt. %) of homogenised melt inclusions

Sample	Label	SiO_2	TiO_2	Al_2O_3	FeO_T	MnO	MgO	CaO	Na_2O	K_2O	P_2O_5	Ol. added	New K_D	Mg#	Host Fo#	T_{cryst}[a]	T_{cryst}[b]	T_{cryst}[c]
TOD70 (IOM)	g 2 mi1	49.44	2.70	10.17	21.78	0.30	8.76	2.75	2.90	0.84	0.34	0.078	0.31	44.9	72.4	1322	1277	1313
	g 3 mi1	47.91	5.49	11.21	19.93	0.23	7.99	1.63	3.41	1.51	0.68	0.164	0.31	44.8	72.2	1302	1257	1255
	g 3 mi2	46.72	1.07	9.55	23.94	0.27	9.50	2.01	5.08	1.20	0.65	0.141	0.31	44.6	72.2	1398	1323	1326
	g 3 mi3-3,2	49.90	1.38	12.92	18.83	0.19	7.46	2.16	3.70	2.46	0.97	0.102	0.31	44.5	72.2	1295	1247	1256
	g 4 mi1	60.37	1.42	12.23	12.55	0.19	4.98	2.02	3.79	2.37	0.08	0.016	0.31	44.6	72.4	1172	1155	1179
	g 5 mi1-1,2	47.77	1.08	11.25	21.77	0.23	8.73	3.78	3.21	1.45	0.70	0.129	0.31	44.8	72.8	1334	1282	1282
	g 6 mi1-1,2	42.11	3.43	4.25	25.97	0.27	10.66	10.44	2.20	0.43	0.25	0.128	0.31	45.4	71.8	1394	1336	1335
	g 6 mi2-2,2	51.91	3.31	11.39	18.88	0.23	7.36	2.21	3.11	0.97	0.63	0.053	0.31	44.1	71.6	1262	1231	1237
	g 6 mi3	49.71	2.72	10.38	21.47	0.24	8.27	1.80	3.89	0.86	0.63	0.12	0.31	43.8	71.6	1319	1271	1273
	g 8 mi1	45.30	1.18	3.00	23.15	0.26	8.92	16.48	1.38	0.21	0.08	0.14	0.31	43.8	72.0	1305	1274	1273
	g 9 mi1	43.06	5.33	10.16	23.37	0.32	9.20	1.78	4.42	1.69	0.63	0.19	0.31	44.4	71.3	1382	1312	1308
	g 9 mi2	46.71	3.80	10.97	20.92	0.25	7.96	1.91	4.39	2.06	0.99	0.136	0.31	43.5	71.3	1331	1272	1274
	g 10 mi1-1,2	46.15	5.40	10.60	21.86	0.21	8.33	1.59	3.73	1.49	0.60	0.143	0.31	43.6	72.2	1331	1278	1268
	g 10 mi2,1	45.95	5.54	13.20	19.73	0.32	7.86	4.66	1.63	0.86	0.24	0.066	0.31	44.6	72.2	1260	1237	1225
	g 11 mi1,2	48.18	2.13	13.67	19.03	0.31	7.58	4.12	3.15	1.23	0.59	0.032	0.31	44.7	72.6	1274	1239	1239
	g 12 mi2	57.52	2.38	11.70	14.91	0.21	5.79	2.89	2.87	1.42	0.32	-0.012	0.31	44.1	71.7	1186	1174	1189
	g 12 mi3	47.35	1.85	9.55	24.44	0.31	9.51	2.50	3.15	0.81	0.49	0.198	0.31	44.1	71.7	1368	1311	1307
	g 13 mi1-1,2	45.34	4.83	15.49	17.85	0.34	6.95	2.97	2.14	3.28	0.80	0	0.31	44.1	72.7	1261	1225	1217
	g 14 mi1,2	45.63	4.21	9.61	22.80	0.33	9.28	2.34	3.73	1.54	0.49	0.145	0.31	45.2	72.5	1368	1305	1300
	g 15 mi1-1,2	48.50	3.93	10.39	20.62	0.22	8.32	1.69	4.69	1.10	0.51	0.103	0.31	45.0	72.7	1330	1274	1277
	g 16 mi1	47.04	3.52	11.01	20.86	0.21	8.51	1.99	4.75	1.51	0.58	0.106	0.31	45.3	73.0	1344	1283	1284
	g 16 mi2-2,2	48.94	1.04	9.35	24.59	0.22	10.21	1.29	2.96	0.98	0.42	0.14	0.31	45.7	73.0	1390	1327	1324
	g 17 mi1	48.18	5.31	10.36	19.39	0.26	8.04	5.13	2.21	0.90	0.19	0.09	0.31	45.7	72.1	1272	1243	1239
	g 18 mi1	46.01	4.48	9.61	23.51	0.24	9.31	1.97	3.15	1.25	0.44	0.142	0.31	44.5	71.9	1361	1304	1297
	g 19 mi1	51.20	6.40	12.57	16.21	0.21	6.35	2.27	2.90	1.66	0.22	-0.02	0.31	44.2	72.2	1218	1196	1195
	g 19 mi2	47.58	7.91	11.77	17.73	0.21	7.06	1.54	3.58	1.89	0.72	0.076	0.31	44.7	72.2	1265	1227	1223
	g 20 mi1	46.02	3.64	10.16	22.34	0.26	8.88	1.86	4.30	1.76	0.74	0.157	0.31	44.6	71.4	1364	1298	1303
	g 21 mi1	47.67	1.07	11.45	20.41	0.23	7.79	7.86	2.25	1.01	0.26	0.021	0.30	43.6	72.1	1274	1244	1239
	g 21 mi2	47.93	4.79	11.68	19.10	0.27	7.56	2.28	4.76	1.10	0.52	0.037	0.29	44.5	72.1	1296	1249	1250
	R1_MI_1,1-1,2	52.16	2.30	12.96	16.39	0.18	6.50	1.69	5.79	1.48	0.55	0.018	0.30	44.6	71.6	1264	1219	1235
	R1_MI_2,1	53.61	4.86	13.61	14.08	0.21	5.46	2.05	3.94	2.00	0.19	-0.04	0.31	44.0	71.6	1195	1172	1182
	R2_MI1,1	46.65	4.41	12.77	20.06	0.32	7.75	2.57	3.98	1.12	0.36	0.047	0.31	43.9	72.0	1298	1253	1248
	R2_MI2,1	50.64	1.77	11.91	18.99	0.27	7.49	3.38	3.37	1.52	0.64	0.049	0.31	44.4	72.0	1279	1240	1244
	R3_MI_1,1-1,2	49.96	4.88	9.56	18.03	0.28	7.10	6.56	2.07	1.21	0.36	-0.029	0.31	44.4	72.0	1235	1215	1211
	R4_MI1,1	46.90	2.90	9.54	22.98	0.19	9.04	1.60	5.20	1.04	0.56	0.154	0.31	44.4	71.7	1376	1307	1310
	R4_MI_1,1-1,2	49.30	3.16	10.57	20.60	0.26	8.01	2.38	4.00	1.24	0.46	0.094	0.31	44.1	71.7	1312	1263	1266

Sample	Label	SiO_2	TiO_2	Al_2O_3	FeO_T	MnO	MgO	CaO	Na_2O	K_2O	P_2O_5	Ol. added	New K_D	Mg#	Host Fo#	T_{cryst}^a	T_{cryst}^b	T_{cryst}^c
TOD70 (IOM) cont.	R6_MI_1,1-1,2	50.06	5.55	11.80	18.03	0.16	7.01	1.79	3.17	2.20	0.22	0.029	0.31	44.1	72.4	1264	1227	1223
	R7_MI_1,1-1,2	46.44	2.34	10.66	22.33	0.22	8.98	1.96	4.70	1.61	0.75	0.149	0.31	44.9	72.0	1371	1302	1306
	R8_MI_1,1-1,2	51.63	3.55	13.03	15.67	0.16	6.16	2.16	5.64	1.41	0.62	-0.031	0.31	44.3	72.2	1245	1205	1217
DO-09-2 (BOM)	MI 1-1-2	51.02	5.15	15.00	11.91	0.11	5.41	2.70	6.68	1.55	0.51	-0.12	0.33	47.9	73.5	1214	1178	1190
	MI 2-1	53.20	2.87	12.64	14.36	0.20	6.04	4.25	3.82	2.35	0.31	-0.1	0.31	46.0	73.3	1219	1190	1194
	MI 3-1	46.11	1.74	17.81	17.60	0.14	7.50	5.50	2.61	0.73	0.28	-0.095	0.31	46.3	73.6	1246	1223	1218
	MI 3-2	54.66	0.84	15.85	13.54	0.11	5.77	2.09	5.02	1.49	0.64	-0.029	0.31	46.3	73.6	1210	1182	1201
	MI 4-1-2	52.28	3.32	14.26	15.27	0.14	6.49	2.41	3.98	1.65	0.24	-0.094	0.31	46.3	73.5	1232	1202	1209
	MI 6-1-2	56.01	3.15	15.67	9.69	0.11	4.16	2.03	6.20	2.46	0.55	-0.13	0.31	46.5	73.8	1164	1139	1155
	MI 7-1-2	53.77	0.47	17.07	13.28	0.19	5.60	2.04	5.02	1.86	0.70	-0.001	0.31	46.1	73.4	1208	1179	1196
	MI 8-1	52.88	0.24	15.95	14.99	0.26	6.30	2.17	5.03	1.46	0.72	0.037	0.31	46.0	73.3	1237	1202	1218
	MI 9-1	47.15	2.25	13.81	17.58	0.18	7.46	7.38	2.87	0.86	0.47	-0.056	0.31	46.2	73.5	1250	1224	1221
	MI 10-1	48.76	0.82	12.02	13.89	0.22	5.99	14.21	1.90	0.49	1.75	-0.111	0.31	46.6	73.8	1158	1162	1157
	MI 11-1	53.56	2.99	14.69	14.71	0.23	6.19	2.02	3.50	2.02	0.11	-0.043	0.31	46.0	73.2	1217	1192	1200
	MI 12-1-2	45.10	3.40	14.13	21.78	0.33	9.12	3.36	2.01	0.66	0.12	-0.038	0.31	45.9	73.2	1317	1278	1266
	MI 13-1	51.62	1.37	10.83	20.66	0.27	8.30	2.86	2.85	1.15	0.09	0.032	0.31	44.9	72.4	1303	1262	1262
	MI 13-2	50.50	3.69	11.99	18.63	0.18	7.48	3.64	2.60	1.17	0.11	0.019	0.31	44.9	72.4	1259	1230	1226
	MI 15-1	58.34	2.88	13.74	11.91	0.11	4.88	2.20	3.84	1.45	0.68	-0.083	0.31	45.4	72.8	1152	1144	1164
DO-09-9 (BOM?)	MI 1-1-3	53.30	5.44	15.32	10.80	0.14	4.31	3.29	5.36	1.68	0.39	-0.098	0.31	44.7	72.2	1151	1136	1139
	MI 1-4	48.62	7.07	12.80	16.27	0.14	6.47	2.57	4.10	1.49	0.49	-0.05	0.31	44.6	72.2	1237	1206	1202
	MI 3-1	53.26	4.06	13.00	15.28	0.17	6.07	3.27	2.84	1.77	0.28	0.009	0.31	44.6	72.2	1203	1185	1187
	MI 5-1-2	47.75	4.51	10.62	20.73	0.20	8.24	2.24	4.00	1.25	0.42	0.107	0.31	44.6	72.2	1320	1269	1264
	MI 6-1	44.55	3.71	11.15	22.06	0.29	8.75	2.09	5.01	1.64	0.72	0.14	0.31	44.6	72.2	1367	1298	1294
	MI 9-1	55.10	5.51	11.23	13.75	0.28	5.53	3.00	3.54	1.79	0.29	-0.052	0.31	44.9	72.5	1186	1169	1173
	MI 9-2	57.11	2.28	13.19	13.62	0.23	5.48	2.82	2.99	2.01	0.28	-0.021	0.31	44.9	72.5	1178	1165	1177
	MI 10-1-2	53.74	2.89	13.56	14.23	0.17	5.64	1.81	5.95	1.38	0.64	-0.049	0.31	44.6	72.1	1222	1187	1203
	MI 11-1	51.92	2.75	14.95	15.37	0.19	6.10	2.33	4.05	1.65	0.69	-0.031	0.31	44.6	72.1	1221	1193	1202
	MI 12-1-2	47.53	6.46	13.48	16.35	0.14	6.60	2.34	5.05	1.41	0.63	0.001	0.31	45.0	72.5	1255	1215	1215
	MI 13-1	56.52	2.41	14.71	12.36	0.10	4.94	2.31	4.13	1.93	0.60	-0.057	0.31	44.7	72.3	1168	1152	1168
	MI 14-1-3	55.42	2.59	15.60	11.77	0.14	4.62	2.88	4.79	1.99	0.21	-0.069	0.31	44.3	71.9	1164	1146	1158
	MI 15-1	46.32	1.05	13.14	22.65	0.33	8.90	2.83	2.51	1.54	0.70	0.116	0.31	44.3	72.0	1337	1287	1284
	MI 16-1-2	49.23	1.62	19.51	12.65	0.08	5.00	6.86	3.65	1.27	0.16	-0.114	0.31	44.5	72.1	1155	1147	1142
	MI 17-1-2	56.38	1.17	18.64	7.79	0.14	3.13	3.61	4.14	4.36	0.66	-0.071	0.31	44.8	72.5	1114	1102	1100
	MI 18-1-2	54.22	4.08	13.15	14.21	0.15	5.72	2.28	3.88	2.11	0.22	-0.032	0.31	44.9	72.5	1205	1180	1188

Major elements are corrected for olivine host wall crystallisation (see Section 2.4). Melt Mg # = $100MgO/(MgO+0.88FeO_T)$. Host olivine Fo # = $100Mg/(Mg+Fe)$. $K_D = (FeO/MgO)_{Ol} /(0.88FeO_T/MgO)_{Liq}$. Temperatures of crystallisation are a) from eqn. 14 of Putirka (2008) using the composition of the melt only; b) from eqn. 15 of Putirka (2008), similar to (a) but considering the effect of pressure at 1 kbar; and c) from eqn. 22 of Putirka (2008) assuming olivine-liquid equilibrium.

Table F.4: Trace element compositions (ppm) of homogenised melt inclusions determined by ion probe

Sample	Label	Rb	Sr	Y	Zr	Nb	Ba	La	Ce	Sm	Eu	Gd	Dy	Er	Yb	Pb	Th
TOD70 (IOM)	g 3 mi1	21.7	1013	31.5	378	42.8	632	57.4	134	14.6	2.49	22.4	7.84	3.36	2.51	11.4	3.29
	g 3 mi2	19.5	1370	40.5	449	55.0	791	79.9	197	17.9	3.19	31.2	9.50	3.74	3.14	16.5	3.93
	g 6 mi1-1,2	16.0	733	109.6	207	27.4	414	40.7	89.7	14.0	1.87	21.1	22.0	9.67	5.68	15.7	1.96
	g 16 mi2-2,2	16.9	629	21.4	187	22.0	318	28.9	69.8	11.3	0.78	13.6	6.54	2.43	1.48	4.94	1.60
	g 21 mi2	15.9	1662	50.8	377	37.6	675	55.8	136	16.6	4.82	25.0	11.4	4.60	3.44	8.56	3.06

See Section 2.4 for details of the analytical procedure.

Appendix G: Geophysical data

Table G.1: Measured magnetic susceptibilities (*k*) for selected samples

Sample	Rock type	*k* (SI x10^3)
Doros Complex		
TOD40	BOM	9.96
		9.42
		8.65
TOD41	BOM	9.90
		10.1
TOD70	IOM	6.58
		6.86
TOD45	MOG	6.72
		6.09
		6.11
TOD22	FOG	13.5
		12.0
TOD26	FG	2.81
		2.60
TOD13B	FMG	9.84
		10.0
TOD13C	FMG	39.4
		35.2
TOD53	FMOG	21.7
		26.9
TOD79	Mgt. Cum.	485
		553
		550
TOD77	Cpx. Cum.	3.25
TOD66	Bostonite	10.3
		6.83
		9.62
		8.51
TOD58	Gabbroic sill	70.4
		58.5
		59.7
		72.3

Sample	Rock type	*k* (SI x10^3)
Other lithologies		
TOD80	Dolerite	57.8
		57.2
TOD4	Damaran schist	2.96
		1.92
		2.33
TOD2	Damaran schist	0.0663
		0.0540
TOD61	Damaran schist	17.5
		18.4
		18.3

Measurements were made with a SM30 instrument, except for samples TOD58, TOD61 and TOD66, where a GMS-2 instrument was used. Readings for the latter were corrected by calibration using repeat measurements. All measurements are also corrected for approximate sample thickness. BOM = basal olivine melagabbro; IOM = intrusive olivine melagabbro; MOG = massive olivine gabbro; FOG = foliated olivine gabbro; FG = foliated gabbro; FMG = foliated magnetite gabbro; FMOG = foliated magnetite olivine gabbro; Mgt. Cum. = magnetite cumulate enclave; Cpx. Cum. = clinopyroxene cumulate enclave.

Table G.2: Typical densities for the Doros intrusion and host rocks

Rock type	Density (g/cm^3)
Basal ol. melagabbro	3.22
Intrusive ol. melagabbro	3.20
Massive ol. gabbro	2.98
Foliated ol. gabbro	3.03
Foliated gabbro	2.95
Foliated mgt. gabbro	3.09
Foliated mgt. ol. gabbro	3.30
Gabbro pegmatite	2.89
Foliated leucogabbro	2.84
Cpx. cumulate enclave	3.17
Bostonite	2.85
Chilled gabbroic sill	3.04
Dolerite	3.07
Granite	2.64
Sediments	2.50

Values for Doros gabbros are averages calculated from the CIPW volume norm; for granite and sediments from Telford *et al*. (1990).